KU LEUVEN

ARENBERG DOCTORAL SCHOOL
Faculty of Engineering Technology

Subwavelength Barium Titanate Pockels modulation through transparent conductive oxide nanopillars

Exploring models for hologram construction from evanescent fields

Guillaume Croes

Dissertation presented in partial fulfillment
of the requirements for the degree of
Doctor of Engineering Technology (PhD)

Supervisor:
Prof.dr.ir. J. Genoe

March 2025

SUBWAVELENGTH BARIUM TITANATE POCKELS MODULATION THROUGH TRANSPARENT CONDUCTIVE OXIDE NANOPILLARS

EXPLORING MODELS FOR HOLOGRAM CONSTRUCTION FROM EVANESCENT FIELDS

Guillaume CROES

Supervisor:
Prof.dr.ir. J. Genoe

Members of the
Examination Committee:
Prof.dr. B. Lauwers, chair
dr. R. Gehlhaar
Prof.dr. C. Merckling
Prof.dr. P. Van Dorpe
Prof.dr.ir. M. Kraft
Prof.dr. C. Fleischmann
dr. Z. Tokei (imec)
Prof.dr.ir. D. Van Thourhout (UGent)
Prof.dr. P. Ghosez (ULiège)

Dissertation presented in partial fulfillment of the requirements for the degree of Doctor of Engineering Technology (PhD)

In collaboration with:

March 2025

Preface

Done. Thesis written. PhD finished. It perhaps took a while to get here, but only when I look at a calendar. It didn't feel like that at all as for me personally, the last several years flew by. It's funny how that goes. It almost feels like yesterday that I started my PhD as totally inexperienced researcher who was immediately tasked with supervising a master thesis student. Together, we looked at various materials in imec's renowned III-V Lab as building block for our metamaterial and eventually learned that knowledge gathered there would not easily transfer to the 300mm line. Instead, we pivoted our focus to the 300mm line which lead to a string of new faces from all kinds of teams found at imec. In most of these the general consensus was rather sceptical. Videoholography asked for too much, the processes do not exist or the bandwidth was to limited. We retorted with "let's just try it as a short test", "push it as far as you can go" or "whenever you have time suits us" and luckily for us, everyone agreed to give Jan's idea a fair chance. To our surprise, all of these short loop tests were successful and arrived more timely than expected. I still remember vividly how the impossible etching recipe was found just after two test wafers. I take it as a sign of just how great the process responsibles are at their stuff.

At the same time, I fostered another master student with whom I looked at optical simulations. I was awarded an FWO strategic basic scholarship. The coronavirus performed a hold-up on the entire world and blocked me from going to my first conference, kept everyone in work from home mode for quite a while and lead to nearly catastrophic shortage of toilet paper. The years after, even when everything went slowly back to normal the virus was always there. It was weird when you think of it now. Two years later I finally got the chance to go to a conference in person, where I presented the theoretical background of the envisioned holographic display. The following year, I attended another conference now centered specifically around holography and presented a more elaborated theoretical model. I managed to successfully submit and defend my first peer reviewed manuscript covering the optical and electrical

properties of the now created metamaterial. I attended a summer school on entrepreneurship which I dreaded at first, but I have to admit was incredibly interesting. Afterwards, I was finally ready to pour the theoretical background into an manuscript which got published a few months later. Given that I now had the right mindset going, I immediately started working on another paper on hologram synthesis when subwavelength features are employed. It was quite busy for a while.

That is five years summarized in two paragraphs. I probably forgot to mention quite a bit. What I won't forget though is all the people that enabled my PhD to happen. It's a long list and I am grateful to all of you. I think it's safe to say that I am able to call many of my colleagues friends as well. I'd like to first thank Jan who took me under his wing when I was still a master student myself and gave me the opportunity to do a PhD. I'd like to thank Robert for his daily guidance, great chats and bicycle rides. I'd like to thank Clement and Philippe for enabling me to get some great measurement results. This PhD greatly benefited from them. I want to also thank Cedric and Roelof for making sure I had a great team to perform my research in. Hence, I can't forget to mention the entire TFLOL and PMICRO teams. I'd like to thank Tsang, Saeed, Marina, Vitaly, Kevin and Halil for simply being great colleagues, helping me when needed and always being available to bounce ideas off. I'd like to thank the coffee corner gang for all the laughs, interesting talks and scientific discussions. Robert, Karim, Nirav, Iakov, Tibor, Yannick, the list goes on. I also owe thanks to Paul and Sarah who made sure that the large area electronics department and later the sensors and actuators technologies department were home to great fundamental research pushing the boundaries of what is possible. I can't forget the rest of the department, Bart, Myriam, Frederik, Steve, Geert, Dirk, ... you were always there when I needed assistance with something. I won't forget that. I'd like to also thank some people from my personal circle. I want to thank the Scouts en Gidsen van Alken with whom I spent countless hours at parties, adventures and summer camps which was always a great way to get away from everything for a while. I'd specifically like to mention the group of guys that colored my wednesday evenings in Leuven. Kobe, Wouter, Jelme, Dieter, Michiel, Lukas, Louis, Ruben, Wietse, Brecht, Mathias and others. There was never a dull moment hanging out with you guys. Great stories, many not suitable to be mentioned in a PhD thesis. I'd like to thank my family for always being there and supporting me. Mom, dad and my brother, thanks for everything. Finally, I want to thank Tara for being my everything for the last few years. You are amazing, even though you'll probably tell me that is not true. Your "gym teacher" almost has a PhD now.

I sincerely hope that the reader finds the answers they are looking for in this thesis.

Abstract

Holography, which is the practice of fully capturing and reconstructing a wavefront was invented nearly 80 years ago. Since then, it has become a vital technique in several scientific fields including microscopy, cryptography and beam shaping. Interestingly, holography has not yet established itself as a commercialized display technology. It is even more peculiar when one considers the scope of the display industry which offers a vast range of technologies for an even longer list of applications. It is nowadays rather common for everyone to own a television, laptop, tablet and smartphone making displays omnipresent.

The issue preventing holographic displays from entering the market is linked to the stringent requirements holography poses for accurate wavefront reconstruction. Holography demands features smaller than half the employed wavelength, which in practice results in features near or below 100nm. While challenging, this is not insurmountable in and by itself, the currently existing lithography technology is more than capable of attaining such structures. The larger issue however is that these already nanoscopic features also need to be tunable, ideally electrically and fast enough for proper display operation. Evidently, this combination of small and fast tunable features has been what withheld holography to the lab.

This thesis proposes a videoholographic display capable of meeting both demands in size and temporal behaviour based on the nanoscale periodic modulation of a slab waveguide. Two aspects are leveraged to achieve this, namely the waveguide material which consists of a strong electro-optically active material and a method capable of supplying the desired modulation to the waveguide. First, this thesis will present an introduction to the human vision system and holography. Afterwards, the various technologies in the holography field are presented and the proposed holographic display and its requirements are introduced in more detail. Attention is then devoted to the material properties

of the nanostructured electrodes and the slab waveguide. Subsequently, the operation of the display is elaborated by finite element and finite difference time domain simulation. Finally, an overview of the available hologram synthesis techniques is presented, after which a method for sub-wavelength pixel hologram synthesis is suggested having minimal memory usage and data loss.

Beknopte samenvatting

Holografie, dat men in staat stelt om een golffront volledig vast te leggen en te reconstrueren, is bijna 80 jaar geleden uitgevonden. Sinds toen, is het een cruciale techniek geworden in verscheidene wetenschappelijke domeinen waaronder microscopie, cryptografie en straal vorming. Het is opmerkelijk dat holografie zich nog niet heeft gevestigd als een commerciële beeldscherm technologie. Dit feit wordt nog vreemder wanneer de grootte van de beeldscherm industrie in rekening wordt gebracht aangezien deze vele technologiëen omvat voor een nog langere resem aan applicaties. Het is hedendaags nogal gebruikelijk dat iedereen een televisie, laptop, tablet en smartphone bezit zodat beeldschermen overal aanwezig zijn.

Het probleem dat ervoor zorgt dat holografische beeldschermen de markt niet betreden is gekoppeld aan veeleisende vereisten die holografie vooropstelt voor accurate reconstructie van een golffront. Holografie eist namelijk onderdelen kleiner dan de helft van de gebruikte golflengte, dit komt neer op onderdelen van of kleiner dan 100nm. Hoewel dat dit een uitdaging is, is het niet onmogelijk aangezien het voor de huidige lithografie technologie meer dan mogelijk is om zulke structuren te realiseren. Het grotere probleem is dat deze nanoscopische onderdelen ook aanpasbaar dienen te zijn, bij voorkeur elektrisch gedreven en snel genoeg voor adequate beeldscherm operatie. Deze combinatie van kleine en snel aanpasbare onderdelen heeft er voor gezorgd dat holografie nog niet uit het labo is kunnen treden.

De thesis stelt een videoholografisch beeldscherm voor dat zowel afmeting- als tijdsgewijs in staat is te voldoen aan de vooropgestelde vereisten, gebaseerd op het periodisch moduleren van een plaat golfgeleider. Two eigenschappen stellen ons hiertoe in staat, namelijk het materiaal van de golfgeleider dat bestaat uit een sterk electro-optisch kristal en een methode die toelaat om de gewenste modulatie aan te brengen in de golfgeleider. Eerst introduceert deze

thesis het menselijk gezichtssysteem en holografie. Daarna worden verscheidene technologiën in het holografie vakgebied gepresenteerd en het voorgestelde holografische beeldscherm en de bijhorende vereisten toegelicht. Aandacht wordt dan geschonken aan de materiaaleigenschappen van de nanogestructureerde electroden en de plaat golfgeleider. Vervolgens wordt de werking van het beeldscherm uit gewerkt door middel van eindige elementmethode simulaties en eindige verschillen in het tijdsdomein simulaties. Ten slotte, wordt een overzicht gegeven van de beschikbare technieken voor hologram synthese, waarna een methode voor hologram synthese wordt uitgewerkt waarbij pixels kleiner dan de golflengte toegelaten zijn, een minimale hoeveelheid geheugen nodig is en het data verlies zo min mogelijk is.

List of Abbreviations

BTO barium titanate. 20, 87, 97, 98, 99, 100, 105, 109, 110, 111, 112, 113, 114, 115, 116, 117, 118, 119, 120, 121, 122, 123, 124, 125, 126, 127, 129, 130, 131, 132, 133, 136, 137, 138, 139, 140, 141, 144, 152, 174, 175, 176

GST germanium-antimony-tellurium. 48, 49

IGZO indium gallium zinc oxide. 19, 20, 75, 76, 79, 80, 82, 86, 87, 88, 90, 91, 92, 93, 94, 95, 96, 137, 138, 174

ITO indium tin oxide. 52, 53

SiO_2 silicon dioxide. 77, 85, 87, 95, 176

SiO_xN_y silicon oxynitride. 19, 77, 78, 79, 95, 174

Si_3N_4 silicon nitride. 19, 20, 77, 80, 82, 85, 86, 87, 88, 90, 91, 92, 93, 95, 137, 138, 174, 176

TiN titanium nitride. 84, 85

1D one-dimensional. 49, 55

2D two-dimensional. 14, 16, 17, 25, 28, 42, 43, 49, 51, 55, 72, 89, 90, 144, 147, 148, 149, 161, 163

3D three-dimensional. 2, 7, 14, 15, 17, 25, 27, 28, 89, 90, 91, 110, 147, 148, 149, 150, 155, 173

4D four-dimensional. 16

AC alternating current. 99, 109, 110, 112, 113, 117, 118, 126, 127, 129

AFM atomic force microscopy. 74, 91, 92, 93, 94, 98

ALD atomic layer deposition. 19, 75, 84, 86, 96, 174

APF advanced patterning film. 83, 84, 85

AR augmented reality. 13, 14, 15

AS angular spectrum. 161, 162, 163, 164

BARC backside anti reflection coating. 84

C-AFM conductive atomic force microscopy. 92, 93, 94, 95, 96, 174

CCD charge coupled device. 11, 12

CD critical dimensions. 84

CGH computer generated hologram. 25, 34, 155, 170

CMOS complementary metal oxide semiconductor. 12, 54

CMP chemical mechanical polishing. 83, 85, 86, 91, 92, 96, 174

CRT cathode ray tube. 13

CVD chemical vapour deposition. 84, 85, 97

DARC dual anti reflection coating. 83, 84, 85

DC direct current. 109, 110, 113, 118, 120, 121, 123, 125, 126, 127, 128, 129, 130, 134

DRAM dynamic random access memory. 60, 71, 72, 73

EO electro-optic. 122

ER error reduction. 155, 157

FDTD finite difference time domain. 147, 149, 151, 153, 170, 175

FE finite element. 95, 137, 138, 140, 141

FFT fast Fourier transform. 26, 161, 164, 170

FOV field of view. 29, 30, 31, 33, 58, 155, 162, 176

FWM four wave mixing. 42, 43

GPU graphics processing unit. 71

GS Gerchberg-Saxton. 26, 27, 150, 151, 155, 156, 157, 170

GSP gap surface plasmon. 39

HWP half-waveplate. 113

IR infrared. 38, 48, 110

IV current voltage. 123, 124, 126, 127, 128, 129

LC liquid crystals. 46, 47

LCD liquid crystal displays. 13, 46

LCOS liquid crystal on silicon. 46, 56

LiDAR light detection and ranging. 49, 51, 54

LN Lithium Niobate. 45, 51

LSP localized surface plasmon. 39, 40

LSQ least square. 89, 90, 91

LUT look-up tables. 28

MBE molecular beam epitaxy. 20, 97, 98, 124, 128, 132, 133, 134, 175

MEMS micro-electromechanical systems. 54, 55, 174

MIM metal insulator metal. 36, 53

MQW multiple quantum well. 42, 43

MR mixed reality. 14

MSE mean square error. 77

MTF modulation transfer function. 166, 167, 168, 169, 175

NSTD normalized standard deviation. 170, 171

OCD optical critical dimension. 89, 92

OLED organic light emitting diode. 7, 13, 62

PB Pancharatnam-Berry. 34, 35, 41

PECVD plasma enhanced chemical vapour deposition. 77, 78

PLD pulsed laser deposition. 20, 97, 98, 133, 134, 175

PSNR peak signal to noise ratio. 151, 175

QWP quarter-waveplate. 112, 113

RCWA rigorous coupled wave analysis. 88, 89, 90, 96, 174

RGB red-green-blue. 11, 30, 33, 61, 67, 151, 153, 175

RS Rayleigh-Sommerfeld. 150, 155

SEM scannning electron microscopy. 35, 38, 40, 43, 44, 49, 55, 74, 84, 85, 86, 87, 88, 90, 91, 92, 118

SHG second harmonic generation. 42, 43

SLM spatial light modulator. 47, 139

SMU source measure unit. 115, 116

SOA semiconductor optical amplifier. 62

SPP surface plasmon polariton. 39, 40

SRR split ring resonator. 47

TCO transparent conductive oxide. 40, 52, 53, 54

TE transvere electric. 69, 70, 136, 137, 147, 149, 151

TEM tunnelling electron microscopy. 100

TFT triple Fourier transform. 162, 163, 164

THG third harmonic generation. 42, 43

TM transvere magnetic. 70, 136, 137, 147, 149, 151

UHD ultra-high definition. 33

UHDTV ultra high definition television. 13

UV ultraviolet. 45, 75

VAC vergence-accomodation conflict. 6, 7, 15, 18

VR virtual reality. 13, 14, 15

VRAM video random access memory. 71

List of Symbols

Å	Angstrom
α	Absorption coefficient
α	Field of view angle
β	Modevector
χ	Susceptibility
$\Delta\theta$	Difference in rotation angle between meta-atom and incident polarization
Δ	Phase shift between reflected s and p polarized light
δ	Phase offset due to Pockels in fit
$\Delta\varepsilon$	Permittivity modulation
η	Impermeability
$\frac{\partial}{\partial x}$	Partial derivative of x
Λ	Wave or grating period
λ	Wavelength
λ_0	Free space wavelength
μ	permeability of vacuum
$\nabla\times$	Curl operator
∇	Divergence operator
ω	Angular frequency
ϕ	Phase offset of a wave

ϕ_{PB}	Pancharatnam-Berry phase
π	Pi
ψ	Ratio of reflected amplitudes between s and p polarized light
ρ	Domain constraint of error reduction algorithm
σ	Electrical conductivity
σ	Helicity of polarized light
σ	Standard deviation
θ	Angle
θ	Field of view angle
ε	Permittivity
ε_2	Imaginary part of the permittivity
ε_r	Relative permittivity
$\vec{B}$	Magnetic flux density vector field
$\vec{D}$	Displacement vector field
$\vec{D}(t)$	Electric displacement field
$\vec{E}$	Electric field
$\vec{H}$	Magnetic field
$\vec{J}$	Current density
$\vec{P}(t)$	Polarization
a	Phase prefactor
A_1	Amplitude of photodetector power fit
A_2	Amplitude of photodetector power Pockels modulation fit
B_1	Background power of photodetector power fit
B_2	Background power of photodetector power Pockels modulation fit
D	Imaging distance
d	distance or thickness

d_{im}	Pixel size in the image plane
e	Euler's number
E_C	Coercive field
$F(\vec{x})$	Least square error error fitting function
$f(\vec{x})$	Simulated data by rigorous coupled wave analysis
I	Intensity
i	Imaginary unit
k	Angular wave vector
k	Imaginary refractive index
K^t	Transverse coupling coefficient
L	Propagation loss
M	Number of pixels in row or column
N	Number of pixels in row or column
N	Number of pixels
n	Real refractive index
n_{eff}	Effective refractive index of a guided mode
nm	Nanometre
$P(z)$	Optical power at z
R	Rotation matrix
r	Distance between two points
r	Pockels coefficient
r_c	Effective Pockels coefficient along [100] or [010]
r_{eff}	Effective Pockels coefficient measured 45° to [100]
s	Kerr coefficient
S_0	Projection or image size
S_h	Hologram size

T_C	Curie temperature
THz	Terrahertz
U	Complex electric field
U	Energy density per unit volume
v	Fraction of contributing ferro-electric domains
x, x', y, y', z, z'	Position coordinate
y	Measured Mueller matrix values

Contents

List of Figures

List of Tables

Chapter 1

Human Image Perception

Good understanding of holography requires having a grasp of current and past imaging systems. To help frame the later chapters better, this chapter details what constitutes an ideal image and how the human eye perceives it. This is followed by a general introduction into light, imaging and photography. Finally, the groundwork is laid towards state-of-the-art imaging by highlighting typical issues encountered in images.

1.1 An Ideal Display For The Human Eye

Every display technology strives towards the same goal, i.e. representing reality as truthfully as possible within the confines of said technology. The ideal projected image is thus rather obvious, it is reality itself. Phrased differently, the light coming from an ideal image has identical properties when compared to light coming from a real scene. In practice, technologies such as photography or display thus try to mimic a real incident wavefront by accurately representing the correct amplitude, color, ... at each point factoring in the response of the human vision system. To assess the quality of these reconstructed images, a good understanding of light propagation and the functioning of the human eye is needed. Several important eye mechanisms are listed below.

1.1.1 Light Propagation

In the context of imaging, light is best considered as electromagnetic wave and never as particle. This is since typical imaging optical effects take place on the scale of a wavelength, which is still orders of magnitude larger than the scale of quantum mechanics. Here, effects such as interference and optical resonances are often encountered and can easily be expressed by considering light as a propagating electromagnetic wave.

A common way to describe a propagating electromagnetic wave, can be deduced from Maxwell's equations. In a material with no free electric charges, these equations are the following:

$$\nabla \vec{D} = 0 \tag{1.1}$$

$$\nabla \vec{B} = 0 \tag{1.2}$$

$$\nabla \times \vec{E} = -\frac{\partial \vec{B}}{\partial t} \tag{1.3}$$

$$\nabla \times \vec{H} = \vec{J} + \frac{\partial \vec{D}}{\partial t} \tag{1.4}$$

Here D is the electric displacement field, B the magnetic flux density, E is the electric field, H is the magnetic field and J is the total current density. The arrows above each indicates it being a vector. This set of coupled equations can be further simplified by considering a linear, isotropic and homogeneous medium, which means that $\vec{D} = \varepsilon \vec{E}$, $\vec{B} = \mu \vec{H}$ and $\vec{J} = \sigma \vec{E}$. Figure 1.1 a) shows a three-dimensional (3D) travelling electromagnetic wave according to Maxwell's equations.

$$\nabla \vec{E} = 0 \tag{1.5}$$

$$\nabla \vec{H} = 0 \tag{1.6}$$

$$\nabla \times \vec{E} = -\mu \frac{\partial \vec{H}}{\partial t} \tag{1.7}$$

$$\nabla \times \vec{H} = \sigma \vec{E} + \varepsilon \frac{\partial \vec{E}}{\partial t} \tag{1.8}$$

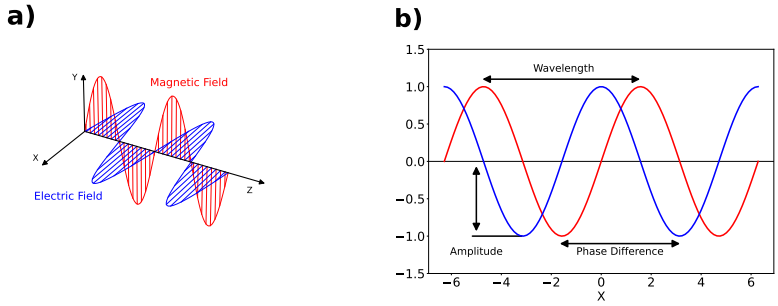

Figure 1.1: a) Three dimensional representation of an electromagnetic wave travelling along the z-axis. b) An electromagnetic fields can be represented as a sinusoidal wave, here several defining features such as the wavelength, amplitude and phase are indicated.

Here μ is the magnetic permeability, σ is the conductivity of the material and ε is the dielectric permittivity. From this, two wave equations can be derived by applying the curl to both equation 1.7 and 1.8, using a vector identity $(\nabla \times (\nabla \vec{A}) = \nabla(\nabla \cdot \vec{A}) - \nabla^2 \vec{A})$ and equations 1.5-1.6. Both wave equations yield solutions that are in the form of harmonic functions. Among the permissible solutions for these electromagnetic waves are:

$$E(t,z) = E_0 \sin\left(\frac{2\pi n z}{\lambda} - \omega t - \phi\right) \tag{1.9}$$

$$H(t,z) = H_0 \sin\left(\frac{2\pi n z}{\lambda} - \omega t - \phi\right) \tag{1.10}$$

Here, E_0 and H_0 are the wave amplitudes, n is the refractive index, λ is the wavelength, ω is the angular frequency and ϕ is the initial phase of the wave as indicated in Figure 1.1 b). Alternatively, these waves can be expressed in an exponential notation which is, in certain cases, easier to handle.

$$E(t,z) = E_0 e^{i\left(\frac{2\pi n z}{\lambda} - \omega t - \phi\right)} \tag{1.11}$$

$$H(t,z) = H_0 e^{i(\frac{2\pi nz}{\lambda} - \omega t - \phi)} \tag{1.12}$$

1.1.2 Human Vision System

The human eye, optically speaking, is a rather simple system. When light enters the eye, two actions occur simultaneously. First, the pupil adjusts itself in size, such that the light intensity does not overwhelm the photosensitive cells near the back of the eye. Secondly, the lens adjusts to create an image in focus. The focused light subsequently hits the retina, an area at the back of the eye covered with photo-receptive cells. Here, the optical signal is transformed into an electrical signal that is transferred to the brain. [1]

However, creating a realistic experience for the eye when observing an image is far from simple even though the optical system itself is not that complex. The outside world and the fact that humans have two eyes complicate imaging extensively. Proper immersion when looking at a display requires that all depth cues are present, which includes vergence, accommodation, binocular disparity and motion parallax. The difficulty obviously lies in providing all of these simultaneously.

Accommodation

The accommodation of the eye, also called the accommodation reflex, refers to the change in the eye lens shape which is accompanied by a change in focal distance. In practice, ciliary muscles attached to the lens contract or relax resulting in varying refractive power intended to keep the focal point at the retina as shown in Figure 1.2.

Vergence

Vergence is an overarching term encompassing both convergence and divergence of the eyes, which respectively refer to their simultaneous movement inward and outward. Next to accommodation, vergence plays a vital role in human vision as it ensures that the image is projected at the center of the retina. As such, convergence occurs when focusing nearby, and conversely, divergence occurs when a distant focus is required as shown in Figure 1.3.

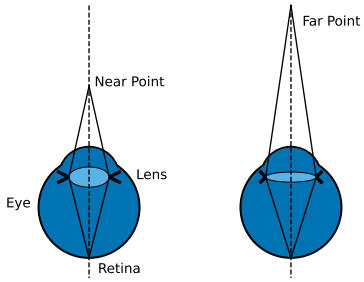

Figure 1.2: Schematic showing the varying power of human eye lens, adjusted to either see nearby (left) or far away (right).

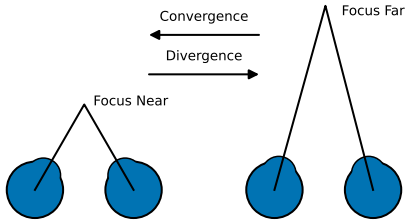

Figure 1.3: Schematic of the vergence depth cue showing the adjustments needed for both convergence as well as divergence.

Parallax

The parallax in the context of the human vision system usually refers to motion parallax i.e. the change in apparent position when an observer attains a different viewpoint. Important factors for this monocular depth cue are the relative distance and movement between object and observer. The effect is very noticeable when an observer passes objects at high speed and depends strongly on their relative distance. Far away objects visually move by slower than nearby objects and give an observer the ability to attain a better vantage point for the desired scene as shown in Figure 1.4.

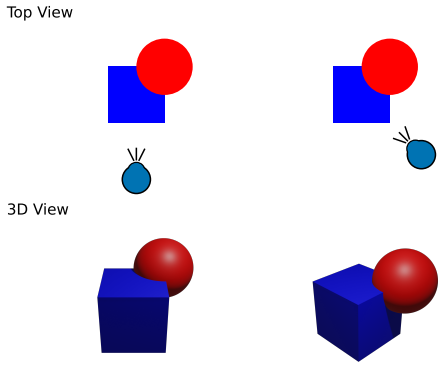

Figure 1.4: Schematic of the motion parallax depth cue showing the same image from different point of views. Both the 3D and top view image are shown.

Binocular Disparity

The slight difference in image both eyes perceive is called binocular disparity or binocular parallax. Since a small gap exists between human eyes they, at all times, have a slightly different viewpoint. The effect is more pronounced for nearby objects as the relative change in viewpoint is larger. Under normal circumstances, our brains takes both offset images and combines them to create one image and allow for depth estimation.

Accommodation-Vergence Reflex

The accommodation-convergence reflex is the automatic adjustment of both accommodation and vergence eyes make when observing an object at a different distance. This effect acts as bottleneck in stereograms projected by augmented and virtual reality displays. [2] Here, two separate images from a slightly different viewpoint each intended to be viewed by a single eye are projected, giving rise to the vergence-accomodation conflict (VAC). These images present our brain with conflicting information, for example when an object is intended to be imaged far away. To get a sharp image, the vergence will adjust to the object whereas the accommodation will stay focussed on the display as shown in Figure 1.5. This typically leads to eye fatigue and an overall ill feeling after certain exposure time. [3] In general, stereoscopic imagers all include a degree of convergence-accommodation mismatch with its severity depending on the exact display design, the intended focal distance of the object and the display distance

to the eye. In fact, no matter the quality of the display pixel (size and color), the vergence-accomodation conflict will always occur for stereoscopic displays. This inability to correctly represent the recorded scene through stereograms is one of the main drivers for advanced 3D displays including holography and volumetric displays. [1]

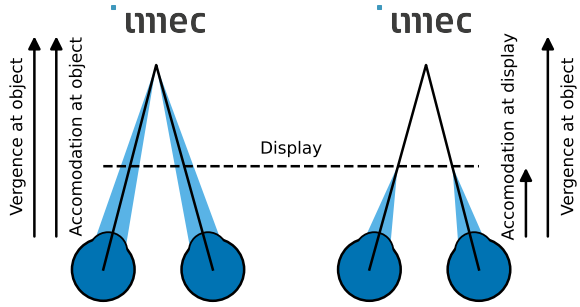

Figure 1.5: Schematic description of the VAC, showing both vergence (black line) and accommodation(blue cone) in both the real world (left) and when observing a stereogram (right)

1.2 A brief history of imaging and photography

Nowadays, imaging is employed everywhere ranging from advanced medical applications such as CT scans to mass produced applications such as smartphone cameras. In the 200 odd years that it has existed it helped shape society and was vital in several cultural revolutions. As an example, a mere 20 years ago the concept of smartphones was non-existent, even though they are omnipresent nowadays. At the beginning of the 20th century the television had not been invented yet. Instead of having a cozy family movie night, people listened to the news on the radio or better yet went to bed early. It is not an understatement that imaging and all the technologies it is found in have shaped the world to what it is today.

In the field of imaging two major components exist, namely the capturing of a scene and the recreation of that scene in a projection elsewhere. Throughout the years, several technologies have fulfilled either one or both. Examples include photography, cathode ray television and organic light emitting diode (OLED)

displays. This chapter will track all these technologies throughout the years and, to keep a good overview, it always presents the recording of the scene first, followed by the recreation of said image.

1.2.1 Analogue Photography

The dawn of imaging can be traced back to the invention of photography. In the early, 19th century several scientists were working on photography related topics, usually completely independent from each other. It is thus difficult to claim with absolute certainty that a specific person at a specific time was simply the first. Prominently recurring names are Nicéphore Niépce, William Henry Fox Talbot and Louis Daguerre whom respectively lay a claim to the title inventor of photography at 1826, 1835 and 1839. Each of their techniques differ, but get to a similar result. [4, 5] It should be noted that some earlier attempts at photography were made, but these never succeeded in fixing an image.

Niépce's earliest technique revolved around silver chloride ($AgCl$) which darkens when exposed to light and created a negative of the desired image. This negative image was simultaneously also the observable image as image capture and recreation were one and the same at this early stage. However, since there was no method to stop further darkening when viewing, the photograph was lost rather quickly. Realizing its limitations, Niépce resorted to a polished pewter sheet having a thin bitumen coating as light sensitive agent. Here, the bitumen would harden during exposure times ranging from 8 hours to several days. After which, the unhardened bitumen was washed away using a solvent.

To optimize his bitumen process, Niépce cooperated with Louis Daguerre, which resulted in Daguerre obtaining Niépce's notes at his untimely death. Daguerre looked back towards silver and found that a silver plate, exposed with iodine vapour resulted in a thin film of silver iodide (AgI) forming. Again, exposure times were excessively long but, to his benefit, he discovered that the photograph developed faster when exposed to mercury vapour. To finalize and fix the image, he used a highly concentrated and heated salt bath. In January 1839 he presented his work to the French Academy of Sciences, after which the news of his invention, called the daguerreotype, quickly spread around the world.

Nearly simultaneously, the Englishman William Henry Fox Talbot had been working on photographic negatives on paper with Silver Chloride. When he heard of Daguerre's discovery, he continued his earlier work and started using

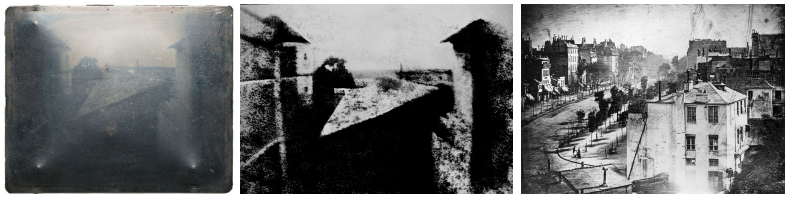

Figure 1.6: left) The oldest preserved photograph originally taken in 1826 by Niépce, known as "Window at Le Gras". Made by using his bitumen technique, a still shot was taken looking outside the window as a long exposure time was needed. center) An enhanced version of the left photograph, increasing its visibility. [6] right) A Daguerreotype photograph called "Boulevard du Temple" taken by Daguerre in Paris in 1838, the first known photograph in which a human is present. [7]

sodium thiosulfate ($Na_2S_2O_3 \cdot H_2O$) to strip the unreacted Silver Chloride from his photograph. Since the method, called calotype, was paper based, a translucent negative could be created which subsequently could be used to create numerous positive images.

Figure 1.7: left) The oldest preserved photograph titled "Lattice Window at Lacock Abbey" made by Talbot of which the original negative still exists. [8] right) The first color image, called "Tartan Ribbon" taken by Thomas Sutton in 1861. [9]

In the decades after, photography became more and more widespread while scientists tried to create multi-color images. First attempts, by Thomas Sutton based on the theory of Maxwell, focused on taking three separate images through color filters which could later be superimposed. [10, 11] Around the turn of the 20th century the Lumière brothers, famous for their short films, devised a method they called autochrome.[12, 13] Here, a pixelated filter was

used which resulted in small color pixels forming on the photograph, bearing some resemblance to typical state-of-the-art displays. Finally, around 1930 the kodachrome film became available, which captured red, green and blue light in separate layers of photoreactive material. This film, again employing Silver Halides, paved the way to the photographic films that are still in use today. The best photographic films employ sub-wavelength Silver Halide crystals around $20nm$ in size which means that, for all intents and purposes it can be considered as a true analogue recording.

1.2.2 Analogue Film

The first hint towards analogue film can be found in a technique called chronophotography. Here, several photographs are taken in rapid succession of a moving object, thus giving the appearance of movement when shown on a rotating wheel. This concept was not entirely new as it was used in stroboscopic animations, however these employed hand drawn images. Initially, chronophotography was hindered by the necessary long exposure times. However, during the 1870's the photosensitive emulsions had improved enough to take photographs requiring less than 1 second exposure time. In 1878, perhaps the most famous chronophotograph, called "The Horse in Motion", was made by Muybridge by placing a set of cameras along the racetrack. This ground breaking set of photos quickly found their way to zoetropes (a rotating cylinder with images on the inside, vertical slits serve as viewing port), which resulted in the illusion of an actual moving picture.

Not much later, in 1884, George Eastman patented the first photographic film roll. He envisioned a film employing gelatin embedded with photosensitive materials on a long paper roll. Two years later, the Frenchman Louis Le Prince tried to patent the first camera designed for motion pictures. He is accredited to have shot the first ever motion picture in 1888 called the Roundhay Garden Scene. In the following years, celluloid based photographic films, patented together with a camera by William Friese-Greene, gained popularity. It is this type of film, that among others found its way into Thomas Edison's kinetoscope and the Lumière brothers's cinématographe. In the meantime, the film industry kept expanding which lead to a large variety of early film cameras and projectors being used. Eventually, the industry standardized employing Edison's 35mm film and the $16Hz$ frame rate of the Lumière brothers. Each of these cameras was capable of capturing a set of negatives which would be copied and spread to numerous cinemas. Subsequent white light flood illumination of the negatives

revealed the captured scene.

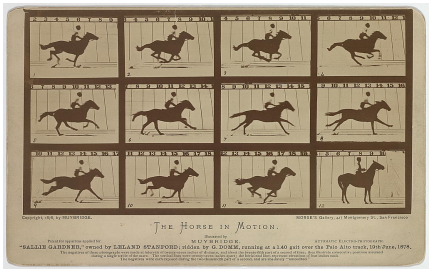

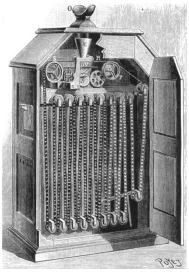

Figure 1.8: left) Chronophotograph by Muybridge, called "The Horse in motion. "Sallie Gardner," owned by Leland Stanford; running at a 1:40 gait over the Palo Alto track". [14] right) Image explaining the inner operation of Edison's kinetograph. [15]

In contrast to photography, the first color film followed rather quickly. Indeed, since color photography by the invention of the first film camera was already being researched, the additional step to create multi-color film from multi-color photographs was more evident. Already in 1899, Edward Turner patented a color motion picture camera that employed three colors filters red-green-blue (RGB) that rotated such that each consecutive frame had a different one. When projecting, the color frames were shown by three at a time. At his death, his work passed through his sponsor to George Smith who simplified the design to only use a red and green filter situated on the rotating shutter on the camera in 1906. The technique called Kinemacolor required a higher frame rate to prevent color flicker known to induce headaches, especially when rapid movement is present in the film. About a decade later, the Technicolor Motion Pictures Corporation improved the camera by employing a beam splitter to illuminate two frames (red-green) at the same time. Again, the camera had to be run at double the normal speed but it did not suffer from color flicker. These early versions of color film were however quite expensive. As such, most moving pictures were simply shot in black and white. Colour film finally became the standard after the television had been introduced in the 1950's.

1.2.3 Digital Photography and Film

Much later still, at the end of the 1960's the charge coupled device (CCD) was invented at Bell Labs. [16, 17] Strangely enough, it was originally designed

as memory storage device and not as imaging sensor. Their impact is still felt today, due to providing a viable alternative to bulky film cameras. In the 1980's, an alternative to CCD cameras appeared when complementary metal oxide semiconductor (CMOS) cameras were invented. These used the same photoelectric effect to convert light to an electrical signal but differed in pixel architecture. Where CCD cameras have a passive pixel, CMOS cameras have active pixel since they include an amplifier in each pixel. Originally, this meant that CMOS cameras enjoyed more noise than their counterpart at the benefit of being vastly more power efficient. Nowadays, no distinct difference exists in image quality and the lower cost of CMOS sensors make them most used.

In either case, it is currently impossible to imagine the world without digital cameras. [18] It should be noted that digital cameras in contrast to film based photography lead to pixel limited images. This is due to their electronic nature which leads to the image being digitized for practical purposes. This obviously reduces the amount of required data for one image, but can also lead to data loss due to insufficient sampling of the desired scene. Hence, widespread adoption of digital cameras only happened after 2000 when they simultaneously became affordable and offered sufficient quality. Nowadays, digital cameras already reach $100Mp$ which for most intentions suffices. [19]

Figure 1.9: left) The first digital photograph, taken by R. Kirsch of his son W. Kirsch in 1957. [20] right) An early 1930's Telefunken television. [21]

The motion picture industry was more hesitant to switch to digital cameras as they initially could not offer the detail analogue films could. By the mid 2010's this however was solved as cameras could shoot moving pictures at 4k resolution, leading to their gradual adoption. Currently, the majority of motion pictures are shot using digital cameras. That said, certain directors swear by analogue film and continue to use it.

1.2.4 Digital Displays

For a long time, all displays relied on cathode ray tube (CRT) as their driving force. Originally invented in 1897 by Ferdinand Braun, CRTs have an electron emitting cathode. This proved to be incredibly useful as the electrons could be steered by electric or magnetic fields and could be used to excite fluorescent materials. In a television, this could be performed sequentially on a rasterized grid to create continuous refreshment of the screen. During the 1920's and 1930's, important contributions were made by Kenjiro Takayanagi, Philo Farnsworth and Allen DuMont for respectively building the first CRT television receiver, building the first all electronic CRT television, and for drastically increasing the lifetime of a CRT. As such, the first commercial television was created in 1934 by the company Telefunken. Their widespread adoption took till the 1950's after which the television became a common household item. CRTs remained synonymous with television till the early 2000's when flat panel displays started emerging. This should be no surprise as CRT based televisions were quite bulky, especially for larger displays, and always carried an implosion risk as the CRT was put in a near vacuum to reduce electron-air interactions. liquid crystal displays (LCD), plasma displays and nowadays also organic light emitting diode (OLED) displays took their place when they became available.

The current state-of-the-art displays employing OLEDs, with typical pixel sizes of 40 to 200μm easily reach $4K$ resolution with refresh rates up to 240Hz . On top of that, their color representation is often perceived better since their individual pixels can turn off completely, thus offering better blacks. About a decade ago, in 2012, the International Telecommunication Union published the currently used standard for ultra high definition television (UHDTV) called Rec. 2020.

A question one might ask now: How can a display still be made better? The Rec. 2020 standard covers 75.8% of the CIE 1931 color space which represents how colors are perceived by the human eye, refresh rates nowadays attain flicker free operation by design and pixel densities are high enough so that improvements are barely visible at the intended observer distance. It seems that for a typical display, only incremental improvements can still be made. When it comes to radical innovation, the display industry looks towards foldable displays and augmented and virtual reality (AR and VR) to offer their customer a further improved experience.

1.3 State of the Art Displays

1.3.1 Stereoscopic displays

Stereoscopic displays form a large range of applications revolving around the difference that exists between observations made by two eyes. Since human vision employs two eyes spaced by a small distance, slight variations in vantage point are attained. As highlighted above, this offset is a crucial aspect of 3D vision. Stereoscopic displays attempt to mimic this naturally perceived difference by feeding each eye a separate two-dimensional (2D) image. The human brain subsequently combines both images giving a 3D perception at the cost of introducing the vergence-accommodation conflict.

In practice, this effect is achieved through several methods which include wavelength filter, shutters, anaglyphs and polarization multiplexing of images. For all of these the viewer needs to wear a visual aid, often glasses, that treat incident light differently for each eye. In case of wavelength filters, two images are superpositioned at slightly different wavelengths and a pair of glasses filters out the undesired image for each eye. Shutters-based stereoscopic displays employ a higher frame rate and glasses that block incident light for half of the frames. Anaglyphs employ superimposed images and leverages the additive and subtractive properties of light that appear to change color when mixing. These are perhaps the most well known example of stereoscopic display, as it uses the typical red-cyan coloured glasses. Finally, polarization based approaches encode two images either at opposite-handed circular polarized light or perpendicularly oriented linear polarized light. This approach requires an expensive cinema screen that maintains polarization as common screens scramble this information. To date, stereoscopic displays have not become widely adopted and are mainly encountered in cinemas for niche blockbuster movies. AR and VR can be thought of as an extension of these concepts and will be expanded on below.

1.3.2 Augmented and Virtual Reality

AR, VR and mixed reality (MR) have been an emerging technology for the last few years. From a distance these technologies might appear very similar, but upon closer inspection they each have their own distinct goals and challenges. For example, AR aims to add useful information to normal vision. Whereas VR intends to completely submerge its user in a, as the name suggests, virtual world where no notion of the outside world is present. For AR, a common challenge is

that the light source needs to compete with light from the outside world, which is difficult due to the size and space constraints a wearable introduces. Currently, these devices thus remain quite bulky as more ideal light sources, such as thin film lasers, are still in a research phase. On the other hand, a VR headset typically encounters the earlier mentioned vergence-accommodation conflict. [22] The main approach to mitigate the VAC in VR applications revolves around light field displays such as varifocal, multifocal and integral imaging displays. [23, 24] That said, several commercial AR and VR applications are available today, with notable examples including Meta's Oculus Quest and Apple's Vision Pro shown in Fig. 1.10.

Figure 1.10: left) CEO of Facebook, Mark Zuckerberg wearing a Oculus Quest 3. [25] right) A backview from Apple's Vision Pro headset. [26]

Indeed, light field displays have been considered as possible solution for VAC, as they can image focus cues and motion parallax. For a more detailed description on their general operation, see Section 1.3.3 below. In essence, all types of light field displays try to mimic the light hitting the retina of a real scene. For example, varifocal displays recreate a 3D image by tracking eye movement and adjusting the focal depth accordingly. This can be achieved by an adjustable lens or deformable mirror inside its optical system. [27, 28, 29] Unfortunately, its translation space is rather constricted limiting the overall focusing power. Multifocal displays create depth information by imaging several focal planes either overlaid spatially or in rapid succession. These displays can only be optimized for a single viewpoint, making them very suitable for wearable applications. [30, 31, 32] Theoretical estimations indicate that a minimum of 14 focal planes should be projected for a good user experience. [33] Current state-of-the-art multifocal displays image three to six focal planes. Integral imaging displays employ a sectioned display and a microlens array to project images with slightly different perspective. When enough perspectives are densely shown, 3D images with their entire parallax can be created. That said, due to splitting of the imager in subsets integral imaging display struggle to achieve higher pixel densities. [34, 35] To summarize, these technologies suffer heavily from the space restriction a head mounted display introduces. That said, further

down scaling of the required components together with the rise of meta optics might introduce new possibilities.

1.3.3 Light Field Displays

Next to their use in head mounted displays, light field displays can also be used as multi user screen. Since light field displays can project different images depending on viewing direction, they can offer depth perception and motion parallax to all users. They achieve this by projecting the light field of a scene, which is a vector function that represents the light travelling in each direction through each point in space. To that end, a seven-dimensional plenoptic function $P(x, y, z, \theta, \phi, \lambda, t)$ can be used to represent all possible light rays of which the magnitude is equal to their radiance. [36] Here, x, y and z represent the viewing point coordinates, θ and ϕ are the angles at which a ray flows through (x, y, z), λ is the wavelength and t represents time. Handling these seven parameters can be difficult. Fortunately, a simplified version with four parameters can be created based on multiple images coming from separate planes. This commonly used 4D light field is defined by the 2D coordinates of a ray when passing through two planes, thus neglecting the wavelength, time and one spatial coordinate. [37]

To achieve their aforementioned depth effect, light field displays either rely on creating a retinal blur leading to a realistic parallax effect by imaging multiple views per eye, or by imaging multiple focal planes spatially or temporally. Both approaches encounter their own set of challenges. [38] For example, the first approach employed in super multi-view displays, requires very densely spaced viewing zones which is difficult at a distance. [39] On the other hand, the multi focal plane approach can only be optimized for a single viewpoint at once. A few commercial light field displays exist but they all face trade-offs in size, image quality and viewing angle.

1.3.4 Volumetric Displays

Volumetric displays approach the problem of imaging similarly to common digital displays. They differ however by physically adding a third dimensions to the display. Hence they do not image through pixels but voxels, hinting at the fact they image volume elements ideally on a rectangular array. Volumetric displays offer all the above mentioned depth cues except occlusion and thus yield high-quality 3D images. [40, 41] Approaches to create a volumetric display

include swept volume displays, static volume displays and optical trap displays.

Swept volume displays typically create 3D images by movement of a standard 2D display or diffusive screen. For example, rapid rotation of a display generates the illusion that the full rotation space is filled by a display. [42, 43, 44] Hence, the refresh rate of the display and individual pixels are vital for proper operation. On the other hand, static volume displays fully fill the display volume. Example technologies include heavy metal doped fluoride glass for up-conversion, liquid crystals and quantum dots. [45, 46, 47] These displays are very similar to some light field displays, hence the names are also used interchangeably. Currently, volume displays form the most established form of volumetric display, partly since some commercial products exist such as VX1 (Voxon Photonics - swept volume) and Looking Glass (Looking Glass Factory - static volume).

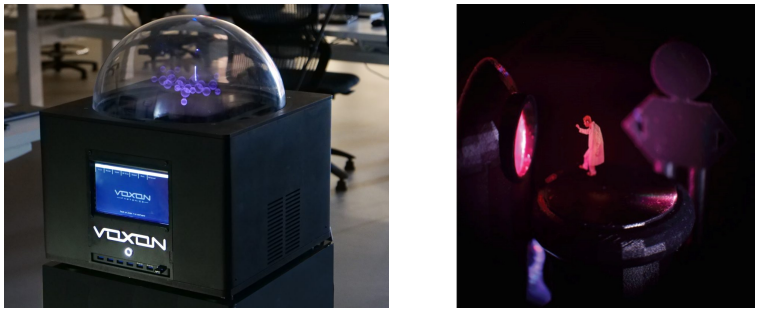

Figure 1.11: left) A Voxon Photonics VX1 swept volumetric display. [48] right) An optical trap display, adapted from [49]

A newer approach, called optical trap displays, work by capturing a diffusive particle on which RGB light can be scattered from. This particle can be thought of in broad terms, as it can be dust, bubbles suspended in liquid or case by case tailored particles. [50, 51] The trapping mechanism is borrowed from the optical tweezers and can be photophoretic or acoustic in nature. [49, 52] Full colour images, several centimetre in size have been shown.

While some commercial volumetric display initiatives exist,they largely remain a rather niche research topic. This can be mainly attributed to their technical shortcomings (low efficiency, low fill factor) and limited usability. On top of that, volumetric displays intrinsically struggle with correctly presenting occlusion for viewers with different vantage point as voxels cannot absorb light. [53] For a more expansive description on the challenges faced by volumetric displays, the

review of B.G. Blundell is a good starting point. [54]

1.3.5 Holographic Displays

Holographic displays do not encounter any of the issues mentioned above. In essence, this is due their operation which, instead of cleverly trying to create an image, completely recreates the wavefront coming from the desired scene. Holographic displays thus create images indistinguishable from reality. Naturally, all depth cues are satisfied and the VAC thus cannot occur.

Currently, holographic displays very much remain a research topic which is due to the stringent requirements holography needs to meet for high quality images. The next chapter explains these topics in more detail. That said, a start-up originating from imec called SWAVE has recently launched a holographic display having pixels smaller than $300nm$. [55]

1.4 Thesis Outline

Reflecting on nearly two centuries of display technology, it is evident that significant progress has been made, from the earliest photographs to the ultimate goal of holography. Despite being an active research area, even 78 years after its discovery, no commercial holography technology has emerged. This can largely be attributed to the stringent requirements for accurate projection. It is, therefore, unsurprising that common methods in literature remain far from their targets, suggesting that a radical new approach is needed to push current technological boundaries further. Consequently, this thesis first aims to better understand the current state-of-the-art and identify what is still lacking. These insights can then be implemented into a novel concept capable of achieving holography at video-rate, which will necessitate new technological developments. Simultaneously, an in-depth understanding of the operation of such a novel holographic display is required. All these aspects will be explored in this thesis. Figure 1.12 shows the videoholographic device central to this thesis. The parts covered by each chapter are indicated on it.

Chapter 2 presents holography as the ultimate display technology. It begins by exploring its history, along with the methods and materials used over the

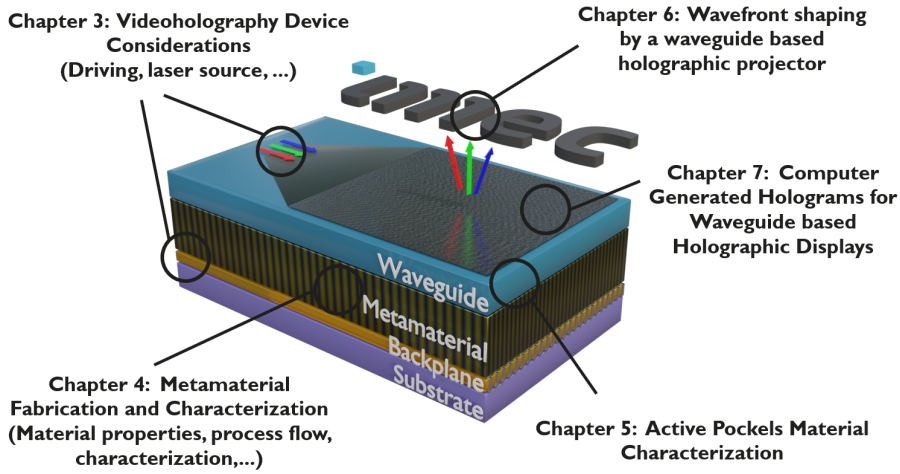

Figure 1.12: Chapter overview highlighting the parts on the envisioned holographic display that they cover.

years. The chapter then shifts to key holography concepts and considerations necessary for working with this technology. In doing so, it highlights the requirements for accurate image projection at large distances and wide fields of view. Next, the current state-of-the-art in the field is introduced, starting with methods to achieve phase and amplitude modulation of light. It then discusses several contemporary technologies for holographic image projection. The chapter concludes with a condensed overview of all possible methods and technologies, contrasted against the previously outlined requirements.

Chapter 3 expands on common holography approaches and what they lack to supplant the current commercially available display technology. Having presented these and other considerations, it introduces the novel holography concept of this thesis. This new approach focuses on solving the aforementioned issues encountered by the current state-of-the-art. In the following sections, several parts of the envisioned device are elaborated, including the optical source, slab mode behaviour, the metamaterial cladding and the driving scheme.

Chapter 4 develops the metamaterial cladding layer of the slab waveguide. To that end, a material screening was first performed in a set of short loop experiments. Since the metamaterial requires high aspect ratio features, ALD deposited $IGZO$ is introduced first. Afterwards, both SiO_xN_y and Si_3N_4 are considered as material that can be index matched to the $IGZO$.

Ellipsometry was used to compare the refractive indices of all materials. Si_3N_4 was found to be most suitable, after which the full process flow for the creation of the metamaterial is detailed. Finally, the chapter presents various characterization techniques revolving around the optical and electrical properties of the metamaterial. Here, the optical measurements reveal that the metamaterial stops behaving like a metamaterial for wavelengths smaller than $400nm$. The electrical measurements confirm that $IGZO$ provides sufficient conduction for the holographic display.

Chapter 5 studies the electro-optically active waveguide of the holographic display. First, the chapter introduces the typical BTO domain microstructure which will influence device operation. The non-linear behaviour of BTO is then elaborated by starting from general non-linear optics, after which the influence of the domain microstructure is expanded. To situate the data near the end of the chapter, the employed measurement technique and data analysis for the Pockels effect in BTO is elaborated. The measurement is then simulated for various BTO crystals and domain microstructures. Several electro-optic measurements are presented. First, the importance of domain poling is highlighted, suggesting that ramp-like poling provides the best performance. Afterwards, the pockels effect at different electric field orientations is tested which reveals $r_{42} = 88pm/V$, $r_{13} = 1.9pm/V$ and $r_{33} = 18.6pm/V$. Lastly, BTO grown with different deposition techniques is tested, indicating that MBE grown BTO is superior over PLD grown BTO.

Chapter 6 investigates the operation of the envisioned holographic display from a theoretical perspective. First, it applies mode coupling concepts to the BTO slab waveguide. Finite element electric field simulations in a-, b- and c-oriented domains are considered, which show that only a- and b-oriented domains allow significant penetration of the electric field into the waveguide. A method to use the simulated electric fields for the reconstruction of a desired grating is then expanded. Following, the required gratings for beam steering, shaping and focusing are elaborated. The aforementioned electric field reconstruction of gratings is then tested for a focusing grating and shows good correspondence, reaching a mean square error of 0.000332 when compared to an ideal grating. Finally, two hologram approaches are introduced, namely point-based and phasemap holograms.

Chapter 7 studies the influence of sub-wavelength pixels in hologram synthesis. To that end, it first presents the commonly used Gerchberg-Saxton algorithm. Subsequently, various solutions to the Rayleigh-Sommerfeld equation are expanded. Unfortunately, each of these is limited either in validity or require

unachievable computational effort. Consequently, a solution employing a coordinate transform is introduced which does not suffer from the same issues, but does encounter data loss. Methods to prevent this data loss are considered, and conclude that upscaling the original image prior to coordinate transform succeeds in this when considering the modulation transfer function. Finally, this method is implemented in finite difference time domain hologram simulations.

Chapter 8 presents a conclusion, reflection and suggestions for future work.

Chapter 2

Holography as solution

This chapter expands on the notion of holography as ultimate display technology. First, it presents a brief history of holography, starting with its discovery, subsequently followed by the materials and techniques that were commonly used throughout its existence. Afterwards, several key metrics for holography are highlighted. These help understand why creating a high-quality holographic display is extremely challenging. Finally, this chapter will focus on state-of-the-art holographic devices.

2.1 Holography history

2.1.1 Gabor's Discovery

In 1947, when working on the electron microscope, Dennis Gabor discovered that he could avoid the near impossible task of improving the spherical aberration of electron lenses. [56, 57] Indeed, when trying to imagine atomic lattices a resolution of about 2 Å is required. At the time, an order of magnitude increase in the resolving power was required to reach this goal. However, due to the link between spherical aberration and resolving power, a four order of magnitude improvement in the aberration was needed, which seemed nearly impossible. Gabor thus steered away from the typical path of trying to improve the lenses and circumvented them completely by recording the complete phase and amplitude of an object through the interference pattern created by a reference electron beam and the object electron beam. He could subsequently

use the reference beam to recreate the original object.

To prove this new principle, he recorded a micrograph using visible light instead of electrons. Herein immediately lies an even more interesting application for holography. Instead of electron microscopy, which always will be a niche scientific technique, he paved the way for holography to be used as the ultimate goal for displays. That said, Gabor was technologically limited in light source as the highest attainable coherence length, the length over which light can be used to create interference patterns, at the time was about $0.1mm$ for a high pressure mercury lamp. Consequently, the light source, object and hologram were placed on the same axis, leading to an undesired virtual image being recorded as well.

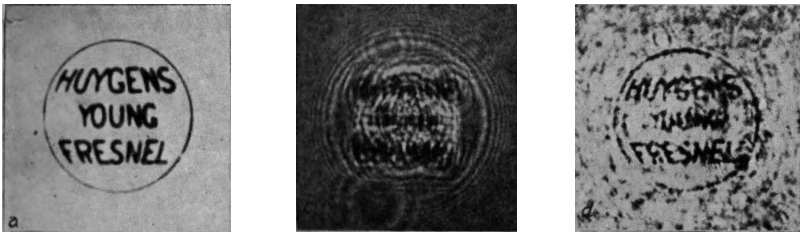

Figure 2.1: left) The micrograph of which the hologram was recorded. center) The recorded hologram, showing interference fringes. right) The reconstructed image. Images reproduced with permission. [56]

The year after, he expanded the theory behind his original discovery. [58] It is here that the term "hologram" is used first, borrowing "holo" from the Greek word "holos" meaning entire or whole, as it contains all information needed to reconstruct any captured object. The theory of holography was further expanded by looking at it as a generalized version of the Fresnel zone plate, that is now continuous instead of binary. It is worth to mention that this displays the phase of the light coming from a point source. [59]

2.1.2 Invention of the Laser

As mentioned above, early on holography was hampered by the available light sources. This changed with the invention of the laser in 1960 by Maiman. [60, 61] Two years prior, Townes and Schawlow published a theoretical paper on masers and lasers which inspired Maiman. [62] This was the invention holography needed, a true game-changer in the context of coherence length that

ushered in a wave of new discoveries.

A world of new holographic possibilities opened up. Using a He-Ne laser, Leith and Upatnieks were able to create a hologram that used a reference under angular incidence. [63] As a consequence of looking at the first order diffracted image, the always present virtual image of the hologram could be both spatially and angularly separated from the real image. Moreover, they were able to record multiple high-quality images in the same hologram. [64, 65]

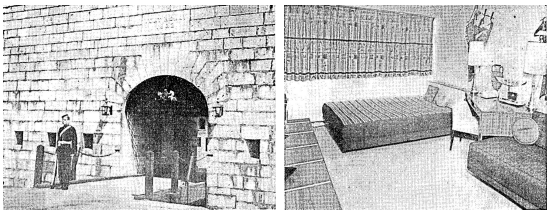

Figure 2.2: left) Reconstruction of a hologram under a specific angle and distance. right) Reconstruction of the same hologram under a different angle and distance compared to the center image. Images reproduced with permission. [65]

Nearly simultaneously, Denisyuk invented a method to record a full colour hologram and project it in its original colors. [66] To this end, he looked towards a famous photography paper from Lippmann. [67] Lippmann employed a photosenstive emulsion backed with a mercury mirror, which creates a standing wave pattern in the emulsion when illuminated. The resulting photograph, under white light illumination, only reflects at the exact colors the Bragg condition is satisfied to create realistic colour images. Denisyuk thus employed a similar concept, but had the reference wave hit the hologram from the back to create the same effect. This theoretical concept was quickly expanded on to create real full colour holograms. [68, 69]

Building on these earlier concepts, Marom showed that it possible to use three separate laser sources to create full colour images. Instead of a single laser, the hologram was now recorded and illuminated by three primary color lasers. Then, by restricting the field of view to large angles only, a good reconstruction of the desired image can be created. On the other hand, when small field of view angles are employed the image interferes with undesired diffractions. [70]

Holography was also considered for information storage and retrieval. It is this second topic of information retrieval that inspired van Heerden to devise

an efficient method based on holography. He envisioned a system in which a large set of data is encoded in a hologram and used as spatial filter in the focal plane. [71] A small fragment of the larger dataset can than be shifted in the object plane and illuminated similarly, forming its image together with a shifted ghost image of the whole dataset in the image plane. Moreover, the image of the shifted fragment will coincide with its own ghost image thus allowing one to retrieve the original location. Next to that, a more simple approach to information storage can be achieved by recording multiple holograms in one sheet and only illuminating a section of it at a time. [72]

2.1.3 Computer Generated Holography

Almost as influential for the field of holography was the rise of the computer, as it allowed holograms to be generated instead of having to be recorded. The theory behind computer generated hologram (CGH) and the first CGH were shown in 1966 by Brown and Lohmann. [73] Concerned with pattern recognition, they employed a computer to create any desired spatial filter. The idea stemmed from the fact that producing such spatial filter experimentally made it challenging to record both phase and amplitude simultaneously.

Next to that, their theory could easily be applied to any object of which a hologram was desired. [74] Shortly after, it was also expanded to create 3D holograms. Here, a 3D object was treated as a set of points of which each can be translated in a Fresnel zoneplate. Simply superpositioning all the zoneplates can thus yield a high quality rendition of any 3D object. [75] Alternatively, holograms were also shown calculated from a contour perspective by sequentially exposing a photographic plate through a lenslet system at varying distance. [76]

2D Holograms

Another major milestone in the field of holography, was the introduction of the Gerchberg-Saxton algorithm. [77] The algorithm offers a method to calculate nearly any 2D hologram using the intensity in the image and back focal plane. To that end, it relies on the Fourier Transform relation between the two planes. The iterative algorithm, shown in Figure 2.3, is initiated by randomizing a phase value between $-\pi$ and π for each sampled intensity point, which are then combined with the square root of said intensities to give a complex valued image. It is subsequently Fourier transformed towards the back focal plane (or

diffraction plane) and the phase and amplitude are extracted. The calculated phase is now multiplied by the desired amplitude in the back focal plane, after which an inverse Fourier transform is done to return to the image plane. Again the phase and amplitude are extracted and the acquired phase is used as input for the next iteration together with the image amplitude. In doing so, the error between the desired and calculated back focal plane amplitudes decreases or remains constant every iteration. The corresponding phase function is not unique, but it does give correct insight in the relative phase differences.

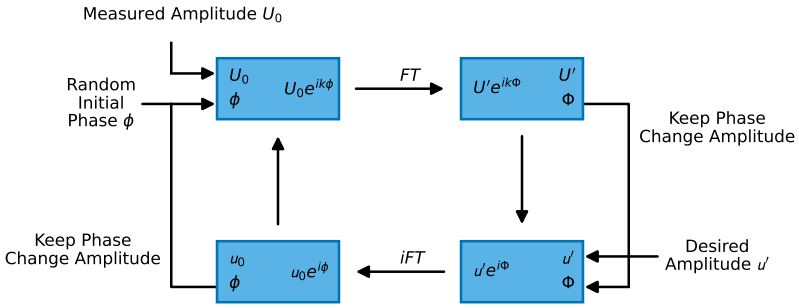

Figure 2.3: Schematic of the Gerchberg-Saxton algorithm

Interestingly, the Gerchberg-Saxton (GS) algorithm does not necessitate the use of the Fourier Transform, even though the fast Fourier transform (FFT) algorithm allows for efficient calculation. Any other lossless transfer function that accurately describes the wave propagation should yield similar results. In fact, the Fourier transform is not the most general transfer function. To that end, the Rayleigh-Sommerfeld diffraction integral, shown in equation 2.1 should be solved, which is known to be computationally intensive. [78] It is thus no surprise, that two approximations of Rayleigh-Sommerfeld are more commonly used. For both the $cos(\theta)$ factor is assumed to be equal to $\frac{z}{r}$. In addition, when z is assumed to be nearly equal to r, the integral loses its r dependence in the denominator. This approximation, also called the Fresnel transform, again leverages the efficiency of the FFT by applying it to the amplitude field multiplied by the Fresnel propagator. When the even more stringent requirement of $\zeta^2 + \eta^2 \approx 0$ is assumed, the Fraunhofer Transform is acquired, which is simply the FFT applied to the amplitude field and afterwards multiplied by a quadratic phase factor.

$$U(x,y,z) = \frac{1}{2\pi}\iint U_0(\zeta,\eta,0)\frac{e^{ikr}}{r^2}(ikr-1)\cos(\theta)d\zeta d\eta \tag{2.1}$$

with :

$$r = \sqrt{(x-\zeta)^2+(y-\eta)^2+z^2} \tag{2.2}$$

Furthermore, it should also be noted that the GS algorithm does not need to be used for phase retrieval. It can similarly be used to extract amplitudes when the phase is known. On top of that, the algorithm can also be used to extract both a desired amplitude and phase profile by, for example, defining regions inside the amplitude and phase and only setting requirements for these regions. Convergence here depends on the exact size and enforced goals on said regions. Next to the GS algorithm, holograms can also be calculated more directly, for instance by backward propagating each pixel towards the hologram plane.

3D Holograms

The aforementioned GS algorithm does not function for 3D images, but can be adapted to calculate holograms at different image planes. To do so, additional object planes are inserted in the iterative loop between hologram and final object plane. At each plane of interest, an amplitude constraint is applied before propagating to the next. Multiple version exist, depending on the propagation direction (backward or forward) and whether they are closed or open loop calculations. This method allows creation of both vergence and accommodation depth cues. But, similar to a volumetric display, it only offers correct occlusion for a single viewpoint. This is due to the planes being calculated separately and not as one whole scene. [79, 80, 81, 82]

In practice, the occlusion error emerges when a single viewpoint is employed, thus possibly hiding parts of an object behind itself. Further improvements have been made to address this issue. In general, it involves the inclusion of more viewpoints in the hologram calculation. This is either done by dividing the hologram in sub-holograms or by assessing occlusion between all consecutive image planes. Both methods create an improved initial set of input for the hologram calculation afterwards. A field of view up to 21.5° by 14° has been achieved. [83, 84, 85]

Multiple approaches exist to calculate true 3D holograms, which are commonly split between ray based methods and wavefront methods. [86] Ray based

methods employ 2D intensity images to either define a hologram element (hogel) based light field or a continuous hologram by backward propagating many viewpoints. Alternatively, wavefront methods employ either point clouds, polygons or multiple planes to define an object.

Ray based holograms distinguish themselves in the fact that they use incoherent illumination making them less susceptible to vibrations and misalignment. In holograms employing hogels, each hogel represents the object from a different viewpoint. On top of that, the holographic information for each is defined as a light field. [87] Consequently, this method encounters similar disadvantages as true light field displays. These devices always have to choose between resolution and 3D depth cues since they are both defined by hogel dimensions. Unfortunately, both are simultaneously adversely affected. For example, smaller hogels would lead to an increase in resolution, but it would restrict the angular range over which the hogels can emit light. [88, 89] Conversely, holographic displays can also employ a larger light field that is calculated using multiple viewpoints of the desired object. [90, 91, 92, 93] However, this method requires a dense angular sampling which is challenging to achieve in practice. Lenslet arrays have been used, but lead to low resolution as a camera's photosensitive region is split in smaller segments. Alternatively, fewer angles can be captured and intermediate angles can be interpolated with the obvious downside that more computational power is required.

Wavefront based hologram do not employ incoherent illumination and the accompanying light fields. Instead, these holograms are calculated by employing coherent illumination to assess interference between the object and reference wave, identical to when they would be recorded experimentally. A few categories can be defined depending on how the object is defined in 3D and how the wavefront propagation is handled. Objects are either defined by point clouds, polygon meshes or a set of parallel planes.

Point clouds models either cast rays from the hologram towards the object, or have sampled the object and ray trace these to the hologram plane. Each point can be treated as point source emitting a spherical wave to define the complex amplitude on the hologram plane. To speed up calculations, look-up tables (LUT) are often employed. Here, predefined Gabor zone plates are stored in a LUT, each focusing at a different distance. During calculation, holograms are compiled by adding these predefined patterns after multiplying with the desired amplitude. [75, 94, 95, 96]

Polygon based models mesh the desired 3D object into a set of light sources each with a polygonal shape. During calculation, each polygon is used as a window through which light is allowed to reach the hologram plane. Propagation commonly employs the angular spectrum method compared to the spherical wave approach for point clouds. [97] Together with point cloud models, polygon models offer photorealistic 3D imaging having correct depth cues and proper handling of surface roughness and illumination conditions without real increase in simulation by including such properties.[98] That said, both models do require a significant amount of computational power compared to other methods.

Lastly, objects defined through multiple parallel planes result in arrays of data containing non-zero elements defining the object and zeros where occlusion occurs. Here, any propagation method can be used. However, to obtain a good reconstruction a large set of parallel planes is required. Still, due to the plane based approach a good reconstruction can only be attained for a limited viewing angle. [99, 100, 101]

2.2 Requirements for High-Quality Holography

To achieve a good holographic display a certain set of benchmarks needs to be attained. These are most easily assessed by considering them from a theoretical point of view. Afterwards, all of them can be combined together to yield an overarching set of requirements which is important when considering the state-of-the-art and the potential of the different technological approaches.

2.2.1 Field of View vs Pixel Size

The field of view (FOV), the angle in which the a holographic image can be viewed without higher order images, is determined by Bragg's law of diffraction which states the following.

$$\theta = \sin^{-1}(\frac{\lambda}{2d}) \tag{2.3}$$

Here, θ is the viewing angle measured from the incident beam towards the hologram plane, λ is the wavelength and d is the pixel size. Figure 2.4 shows a schematic of the diffraction, in which the blue line indicates the additional

distance covered by light between adjacent pixels. The FOV can be calculated by doubling the viewing angle θ. Ideally, a hologram reaches a FOV of 180° such that it yields life-like images viewed from any direction. To that end, equation 2.3 can be used inversely. By assuming a viewing angle of 90° and taking the sin, the left hand side becomes 1. Hence, the pixel size needs to be equal to half the employed wavelength. For a display operating with red-green-blue (RGB) illumination, typical laser wavelengths might be $640nm$, $550nm$ and $465nm$ for red, green and blue respectively. This requires a maximum pixel size of $320nm$, $225nm$ and $232.5nm$, which can be further exacerbated when the modulation occurs in a non unitary refractive index.

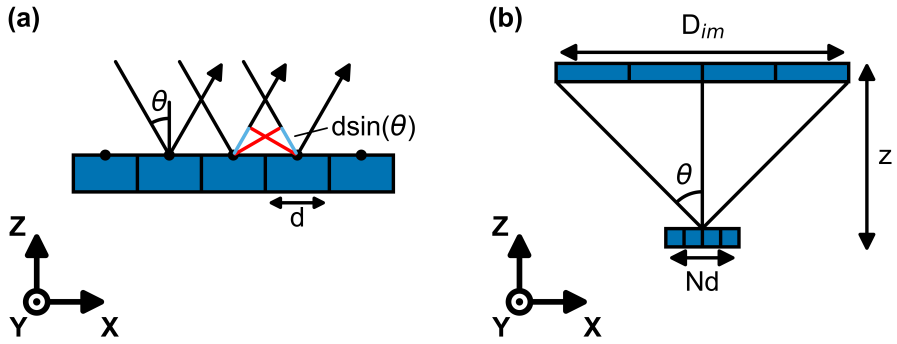

Figure 2.4: a) Bragg's law applied to a holographic display. b) Image scaling due to the numerical aperture.

2.2.2 Image Distance and Pixel Size Trade-off

A consequence of the diffraction limit, is that the pixel size, the wavelength, the imaging distance and the image size are linked together. The diffraction limit is known as:

$$d = \frac{\lambda}{2NA} = \frac{\lambda}{2n\sin(\theta)} \tag{2.4}$$

Here NA is the numerical aperture, n is the refractive index, θ the half-angle of the diffraction and d is the pixel size. In the same geometry, the angle θ can also be found through the tangent, for which we assume $n = 1$ in free space:

$$\tan(\theta) = \frac{D_{im}}{2z} \tag{2.5}$$

Here D_{im} is the image size and z is the imaging distance. Depending on the magnitude of angle θ, there are two options relating the pixel size d to the image size D_{im}.

θ **small**	θ **large**
$\sin(\theta) \approx \tan(\theta) \approx \theta$	$\sin(\theta) \neq \tan(\theta)$
$d = \frac{\lambda z}{D_{im}}$	$d = \frac{\lambda}{2\sin(\arctan(\frac{D_{im}}{2z}))}$
$D_{im} = \frac{\lambda z}{d}$	$D_{im} = 2z\tan(\arcsin(\frac{\lambda}{2d}))$

(2.6)

The equation for θ small is only applicable for large pixel sizes. Employing it for small pixels would only allow reaching a FOV of 180° with an ever decreasing pixel size, which is not realistic. The correct approach, which employs a *tan*-function, indicates that the maximum image size can be attained when pixels are equal to half the wavelength λ. Even smaller pixels lead to the *arcsine* becoming complex as the Nyquist sampling limit is no longer valid ($\lambda > 2d$). This is in correspondence of the Rayleigh-Sommerfeld diffraction integral, which when solved by means of angular spectrum poses a limit on pixel size that can meaningfully contribute to the farfield as too small pixel sizes lead to evanescent waves.

2.2.3 Hologram Encoding

Hologram encoding differs depending on the intended technology. Not only are there amplitude, phase and complex amplitude holograms. They can additionally be stored as binary and analogue signal.

Amplitude vs Phase

To create a holographic image, a display can either modulate the amplitude, the phase or both at the same time. Amplitude holograms modulate either the

reflected or transmitted amplitude on a pixel by pixel level. Of all possibilities, they have the lowest diffraction efficiency since many pixels contribute no light. On the other hand, phase holograms have a unitary contribution at every pixel and modulate the phase to create the desired image. Complex amplitude holograms achieve modulation for both phase and amplitude simultaneously and thus also create the best image.

Binary, Multi-level or Analogue

During hologram calculation the encoding can be set binary, multi-level or analogue in nature, thus defining the allowed states a pixel can have. A binary hologram, as the name suggests, is limited to two allowed pixel values. For an amplitude hologram this is "1" and "0", whereas for a phase hologram $\pm 90°$ jumps are most common. Multi-level holograms expand on the number of allowed values, resulting in increased control on the incident wavefront. Finally, analogue encoding allows pixels to have any value. That said, a high enough multi-level encoding can be considered to be quasi-analogue, and will similarly result in high quality images.

To illustrate the effect of a limited numbers of pixel values, the fundamental hologram for a point source i.e. a zone plates can be considered. Figure 2.5 compares a continuous zone plate, also called a Gabor zone plate, and a binary zone plate, also called a Fresnel zone plate. On first look, they appear and behave quite similar, however they deviate strongly in their frequency spectrum. [59] By defining sharp boundaries in the Fresnel zone plate, higher order frequencies are introduced. These lead to the Fresnel zone plate having additional foci positioned closer to the lens. Similar effects thus also take place in more complex binary holograms. In case a distortion free image at the intended focal plane is desired, analogue encoding yields the best results.

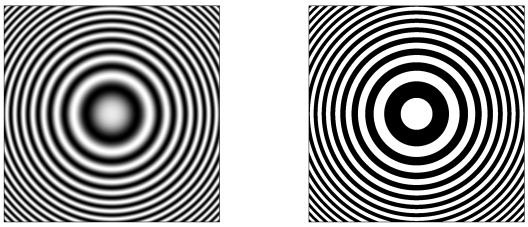

Figure 2.5: left) A Gabor zone plate. right) A Fresnel zone plate.

2.2.4 Data-rate

Videoholography requires an incredibly large data-rate, mainly due the required small pixel size. To put this in perspective, a typical holography data-rate is compared to that of a 4K display. A 4K ultra-high definition (UHD) display has 3840×2160 pixels, refreshes at 60Hz, represents colors with 8 bits to create 256 channels and requires 3 of these for its RGB operation. This results in:

$$\text{data-rate 4K UHD} = 3840 \times 2160 \times 60 \times 8 \times 3 \approx 11.9 \times 10^9 \; bit/s \tag{2.7}$$

For holography, only the number of pixels needs to be adjusted. For a 55inch display, about 2.5×10^{13} pixels exist, assuming that the pixels are 180nm in size. The equation from above than becomes:

$$\text{data-rate holography} = 2.5 \times 10^{13} \times 60 \times 8 \times 3 \approx 36 \times 10^{15} \; bit/s \tag{2.8}$$

This unfortunately forms a major bottleneck for video-rate holography as the required computational power and data bandwidth is simply not at hand at this scale. Estimates put the end of the current century i.e. 2100 forward as date at which the required data-rates become attainable assuming the historical progress can be extrapolated. [102] In case of a smaller device, for example with an area of $2cm^2$, the number of pixels becomes more manageable at 3×10^9. Consequently, its required data bandwidth is:

$$\text{data-rate small holography} = 4 \times 3 \times 10^9 \times 60 \times 8 \times 3 \approx 16.8 \times 10^{12} \; bit/s \tag{2.9}$$

2.2.5 A High-Quality Hologram

Taking in the considerations of the previous sections, an ideal holographic display requires the following.

1. A pixel size smaller or equal to half the size of the employed wavelength to enable full 180° steering and a maximal FOV.
2. A refresh rate at 60Hz or higher to enable flicker free viewing.
3. Analogue phase modulation is preferred, due to its superior detail.

Individually, each of these are attainable but it remains a challenge to combine these on a large scale.

2.3 Current State of The Art

2.3.1 Phase and Amplitude Modulation for Static Holography

When it comes to static holograms, two main technologies form the backbone of the majority of applications. Namely, Silver Halide based photographic film and photolithography in various forms. Since the onset of photolithography it has been used to etch holographic patterns in photoresist, metals and dielectrics, below several phase and amplitude modulation approaches are expanded on in the framework of metasurfaces.

Photographic Film

It might be surprising to find photographic film, nearly identical to the one used 100 years ago, as a state-of-the-art application. In practice though, it offers everything one would need for high-quality static holograms ranging from high sensitivity to light and feature sizes down to 10nm. Their downside is that they need to be physically recorded which limits their reproducibility.

Photolithographic Metasurfaces

Photolithography does not require an object to be physically recorded and can be used to create CGHs down to a few tens of nanometre. This technique is incredibly versatile, but much slower than standard photographic film when small feature sizes are required. Nowadays, devices created by photolithography are often referred to as metamaterials or metasurfaces given that their features are smaller than the wavelength of incident light. Many approaches exist to tailor a sub-wavelength structure such that it delivers a desired interaction with incident light. [103, 104, 105] Below several design approaches to influence the phase of incident light are expanded on. First, a general description of the method is explained followed by their current state-of-the-art applications. Finally, the tunability of these methods is highlighted.

Geometric or Pancharatnam–Berry Phase Geometric or Pancharatnam-Berry (PB) phase modulation originates from the spin-orbit interaction of light. Hence, this effect differs strongly from most other phase modulation techniques that

typically rely on some kind of resonating structure. The effect can be found in anisotropic media, which in the context of metasurfaces most often means a bar shaped metallic or dielectric meta-atom. Here, the PB formalism describes the link between the polarization conversion and phase change upon reflection or transmission of circularly polarized light. The effect was initially observed in 1956 by Pancharatnam when working on a method to find the phase difference between optical beams having different polarizations. [106] It took however till 1984 for Berry to formulate the theory behind geometric phase modulation when he found that when a quantum system in an eigenstate is adiabatically transported around a circuit C by changing parameter R in its Hamiltonian $H(R)$, it acquires a geometrical phase factor $e^{i\gamma C}$. [107, 108, 109] Afterwards, the general description of the geometric phase became known as the Aharonov–Bohm phase for electrons and the Pancharatnam–Berry phase for photons. [110, 111, 112]

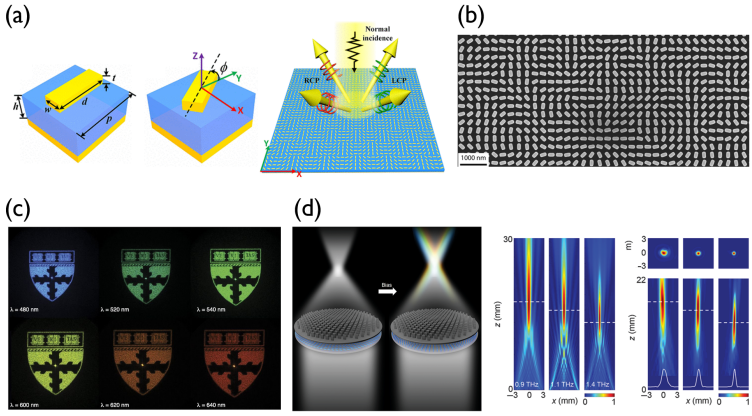

Figure 2.6: a) Basic unit cell of a geometric phase element and metasurface layout indicating various types of meta-atoms and their operation. b) Top view SEM image of geometric phase metasurface. c) Holographic images covering the visible spectrum, measured at various wavelength from a single device. d) Simulated and measured beam focusing from a geometric tunable metalens in the THz range. Images reproduced with permission. [113, 114, 115]

The PB phase is especially suitable for the creation of achromatic optics given that geometric phase modulation occurs at every wavelength. Only the shape, dimensions and the orientation of the meta-atoms determine the phase response. When circularly polarized light hits an anisotropic meta-atom, two separate electrical oscillations are excited. These are oriented perpendicular to each other and differ in amplitude and phase. One leads to spin-conserved generation

of electromagnetic fields, the other to spin-reversed generation. The additional geometric phase occurs solely in the spin-reversed component. The rotation angle of the meta-atom in regard to the incident light determines the accumulated phase difference. It is generally, written as:

$$\phi_{PB} = -2\sigma\Delta\theta \tag{2.10}$$

Here, σ represents the helicity of the incident polarized light and $\Delta\theta$ represents the rotation angle between the meta-atom and the incident light.

Unfortunately, the polarization conversion efficiency of single layer geometric metasurfaces is typically very low. In metallic meta-atoms, this is combated by employing a metal insulator metal (MIM) cavity. The resonance formed here leads to a plasmonic oscillation that enables efficient polarization conversion. For dielectric meta-atoms, the anisotropic shape (rectangular or elliptical) is chosen such that they function as half-wave plate i.e. they have a π phase shift between major and minor axis. Geometric phase modulation in transmission has shown efficiencies up to 91% for metallic meta-atoms and 82% for dielectrics. [116, 114] Reflection based metasurfaces typically employ metals and have achieved up to 80% efficiency. [117] They have been found useful in achromatic lenses, holography and spectropolarimetry sensing for orbital angular momentum. [113, 118, 119, 120]

Currently, geometric phase modulation is not employed extensively to create tunable metasurfaces. Its cause can likely be found in the same reason why this type of modulation is interesting in the first place. Geometric phase modulation offers an easy solution to attain phase control, as only the meta-atom orientation plays a deciding factor. Most tunable approaches however tune a material property such as the refractive index, which conflicts given the achromatic nature of geometric phase. Currently, two modulation approaches are common. First, some metasurfaces are constructed such that they respond differently to left hand polarized and right hand polarized light and can thus be switched between two possible states. [121, 122, 123] Alternatively, the metasurface can be detuned, for example by phase change material or liquid crystal, such that the phase modulation is disturbed and it is turned off. [115, 124, 125, 126]

Huygens' Principle Phase Phase modulation based on Huygens principle are mostly high index dielectric in nature, as to avoid the parasitic losses that are

typically encountered in metal based metasurfaces. [127] In practice, this leads to highly efficient transmission based metasurfaces. They are based on Shelkunoff's equivalence principle, which is a generalized form of Huygens' principle that states that every point of a wavefront acts as a source for the propagation of the wavefront. [128] Huygens' principle metasurfaces are thus designed such that meta-atoms create the desired electric and magnetic resonances, leading to incredibly high transmission.

The more rigourous formulation by Shelkunoff states that a purely forward propagation wave requires that every constituent point source needs to act as an overlapping electric and magnetic dipole resonance of equal strength. This can be interpreted broader than perhaps initially thought, as an incident wave can be transformed to any outgoing wave on the condition that the field induces the required electric and magnetic currents for the outgoing wave. The electromagnetic field can thus be discontinuous at the interface in the most general case. Furthermore, the required currents can either be induced (passive metasurfaces) or externally impressed (active metasurfaces). In case of passive metasurfaces, the desired currents can be created through one of three methods based either on susceptibility [129, 130, 131], polarization [132, 133, 134] and impedance/admittance. [135, 136] These concepts have been applied to both dielectrics and metals, but since metallic metasurfaces verge into the realm of plasmonics they are not expanded on here.

Huygens' principle metasurfaces share many commonalities with reflectarrays and transmitarrays used in the microwave regime. Hence, with the increasing interest in metasurfaces in infrared and visible frequencies, Huygens principle was first applied here in 2013 to create a beam deflector and shaper. [135] Given their unique features yielding very high transmission efficiencies, especially since no metals are considered, they were quickly employed to create flat lenses [140, 141], waveplates [142, 143], beam deflectors [140, 144] and optical cloaking. [136] Next to these, several holographic metasurfaces have been made in the microwave, infrared and visible frequencies. [145, 146, 147, 148, 138, 149] For both the real image and the general transmission, efficiencies around 90% have been achieved.

Some works, refer to the earlier mentioned reflectarrays and transmitarrays as a separate category of metasurface, called circuit-based metasurfaces. Here, the desired resonances are formed in metallic nano-circuits that entail a certain capacitance and inductance resulting in the same effect as encountered in dielectric Huygens' principle metasurfaces. To create the required capacitance and inductance, metal is commonly patterned in shapes such as I-beams, templar

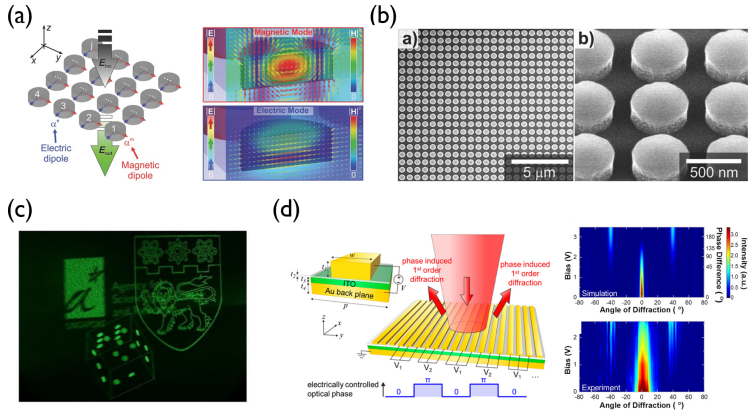

Figure 2.7: a) Array of Huygens' Principle meta-atoms where the electric and magnetic dipoles are shown. The fields distributions of a single meta-atom are magnified. b) Top view SEM image of a Huygens' Principle metasurface. c) Hologram projected by a transmission metasurface intended for near-eye displays. d) Tunable metasurface through carrier injected refractive index modulation of a thin conductive oxide layer. Images reproduced with permission. [137, 138, 139]

crosses and spiralling crosses. [150, 151, 152, 153] Given the unfavourable optical properties of metals, these tend to only be considered in the microwave regime and are thus not very important for the field of optical holography.

Interestingly, it is exactly these Huygens' principle metasurfaces in the microwave regime that where initially employed using impressed currents, yielding actively modulated metasurfaces. They allow modification off a passive metasurfaces by an auxiliary input through thermal, optical or electrical means. These inputs then locally change either refractive index or the meta-atom conductivity to create the desired response in transmission or reflection. At longer wavelengths, starting at the far infrared, active metasurfaces have been made employing varactor diode [154, 155], PIN diode [156] and graphene [157, 158] to control reflection, tune phase and deflect beams.

For short wavelengths, including visible and infrared (IR), similar devices architecture cannot be so readily applied. Instead, devices here revolve around phase change materials (including liquid crystals) [159, 160, 161, 162, 163], carrier injection [139] and MEMS [164] to create tunable waveplates, beam steering and focusing. Unfortunately, these materials often have higher losses than can be found in the IR. Additionally, it should be said that these metasurfaces are very sensitive to manufacturing defects and thus typically

require e-beam lithography to attain the desired operation.

Plasmonic Resonant Phase Plasmonics aim to form the bridge between electronics and photonics, by coupling light to the collective oscillation of the electron cloud at a dielectric–metal interface. In doing so, they aspire to combine the best of both fields. [165, 166, 167] Looking at both technologies, we find that photonics are capable of incredibly high modulation speeds and offer a high bandwidth paired with a high data-rate compared to electronics. Unfortunately, photonics are limited by the diffraction limit, which is linked to the employed wavelength and refractive index. Electronics on the other hand, can operate at sub-wavelength scale, down to a few nanometre in size. Plasmonics thus attempt to confine light in a plasmonic mode at a sub-wavelength scale. A few distinct types of plasmons exist. Namely, localized surface plasmon (LSP) and surface plasmon polariton (SPP) and gap surface plasmon (GSP). [168] SPPs occur at a metal-dielectric interface and can exist as guided mode. LSPs occur in metallic meta-atoms that often have C-, V- or bar-shapes, which when excited confines the electric field. The resulting collective electron oscillation, thus also remains localized to the meta-atom and its near surroundings. GSP's cover the middle ground in between LSPs and SPPs, when metallic meta-atoms are situated close enough such that they interact with each other. Both LSPs and GSPs, are used for plasmonic phase modulation in metasurfaces.

Under incident light, a dipole or higher order multipole electron cloud oscillation forms with frequency identical to the employed wavelength. The properties of this resonant mode can be tuned by changing the size, shape, orientation and refractive index of the employed nano-antenna. As such, the nano antenna allow amplitude modulation, phase modulation between 0 and 2π and polarization modulation of the scattered wavefront. [171, 172, 173, 169, 174] Numerous shapes exist, but C, V and rectangular block shapes are commonly used. Since the resonant mode is excited at the frequency of the incident light, the radiated field will have the same frequency,, but can be altered in phase or polarization. [175]

Plasmonics have shown excellent results in biosensing, holography and sub-wavelength optics. [176, 177, 178] However, the field hasn't found a reliable way yet towards widespread adoption. Most applications seem impractical at the moment as plasmonics tend to suffer from high absorption losses linked to the metals required to create an allowed plasmonic mode. As a consequence, low efficiencies (10%) are attained in transmission hence why most plasmonics are

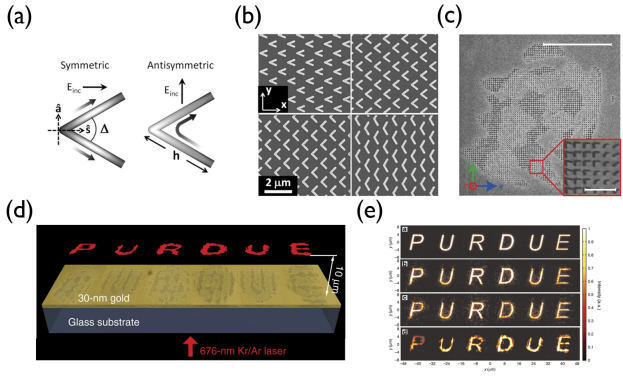

Figure 2.8: a) Schematic of V-shaped optical antenna, having two orthogonal modes i.e. symmetric and antisymmetric. The current distribution is indicated in the antenna through its grayscale. b) Top view SEM image of a plasmonic resonant meta-atom array. c) Top view SEM image of a hologram encoded through transmission of plasmonic resonant meta-atoms. d) Operation principle of the transmission based plasmonic hologram shown in c). e) Simulation and measurement of the plasmonic transmission hologram in c)-d). Images reproduced with permission. [169, 170]

intended for reflection ($> 80\%$). [179, 180] New materials are currently being explored including transparent conductive oxide (TCO) and diluted metals to resolve the aforementioned issue. [181, 182, 183, 184, 185] That said, these issues need not occur when plasmons are employed more locally such as metasurfaces for beam shaping and holography.

Nevertheless, in the context of holography both SPP and LSP approaches have shown excellent control over phase, amplitude. [170, 186, 187] Additionally, the field now aims to create tunable plasmonics, similar to other metasurface technologies. Here several routes remain available including using graphene, carrier accumulation and phase change materials as driving force. [188, 189, 163]

Propagation Phase Propagation phase approaches phase modulation from a waveguide perspective, hence why they are occasionally referred to as waveguide phase. [190, 191] These metasurfaces are generally covered in a hexagonal or rectangular grid of dielectric nanoposts that act as small waveguides. Phase differences between unit cells can be introduced by changing the nanopost diameter as it is linked to the effective refractive index of the waveguided mode.

Consequently, varying the mode dynamics through its effective index, will result in different outgoing phase for each post. Propagation phase nanoposts are typically taller than structures encountered in other metasurfaces types since full 2π phase modulation requires sufficient propagation distance. Materials with high refractive indices are usually considered as they allow for shorter posts. To attain high efficiencies, resonant conditions (Fabry-Perot) are typically avoided.

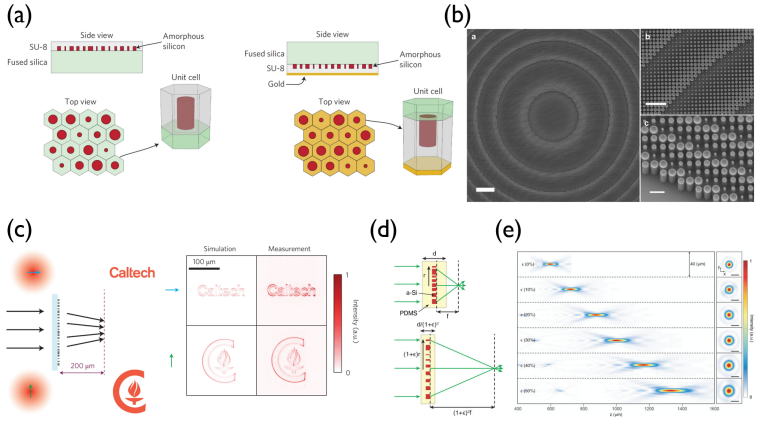

Figure 2.9: a) Schematic of a hexagonally designed propagation phase meta-atom. Both transmission (left) and reflective (right) based approaches are shown. b)Top view SEM image of a rectangularly patterned propagation phase metalens. c) Operation principle of a transmission based polarization switchable metahologram employing propagation phase. d) Schematic of a tunable metalens through stretching of the substrate. e) Tunable focus of a metalens following the principle shown in d). Images reproduced with permission. [192, 193, 194, 195]

Propagation phase modulation has shown efficiencies up to 93%. [196] These metasurfaces have been used extensively to create metalenses [197, 193, 198, 199], blazed gratings [200], retroreflection [192], single molecule microscopy [201] and holography [194] in both visible and infrared. Unfortunately, propagation phase modulation offers no straightforward method to enable tunability, given that the diameter of each individual nanoposts needs to be altered. One notable example that found a workaround, was the inclusion of a stretchable substrate such that the focal distance of a metalens could be tuned. [195] Instead of tunability, the field looks to other applications such as spatially multiplexed lenses to enable focusing at multiple wavelengths and combining PB phase together with propagation phase to attain a higher degree of phase control.

[202, 203]

Non-linear Phase Another approach that has recently gained traction is the use of non-linear materials in metasurfaces. [204, 205, 206] This is especially interesting since metasurfaces offer methods to engineer strong non-linear effects. In doing so, they are capable in addressing their main challenge namely that non-linear effects are by default very weak. In practice, to have adequate results in bulk structures, non-linear effects require either a substantial electric field or long propagation distances to overcome linear behaviour. In case of metasurfaces, the former asks careful attention as too high fields can easily damage the meta-atoms in question. On the other hand, the latter is simply not possible as they inherently have limited propagation space. As indicated above though, metasurfaces allow for the creation of strong non-linearities through for example metal organic frameworks, 2D materials and multiple quantum well (MQW).

It should be noted that non-linear phase modulation does not form a complete separate type of phase modulation, instead these metasurfaces use geometric phase, plasmonic resonances, Huygens' principle and detour phase. Crucially though, they add a non-linear component to the phase modulation. For example, a non-linear metasurface illuminated by plane wave in infrared might emit a wave with a holographic phase profile in the visible. Similarly to the approaches these are based on, the meta-atoms can be tuned by size, shape and orientation.

Non-linear metasurfaces have been created to employ a multitude of processes including second harmonic generation (SHG), third harmonic generation (THG) and four wave mixing (FWM). These processes have been used to solve several challenges such as in beam shaping, metasurface lenses, beam splitting and holography. To that end, beam shaping has been achieved by employing topologically charged crystals [209, 210, 211], plasmonic resonances [212] and Huygens' principle [213] to provide the necessary phase modulation. On the other hand, geometric phase was used to create both a beam splitter and polarizing beam splitter. [214] Finally, for beam focusing and holography, metasurfaces commonly use geometric [215, 216, 217, 208] and plasmonic [218, 207] phase modulation. The origin of the non-linearities for these examples is very diverse as it includes typical non-linear crystals, ring resonators with a broken symmetry, and MQWs.

When it comes to tunable non-linear effects, these metasurfaces have as major

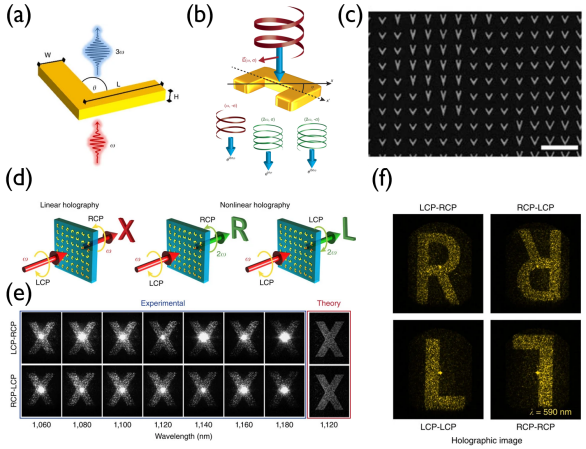

Figure 2.10: a) Schematics of 2 grating slits spaced by D such that they result in a desired phase difference $\delta\phi$. Smaller features are added inside each slit, indicate by m and n to add additional features. b) 2D top view of a pixelated detour phasemap. Amplitude is tuned by widening are narrowing a slit, the phase is tuned by tuning the slit position. Again, inside each slit an additional element can be added, for example a wire grid polarizer. c) Top view SEM image of a detour phase hologram. d) Operation mechanism of a spin and wavelength multiplexed hologram. e) Simulated and measured linear hologram, optimized for $1120nm$. f) Measured holographic projection created through frequency doubling. Images reproduced with permission. [207, 208]

advantage that non-linear effects intrinsically occur at ultra short time-scales. Unfortunately, the current state-of-the-art non-linear metasurfaces have rather limited capabilities and are nowhere near the intrinsically attainable switching speeds. As hinted at above, non-linear metasurfaces employ commonly used phase modulation mechanisms such as geometric or plasmonic phase but have the added value of enabling SHG, THG and FWM. As such, to introduce tunability in these metasurfaces the same underlying effects and materials found in linear metasurfaces can be used. Tunable non-linear metasurfaces have mainly been used to show beam steering. Approaches include voltage modulated quantum confined Stark effect to tune intersubband non-linearities in a MQW sandwich between metallic electrodes to attain phase and amplitude modulation, thermo-optical tuning of AlGaAs meta-atoms such that the meta-atom temperature determines the outgoing phase profile and non-linear phase array atennas in which the outgoing phase is determined by the near fields in nanorod resonances which depend on the incident angle of the illumination. [219, 220, 221]

Detour or Lohmann Phase Detour phase modulation is one of the earliest implementations capable of producing the phase modulation required for holography. It was pioneered by Brown and Lohmann in 1966 when working on matched filters. [73] In doing so, they also created a robust method to encode complex amplitude holograms in a photo-lithographically etched metal layer. Their approach relies on the so called detour phase, which according to them is best described by considering a grating. When two rays leaving two adjacent grating slits both go to the first diffraction order, they must have a path difference of 2π. When one of the grating slits is now moved ever so slightly, it will impact the 2π phase accumulated due to the path difference. From a pixel perspective, any desired phase difference can be encoded by moving slits closer and further away from the center of each pixel. Furthermore, by controlling the size or width of the grating slit the amplitude of the pixel in question can be tuned.

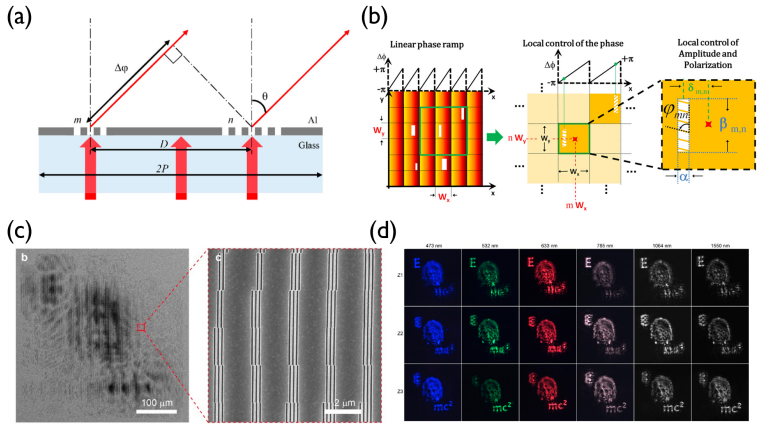

Figure 2.11: a)- b) Schematics of different meta-atom shapes designed to amplify non-linear effects, intended for second and third harmonic generation. c) Top view SEM image of a non-linear meta-atom array. d) Reconstructed images of a detour hologram, measured at various wavelengths and at different distances. Images reproduced with permission. [222, 223]

Recent works have expanded on the initial matched filter by adding additional features inside each pixel to yield improved control. One example includes the use of a wire grid polarizer inside each grating slit to offer simultaneous outgoing polarization control. [223] Alternatively, downscaling the grating slits allowed the creation of plasmonic nanoslits. These can be created such that they act different to s- and p-polarization, transmitting one and reflecting the other. By

including both features in each pixel, a polarization multiplexed metasurface could be created capable of beam shaping and holography. [222] Unfortunately, due to the operation mechanism, a large portion of incident light is reflected or absorbed by the metallic film thus resulting in rather low efficiencies of up to 9% and 75% for visible and infrared. [224, 225]

2.3.2 Modulation Mechanisms for Dynamic Holography

Through the years, a wide range of technologies has been used to create dynamic holography. Each with their own merit. Below, the field of dynamically tunable holograms is elaborated. This section brings together the earlier parts of the chapter ranging from the requirements to form realistic holograms to the type of phase modulation. A summary of the field is provided at the end of the section.

Doped Lithium Niobate

Various doped Lithium Niobate (LN) crystals show a photorefractive effect, i.e. when locally exposed to light, they change in refractive index. [226] Originally, this effect was thought to be optical damage to the LN, but Iron impurities were quickly found to be the root cause. [227, 228] Afterwards, a wide range of dopants were employed, each offering different results in spectral response and writability. [229]

The effect originates due to redistribution of charges, which causes electric fields to form inside the crystal. Said fields, through the Pockels effect change the refractive index. Homogeneous illumination can be used to probe the modulated refractive index but has a tendency to erase the stored data depending on intensity and wavelength. Similarly, the stored data can be reset by a thermal anneal. More advanced crystals employ two separate dopants to create a photochromic behaviour in which the absorption changes when illuminated with a certain wavelength. One notable example is the combined use of Iron and Manganese, which form shallow and deep traps respectively. [230] Here, the shallow traps initially tend to be empty and can become populated after the deep traps are excited by ultraviolet (UV) light. The crystal then gains an absorption shoulder at longer wavelengths corresponding to the population of the shallow traps. This proofs useful for non-volatile holographic storage as recordings can be made using a combination of short and long wavelengths, after which reading can be done using just the long wavelength for which the

deep traps do not respond. This re-writability made this set of materials very interesting for holographic storage. [231] Unfortunately, the write-rewrite speed remains too low for any practical holographic display.

Liquid Crystals

Liquid crystals (LC) form a special phase of matter situated between crystalline and liquid phases. They form a collection of long molecules, often polymers, that can have a permanent electric dipole with a positive and negative charge on either side of the molecule. This enables them to be reoriented under influence of electric and magnetic fields. They are most known from their use in liquid crystal displays (LCD), which was one of the earliest flat panel displays. In the context of beam shaping and holography, they are mostly used in liquid crystal on silicon (LCOS) phase modulators. This is a rather mature platform, for which many commercial versions are available. That said, they are now also being considered as active component in metamaterials.

LCOS modulators were first introduced in the 1970's by the Hughes aircraft company. [232] These initial devices employed an electric current instead of the now commonly used electric field, as driving force. Consequently, they weren't suitable for phase modulation. That said, the prospect of a silicon backplane combined with the tunability of liquid crystals remained promising. Further research lead to more practical implementations capable of phase modulation around the early 1990's. [233, 234] From then onward, the technology gradually found its footing in industry but always stayed in the shadow of the much better known liquid crystal displays (LCD)s. LCOS was quickly used for beam steering applications and eventually for holography as well. [235, 236] For a good overview on the types of LCOS, their applications and an industry perspective, the reader is referred to [237, 238]. Fig. 2.18 contains several state of the art LCOS modulators that are currently commercially available. [239, 240, 241, 242, 243]

More recently, liquid crystals are being considered as active component in tunable metasurfaces. Indeed, metasurfaces have shown excellent control over incident light in the context of lenses, plasmonics and beam shaping. On top of that, they have shown properties that are unachievable with normal materials such as perfect absorption and negative refractive indices. [246, 247, 248] However, their use cases remain limited due to their static nature. Hence, recent works aim to create tunable metasurfaces. Numerous, excellent reviews cover

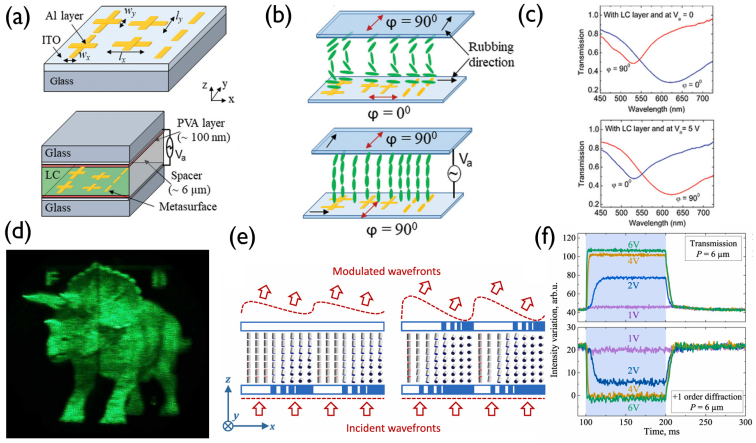

Figure 2.12: a) Schematic of a tunable liquid crystal metamaterial. The metamaterial is patterned on the bottom electrode, whereas a brushed PVA layer ensures liquid crystal alignment at the top electrode. b) Operational schematic of a liquid crystal reorienting. c) Transmission behaviour for various wavelengths and bias of the LC cell shown in a). Supplying sufficient bias switches the transmission. d) Photograph of holographic reconstruction projected by LC spatial light modulator (SLM). e) Schematic of a LC cell employing electrodes to create tunable gratings. f) Out coupling intensity for a grating with $6\mu m$ period as shown in e). Images reproduced with permission. [244, 236, 245]

the field of dynamic metasurfaces. [194, 249, 250, 251, 252, 253, 254, 105, 255]. The groundwork for LC metasurfaces was laid when they were considered in split ring resonators SRR and core-shell nanosphere metamaterials. [256, 257] Through the years, their tuning architecture and feature size was improved and downscaled respectively, pushing these devices gradually into the visible optical regime. However, rapid switching and individual pixel addressing remains absent. Multiple approaches attempt to tackle this challenge including SRR's, embedded fishnet metamaterials, meta-atoms and LC enabled plasmonics. [258, 259, 260, 244, 261, 262, 245, 263] A selected set of these is shown in Fig. 2.18 .

Thermo-Optics

Thermo-optics employ heat to tune the optical properties of a material. This can be achieved through the thermo-optic coefficient i.e. the link between the

refractive index and the temperature of a material but also through a phase change or transition. First phase change materials will be covered, after which devices using the thermo-optic coefficient will be highlighted.

Phase change materials form a collection of materials that have two or more crystalline phases with distinct optical properties. Through the years, they have become a staple material whenever a tunable meta-atom is desired. Commonly used materials include $Ge_2Sb_2Te_5$ often abbreviated as GST, Vanadium Dioxide (VO_2), PbTe and liquid crystals. The desired phase change is thermally activated by raising the material's temperature above the phase transitions temperature. For some materials such as VO_2 and liquid crystals, the phase transition back to the original state occurs automatically. For others such as GST, an amorphous highly resistive phase is typically encountered after deposition. Heating up to about $150°C$ leads to crystallization into a stable more metallic phase having lower resistivity. To return to the initial amorphous state, GST needs to be heated above is melting point ($600°C$) and quickly cooled such that it cannot form a metallic lattice. Heating can either be done optically, by a focused laser or through the inclusion of heating elements enabling current generated Joule heating.

Metasurfaces employing phase change materials have shown excellent results in a multitude of applications ranging from transmission and reflection tuning [267, 268, 269, 270, 271] to beam steering [272, 273]. For example, modulation depths of up to 90% have been achieved for absorption tuning [274], relative transmission changes of 500% have been reported [159] and beam steering angles up to 40° have been shown. [162] Additionally, slightly more advanced metasurfaces have been used to create tunable metalenses. [275, 266] Several approaches have even been able to go even one step further and have shown beam shaping and holography. Indeed, holographic metasurfaces have been made by hydrogenation-dehydrogenation of Mg meta-atoms [265], tuning of a resonance [266, 276, 264, 277, 278], and tunable split ring resonators. [279] Pixel sizes down to $600nm$ have been achieved for devices operating in On-Off state (50s switch time). On the other hand, faster switching ($500ns$ rise time - $100\mu s$ fall time) is possible at slightly larger pixel size ($4\mu m$). It should be noted that these approaches mostly employ longer wavelengths starting from the near IR to THz frequencies. On top of that, the meta-atom switching rate remains limited at the moment given that integrated heaters are only included in a minority of works such that others either rely on a laser pulse or hot plate for write-rewrite. The most impressive result currently has been achieved by SWAVE Photonics which managed to incorporate a modulated phase change material into a complete display stack, reaching pixel sizes down to 300nm and

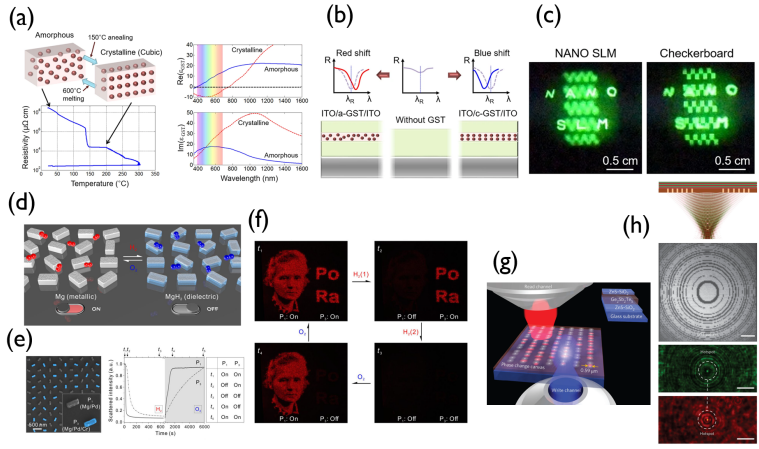

Figure 2.13: a)Optical behaviour of commonly employed phase change material GST, which can be switched between amorphous and crystalline phases. b) The effect of the different phases of a thin GST layer have on the reflectivity of an optical stack. c) Holographic projected of a GST patterned metasurface made tunable by laser scribing. d) Artists impression of the operation of a Magnesium based metasurface, which can undergo a phase change due to hydrogenation of the meta-atoms. e) SEM image of Magnesium meta-atoms and their scattering behaviour versus time. f) Holographic projection fo the device shown in d) and e). The optical is shown for various states of the phase change material to showcase its tunability. g) Artists impression of a GST metasurface, showing both write and read lasers. h) Optical behaviour of a GST metalens, encoded in to the laser by laser writing. Images reproduced with permission. [264, 265, 266]

video-rate capable refresh rates. This display almost reaches the requirements for a true videoholographic display. [55]

Alternatively, the thermo-optic coefficient can be used to tune the refractive index more directly. Here, at low temperatures, any variation leads to a linear change in refractive index. The effect is typically very small with coefficients ranging from 10^{-6} to $10^{-3}/°C$. [283] Nevertheless, the effect is often used in waveguide or resonator structures given that it enables extremely fine control or that the resonance leads to amplification of the effect. Thermo-optically tuned waveguide modulators form an active topic in the field of light detection and ranging (LiDAR), since they can be used to create on chip beam steering platforms. Both one-dimensional (1D) [284, 285, 280] and 2D beam steering based on thermo-optical modulation has been shown. [286, 281, 287, 288, 289,

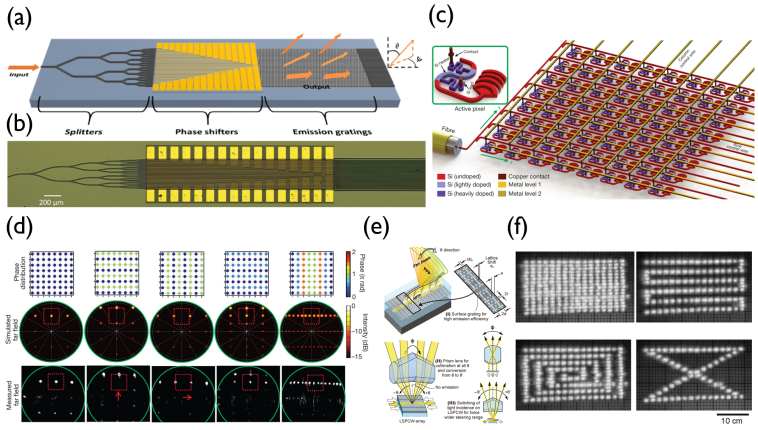

Figure 2.14: a)- b) Schematic and microscope image of a waveguide fed beam steerer that employs thermo-optics phase shifters and out coupling gratings. c) Schematic of an advanced 8 by 8 optical phased array that has independent control over each out coupling element. d) Simulation and measured results from c), by applying various bias conditions. e) Schematic of a 2D beam steerer employing a lattice-shifted photonic crystal waveguide in combination with a prism lens. f) Measured farfield out coupling from the device in patterns from the device in e). Images reproduced with permission. [280, 281, 282]

282, 290] One noteworthy example was the creation of a 64 by 64 optical phased array with individual phase shifters for each emitter, which theoretically could be used to create a holographic display.

Acousto-Optics

Acousto-optics offer a straightforward method to dynamically control incident light. Standard acousto-optic modulators only require three components, namely a grating or prism coupler, an acoustic-optic waveguide and an ultrasound transducer. Here, the grating or prism ensures efficient coupling to a guided mode and the transducer creates a surface acoustic wave. In doing so, the refractive index of the waveguide can be tuned dynamically by the compression and expansion linked to the travelling acoustic wave. The effect is a specific type of photo-elasticity for which is known that mechanical strain leads to changes in permittivity. Similar to the electro-optical effect, a tensor calculation is required to understand the full scope of the modulation. When the applied surface acoustic wave meets the Bragg condition, light can be coupled out of the

waveguide. Nowadays, LN is commonly used as acousto-optic material given that it has a strong response combined with low optical waveguide losses.

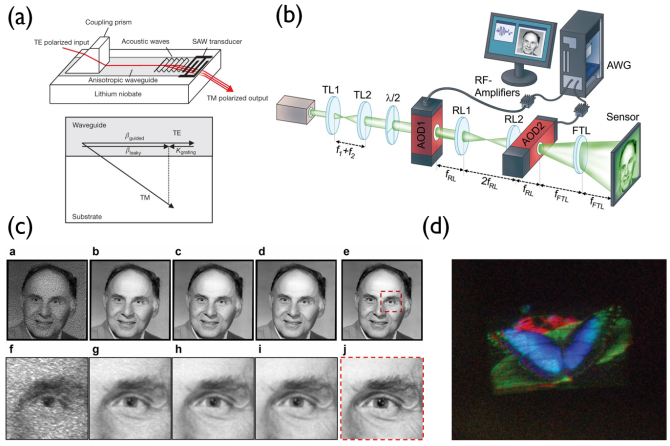

Figure 2.15: a) Schematics of the side and top view of a waveguide based acousto-optic spatial light modulator. b) Schematic of a free space acousto-optic holographic projector. c) Measured holographic projections at various detector integration time employing the device from b). d) Observed holographic projection employing a device structure similar to a). Multicolors were achieved through wavelength superpositioning. Images reproduced with permission. [291, 292]

Acousto-optic beam deflectors on LN have been around since the 1970's. [293] Initially, these devices contained a single modulated channel capable of 1D beam steering. [294, 295] Devices were limited in frequency and thus could only supply acoustic waves capable of creating gratings coupling between guided and cladding or substrate modes. As such, steered light exited the device at the end of the LN wafer. The addition of a second transducer eventually lead to 2D beam steering. [296] In more recent years, a larger degree of control was attained by using the device in a leaky mode state instead. [297] Here, by modulating the device at higher frequencies, guided mode to radiation mode coupling is enabled such that light can be coupled out along its entire surface. This concept has been applied to both beam steering for LiDAR and visible holography. [298, 292, 299, 291] More specifically, a holographic display reaching about 5Hz in refresh rate and a pixel size of $12\mu m$, calculated from the applied acoustic frequency, was achieved. The device excelled in its resolution as it was capable of creating compositional images having up to 355200 pixels by 156 pixels. Consequently, it is one of the best implementations of holographic

display technology yet.

Carrier Injection

TCOs have emerged since the beginning of 21st century as a crucial component in solar cells and flat panel displays. [300, 301, 302] They excel, for example, as transparent electrodes or thin film transistors. This is due to their unique optical and electrical properties that combine good conductivity with low absorption. TCO conductivity can vary widely between values typically attributed to dielectrics and semiconductors depending on the amount of present carriers. Stoichiometric TCOs are in general more dielectric. Conversely, larger conductivities comparable to semiconductors, require more free carriers to be present which for most TCOs can be solved by creating oxygen vacancies. [303, 304] Tuning of TCO properties is easily achieved through deposition parameters and post deposition anneals. [305, 306, 307] Next to that, a wide variety of TCOs such as Indium Tin Oxide (ITO), Zinc Oxide (ZnO), Indium Gallium Zinc Oxide (IGZO), ... have been investigated. Interestingly, due to their oxide behaviour they tend to have remarkably low absorption accompanying their electrical behaviour. TCOs thus occupy a rather rare position in the semiconductor realm and are now considered as backbone for the next generation of plasmonics and in epsilon near zero and near zero index materials. [185, 308, 309]

Their uniqueness however, does not end there. About a decade ago, it was found that the permittivity of TCOs can be actively modulated through the injection or extraction of carriers. [310] By employing indium tin oxide (ITO) as active layer in a a metal-oxide-semiconductor heterostructure, a thin charge accumulation layer could be formed at the interface. Here, the carrier density could be altered between 10^{18}cm^{-1} and 10^{23}cm^{-1} resulting in a $5nm$ layer in which a refractive index change (Δn) of 1.39 was recorded at $800nm$. Optically, this behaviour can be described by a Drude model which links the carrier concentration to the permittivity. The modulation is primarily prevalent in the infrared as free electrons influence optical properties here, but a tail of the effect stretches up to the visible regime. Even though the effect only occurs at the interface, its exceptional size makes it a viable candidate for optical modulators, ideally through the use of ultra-thin layers ($< 10nm$) to limit optical losses and maximize modulation. Lastly, it should be mentioned that the modulation is fast when compared to other techniques since it is only limited by its RC time constant.

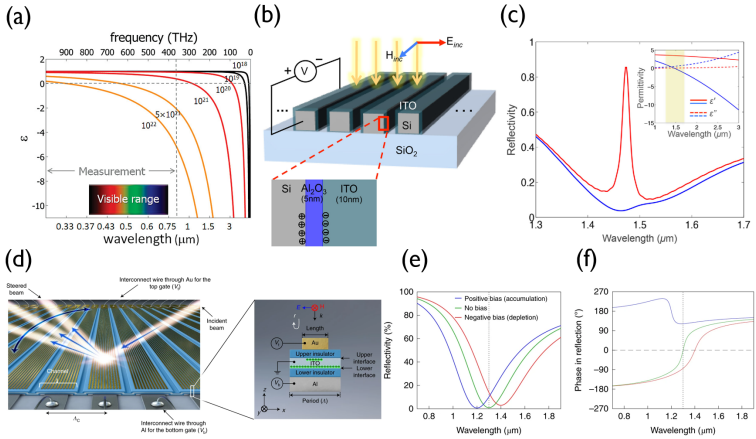

Figure 2.16: a) Variation of refractive index of transparent conductive oxides through carrier accumulation. Measured by ellipsometry in a thin accumulation layer. b) Schematic of a grating structure, covered with *ITO*. Through accumulation of charges the behaviour of the grating can be tuned. c) Observed reflectivity change from the device in b). The inset shows the perceived change in permittivity. d) Artists impression of a plasmonic metasurface grating, tuned though carrier injection. Incident light is steered by the applied bias. A single nano-resonator is highlighted, indicating where the accumulation layer resides. e) - f) Reflectivity and phase change under positive and negative bias, observed for the device shown in d). Images reproduced with permission. [310, 311, 312]

To date, the effect has been applied in tunable epsilon near zero materials [313, 314], plasmonic modulators [315, 316, 317, 318] and a variety of beam steering applications. This last topic was pioneered by a gate tunable metasurface constructed from a Gold - *ITO* - Aluminium Oxide back plane on which a Gold grating electrode was patterned to enable MIM plasmonic modulation. Here, the grating serves as reflection antenna which can be modulated by applying electrical bias to both gold electrodes, in doing so changing reflection characteristics. [139] At an incident wavelength of $1550nm$ and $2.5V$ bias a normalized reflectance change of 28.9% and phase shift of $180°C$ was found. Beam steering was enabled by biasing periodically with varying voltage, which allowed switching between 0 order and -1 and $+1$ order reflection. Changing the periodicity of the applied bias tunes the steering angle. Afterwards, both amplitude and phase modulation metasurfaces implementing TCOs were investigated. Amplitude modulation proved especially interesting in tunable absorbers which often utilize a similar MIM structure that acts as a tunable resonant cavity showing a reflectance change of up to 82% at $1550nm$.

[314, 311, 319, 320] On the other hand, TCO based phase modulators have steadily been improved towards full 2π phase modulation. [321] Currently, phase modulation up to $300°C$ has been shown in the infrared. [322] Next to that, phase modulation devices using carrier injection have shown beam steering, LiDAR and beam focusing. [323, 312, 324] To my knowledge, no TCOs based modulators have been implemented into a holographic display even though this could be achieved by a 2D array of individually addressed elements.

Micro-electromechanical Systems

Micro-electromechanical systems (MEMS) are a well established technology that form a bridge between typical silicon based electronic driving and mechanical movement. In doing so, MEMS create a unique set of capabilities that proved relevant in sensors (inertial and pressure), optical scanning and surface probes. Commonly used device actuation schemes are based on electrostatics, thermoelectric, piezoelectrics and electromagnetic effects. Of these, electrostatics and thermoelectrics are most used. Electrostatic based MEMS offer a fast response, lower power consumption and ease of fabrication. [325] Thermoelectric MEMS, on the other hand, provide slower modulation and higher power consumption but are often used in out-of-plane actuation. Manufacturing-wise these MEMS types are compatible with complementary metal oxide semiconductor (CMOS) technologies as they leverage many of the same principles. Both piezoelectric and electromagnetic approaches require more uncommon materials, and thus are not as prominently used. [326, 327]

Due to their unique tuning capabilities MEMS are now also considered as tunable element in metamaterials. Here they can serve two roles, either they add tunability to a metasurface as a whole or they provide tunability to each individual meta-atom. The first scenario has for example, been applied to metalenses which by positioning them on a MEMS actuator can be used for dynamically steering the focusing point. [330, 331, 164, 332] Other approaches have achieved beam steering at visible frequencies by tuning a cavity grating and transmission tuning of up to 80%. [333, 334, 328] These devices are relatively easy to manufacture and might prove useful in sensing in LiDAR applications. They do however not offer complete reprogrammable phase profiles. Indeed, more advanced tunability requires individually addressed pixels, which quickly drives up device complexity. Device arrays up to 160 by 160 pixels have been reported and have achieved beam steering at THz and infrared frequencies. [335, 329]

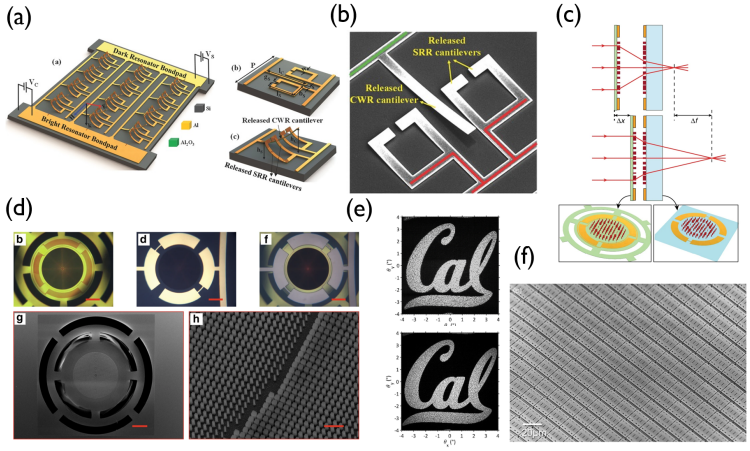

Figure 2.17: a) Artists impression of a split ring resonator actuated by electrostatic MEMS. b) SEM image of a single unit cell of the device in a). c) Schematic o a doublet metalens built on a MEMS actuator to provide tunability. d)Microscope and SEM images of the doublet metalens constituents shown in c) e) Simulated and measured holographic projection from a grating metasurface actuated by MEMS. f) SEM image of MEMS actuated gratings used in e). Images reproduced with permission. [328, 164, 329]

Limited efforts have attempted to create a MEMS driven holographic display. That said, MEMS holographic projection was achieved by creating phased arrays and metal insulator metal cavities. Phase differences between individual pixels were created by lateral displacement of reflection gratings (Lohmann) and by cantilever based tuning of a plasmonic resonance respectively. [329, 336, 337] In general, these attempts have been hindered by the pixel size of MEMS which currently still around the micrometer to tens of micrometer range. For example, the DLP technology from Texas Instruments is capable of switching $5.4/mum$ pixels at $9352Hz$. [338] An alternative noteworthy approach is to employ a 1D MEMS array called "grating light valve" together with a metasurface that transforms the 1D steering to 2D. [339] These can be made from electrostatically driven ribbons which allows for fast switching, refresh rates up to $250kHz$ have been show for pixels down to $5\mu m$. [340] Still due to larger pixel sizes these devices are not ideal for visible wavelengths and the examples mentioned above also operate at infrared wavelengths to retain adequate control. More advanced beam steering, shaping and holography require modulation at a sub-wavelength scale. Further downscaling of MEMS leads to, so called, nano-electromechanical systems. [341] These devices do attain the desired modulator scale, but again bring about complex design.

Summary

Evidently, a myriad of approaches, both in tunable effect and type of phase modulation exist in the field of holography. Figure 2.18 contains a summary of the highlighted technologies from the previous chapter and indicates the region in which a good holographic display finds itself. Many of the results come from the field of metasurfaces. These have shown excellent results, but only a small portion of them has achieved re-writability, and those who have often at very low frequencies. Alternatives, such as acousto-optics and LCOS have similarly shown impressive results but still do no reach the required combination of high refresh rate and small feature size. As such, a clear knowledge gap remains, which requires further downscaling of the employed structures and more rapid switching.

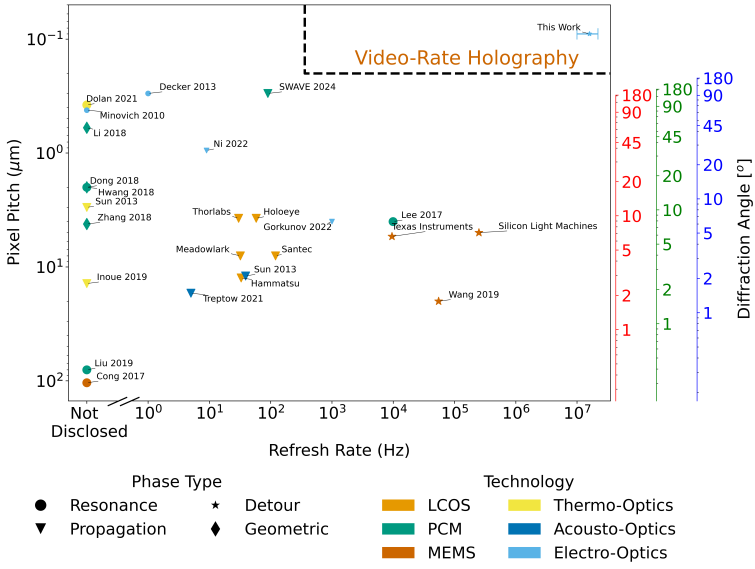

Figure 2.18: State-of-the-art overview of dynamic holographic projectors presented in terms of pixel resolution versus maximal hologram refresh rate. The maximum diffraction angle that corresponds to the pixel pitch for each of the RGB colors is indicated on the right hand axis. We classify the reported results in terms of technology and hologram construction methodology. The domain allowing video-rate holography applications is enclosed by the dashed rectangle. Only rewritable holography results have been included. When no actual refresh rate was reported, we included the result as Not Disclosed.

Chapter 3

Videoholography Device Considerations

This chapter presents our solution to fill the current gap in holographic displays. First a brief overview of the technology platform is given, after which specific sections of the device are elaborated.

3.1 Device Considerations and Selected Methodology

Looking back to Section 2.2, three requirements should be met for an accurate and large FOV holographic display. Namely, (1) a pixel size equal or smaller than half the size of the employed wavelength, (2) refresh rate of 60Hz (or a multiple if colors are treated separately), (3) analogue phase and perhaps even complex amplitude modulation. As highlighted in Chapter 2, the current state-of-the-art has not yet enabled these requirements. The combination between small features and sufficient refresh rate appears especially challenging. Metasurfaces have shown excellent control of light at the desired pixel size, but lack tunability. On the other hand, integrated devices such as thermo-optic optical phased arrays reach the required refresh rate but lack small pixels.

Clearly, a novel approach is required to overcome the limitations of current technologies. One potential solution is to combine the two aforementioned

methods to create a metasurface illuminated through integrated photonics, leveraging their strengths while mitigating their respective weaknesses. This approach, however, faces a challenge common to all integrated devices: waveguide operation does not permit the aggressive downscaling necessary for holography, as no waveguide modes exist in the desired sub-wavelength regime, rendering typical routing impossible. Fortunately, a slab waveguide could be employed to supply light to each active pixel of the metasurface. This could lead to a device where an array of scattering pixels covers the entire slab waveguide. By carefully programming the location or state of all pixels, the desired wavefront can be generated.

To modulate such pixels electrical connections are needed which ideally remain far removed from the waveguide to prevent undesired scattering and absorption. Fast switching is not require to enable video-rate operation which offers the possibility to use poorly conductive materials with low optical absorption to bridge the electrical signal between the active region and the metallic backplane. Several materials such as Indium Tin Oxide (ITO) and Titanium Nitride (TiN) have become established for their properties that situate between that of a metal and dielectric. The individual electrodes will need to be embedded into a dielectric, together forming the cladding layer of the waveguide. Ideally, this layer has a low refractive index which results in strong confinement of the waveguided mode into the waveguide and further limiting undesired scattering from the backplane.

Finally, the operating mechanism and technology of the active pixel needs to be addressed. Looking back at Chapter 2, a variety of options exist of which some are more suited than others. For example, geometric phase requires a reconfigurable anisotropic meta-atom which is difficult to create practice. On top of that, it offers only low conversion rate unless in an MIM cavity. This approach would reintroduce metals near the optically active layer which defeats the purpose of the metamaterial cladding. A similar argument can be made concerning plasmonic phase modulation. Another suboptimal option is Huygens' principle phase for which operation is very sensitive to manufacturing defects. As a consequence, rapid pixel switching will likely not provide control to the required level. Next to that, propagation phase cannot use the benefits of a waveguide as it requires a sufficiently long propagation length for phase differences to occur. Lastly, detour phase appears well suited as it can leverage the naturally accumulated phase of the mode travelling along the waveguide. The metamaterial cladding layer can subsequently enable or disable a scatterer or meta-atom leading to the desired wavefront.

A wide range of materials and technologies can be employed to achieve the desired phase modulation effect. However, for future holographic displays targeting large surface areas, thermo-optics are not ideal. These materials require large currents, which the optically transparent electrodes might not be able to supply. If they do manage, they will cause significant heating of the device, necessitating active cooling for stable operation, which further complicates the device. Finally, common thermo-optic materials, such as phase change materials, are also known to degrade quickly in performance.

Other options, such as liquid crystals and MEMS, cannot be scaled down sufficiently to meet the required pixel size. Conversely, carrier injection appears more suitable for the envisioned geometry. Here, the pillar electrodes could act as capacitor plates that change their refractive index when charged. Careful modulation on a large scale could create a grating to couple out light. A downside to this approach is that the refractive index change is a skin depth effect, occurring only at the outer edge of the electrodes. This results in a very low duty cycle for the applied grating, limiting the amount of out coupling that can be achieved.

Acousto-optic modulation of a non-linear waveguide is another interesting approach and has been used for waveguide-based holographic projectors. Unfortunately, this is not compatible with a slab waveguide, and using normally spaced waveguides would limit the display resolution in one direction. However, non-linear crystals offer an intriguing possibility when combined with a metamaterial cladding layer. This approach has several advantages: it leads to efficient and fast modulation due to capacitive and non-linear effects, the metamaterial electrode pillars in the cladding offer sub-wavelength control, and there is no need for patterned meta-atoms as they can be locally induced into the waveguide, reducing manufacturing complexity. This final approach seems to best suited to meet the required specifications.

Summarized, we propose a novel approach based on a locally modulated waveguide addressing all three requirements simultaneously shown in Figure 3.1. Two crucial components are combined. First, a waveguide that changes refractive index due to electrical bias, and secondly, a metamaterial cladding layer that allows electrodes to contact the waveguide without interfering or scattering the waveguided mode. Both of these parts will be expanded on below. Due to the metamaterial, the proposed device shares structural and operational similarities with dynamic random access memory (DRAM). DRAM namely uses densely packed arrays of pillar shaped capacitors to store data. The holographic display will similarly have pillar shaped electrodes which will operate

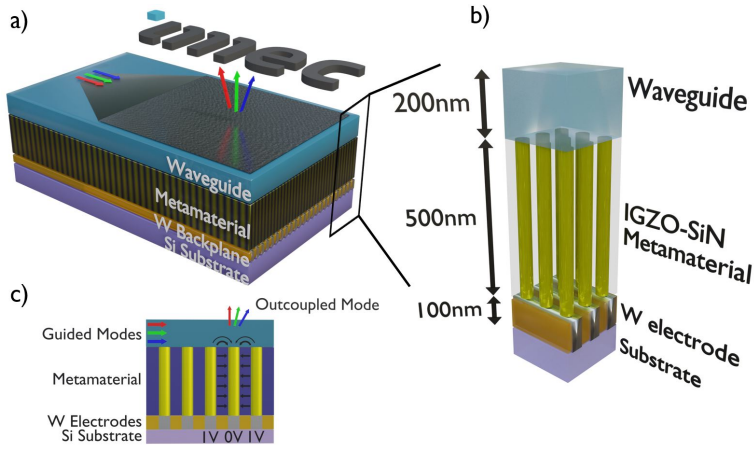

Figure 3.1: a) Schematic of the locally modulated waveguide based holographic display. b) Enlarged section of the device at true scale. c) Schematic of the device operation, which through fringing electric fields locally induces a refractive index difference in the waveguide to enable light out coupling. Image reproduced with permission. [342].

as capacitors to induce the desired modulation. Building on already existing technology, a possible driving scheme and data bandwidth considerations are elaborated below as well.

3.2 Laser Requirements and Power Routing

The holographic display aims to create lifelike realistic images in the entire visible spectrum. A common approach to cover this range of wavelengths is to employ separate sources in red, green and blue which can be tuned in relative intensity to yield different perceived colors. RGB operation can be achieved both through wavelength multiplexing and time multiplexing. Wavelength multiplexing operation has all three wavelengths simultaneously injected into the waveguide, whereas time multiplexing operation injects sequential pulses off the three wavelengths. While wavelength multiplexing is in theory possible in the envisioned waveguide structure, it would result in significant undesired scattering on the superpositioned modulation. A clear advantage here exists for time multiplexing in which the modulation can be separated from each other at

the cost of a higher refresh rate.

The optical power can be supplied both with integrated and external lasers. Integrated lasers would offer an all encompassing on-chip solution but are often limited in power and expensive. On the other hand, external lasers offer easier prototyping and higher power but can be bulky. In a standalone mature product, an integrated laser is required hence this will be targeted below. Next to the integrated laser, other components such as splitters, amplifiers and beam expanders will be needed. To achieve a similar power density to a bright OLED, a luminance above $1000cd/m^2$ should be reached. This can be converted to power using the following equation:

$$P = \frac{LA\Omega}{K} \tag{3.1}$$

Here, L is the luminance, A is the display area, Ω is the emission solid angle and K is the luminous efficacy. Using a device area of $2cm^2$, a π solid angle and a luminous efficacy of $50lm/W$, the typical output power of an OLED display is around $12.57mW$. [343] For laser sources the typical luminous efficacy is different ranging from about 25lm/W for blue, $680lm/W$ for green and $75lm/W$ for red. [344] This results in strong variations for the required luminance, resulting in the same optical power. State of the art Fabry-Pérot on-chip lasers already reach these required power values. [345] Alternatively, an on-chip semiconductor optical amplifier (SOA) can be used to boost the output power of the laser. The output of the laser will need to be transported and split off into smaller lines along the entire slab waveguide input face. Next, a phase shifter and phase interrogator is needed to ensure that all light is injected in phase, as random deviations in path length exist due to manufacturing errors like line edge roughness. Finally, the light will need to be expanded further to be uniform in phase and amplitude when injected into the waveguide. To that end, custom designed beam expanders for leaky wave antennas seem best suited. [346]

3.3 Slab Waveguide Modes

Based on the points elaborated in Section 3.1, a slab waveguide is preferred over other types of waveguides which would need be closely spaced. The mode profile and their properties in a slab waveguide can be calculated starting from Maxwell's curl equations. [347]. Equation 1.7 and 1.8 can be expanded to yield the following:

$$(\frac{\partial E_z}{\partial y} - \frac{\partial E_y}{\partial z})\vec{e_x} + (\frac{\partial E_x}{\partial z} - \frac{\partial E_z}{\partial x})\vec{e_y} + (\frac{\partial E_y}{\partial x} - \frac{\partial E_x}{\partial y})\vec{e_z}$$
$$= -i\omega\mu_0 H_x\vec{e_x} - i\omega_0\mu H_y\vec{e_y} - i\omega\mu_0 H_z\vec{e_z} \quad (3.2)$$

$$(\frac{\partial H_z}{\partial y} - \frac{\partial H_y}{\partial z})\vec{e_x} + (\frac{\partial H_x}{\partial z} - \frac{\partial H_z}{\partial x})\vec{e_y} + (\frac{\partial H_y}{\partial x} - \frac{\partial H_x}{\partial y})\vec{e_z}$$
$$= i\omega\varepsilon E_x\vec{e_x} + i\omega\varepsilon E_y\vec{e_y} + i\omega\varepsilon E_z\vec{e_z} \quad (3.3)$$

Here, we assume a non-magnetic material such that only the vacuum permeability (μ_0) remains. The permittivity is equal to the vacuum permittivity multiplied by the relative permittivity. Hence, $\varepsilon = \varepsilon_0\varepsilon_r = \varepsilon_0 n^2$ where n is the refractive index. In case of a slab waveguide, the structure is invariant along the y axis ($\frac{\partial}{\partial y} = 0$). The vector components on both sides need be equal, which results in six equations.

$$\begin{aligned} -\frac{\partial E_y}{\partial z} &= -i\omega\mu_0 H_x & -\frac{\partial H_y}{\partial z} &= i\omega\varepsilon_0 n^2 E_x \\ \frac{\partial E_x}{\partial z} - \frac{\partial E_z}{\partial x} &= -i\omega\mu_0 H_y & \frac{\partial H_x}{\partial z} - \frac{\partial H_z}{\partial x} &= i\omega\varepsilon_0 n^2 E_y \\ \frac{\partial E_y}{\partial x} &= -i\omega\mu_0 H_z & \frac{\partial H_y}{\partial x} &= i\omega\varepsilon_0 n^2 E_z \end{aligned} \quad (3.4)$$

Just like the structure, the guided mode is also invariant in both x and y. Its electric and magnetic field can thus be written as:

$$E(x, y, z) = E(x)e^{-i\beta x} \quad (3.5)$$

$$H(x, y, z) = H(x)e^{-i\beta x} \quad (3.6)$$

When these are entered in to the six equations from 3.4, two sets of equations can be defined that all relate to each other.

$$\begin{array}{cc} \textbf{TE} & \textbf{TM} \\ \dfrac{\partial E_y}{\partial z} = i\omega\mu_0 H_x & -\dfrac{\partial H_y}{\partial z} = i\omega\varepsilon_0 n^2 E_x \\ \dfrac{\partial H_x}{\partial z} + i\beta H_z = i\omega\varepsilon_0 n^2 E_y & \dfrac{\partial E_x}{\partial z} + i\beta E_z = i\omega\mu H_y \\ i\beta E_y = i\omega\mu_0 H_z & -i\beta H_y = i\omega\varepsilon_0 n^2 E_z \end{array} \tag{3.7}$$

Equation 3.7 define the transverse electric (TE) and transverse magnetic (TM) modes from the waveguide. Both sets can be used to find the wave equation that determines their mode profile, by combining and only keeping E_y and H_y the following is found:

$$\frac{\partial^2 E_y}{\partial z^2} + (n^2 k_0^2 - \beta^2) E_y = 0 \qquad (\textbf{TE}) \tag{3.8}$$

$$\frac{\partial^2 H_y}{\partial z^2} + (n^2 k_0^2 - \beta^2) H_y = 0 \qquad (\textbf{TM}) \tag{3.9}$$

Calculating the allowed TE and TM modes now comes down to solving the encountered eigenvalue problem. As boundary conditions, we require the tangential electric and magnetic field components (E_y, E_z, H_y and H_z) to be continuous at the material interfaces ($z = 0$ and $z = d$). As a consequence, the partial derivative of E_y and H_y also need be continuous. Lastly, the envisioned guided modes need to exponentially decay towards infinity. Taking into account all these conditions, the solutions for the equations 3.8 and 3.9 take on the following identical shape.

$$\begin{cases} Ae^{-\alpha(z-d)}e^{-j\beta x} & z > d \\ [Bsin(\kappa z) + Ccos(\kappa z)]e^{-j\beta x} & 0 < z < d \\ De^{\gamma z}e^{-j\beta x} & z < 0 \end{cases} \tag{3.10}$$

Here, $\alpha = \sqrt{\beta^2 - n_f^2 k_0^2}$, $\gamma = \sqrt{\beta^2 - n_c^2 k_0^2}$ and $\kappa = \sqrt{n_w^2 k_0^2 - \beta^2}$. By now considering the continuity of E_y for TE modes or H_y for TM modes at the interfaces, one finds that:

$$C = D \qquad (z = 0) \tag{3.11}$$

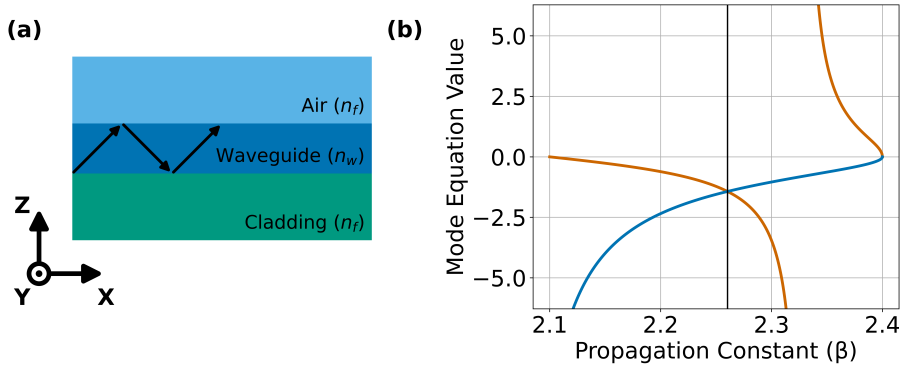

Figure 3.2: a) Cross-section of a slab waveguide. b) Graphical representation of the solution to the TE transcendental equation 3.18.

$$A = Bsin(\kappa d) + Ccos(\kappa d) \qquad (z = d) \tag{3.12}$$

Equation 3.10 can thus be rewritten:

$$\begin{cases} [Bsin(\kappa d) + Ccos(\kappa d)]e^{-\alpha(z-d)}e^{-j\beta x} & z > d \\ [Bsin(\kappa z) + Ccos(\kappa z)]e^{-j\beta x} & 0 < z < d \\ Ce^{\gamma z}e^{-j\beta x} & z < 0 \end{cases} \tag{3.13}$$

Here, a distinction has to be made between the TE and TM solution. The continuity of $H_x = -\frac{i}{\omega\mu_0}\frac{\partial E_y}{\partial z}$ for TE and $E_x = -\frac{i}{\omega\epsilon_0 n^2}\frac{\partial H_y}{\partial z}$ for TM can similarly be considered at both interfaces, and yields:

$$\gamma C = \kappa B \qquad (z = 0) \tag{3.14}$$

$$-\alpha Bsin(\kappa d) - \alpha Ccos(\kappa d) = \kappa Bcos(\kappa d) - \kappa Csin(\kappa d) \qquad (z = d) \tag{3.15}$$

These can be combined to create:

$$-\alpha Bsin(\kappa d) + \frac{\kappa^2}{\gamma}Bsin(\kappa d) = \alpha\frac{\kappa}{\gamma}Bcos(\kappa d) + \kappa Bcos(\kappa d) \tag{3.16}$$

$$[\frac{\kappa^2}{\gamma} - \alpha]sin(\kappa d) = [\alpha\frac{\kappa}{\gamma} + \kappa]cos(\kappa d) \tag{3.17}$$

$$tan(\kappa d) = \frac{\alpha\kappa + \kappa\gamma}{\kappa^2 - \alpha\gamma} \tag{3.18}$$

This transcendental equation can be solved to find the wavevector β of a guided slab mode. Figure 3.4 b) illustrates both sides of equation 3.18 with parameters $d = 200nm$, $n_f = 1$, $n_w = 2.4$, $n_c = 1.9$ and $\lambda = 465nm$. At the first intersection ($\beta = 2.2603k_0$), a slab mode is allowed. Entering these parameters back into equation 3.13 results in the mode profile when all prefactors are simplified to only include D. If the calculation for TM modes was continued from equation 3.13, the following transcendental equation is found. The first mode would than occur at $\beta = 2.2039k_0$.

$$tan(\kappa d) = \frac{\frac{n_w^2}{n_c^2}\kappa\gamma + \frac{n_w^2}{n_f^2}\kappa\alpha}{\kappa^2 - \alpha\gamma\frac{n_w^4}{n_f^2 n_c^2}} \tag{3.19}$$

The mode profile for the first allowed slab mode for both types is shown in Figure 3.3.

3.4 Metamaterial Cladding

The cladding layer, which enables the driving of the holographic display, has to make the driving scheme and waveguides dynamics compatible with each other. This is not an easy task, as the electrical bias is typically supplied by metallic electrodes. These obviously do not combine well with light propagation due to their inherent absorption and scattering. This problem is often addressed, for example in electro-optic modulators, by moving electrodes far away from the optically active parts. It reduces optical losses, but lowers the strength of the electric fields that can be applied for the same voltage. Devices designed by this principle, either employ larger voltages, which cannot be increased endlessly, or rely on larger propagation distances to supply the same cumulative effect. Both options are not ideal. Instead, we opt to employ materials with lower optical losses such as dilute metals or transparent conductive oxides. These lead to a different trade-off as the improved optical behaviour stems from a limited conductivity compared to metals, which impacts the upper limit of the driving frequency through its resistor capacitor time constant. In the end, we opt to

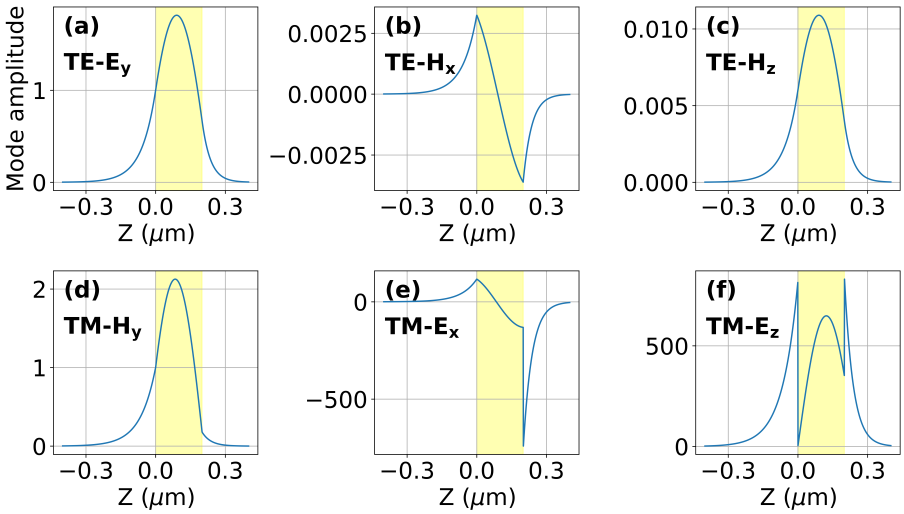

Figure 3.3: a)-c) Mode profile of a TE mode, respectively showing the E_y, H_x and H_z. d)-f) Mode profile of a TM mode, respectively showing the H_y, E_x and E_z.

use both options. Ideally, the backplane is made from the standard metallic interconnects providing the necessary conductivity for a sufficiently high data bandwidth. Next to that, we aim to use low loss electrodes to bridge the gap between the optically active layer and the lossy electrical backplane. In doing so, we allow for strong modulation of the waveguide at low voltages. This is an acceptable solution due to the rather low required driving speed. Indeed, individual electrodes only need to switch at $60Hz$ or a multiple of it if RGB colors are treated separately, which should be well within reach.

An additional challenge is that the modulation needs to be applied locally, on a sub-wavelength scale. Consequently, we envision a periodic electrode structure to be the most straightforward method. However, periodic structures also lead to unwanted scattering. Hence a metamaterial, i.e. a material which has features so small that incident light perceives it as an effective medium, is the ideal solution. Luckily, the envisioned electrode size is already sub-wavelength. However, to further limit any possible scattering the surrounding matrix can be made of a refractive index matched material. Chapter 4 details the material requirements in depth.

3.5 Waveguide Losses

The second crucial component to the envisioned holographic display is the optically active waveguide. Some of its properties can be extrapolated from the previous sections, but in general it should offer (1) good mode confinement, (2) low optical losses and (3) local refractive index modulation through electrical contacts.

Good mode confinement can be achieved by the refractive index and its relative contrast with the cladding. This has two main benefits. First, waveguide modulation will have a more significant impact when nearly all light is confined in the same layer. Secondly, strong confinement also prevents the guided mode from interacting with the lossy backplane.

Waveguide optical losses are linked to scattering, absorption and radiation. Both scattering and absorption are determined by a combination of factors including the surface roughness, intrinsic loss of the material and impurities. These parameters are heavily influenced by the deposition and processing conditions of the material. The aspired device die has a propagation length of $2cm$, which is on the larger size of the allowed reticle size of state of the art lithography tools. Proper operation requires a significant portion of power to remain after propagation, as radiating constant power to the far field becomes challenging when the remaining waveguide power is too low. To get an idea of the desired loss characteristics, a remaining power factor of 50% is assumed. The propagation loss L is than defined as: [348]

$$L = -10 \log_{10} \left(\frac{P(z = 2cm)}{P(z = 0cm)} \right) \tag{3.20}$$

Here, $P(z)$ is the power present at position z. When 50% of the power is retained, a propagation loss of $1.55dB/cm$ is required. This can be related to the imaginary part of the refractive index, which is more often used to describe optical properties of thin films. The required imaginary refractive index (k) can be found through:

$$k = \frac{L \cdot \lambda_0}{20 \cdot 2\pi \log_{10}(e)} \tag{3.21}$$

Here, λ_0 represents the free space wavelength. Using the value from above, a target k value of 1.56×10^{-8} is found at $\lambda_0 = 550nm$. Above, the influence of radiation on optical losses was touched on. Since radiation is a cornerstone for the functioning of the device, it is addressed separately. Radiative out coupling through a grating typically follows an exponential decay. However, most gratings are designed to be as efficiently as possible such that only few periods are needed. The envisioned holographic display on the other hand, aims to couple out light over $2cm$ in propagation length. Evidently, a lower efficiency is needed to preserve enough power in the mode to enable operation. In that sense, the device shares similarities with both long period gratings and grating couplers. The remaining power after a desired propagation length can be estimated using the coupling coefficient between the guided and radiation modes. In case of a transvere electric (TE) mode, no longitudinal coupling can occur. The transverse coupling coefficient can then be found as:

$$K^t_{\nu,p\rho} = \frac{\omega}{4} \int_{-\infty}^{+\infty} \Delta\varepsilon_{ij}(x,z) \vec{E_{t\nu}} \cdot \vec{E_{p\rho}} dz \tag{3.22}$$

Here, a forward propagating bound mode along the z axis is denoted with ν. A continuous spectrum of radiation modes is indicated by p, whether the modes are symmetric or antisymmetric is denoted by ρ. ω represents the angular frequency and $\Delta\varepsilon$ represents the permittivity modulation. A propagating mode influenced by a coupling grating loses power exponentially according to:

$$P(z) = P_0 e^{-\gamma z} e^{i\Delta\beta z} \tag{3.23}$$

Here, $P(z)$ represents the remaining power after a propagation distance z, γ is the coupling loss and $\Delta\beta$ is linked to a frequency shift. This last part often only has a negligible impact as it includes the coupling coefficient, which typically only couples to few modes. The coupling loss γ is further defined as: [349]

$$\gamma = \pi \sum_{p\rho} \left(\frac{\beta_{p\rho}}{\sqrt{n_s^2 k_0^2 - \beta_{p\rho}^2}} \mid K^t_{0,p\rho} \mid^2 \right) \tag{3.24}$$

Eq. 3.24 states that the coupling loss requires a summation over all possible radiation modes, again most of these are negligible except for the intended coupling. Furthermore, $\beta_{p\rho}$ is the radiation mode wavevector, n_s the refractive index of the cladding and k_0 is the free space wavevector. Given that equation 3.22 requires an integral, an iterative approach to extracting the desired refractive index modulation is a good option. To that end, equation 3.23 and 3.24 can be used to find an estimate of the coupling coefficient. Here, both the device length and the remaining power should be considered. In the proposed device, the device length is 2cm due to the available reticle size. The display efficiency is related to the power remaining after the full propagation distance and has an upper limit since the grating amplitude is constrained by the electro-optic properties of the active layer and the field that can be created. Ideally, the amplitude of the applied grating exponentially increases to accommodate the decrease in optical waveguide power in eq. 3.23. In reality, this is an impractical solution and a certain level of power should be maintained in the waveguide to prevent excessively increasing the required modulation.

The remaining waveguide power after propagating through the full die can be estimated by assuming a refractive index modulation of 10^{-3}. To that end, the coupling coefficient can be calculated by 3.22 but requires the modal electric fields as input. These were calculated using the film mode matching solver from *Electromagnetic Python* employing refractive indices of 1.9813, 2.4517 and 1 at $550nm$ respectively for the cladding, waveguide and air. The radiation mode fields were calculated according to Kogelnik. [347] Mode conversion between TE and transvere magnetic (TM), leads to reduced noise in the out coupled signal. [292] The guided mode is assumed TE, and the radiation mode is assumed TM meaning that there is a degeneracy (odd-even). For a wavelength of $550nm$, the guided mode has a wavevector of $\beta_0 = 2.5228 \times 10^7 m^{-1}$. When a grating of $300nm$ is present in the waveguide, the coupled radiation mode has a wavevector of $\beta_{rad} = \beta_0 - \frac{2\pi}{300nm} = 4.28 \times 10^6 m^{-1}$. The coupling coefficient ($K^t_{\nu,p\rho}$) for a conservative refractive index modulation of 10^{-3} or conversely a permittivity modulation of 10^{-6}, is equal to 3.10 and 2.74 for the even and odd radiation mode respectively. The accompanied coupling loss γ is then 12.20 and 9.54, which means that after a propagation distance of $2cm$, 61.63% of the power remains. Consequently, a conservative refractive index modulation of 10^{-3} already nearly suffices for the intended application.

3.6 Driving Scheme

As indicated above, the proposed concept resembles a typical DRAM structure meaning that the backplane can leverage pre-existing technology. One striking similarity is the driving architecture which in both applications addresses capacitors individually and in quick fashion. On top of that, with clever pixel encoding, the device could be built according to a video random access memory (VRAM)) design which now commonly serves as framebuffer on a graphics processing unit (GPU) before sending data to the display. In our case, a VRAM backplane can be nearly copied in its entirety and combined with the metamaterial, reducing the number of components required to create an image on the display side.

Employing a DRAM-like structure brings other advantages such as a high data bandwidth and large device area. Section 2.2 set forward a desired bandwidth of $16.8 \times 10^{12} bit/s$ for a device area of $2cm^2$. Current state of the art GPUs, for example NVIDIA RTX A5000 can reach a data bandwidth of $768GB/s$ through its $384 - bit$ interface to the GPU at a clock frequency of $1170MHz$. In terms of bits, this becomes $6.14 \times 10^{12} bit/s$ meaning that the combined input from three currently available GPUs covers the desired data bandwidth. Additionally, a typical VRAM is similarly sized as the holographic display.

In later stages, multiple VRAM chips will have to be combined together resulting in visual stitching errors. Their impact will depend on the size of the display, the spacing between chips and the image viewing distance. Perhaps an apt comparison to an insect screen can be made. Both a stitched holographic display and an insect screen can be thought of as filtering an incident wavefront by a wire grid pattern. From a distance, an insect screen can be easily viewed through and in some cases it is even barely noticeable. Close by, it is more noticeable and individual parts of the filter can be distinguished depending on to focus of the observer. Insect screen apertures however are an order of magnitude smaller, hence the stitching error impact should be rather acceptable.

In the envisioned device, the electric field between two neighbouring sub-wavelength pillar electrode serves the purpose of a single pixel. To individually address each pillar electrode a circuit with at least one transistor and capacitor per pillar is needed. The device can then be operated by setting the analogue data lines located horizontally in Fig. 3.4 a) to the desired voltage. Afterwards, the digital select lines can be sequentially stepped through, each time activating the gate of a full column of transistors. In doing so, the desired analogue signal

of the entire column can be placed on each accompanying capacitor. Repetition of this process enables each column of the display to be addressed at once. This driving method does however not factor in the capacitance existing between each column, which in case of 2D steering applications cannot be ignored. By biasing only a single select line at a time, the pillars of the next column remain floating which prevents the desired charge to be stored. To combat this, the addressing of the select lines can be done in a rolling fashion, shown in Fig. 3.4 b) such that a brief moment (indicated in orange) exists in which the column spanning capacitors can be charged.

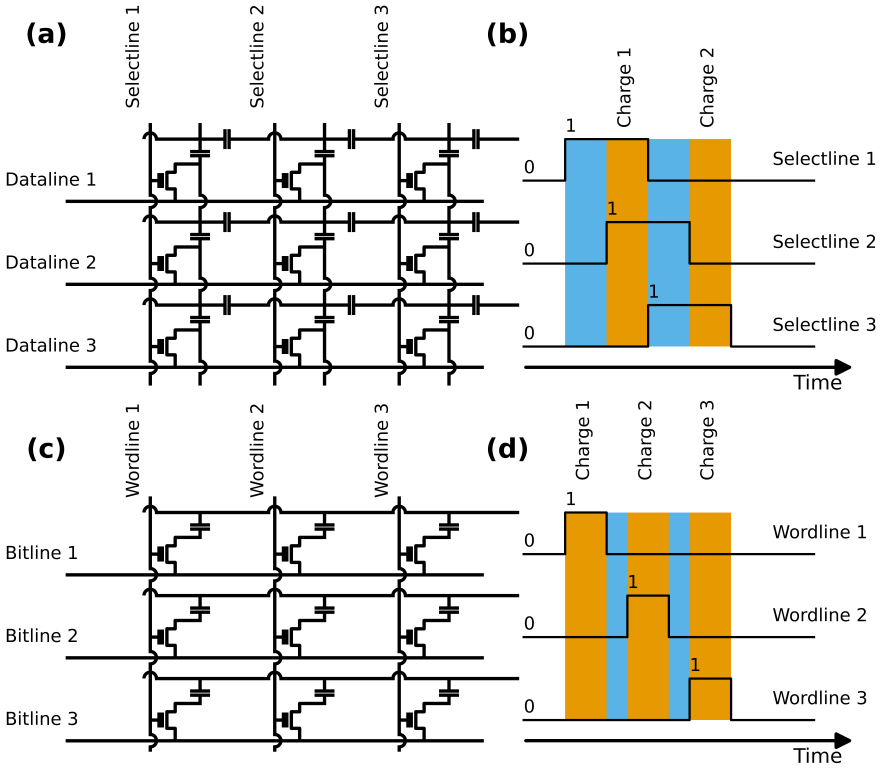

Figure 3.4: a) Electrical schematic of holographic display. To address each pillar separately, a matrix is formed with digital select lines and analogue data lines. b) An example of the rolling charging operation that is needed to ensure a 2D electric field pattern. c) Electrical schematic of typical DRAM. To address each capacitor separately, a matrix is formed with digital word lines and analogue bit lines. d) Electrical operation of a typical DRAM architecture.

Figure 3.4 c) and d) present a similar scheme for a typical DRAM as comparison. Here the data line and select line are usually referred to as bit line and word line. Comparatively, this device is much simpler as the proposed holographic display as no capacitances between individual pillars have to be accounted for. DRAM pillars consist of a layered structure that contains the anode, cathode and the capacitor dielectric. During operation no care has to be taken about floating capacitors and a rolling shutter approach is not needed.

Chapter 4

Metamaterial Fabrication and Characterization

This chapter highlights the creation and characterization of the metamaterial. To that end, early short loop experiments are first looked at. Subsequent learnings were then implemented into a mature metamaterial process flow. Afterwards, various characterization techniques including SEM, ellipsometry and atomic force microscopy (AFM) are shown to prove the desired optical and electrical characteristics of the metamaterial.

This chapter is partially based on the following journal article, which was reproduced with permission:

Guillaume Croes, Renaud Puybaret, Janusz Bogdanowicz, Umberto Celano, Robert Gehlhaar, and Jan Genoe. Photonic metamaterial with a subwavelength electrode pattern. *Applied Optics*, 62(17):F14, 6 2023

4.1 Material Screening Short Loop Experiments

Before defining a full process flow for the metamaterial, a range of short loop experiments was done to quickly assess feasibility and material properties. The intent here was to limit as much as possible, time expensive development of the metamaterial by initiating the final process flow with a carefully selected set of

parameters. To that end, the optical properties of the metamaterial constituents were looked into.

The considered materials were selected based on processing, optical and electrical requirements. A primary concern was the accurate filling of the high aspect ratio pillar electrodes with a conductive material. Common deposition techniques such as physical vapour deposition or thermal evaporation would lead to closing the pillar mouth prematurely, leaving a non-conductive air gap between the backplane and the electrode. Consequently, only atomic layer deposition (ALD) deposited materials seemed well suited due to their conformal filling property. This narrowed down the search extensively, to one remaining candidate i.e. indium gallium zinc oxide ($IGZO$) which is a transparent conductive oxide often employed in thin film electronics and backplanes. Given that the combination of optical and electrical behaviour is so critical, the optical behaviour of an established $IGZO$ recipe was used as benchmark for the rest of the metamaterial. Next to that, a material for the rest of cladding is needed for which common materials like SiO_2, SiO_xN_y and SiN seem well suited. To prevent undesired scattering, the material ideally is index matched to $IGZO$.

4.1.1 Indium Gallium Zinc Oxide

Indium Gallium Zinc Oxide was deposited as blanket layer using both sputtering and thermal ALD in an EmerALD® XP chamber of Advanced Semiconductor Materials on 300mm wafers. Afterwards, the wafer was measured by ellipsometry (Woollam RC2®) and fitted with an optical model employing a Tauc-Lorentz and Drude oscillator.[350] Here, the Tauc-Lorentz oscillator accurately models the light-matter interaction in the UV and visible range, whereas the Drude oscillator is used to properly model the electrical conductivity and accompanying absorption.

Figure 4.1 shows the fitted measurement containing data averaged over the entire wafer, the fitting parameters of the employed model can be found in Appendix A. The real refractive index falls between 2.1 and 1.9 over the visible range. The standard deviation becomes larger at higher wavelengths. At the same time, the imaginary refractive index indicates low optical losses. This result should however be nuanced given that ellipsometry as measurement technique is not well suited to observe the optical losses of transparent ($k \sim 0$) films. The origin of this behaviour can be traced to the error $(\delta\psi, \delta\Delta)$ accompanying the measurement of (ψ, Δ) which respectively is the amplitude ratio and phase shift upon reflection between the recorded s and p polarization. Indeed, the $\delta\Delta$ error can be used to estimate an error range for the permittivity through the

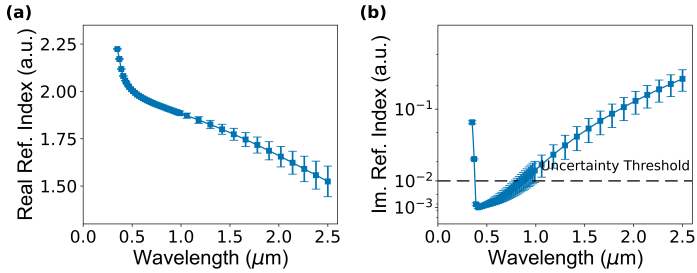

Figure 4.1: IGZO real (a) and imaginary (b) refractive index extracted from ellipsometry measurements using a combined Tauc-Lorentz model and Drude model. The uncertainty threshold for the imaginary refractive index is indicated by the highlighted area. A *asinh* transform with base 10 and linear width 0.01 was used to accurately represent zero values in a logarithmic-like scale. Data was averaged over the entire wafer, the error bars indicate the standard deviation.

employed model. [351] Given that the model employs several oscillators, it is challenging to assess which set of parameters led to an adequate change in Δ. Instead, a Cauchy model can locally be used as approximation to assess the influence of $\delta\Delta$ on the imaginary part of the permittivity (ε_2) as its amplitude parameter for both n and k scales quadratically with the permittivity. At a wavelength of $440nm$ and 65° incidence angle, the measured $\delta\Delta = 0.033$. Adjusting the k amplitude to account for this, ε_2 increases from 0.0767 to 0.0983, or $\delta\varepsilon_2 = 0.0216$. The subsequent effect on the imaginary refractive index or absorption coefficient α can be found through:

$$\delta\alpha = \frac{2\pi}{n\lambda}\delta\varepsilon_2 \tag{4.1}$$

Substituting $\delta\varepsilon_2$ and λ results in an absorption coefficient error of $1542cm^{-1}$. Since $k = \frac{\alpha\lambda}{4\pi}$, the equivalent error on the k value is 0.0054. These results align well with literature. [352] Furthermore, at other wavelengths, especially where Δ approaches 0° or 180° and undergoes a phase jump the uncertainty increases significantly beyond the example shown here. Thus, for very transparent materials like the *IGZO* layer presented here, it is often said that ellipsometry cannot confidently be used to report k values below 0.01.

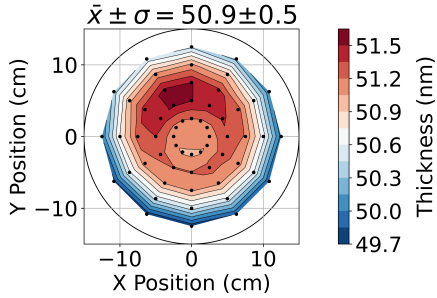

Figure 4.2: Thickness mapping of the 300mm blanket amorphous IGZO wafer.

Figure 4.2 shows the ellipsometry thickness fit over the full 300mm wafer. A thickness around $50nm$ was found, with the film showing good uniformity. The MSE was 11.71. The fitting parameters are shown in Table A.1. The $IGZO$ resistivity is comparable to a weakly conducting semiconductor.

4.1.2 Silicon Oxynitride

Silicon oxynitride SiO_xN_y was first selected to possibly serve as dielectric in which electrodes could later be embedded. It was initially chosen due to its large range of optical flexibility, given that it can gradually be varied between silicon dioxide (SiO_2) and silicon nitride (Si_3N_4) which allows refractive index tuning between 1.5 and 2 respectively. SiO_xN_y with varying oxide and nitride content was deposited on six test wafers. These were created using a Producer® plasma enhanced chemical vapour deposition (PECVD) platform from Applied Materials that employs SiH_4, N_2, NH_3, N_2O and He as precursors. Here, N_2 and NH_3 lead to the formation of Si_3N_4 and N_2O and He lead to the formation of SiO_2. The ratio of oxide to nitride was tuned through the flow of either set of precursors under constant SiH_4 flow, as shown in the inset of Figure 4.3. This altered both the deposition rate, and the refractive index of the deposited layer. Afterwards, ellipsometry maps were measured and fitted using a Tauc-Lorentz model, the fitted parameters of the wafer center can be found in Table A.2. Figure 4.3 shows the optical characteristics for each of the wafers, averaged over the full wafer. The error bars indicate the standard deviation. We find that the refractive indices do not reach the desired range, even at small amounts of incorporated oxide. It should be noted, that the employed fit results in an imaginary refractive index of zero, which is not physical possible at these wavelengths. This can be evaluated through the Kramers-Kronig

relations, which couple the behaviour of the real and imaginary refractive to each other. When the absorption is assumed zero, the relations dictate that the real refractive index is constant. Given that there is always a slight degree of dispersion at visible and infrared wavelengths due to present oscillators, this is impossible in reality. At higher frequencies, when all oscillations have been frozen out, the refractive index flattens out and no absorption can be present. For the current fit, this is an artefact of the measurement and fitting procedure, again imaginary refractive index values below 0.01 should be considered with caution as detailed in Section 4.1.1.

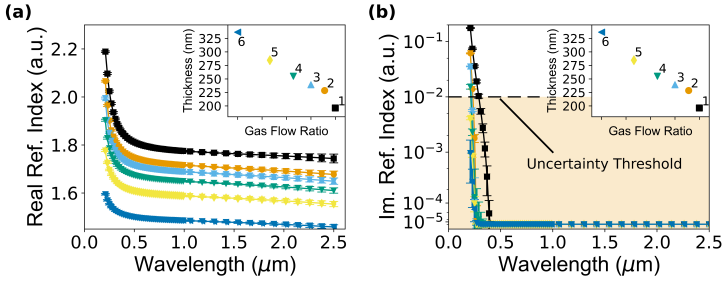

Figure 4.3: SiON real (a) and imaginary (b) refractive index extracted from ellipsometry measurements using a Tauc-Lorentz model. A *asinh* transform with base 10 and linear width 0.0001 and was used to accurately represent zero values in a logarithmic-like scale. The inset indicates the employed glas flow ratios and resulting thickness. The data was averaged over the entire wafer, the error bars indicate the standard deviation.

Figure 4.4 shows an overview of the measured wafer maps and their fitted thickness. Only minor deviations between the center and wafer edge were found regarding thickness and optical properties. The relative standard deviation or coefficient of variation (CV) for the thickness ranges from .3% and 1.7% respectively for 1) and 3) with the others in between, which indicates a uniform deposition over the full wafer.

4.1.3 Silicon Nitride

Silicon nitride was studied as alternative to SiO_xN_y as it seemed unable to reach the desired refractive index. Here the ratio between Silicon and Nitrogen and the density of the material mainly determine the optical behaviour. Again, a set of blanket layers was deposited using a the Producer® PECVD platform

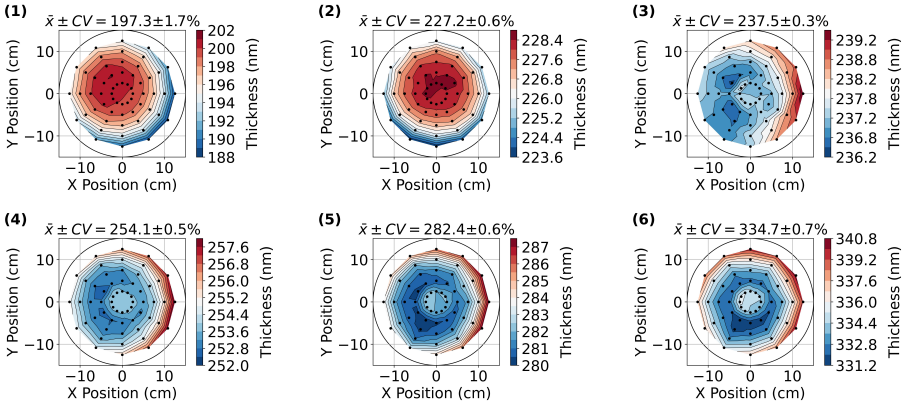

Figure 4.4: Thickness mapping of the 300mm blanket wafers for SiO_xN_y wafers at various precursor flows. The same numbering as in the inset of Figure 4.3 is used. The average thickness and relative standard deviation is indicated above each plot.

from Applied Materials but now employing SiH_4, N_2 and NH_3 as precursors. Deposition rate and optical properties were changed by tuning the flow ratio of SiH_4, while keeping the N_2 and NH_3 flow constant, as shown in the inset of Figure 4.5. The average refractive index data fitted using the entire wafer map is shown in Figure 4.5. The error bars show the standard deviation of the fit at each wavelength, indicating uniform deposition over the full wafer. The fitting parameters of the center of the wafer can be found in Table A.3. Within the visible spectrum, the real refractive index ranges from 1.8 to 2.3 and thus fully covers the refractive index of $IGZO$. The imaginary refractive index quickly drops below values measurable by ellipsometry.

Ellipsometry mapping measurements, following a similar fitting procedure as for SiO_xN_y, are shown in Figure 4.6. The relative standard deviation off the thickness ranged from 0.2% to 0.8%.

4.1.4 Material of Choice

Given that the device needs to operate for visible light, the wavelength range between $400nm$ and $700nm$ is of most interest. Figure 4.7 shows a zoomed in comparison between the $IGZO$ refractive index and the nearest matching silicon nitrides. Again, the error bars indicate the standard deviation factoring

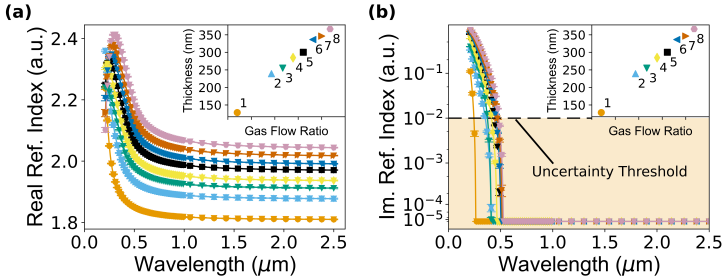

Figure 4.5: Si_3N_4 real (a) and imaginary (b) refractive index extracted from ellipsometry measurements using a Tauc-Lorentz model. A *asinh* transform with base 10 and linear width 0.0001 and was used to accurately represent zero values in a logarithmic-like scale. The error bars indicate the standard deviation at each wavelength.

in data from a full 300mm wafer. The relative differences at three common laser wavelengths i.e. $465nm$, $550nm$ and $640nm$ are 0.033, 0.018 and 0.005 respectively for wafer 3. Similarly, for wafer 4 the relative differences are 0.015, 0.023 and 0.033. Since an intermediate of wafer 3 and 4 would offer an even better match, the recipe moving forward was based on intermediate precursor flows.

4.2 Metamaterial Process Flow

4.2.1 Overview

A process flow was designed to bring forward the desired metamaterial structure and its driving backplane, shown in Figure 4.8. Starting on a Si wafer the flow sequentially entails a blanket oxide deposition, a damascene etch, metal deposition, planarization, nitride deposition, high aspect ratio etch, $IGZO$ atomic layer deposition filling, planarization and an optional oxide capping layer deposition. Below, several process steps are expanded on.

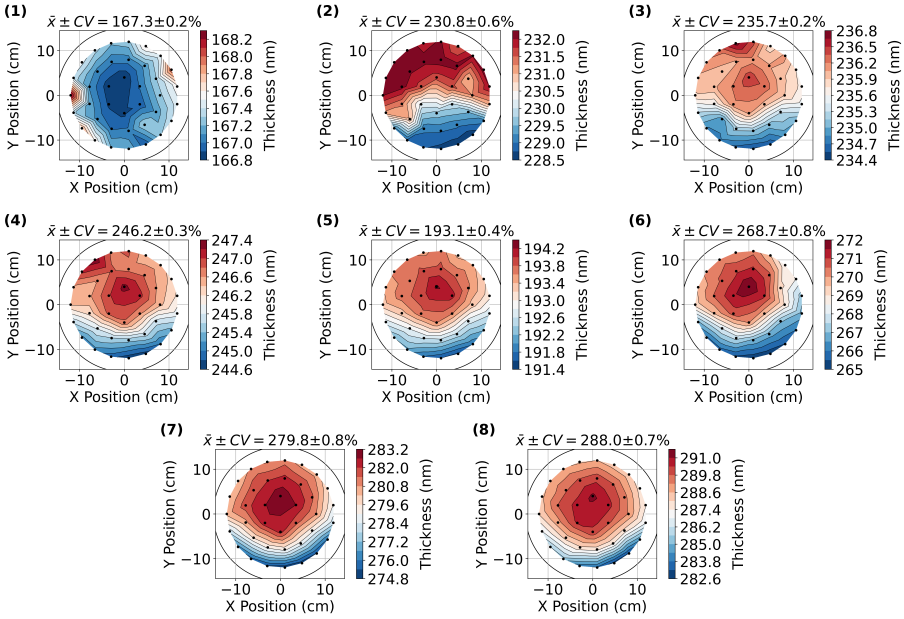

Figure 4.6: Thickness mapping of the 300mm blanket wafers for a range of Si_3N_4 wafers with varying deposition parameters.

4.2.2 Topaz Mask

A mask was designed for the metallic backplane of the device. To that end, various test structures were included among which normal gratings, gratings focusing into a line, gratings focusing into a point and gratings focusing into a point cloud. Each of these was patterned on a $200\mu m$ by $200\mu m$ area. Different variations in focusing distance, repeated patterns and metallic probe contacts led to a total size of about 1 by $1.25cm$. The calculations for the focusing gratings were made assuming an operating wavelength of $640nm$ and refractive indices of 1.963, 2.446 and 1 for the metamaterial, BTO and air respectively.

First, a continuous focusing grating was designed by considering each position at which constructive interference is required inside the waveguide. Consider a focal point (x_{P1}, y_{P1}, z_{P1}) for which light is coupled out of the waveguide. Attaining constructive interference between the two different paths between waveguide and focal point, requires equal phase or a 2π phase difference at the focal point. In case one of the paths originates from the waveguide center (x_0, y_0), the total accumulated phase ϕ_1 from the center (x_0, y_0) of the grating to the focal point

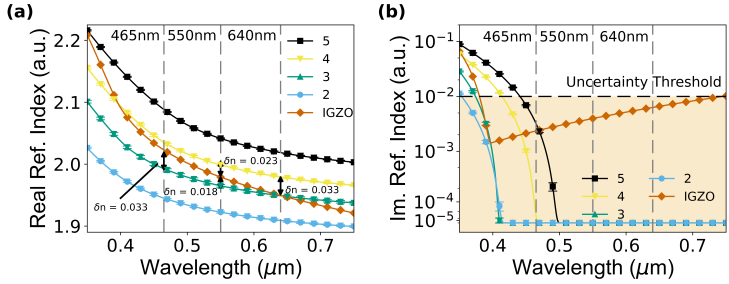

Figure 4.7: Comparison between the real (a) and imaginary (b) refractive index of Si_3N_4 and $IGZO$. A $asinh$ transform with base 10 and linear width 0.0001 and was used to accurately represent zero values in a logarithmic-like scale. The same numbering and colouring from Figure 4.5 is used. The error bars indicate the standard deviation occurring over the blanket wafer.

(x_{P1}, y_{P1}, z_{P1}) is the following. A schematic of the phases is shown in Figure 4.9.

$$\phi_1 = \frac{2\pi}{\lambda}\sqrt{(x_0 - x_{P1})^2 + (y_0 - y_{P1})^2 + (-z_{P1})^2} \tag{4.2}$$

The other path attains the required phase at a different position (x, y). The path difference between the two waveguide points needs to be accounted for such that the total accumulated phase is equal to:

$$\phi_2(x,y) = \frac{2n_{eff}\pi}{\lambda}(x - x_0) + \frac{2\pi}{\lambda}\sqrt{(x - x_{P1})^2 + (y - y_{P1})^2 + (-z_{P1})^2} \tag{4.3}$$

Here, n_{eff} represents the effective index of the guided mode. The focusing grating equation can than be extracted by setting the argument of a cosine to $\phi_1 - \phi_2$.

$$\Lambda(x,y) = \cos\left(\frac{2\pi n}{\lambda}\sqrt{(x_0 - x_{P1})^2 + (y_0 - y_{P1})^2 + (-z_{P1})^2}\right.$$
$$\left. - \frac{2\pi n}{\lambda}\sqrt{(x - x_{P1})^2 + (y - y_{P1})^2 + (-z_{P1})^2} - \frac{2\pi n_{eff}}{\lambda}(x - x_0)\right) \tag{4.4}$$

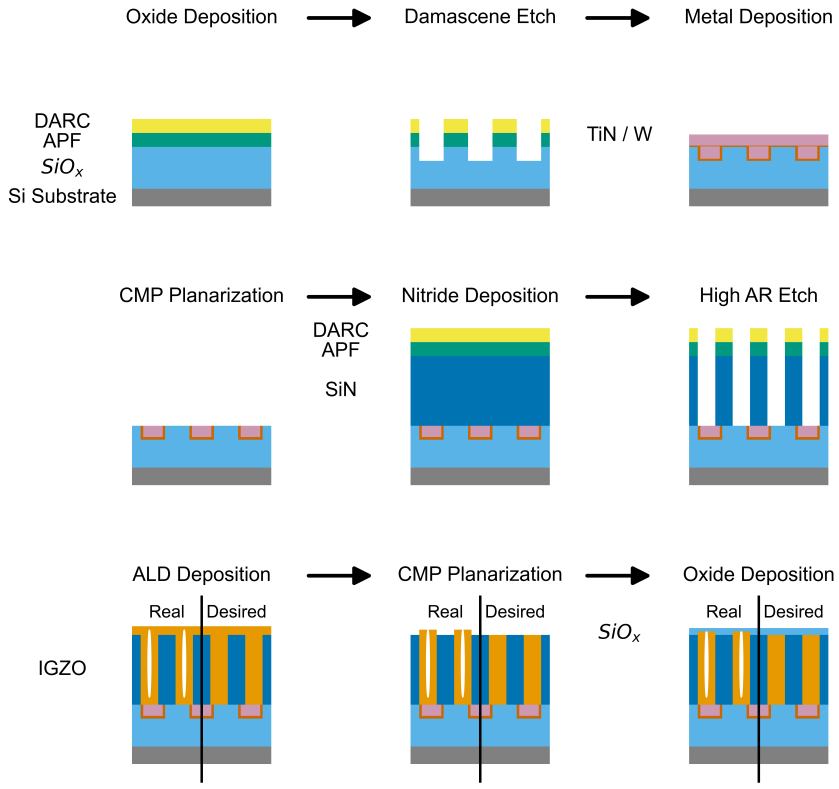

Figure 4.8: Schematic overview of the designed process flow for the creation of the material and its backplane. The materials are indicated next to the layers. Here, DARC refers to dual anti-reflection coating, APF refers to advanced patterning film, CMP refers to chemical-mechanical polishing and AR refers to aspect ratio.

However, the mask requires a binary grating for which equation 4.4 is set to 1 and 0 for respectively positive and negative values. The acquired pattern can now serve as building block for the desired modulation, by superpositioning the pattern at every desired focal point.

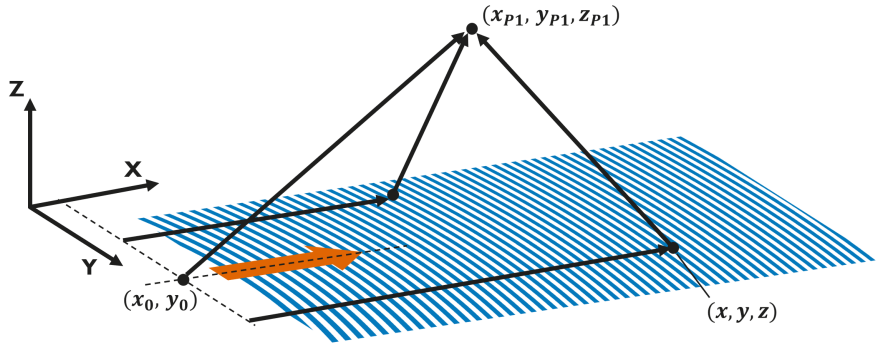

Figure 4.9: Schematic of the parameters employed for the design of a focusing grating coupler in the topaz mask. The red arrow indicates the travelling direction of the slab mode.

4.2.3 Metal Backplane

The metallic backplane is created with a damascene process. First, a $300nm$ thick layer of SiO_x is deposited on a Si substrate by chemical vapour deposition (CVD). The Topaz mask has a critical dimensions (CD) between $53nm$ and $90nm$ with an average of $74nm$, meaning that an advanced patterning technique is needed. To reduce back reflection from the substrate into the photoresist, which would distort the photoresist patterning, a dual anti reflection coating (DARC) together with a common backside anti reflection coating (BARC) is applied. To achieve this, the wafer is covered by a $200nm$ thick advanced patterning film (APF) made of hydrogenated amorphous ($\alpha-$) Carbon and a $35nm$ thick DARC made of a carbon doped silicon oxide. Both layers are deposited by CVD. Afterwards, the normal $38nm$ of BARC and $100nm$ of photoresist can be deposited, which is subsequently exposed by $193nm$ immersion lithography and developed. A fluorine dry etch can then be used to transfer the photoresist pattern into the BARC and DARC layer, as shown in Figure 4.10 a). An additional W layer was deposited on top to reduce charging effects during SEM measurements.

Next, an oxygen dry etch propagates the acquired pattern further into the APF film and the SiO_x and partly removes the photoresist. Only part of the SiO_x ($100nm$) is etched such that the electrodes do not short by connecting to the Si wafer. The etched layer is filled by a $10nm$ ALD layer of titanium nitride (TiN) after which $200nm$ of Tungsten was deposited. Figure 4.10 b) and c) show the

etched pattern and subsequent titanium nitride (TiN) and W filling. Finally the layer is planarized by a tungsten chemical mechanical polishing (CMP) in which part of the $SiO_x - W$ layer is consumed. The end result is shown in Figure 4.10 d).

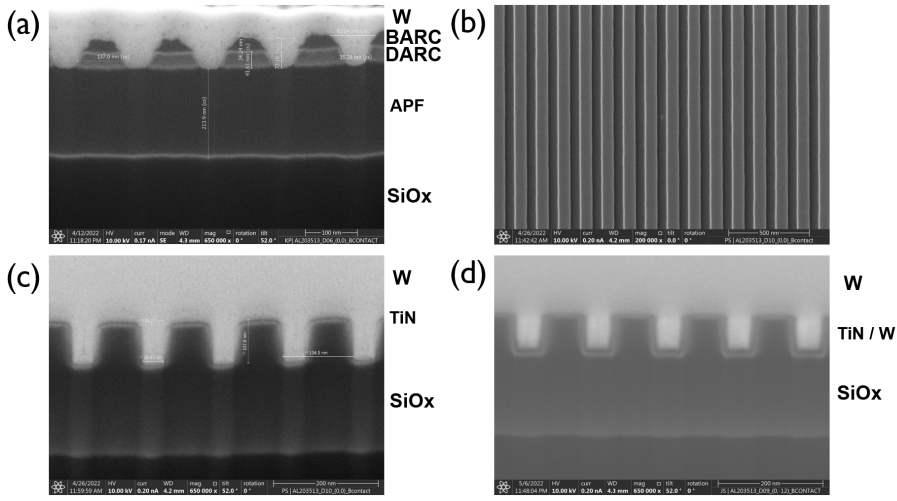

Figure 4.10: SEM images taken at various stages of the metal backplane development. a) Cross section after the photoresist pattern has been propagated into the anti reflection layers by dry etch. b) Top view of the etched SiO_2. c) Cross section after filling by TiN and W. d) Cross section after planarization.

4.2.4 Metamaterial

To create the metamaterial, a $500nm$ thick Si_3N_4 layer is deposited by CVD on top of the metallic backplane. Again, to prepare for an etch, a stack of APF and DARC was deposited by CVD. Similar to the metallic backplane, photoresist was deposited, exposed and developed after which the pattern was transferred in the subsequent layers by etching. The final step, etching through the Si_3N_4 to access the metallic backplane below, has an aspect ratio of 12 due to the pillar array having $45nm$ sized holes. Figure 4.11 a) shows a top down view SEM image of the etched wafer in which the metallic backplane can be observed behind the etched Si_3N_4.

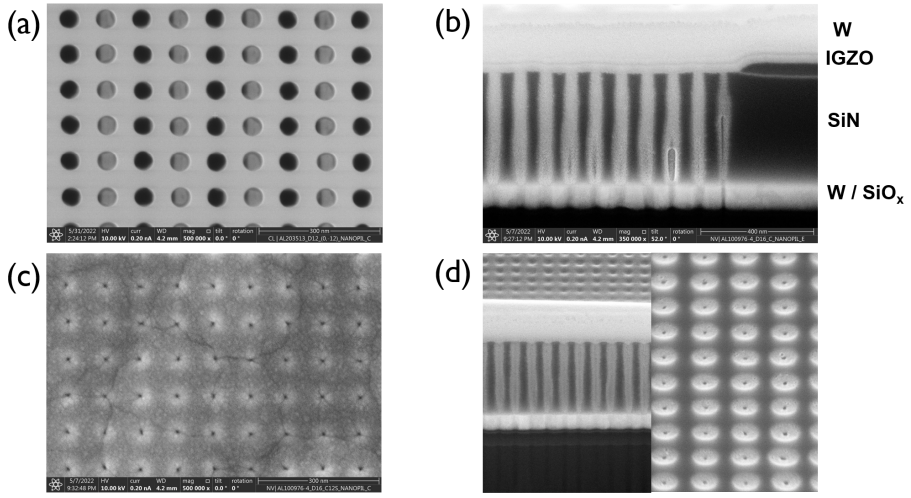

Figure 4.11: SEM images taken at various stages of the metamaterial development. a) Top down view of the etched Si_3N_4 layer showing the metallic backplane below. b) Cross section of the $IGZO$ filled pillars. c) Top view of the Si_3N_4 after ALD filling. The pillar core seems to have remained empty, indicating excellent conformal filling. d) Two images from after planarization showing a slight recess of the $IGZO$ pillars.

To ensure proper filling of the hole array, $35nm$ of $IGZO$ is deposited by ALD. Other techniques, such as physical vapour deposition would lead to prematurely closing the hole near to top as deposition rates are lower inside the etched holes. ALD on the other hand, only encounters this issue near the end of the deposition due to its conformal deposition rate. Consequently, a small keyhole with radius around $10nm$ (estimated from SEM) at the center of each pillar is created. Figure 4.11 b) and c) show both a cross section and top view after $IGZO$ filling and clearly illustrate the conformal filling achieved by ALD given that the whole length of the pillar is filled. Again, a layer of W is deposited on top to prevent undesired charging effects from influencing the measurements. An additional SiO_x capping layer is subsequently deposited to be consumed during CMP. Once deposited, the stack can undergo oxide CMP planarization in which the entire top $IGZO$ layer and part of the Si_3N_4 is consumed to ensure completely disconnected $IGZO$ electrodes at the top surface. Figure 4.11 d) shows the metamaterial after planarization.

Here, it became clear that the $IGZO$ pillars are slightly recessed into the Si_3N_4. This is a commonly encountered effect, as materials typically have a

different planarization rate, meaning that height differences can occur. For the metamaterial, if equal heights cannot be attained, the $IGZO$ electrode preferably extrudes slightly as this enable the electrode to be in close contact with the waveguide. Inversely, slightly recessed electrodes would require the fringing electric fields to penetrate both Si_3N_4 and BTO. This is detrimental to the application, as the dielectric constant of these materials differs strongly and would lead to strong confinement of the field within the SiN thus worsening the attainable optical modulation. To remedy the uneven planarization an additional fluoride based dry etch selective to Si_3N_4 was performed. Figure 4.12 shows the finished metamaterial from various viewpoints. An optional capping layer of SiO_2 can be added to improve bonding behaviour.

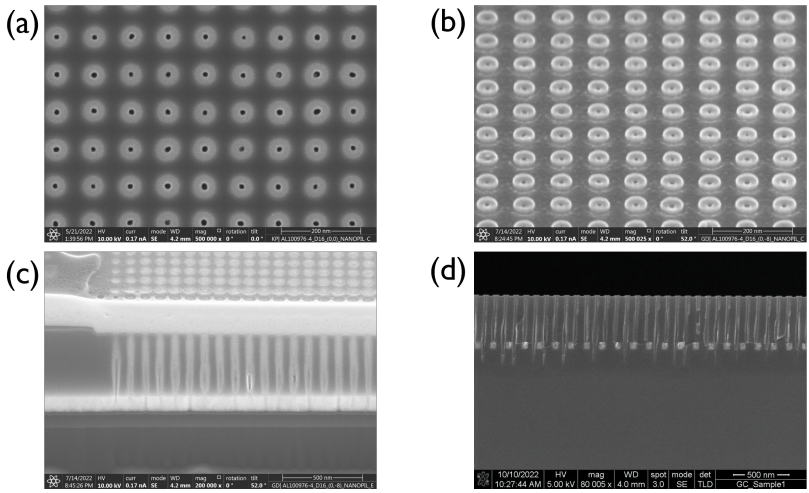

Figure 4.12: SEM images taken at various stages of the metamaterial development. a) Top down view of the planarized metamaterial. b)-c) Angled view of the planarized metamaterial. d) Cross section of the planarized metamaterial.

4.3 Metamaterial Characterization

4.3.1 Optical Characterization

Ellipsometry Characterization

The completed metamaterial was characterized by ellipsometry on a wafer without metallic backplane to reduce the number of possible fit parameters and mimic previous measurements on planar layers. The measurements were initially fitted using the combined models employed previously for Si_3N_4 and $IGZO$, hence two Tauc-Lorentz and one Drude oscillator. Unfortunately, we repeatedly find unrealistic values for one of the Tauc-Lorentz oscillators which we attribute to them being nearly identical for Si_3N_4 and $IGZO$ given their refractive indices and the sub-wavelength patterning. In the end, we opted to use a single Tauc-Lorentz oscillator instead.

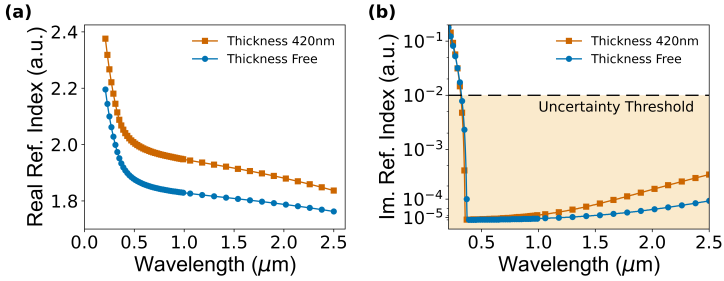

Figure 4.13: Comparison between the real (left) and imaginary (right) refractive index for a model with constrained and unconstrained thickness.

The outcome of the fit however remains peculiar. For example, we find a poor match between the fitted thickness ($460nm$) and the measured thickness from SEM ($420nm$). Additionally, the fitted refractive index is significantly lower than that of the constituent materials. As solution we opt to confine the metamaterial thickness to the value found by SEM. As a consequence, the quality of the fit (MSE 47.3 vs 82.8) reduces. However, the refractive index aligns better with the values for Si_3N_4 and $IGZO$. This indicates that an isotropic model no longer succeeds in accurately representing the metamaterial. Only at the wavelength where both refractive indices are identical an isotropic model suffices. Instead, an anisotropic model should be used. As such, we opt to use more advanced measurement techniques, such as rigorous coupled wave

analysis (RCWA) of Mueller matrices and optical critical dimension (OCD) spectroscopy, to gain insight in the metamaterial.

RCWA Characterization

The aforementioned Woollam RC2 ellipsometer is based on a rotating compensator, which gives it the possibility to measure the full Mueller matrix. This matrix can be viewed as an extension of the Jones vector, which is used to represent polarized light. However, where the 2×2 Jones vector can represent linearly, circularly, and elliptically polarized light, the Mueller matrix can describe any polarization state including depolarization. To that end, a 4×4 matrix is employed in combination with the Stokes vector having four elements (S_0, S_1, S_2, S_3). Here, S_0 represents the total intensity of the beam, S_1 represents the intensity of the light polarized at $90°$, S_2 represents the intensity of light at $45°$ and S_3 represents the intensity of left and right circularly polarized light. Usually all elements of the Mueller matrix are divided by its first element M_{00} to normalize them. For the Mueller matrix in question six elements remain, in which three symmetries exist namely $M_{01} = M_{10}$, $M_{23} = -M_{32}$ and $M_{22} = M_{33}$. Of these, M_{01} is determined by extinction, M_{23} is linked to optical retardance and M_{22} is again linked to extinction. [353]

RCWA simulations were used to assess the Mueller matrix measurements. This is a Fourier based method, which is commonly used for solving the scattering of periodic structures. Since RCWA can also be used to simulate the full scattering matrix, the Mueller matrix is a common output. Anisotropic structures, such as the one employed here, form no problem for RCWA. As such, Mueller matrices were measured on one of the test wafers having a continuous W layer before touch up etch. The Mueller matrices, shown in Figure 4.14, contain several zero elements due to the structure's symmetry. [354] A fitting script was developed in python to fit the data to simulations employing a robust least square (LSQ) fitting algorithm and the python interface of the SCATMECH library. (pySCATMECH) The script leverages a Jacobian matrix to assess the influence of each fit parameter on the Mueller matrix data space, after which it suggests a new input value with decreased LSQ for all fit parameters. Both 2D and 3D models are possible, depending on the desired complexity.

$$F(\vec{x}) = \sum_{j=1}^{m} \frac{(y_j - f_j(\vec{x}))^2}{\sigma_j^2} \tag{4.5}$$

Here, $\mathbf{x}$ is the vector representing the RCWA structural parameters, y_j represents the measured Mueller matrix data points at the j-th wavelength, $f_j(\mathbf{x})$ are simulated data points by the RCWA model and σ_j^2 is the variance of 30 separate measurements. We opt to use measurement data acquired between $0.3\mu m$ and $1.2\mu m$ under an incident angle of 75° since this leads to a longer optical path. Several models with increasing complexity were created. Initially, data was fitted by sweeping the thickness of a single 2D SiN layer, without Jacobian matrix. The best fit was found at an LSQ of 6630 at a thickness off $422nm$, shown in Figure 4.15. Looking at the SEM data above, a good thickness match was found. On the other hand, we attribute the difference between the ellipsometry fit and this model to the inclusion of additional data by using the full Mueller matrix. Afterwards, a more realistic model was created by including the influence of the $IGZO$ electrode. As such, the metamaterial was fitted with an effective medium refractive index assuming $45nm$ electrodes embedded in $90nm$ of SiN. Again, only the thickness of the 2D layer was swept. The best fit was obtained at a thickness of $417nm$ resulting in an LSQ of 15089. A nearly identical thickness was found to the model employing Si_3N_4 optical constants, further indicating the similarity in refractive index between the two materials. The increase in LSQ can be mainly attributed to a worse fit a short wavelengths. Subsequently, a 3D counterpart of the second model was created, now fully including the $IGZO$ electrode in Si_3N_4. Unfortunately, no sensitivity was found to the pillar width and period by using the LSQ function, likely due to the similarity of the optical constants of both material. Identical to model 2, only the thickness was swept which leads to a minimum LSQ of 12351 at $416nm$. Compared to model 2 a slightly improved fit is found. At the same time, the model encounters a similar issue as model 2 at shorter wavelengths.

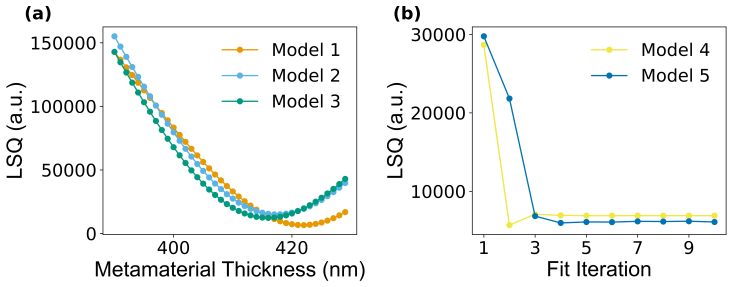

Figure 4.14: Least square error of the employed RCWA fits. a) LSQ for model that only include a single parameter i.e. the thickness. b) LSQ for more extensive models plotted against the fit iteration. Image reproduced with permission. [355]

More advanced models were created using SEM and AFM data as input, which indicate the existence of a hollow center in each electrode and uneven CMP rate during planarization. Consequently, 2 additional models were created. For these new models, again no sensitivity was found to the pillar width and period, such that they were kept constant at $45nm$ and $90nm$ respectively. The fourth model recreates the unequal CMP rate between Si_3N_4 and $IGZO$ by having recessed electrodes. The optimal fit indicates a thickness of $426.5nm$ and a recess of $18.2nm$ resulting in an LSQ of 6885. Evidently, the inclusion of a slight recess leads to a significant improvement in the fit, especially around finer data oscillations. The fifth and final model adds a hollow core at the center of the electrodes. The LSQ after 10 iterations was 6085, for a thickness and core width of $440nm$ and $20.4nm$ respectively. Unfortunately, no further improvements could be made to the model as the combination of both 3D models resulted in unrealistic fit values.

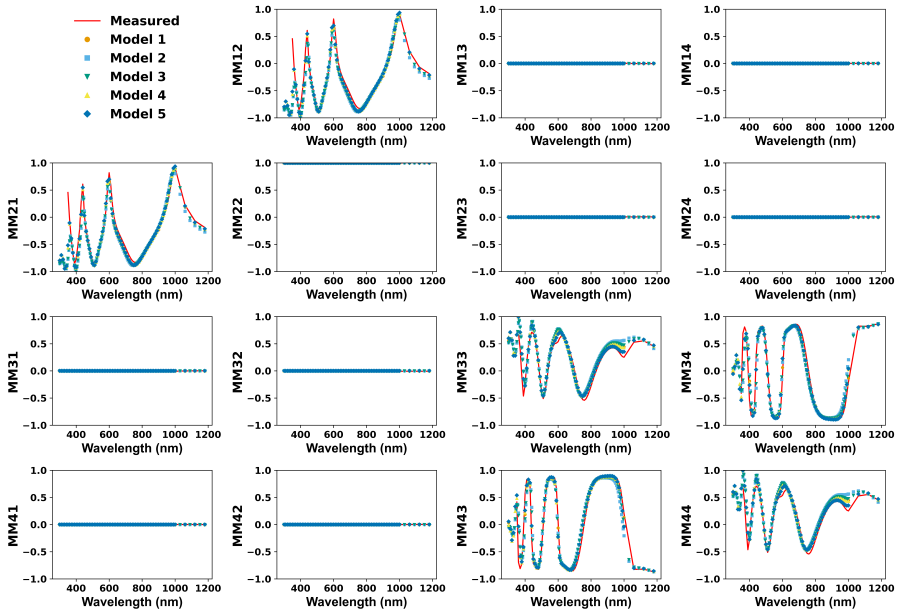

Figure 4.15: An overview of the measured Mueller matrix and the outcome of the fitted models. Image adapted from [355]. Image reproduced with permission. [355]

Optical Critical Dimension Spectroscopy

OCD spectroscopy, sometimes also called scatterometry, measurements were performed on similar wafers using a Nova T600 MMSR+. This is a non-destructive metrology technique used to measure the dimensions and shapes of nano-scale structures on wafers. It functions by measuring and fitting the light scattered from a patterned surface to determine critical dimensions, such as feature width, height, and sidewall angles. Afterwards, similar models to above were fitted using the refractive indices extracted from the planar test wafers in Nova MARS®, shown in Figure 4.16. Two models were created. First, a model assuming only a Si_3N_4 layer on top of W. The model results in a good fit for wavelengths longer than $400nm$. However, at shorter wavelengths, the model loses accuracy. We attribute this to the omission of the $IGZO$ electrodes, which deviate most in real refractive index at short wavelengths from the Si_3N_4. Afterwards, the model was improved by adding the $IGZO$ pillars. A layer thickness, pillar height and pillar width of respectively $408nm$, $423nm$ and $74nm$ were found. This second model fits the complete wavelength range well, showcasing that the created metamaterial matches with the design and the measured SEM data

4.3.2 Electrical Characterization

A combination of AFM and conductive atomic force microscopy (C-AFM) was performed to gain insight in the surface relief and electrical behaviour respectively. This was done both during development before the CMP process was optimized and afterwards when development was completed. Below a distinction is made between two measurement techniques due to the different top surface of the employed metamaterial.

Scalpel PFM - c-AFM

Initial measurements required scalpel AFM to remove excess Si_3N_4 from the cladding. Beforehand, during standard AFM measurements, shown in 4.17 a), a probe was scanned in direct contact with the sample indicating that the $IGZO$ pillars were recessed into the Si_3N_4 layer. After removal of the top layer to create a flat surface using a scalpel tip, conductive atomic force microscopy (C-AFM) measurements were realized by adding a grounded electrode to the sample and ensuring a conductive scanning probe such that an electrical loop

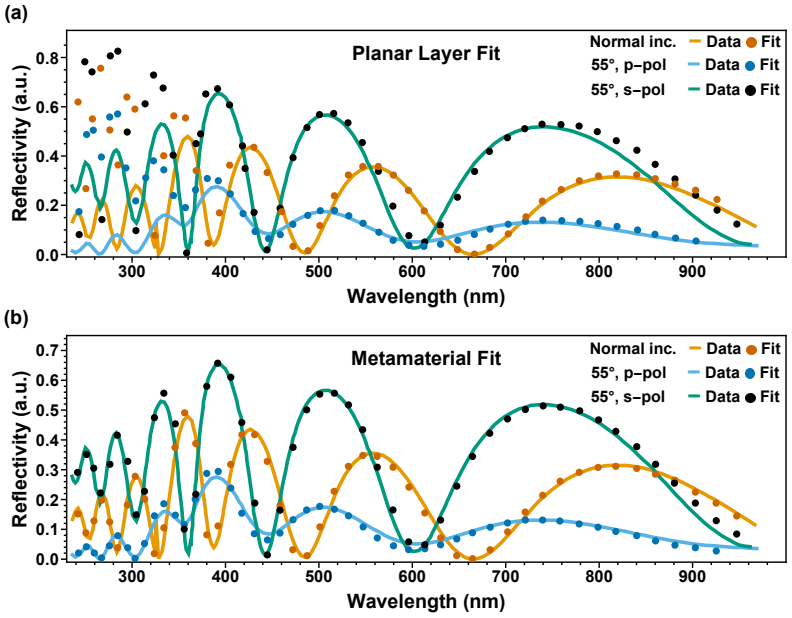

Figure 4.16: Comparison between the real (left) and imaginary (right) refractive index for a model with constrained and unconstrained thickness. Image reproduced with permission. [355]

could be formed through the sample, as shown in Figure 4.17 b). The perceived current in Fig. 4.17 c) now gives insight in the electrical characteristics of the metamaterial $IGZO$ electrodes. The pillar shape appears different in the standard AFM and C-AFM measurement. It is possible that through removal of the Si_3N_4 top layer through scalpel AFM the $IGZO$ underneath may have been damaged. Next to that, normal wear of an AFM tip can lead to measurements artefacts.

Note, that although the probe is scanning the surface in direct contact, a relatively high tip-sample contact resistance exists between the tip and the $IGZO$ resulting in low detectable leakage (i.e., in the pA range). Furthermore, the observed conduction is linked to a convolution of all the present resistive terms. Hence, this is a combination of the electrode pillar, the metallic back contact, and the Si substrate. Consequently, the dominant resistance is perhaps not the tip-sample junction and the absolute value of current is not the best indicator of the layers properties. Additionally, local fluctuations must be ascribed to small surface modifications of the $IGZO$ top surface such

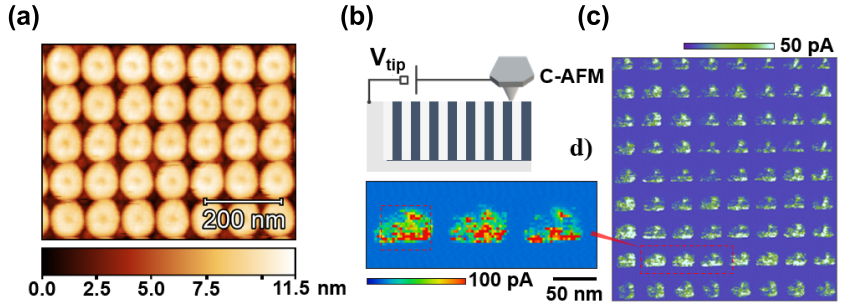

Figure 4.17: a) AFM measurement of the relative sample height. b) Schematic of the C-AFM measurement. c) Current map of individual metamaterial pillars by C-AFM. d) High resolution C-AFM image of the metamaterial. Image reproduced with permission. [355]

as stoichiometry variations or intra-grains scattering that can locally make the resistance of the tip-sample junction dominant. That said, these initial measurements clearly indicate the electrical conductivity of the embedded electrode.

Top Surface PFM - c-AFM

A similar experiment was performed after the complete metamaterial process was developed which now presents a level surface requiring no further modification. Here, various anneal conditions were investigated as it is well known that the conductive properties of metal oxides change depending on their oxygen content through the amount of present oxygen vacancies. The employed $IGZO$ is known to be rather conductive as deposited, and anneals are typically used to reduce the conductivity. [356, 357, 358] Samples were annealed in air and under N_2 environment for 1 hour, as well as at four different temperatures starting from $165°C$ up to $300°C$. All samples were compared to a non-annealed sample from the same wafer.

The current maps of the annealed samples can be found in Fig. 4.18. During these measurements, the metamaterial backplane was used as intended to form a connection between the grounded electrode pad and the pillar electrode. The applied voltage was 1V and a full diamond tip was used. The average current

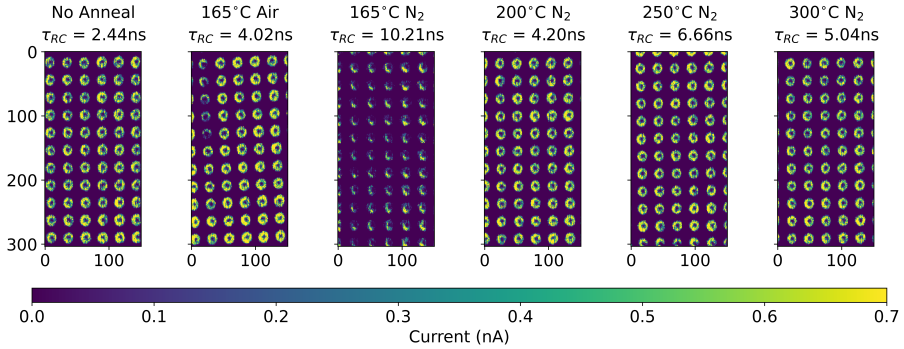

Figure 4.18: C-AFM measurement of the finished metamaterial under various annealing conditions varying in temperature and environment.

and standard deviation of each set of pillars were calculated to be 92 ± 17 nA, 56 ± 29 nA, 22 ± 8 nA, 54 ± 13 nA and 34 ± 13 nA for no anneal, $165°C$ (air), $165°C$ (N_2), $200°C$ (N_2), $250°C$ (N_2), $300°C$ (N_2). At the same time, COMSOL FE simulations reveal a capacitance of 2.25×10^{-16} F per pillar. Here, a 4nm thick bonding oxide (SiO_2) was assumed between cladding and waveguide. This layer ideally is as thin as possible to attain proper electric field penetration into the waveguide (See Chapter 6). That said, a thin bonding layer will always be needed in reality. To our benefit, the bonding oxide reduces the capacitance of the structure enabling faster switching. As a consequence, the RC time constant τ_{RC} of each of the samples are expected to be 2.4 ± 0.5ns, 4 ± 2ns, 10 ± 4ns , 4 ± 1ns, 7 ± 3ns and 5 ± 2ns and thus indicates that annealing affects the electrical properties of the $IGZO$ pillars as expected. Since all time constants are similar, the non-annealed layer is favoured due to it requiring fewer processing steps. Continuing with this value, a cut-off frequency of 65 ± 12 MHz is encountered which more than suffices for the envisioned holographic display.

4.4 Conclusion

Blanket layer depositions of metamaterial candidate materials $IGZO$, SiO_xN_y and Si_3N_4 were performed. Ellipsometry measurements revealed $IGZO$ and Si_3N_4 are closely matched in the visible range for their real refractive index when proper Si_3N_4 growth conditions are used. A high aspect ratio etch process was developed to fabricate a hole array into a thick Si_3N_4 layer, which was

then filled by ALD *IGZO*. CMP was employed to planarize the metamaterial. Optical metrology was performed through OCD spectroscopy and Mueller matrix ellipsometry combined with RCWA. They showed that accurate fitting requires optical models that include the *IGZO* electrode. Finally, C-AFM measurements revealed the conductive behaviour of the electrode pillars. As deposited pillars appear the most suitable, attaining a cut-off frequency of 65MHz. Consequently, it is possible to create an optically isotropic layer with embedded electrodes which offers potential for innovation in the field of tunable optically active nanostructures.

Chapter 5

Active Pockels Material Characterization

The focus of this chapter lies on the active material of the envisioned spatial light modulator. First, a brief overview of barium titanate growth and its typical characteristics is given. BTO growth is however not the topic of this PhD, for a deeper insight the reader is referred to the publications and thesis of a colleague. [359, 360, 361] Afterwards, the chapter presents a commonly employed measurement technique based on a de Sénarmont compensator to assess the electro-optical behaviour of the grown material. Finally, the data analysis procedure and results are shown.

5.1 BTO Growth and Characteristics

5.1.1 BTO Growth

BTO can be grown by a large variety of methods including molecular beam epitaxy (MBE), pulsed laser deposition (PLD), sol-gel process and CVD. Not surprisingly, the large growth variety brings about significant differences in material characteristics. During this PhD only *BTO* deposited in vacuum chambers was employed as this typically yields good quality crystals which leads to better optical properties. [362]

High quality BTO can be made by epitaxial deposition for which the lattice matching between substrate and the desired layer is crucial. To that end, a strontium titanate ($SrTiO_3$) buffer or template is grown on (100) silicon, given its lattice constant lies between the one of Si and BTO, thus relaxing the present lattice strain. The employed solid state methods (PLD and MBE) were all applied to the same template matched substrate. Layers were typically grown about $100nm$ thick and characterized by AFM and X-ray diffraction to assess surface and crystalline quality. Of these, several interesting samples were selected for electro-optical tests. For more details on the material growth the reader is directed to the work of my colleagues. [359, 360, 361]

5.1.2 Ferroelectric Behaviour

One of the interesting properties of BTO is its ferroelectricity which is due to its non-centrosymmetric crystallographic structure ($4mm$) at room temperature. [363, 364, 365] This includes a slightly displaced titanium atom at the center which lies at the origin of its ferroelectric and electro-optical behaviour. Under the application of an external electric field, this ionic titanium can be displaced slightly causing these effects. Interestingly, the local electric fields inside the crystal change faster than any present elastic forces thus leading to a new equilibrium position for the titanium and the creation of permanent dipole moment.

Another consequence of the $4mm$ tetragonal crystallographic point group is the elongation of one axis. Its lattice constant is 4.0254Å, while for the normal axis it is 3.9865Å [366] This leads to birefringent optical behaviour, with a slightly lower refractive index along the elongated axis. In the case of BTO this additionally leads to the formation of a crystal consisting of nano-patches, each having a different polarization vector to reduce the stress in the crystal. A few possibilities exist depending on the orientation of the elongated axis. Domains with their elongated axis out of plane or along the [001] direction are referred to as c-oriented. On the other hand, domains with their elongated axis in the plane of the substrate are called a^+, a^-, b^+ and b^- oriented if their polarization vector aligns with the [100], [$\bar{1}$00], [010] and [0$\bar{1}$0] direction respectively. The aforementioned ferroelectric domains have a distinctly different impact on both crystal orientations. For c-oriented BTO, domains can only align perpendicularly to the substrate and thus can only form an alternating or completely aligned pattern. A- and b-oriented BTO typically leads to more complex patterns as the domains have an additional degree of freedom. An as-grown layer thus typically has a completely mixed layer consisting of 4

different types of ferroelectric domains. These in-plane domains can be oriented both at 90° to each other (a compared to b), and they can be oriented 180° to each other (for example, a^+ compared to a^-). Optically speaking, domains rotated 90° to each other respond similarly to an applied electrical bias. At the same time, domains rotated 180° to each other behave oppositely. All four orientations are thus required to accurately model the behaviour of unpoled films.

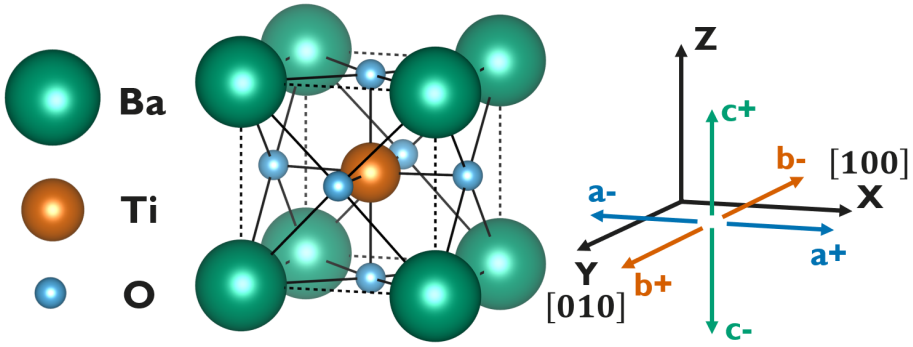

Figure 5.1: Schematic of the *BTO* perovskite crystal structure (4mm).[367] Standard notation describes in a c-oriented crystal having its extraordinary axis out-of-plane. The other orientations (a^+, a^-, b^+ and b^-) can be achieved through tensor rotation.

The ferroelectric domain structure also has a significant impact on the electro-optic behaviour as this is similarly coupled to the position of the central titanium atom. Indeed, antiparallel domains i.e. domains oriented 180° in respect to each other have an opposite optical response (Pockels) on the polarization of light. Their net effect will thus depend on the exact amount of each domain orientation and can completely be cancelled out in a worst case scenario. To prevent this, ferroelectric domains can be aligned by electrical poling. This can be done by several methods which have shown to yield similar results. [368, 369, 370] A common approach applies a slowly oscillating and gradually increasing alternating current (AC) bias ($1 - 10Hz$), possibly under thermal heating. Alternatively, the DC field can be gradually ramped up to its final value. The idea in both methods is to only gently stress the crystal as sudden and intense electric fields can cause damage. Fast switching of the electric field has been found to create sub-optimally poled crystals. [371] The applied bias should at minimum be sufficient to surpass the coercive field, which is the electrical field at which domains flip orientation. Literature indicates that two separate coercive fields exist, one for both 180° and 90° oriented domains respective to the applied electric field. [372, 373] For *BTO* the coercive field to

pole the entire film is known to be $\approx 5 \times 10^5 V/m$ or $0.5V$ per μm of electrode spacing. [374] Whether or not ferroelectric domains have been aligned can be assessed through current-voltage measurements, which in case of aligned domains show a hysteresis.

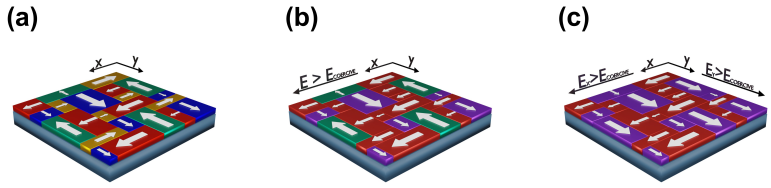

Figure 5.2: a) Scrambled domain orientation. b) An electric field above the coercive field along the x-axis causes half of the domains to become aligned. c) An electric field applied under a 45° angle to the x-axis leads to all domains aligning.

BTO ferroelectric domains have shown to widely vary in size. For example, polarized light microscopy, bright field tunnelling electron microscopy (TEM) and differential phase contrast scanning tunnelling electron microscopy measurements on bulk crystals resulted respectively in domain size of $100\mu m$, $3\mu m$ - $100nm$ and $100nm$. [375, 376, 377, 378] On the other hand, thin film measurements using TEM holography found domains ranging from $1\mu m$ - $50nm$. [379] It is thus difficult to conclude on a single value, especially keeping in mind that stress and strain will have significant impact on the crystal. That said, similar measurements on other ferroelectric thin films seemingly indicate that the domain size situate itself near the lower end. Below, measurements are performed with electrodes with size $150\mu m \times 350\mu m$ spaced $10\mu m$ apart. These indicate that a scrambled domain state is present, as measurements on a (primarily) single type of domain orientation would yield different data.

5.1.3 Electro-Optic Behaviour

Non-Linear Optics

The interaction of materials such as *BTO* and incident light is described by non-linear optics. To that end, the polarization (or dipole moment per volume)

of a material $\vec{P}(t)$ should be considered. For a normal (i.e. a linear material) the polarization is related to the applied electric field $\vec{E}(t)$ through the linear susceptibility $\chi^{(1)}$ and the vacuum permittivity ε_0 as shown in eq. 5.1. The susceptibility has 9 components since both the crystal and the electric field have three spatial directions. This polarization can be linked to more tangible properties such as the refractive index. In the simplest case, the electrons of a material oscillate in a parabolic potential governed by $\vec{P}(t)$. It is their oscillation frequency that determines the optical behaviour of the material. Changing the frequency of the incident light results in a different optical response, given that the susceptibility is frequency dependent.

$$\vec{P}(t) = \varepsilon_0 \chi^{(1)} \vec{E}(t) \tag{5.1}$$

For non-linear media, eq. 5.1 can be generalized to eq. 5.2 with $\chi^{(2)}$ and $\chi^{(3)}$ respectively as second and third order non-linear susceptibility. The second order non-linear susceptibility has 27 components, three for the crystal direction and two times three for the electric field, the third order non-linear susceptibility similarly has 81 components. Fortunately, symmetry typically leads to a significant reduction in components.

$$\vec{P}(t) = \varepsilon_0 \chi^{(1)} \vec{E}(t) + \varepsilon_0 \chi^{(2)} \vec{E}(t)^2 + \varepsilon_0 \chi^{(3)} \vec{E}(t)^3 \tag{5.2}$$

$$\vec{P}(t) = \vec{P}(t)^{(1)} + \vec{P}(t)^{(2)} + \vec{P}(t)^{(3)} \tag{5.3}$$

In practice, these susceptibilities distort the parabola mentioned above and lead to a range of interesting optical effects which become noticeable when multiple electric fields are present simultaneously, like in a pump-probe measurement or the de Sénarmont compensator mentioned below. Here, a first applied electric field leads to slight changes of the optical properties and a second field is used to probe them. In general, these effects depend on the wavelength of the applied light with the strongest effects only appearing near an optical resonance. The non-linear susceptibilities are unfortunately very small meaning that strong electric fields, for example from a powerful laser, are required for significant changes.

The Electro-Optic Effect

The electric fields in equation 5.2 do not have to originate from incident light, in fact any electric field will do. In the case of the Pockels measurement presented here, the electric field originates from a potential difference between two electrodes patterned on the active material. The second order non-linear polarization and its influence is often referred to as the Pockels effect, whereas the third order effect is usually called the Kerr effect. In the context of video-holography, the Pockels effect is of primary interest because it is generally stronger than the Kerr effect. Crucial to the Pockels effect is that it can only occur in non-centrosymmetric crystal structures, since these media do not posses inversion symmetry. As a consequence, the electron potential well is not symmetric which leads to non-linear effects under influence of an electric field.

To describe the extend of the electro-optic effect on the optical behaviour of a material, the index ellipsoid can be used. Here, the electric displacement field $\vec{D}$ is used as it accounts for both bound charges and an externally applied field. For $\vec{D}$ is known that:

$$\vec{D}(t) = \varepsilon_0 \vec{E}(t) + \vec{P}(t) = \varepsilon_0 \vec{E}(t) + \varepsilon_0 \chi^{(1)} \vec{E}(t) \tag{5.4}$$

Hence, by defining the relative permittivity as $1 + \chi^{(1)} = \varepsilon_r^{(1)}$:

$$\vec{D}(t) = \varepsilon_0 \varepsilon_r \vec{E}(t) \tag{5.5}$$

Or by writing this component-wise:

$$\begin{bmatrix} D_x \\ D_y \\ D_z \end{bmatrix} = \varepsilon_0 \begin{bmatrix} \varepsilon_{xx} & \varepsilon_{xy} & \varepsilon_{xz} \\ \varepsilon_{yx} & \varepsilon_{yy} & \varepsilon_{yz} \\ \varepsilon_{zx} & \varepsilon_{zy} & \varepsilon_{zz} \end{bmatrix} \begin{bmatrix} E_x \\ E_y \\ E_z \end{bmatrix} \tag{5.6}$$

In the case of a lossless, non-optically active material the permittivity tensor is represented by a real and symmetric matrix which can always be diagonalized. Physically this means that there is a coordinate system, typically called the principal axis system, for which the following is true:

$$\begin{bmatrix} D_X \\ D_Y \\ D_Z \end{bmatrix} = \varepsilon_0 \begin{bmatrix} \varepsilon_{XX} & 0 & 0 \\ 0 & \varepsilon_{YY} & 0 \\ 0 & 0 & \varepsilon_{ZZ} \end{bmatrix} \begin{bmatrix} E_Z \\ E_Y \\ E_Z \end{bmatrix} \tag{5.7}$$

Here, the capital subscripts refer to the principal axis system. By now considering the energy density per unit volume (U) of a wave travelling through the anisotropic media, the index ellipsoid can be found.

$$U = \frac{1}{2}\vec{D} \cdot \vec{E} \tag{5.8}$$

Rewriting this in terms of the electric displacement field and using the fact that the permittivity is related to the square of the refractive index results in the following.

$$U = \frac{1}{2\varepsilon_0}\left[\frac{D_X^2}{\varepsilon_{XX}} + \frac{D_Y^2}{\varepsilon_{YY}} + \frac{D_Z^2}{\varepsilon_{ZZ}}\right] = \frac{1}{2\varepsilon_0}\left[\frac{D_X^2}{n_x^2} + \frac{D_Y^2}{n_y^2} + \frac{D_Z^2}{n_z^2}\right] \tag{5.9}$$

Dividing by U on both sides and simplifying yields an ellipsoid in normalized coordinates that only depends on the components of the refractive index.

$$1 = \left[\frac{\left(\frac{D_X}{\sqrt{2\varepsilon_0 U}}\right)^2}{n_x^2} + \frac{\left(\frac{D_Y}{\sqrt{2\varepsilon_0 U}}\right)^2}{n_y^2} + \frac{\left(\frac{D_Z}{\sqrt{2\varepsilon_0 U}}\right)^2}{n_z^2}\right] = \left[\frac{x^2}{n_x^2} + \frac{y^2}{n_y^2} + \frac{z^2}{n_z^2}\right] \tag{5.10}$$

This represents the index ellipsoid in the principal axis system. In case a material is considered in a different coordinate system, a few additional terms appear that correspond with the off axis elements in eq. 5.6 assuming they are symmetric. This equation can be simplified to eq. 5.10 by finding a new base.

$$1 = \left(\frac{1}{n^2}\right)_1 x^2 + \left(\frac{1}{n^2}\right)_2 y^2 + \left(\frac{1}{n^2}\right)_3 z^2 + 2\left(\frac{1}{n^2}\right)_4 yz + 2\left(\frac{1}{n^2}\right)_5 xz + 2\left(\frac{1}{n^2}\right)_6 xy \tag{5.11}$$

Similarly, by starting from the non-linear polarization the modulation of the impermeability can be written as:

$$\eta_{ij} = \left(\frac{1}{n^2}\right)_{ij} = \left(\frac{1}{n^2}\right)^{(0)}_{ij} + \sum_k r_{ijk}E_k + \sum_{kl} s_{ijkl}E_kE_l \tag{5.12}$$

Here η_{ij} is the impermeability tensor, r_{ijk} is the tensor describing the linear electro-optic effect, also called the Pockels coefficients and s_{ijkl} is the tensor describing the quadratic electro-optic effect. Since the permittivity tensor ε_{ij} is real and symmetric, its inverse $\eta_{ij} = \left(\frac{1}{n^2}\right)_{ij}$ must also be real and symmetric. As a consequence, both r_{ijk} and s_{ijkl} are also real and symmetric for their first two indices. This property can now be used to simplify the tensors and reduce the amount of needed elements substantially. In the case of the linear electro-optic effect the third rank tensor r_{ijk} can be written as a two dimensional matrix r_{hk} for which the following contracted notation applies.

ij	11	22	33	23 or 32	13 or 31	12 or 21
h	1	2	3	4	5	6

The influence of the linear electro-optic effect on the refractive index is thus:

$$\Delta\left(\frac{1}{n^2}\right)_i = \sum_j r_{ij}E_j \tag{5.13}$$

Or more explicitly.

$$\begin{bmatrix} \Delta\left(1/n^2\right)_1 \\ \Delta\left(1/n^2\right)_2 \\ \Delta\left(1/n^2\right)_3 \\ \Delta\left(1/n^2\right)_4 \\ \Delta\left(1/n^2\right)_5 \\ \Delta\left(1/n^2\right)_6 \end{bmatrix} = \begin{bmatrix} r_{11} & r_{12} & r_{13} \\ r_{21} & r_{22} & r_{23} \\ r_{31} & r_{32} & r_{33} \\ r_{41} & r_{42} & r_{43} \\ r_{51} & r_{52} & r_{53} \\ r_{61} & r_{62} & r_{63} \end{bmatrix} \begin{bmatrix} E_Z \\ E_Y \\ E_Z \end{bmatrix} \tag{5.14}$$

The new impermeability tensor is than equal to.

$$\eta' = \left(\frac{1}{n^2}\right)' = \begin{pmatrix} 1/n_x^2 + \Delta\left(1/n^2\right)_1 & \Delta\left(1/n^2\right)_6 & \Delta\left(1/n^2\right)_5 \\ \Delta\left(1/n^2\right)_6 & 1/n_y^2 + \Delta\left(1/n^2\right)_2 & \Delta\left(1/n^2\right)_4 \\ \Delta\left(1/n^2\right)_5 & \Delta\left(1/n^2\right)_4 & 1/n_z^2 + \Delta\left(1/n^2\right)_3 \end{pmatrix} \tag{5.15}$$

The Pockels perturbation leads to a new index ellipsoid, luckily the perturbation is also symmetric such that the symmetry of the tensor is not disturbed.

$$1 = \left(\frac{1}{n^2}\right)'_1 x^2 + \left(\frac{1}{n^2}\right)'_2 y^2 + \left(\frac{1}{n^2}\right)'_3 z^2 + 2\left(\frac{1}{n^2}\right)'_4 yz + 2\left(\frac{1}{n^2}\right)'_5 xz + 2\left(\frac{1}{n^2}\right)'_6 xy \tag{5.16}$$

C-oriented Barium Titanate

Barium titanate has $4mm$ as crystallographic point group at room temperature meaning that most Pockels coefficients are zero, as shown in eq. 5.17 which applies to a c-oriented BTO crystal. Of the five remaining coefficients only three unique ones remain, as $r_{13} = r_{23}$ and $r_{42} = r_{51}$. In absolute size, r_{13} is known to be smaller than r_{33} which in turn is smaller than r_{42}. The values below (in pm/V) are taken from [380]. It should be noted here that depending on the source these values can vary significantly, especially for thin films.

$$r_{ij} = \begin{bmatrix} 0 & 0 & r_{13} \\ 0 & 0 & r_{13} \\ 0 & 0 & r_{33} \\ 0 & r_{42} & 0 \\ r_{42} & 0 & 0 \\ 0 & 0 & 0 \end{bmatrix} = \begin{bmatrix} 0 & 0 & 19.5 \\ 0 & 0 & 19.5 \\ 0 & 0 & 97 \\ 0 & 1640 & 0 \\ 1640 & 0 & 0 \\ 0 & 0 & 0 \end{bmatrix} \tag{5.17}$$

The modulated impermeability tensor for c-oriented BTO can be found by combining eq. 5.14 and 5.17, the electric field components in the context of this work represent the electrical bias applied to the crystal.

$$\left(\frac{1}{n^2}\right)' = \begin{pmatrix} 1/n_x^2 + r_{13}E_z & 0 & r_{42}E_x \\ 0 & 1/n_y^2 + r_{13}E_z & r_{42}E_y \\ r_{42}E_x & r_{42}E_y & 1/n_z^2 + r_{33}E_z \end{pmatrix} \tag{5.18}$$

The modulated index ellipsoid is thus equal to:

$$1 = \left(\frac{1}{n_x^2} + r_{13}E_z\right)x^2 + \left(\frac{1}{n_y^2} + r_{13}E_z\right)y^2 + \left(\frac{1}{n_z^2} + r_{33}E_z\right)z^2 + 2\left(r_{42}E_y\right)yz + 2\left(r_{42}E_x\right)xz \quad (5.19)$$

Equation 5.19 can be used to assess practical implementations as it gives direct insight into the electric fields (from a waveguided mode) that can couple to each other in the principal axis coordinate system. For example, element $2\left(r_{42}E_x\right)xz$ describes the modulation of the index ellipsoid under influence of an electrical bias in the xz-plane and thus can be used to couple the optical E_x to E_z fields and vice versa.

A-oriented Barium Titanate

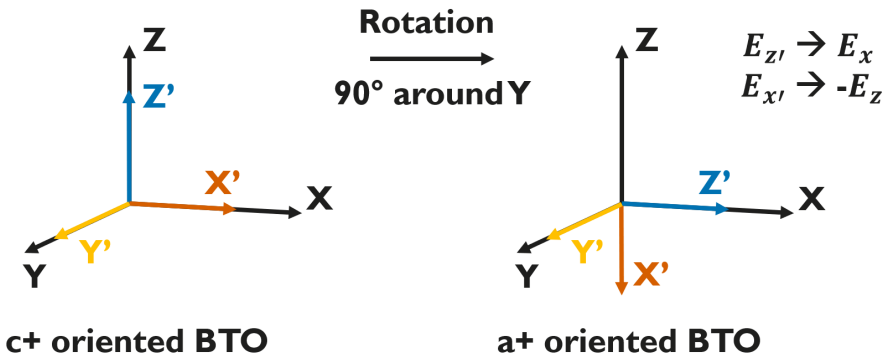

Figure 5.3: Schematic of the optical coordinate system (coloured - accented) and electrical coordinate system (black - no accent) and the influence of the rotation needed for an a^+ oriented crystal. The acquired fields in the rotated tensor need to be altered to keep the coordinate systems interchangeable.

In case of an a-oriented crystal, having its extraordinary axis laying along the x-axis, the permittivity tensor from eq. 5.18 is rotated around the y-axis by

90° resulting in the desired crystal orientation. Hence, an appropriate tensor rotation according to $A' = RAR^{-1}$ is needed. The required rotation matrix then is:

$$R_{y90^\circ} = \begin{pmatrix} 0 & 0 & 1 \\ 0 & 1 & 0 \\ -1 & 0 & 0 \end{pmatrix} \tag{5.20}$$

On top of the rotation, the field notation needs to be adjusted since the coordinate system for the applied electric field and the optical behaviour of the crystal has now changed as shown in Figure 5.3. Here, symbols without accents indicate the original and preferred coordinate system, the accents indicate the new coordinate system of the rotated crystal. To ensure optical and electrical fields are employed in the same coordinate system, $E_{z'}$ equals E_x and $E_{x'}$ equals $-E_z$. The impermeability tensor for an a-oriented crystal having its extraordinary axis along the original x-axis then becomes:

$$\left(\frac{1}{n^2}\right)' = \begin{pmatrix} 1/n_z^2 + r_{33}E_x & r_{42}E_y & -r_{42}E_z \\ r_{42}E_y & 1/n_y^2 + r_{13}E_x & 0 \\ -r_{42}E_z & 0 & 1/n_x^2 + r_{13}E_x \end{pmatrix} \tag{5.21}$$

The modulated index ellipsoid for an a-oriented crystal thus equals to:

$$1 = \left(\frac{1}{n_z^2} + r_{33}E_x\right)x^2 + \left(\frac{1}{n_y^2} + r_{13}E_x\right)y^2 + \left(\frac{1}{n_z^2} + r_{13}E_x\right)z^2 + 2\left(r_{42}E_y\right)xy - 2\left(r_{42}E_z\right)xz \tag{5.22}$$

B-oriented Barium Titanate

The same approach can be taken for a b-oriented crystal which has its extraordinary axis laying along its y-axis. Here, the permittivity tensor in eq. 5.18 should be rotated by a rotation of 90° around the x-axis. The required rotation matrix is:

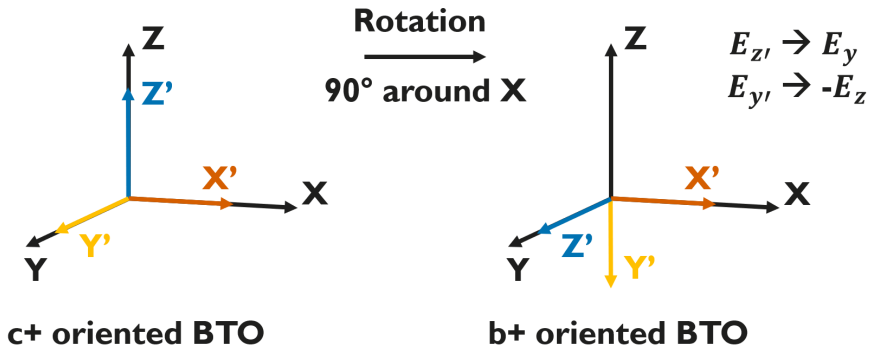

Figure 5.4: Schematic of the optical coordinate system (coloured - accented) and electrical coordinate system (black - no accent) and the influence of the rotation needed for an b^+ oriented crystal. The acquired fields in the rotated tensor need to be altered to keep the coordinate systems interchangeable.

$$R_{x90^\circ} = \begin{pmatrix} 1 & 0 & 0 \\ 0 & 0 & -1 \\ 0 & 1 & 0 \end{pmatrix} \tag{5.23}$$

Next to the rotation, the field notation again needs to be adjusted since the coordinate system for the applied electric field and the optical behaviour of the crystal has now changed as shown in Figure 5.4. Here, symbols without accents indicate the original and preferred coordinate system, the accents indicate the new coordinate system of the rotated crystal. To ensure optical and electrical fields are employed in the same coordinate system, $E_{z'}$ equals E_y and $E_{y'}$ equals $-E_z$. The impermeability tensor for an b-oriented crystal having its extraordinary axis along the original y-axis then becomes:

$$\left(\frac{1}{n^2}\right)' = \begin{pmatrix} 1/n_x^2 + r_{13}E_y & -r_{42}E_x & 0 \\ -r_{42}E_x & 1/n_z^2 + r_{33}E_y & -r_{42}E_z \\ 0 & -r_{42}E_z & 1/n_y^2 + r_{13}E_y \end{pmatrix} \tag{5.24}$$

The modulated index ellipsoid for an b-oriented crystal thus equals to:

$$1 = \left(\frac{1}{n_x^2} + r_{13}E_y\right)x^2 + \left(\frac{1}{n_z^2} + r_{33}E_y\right)y^2 + \left(\frac{1}{n_y^2} + r_{13}E_y\right)z^2 - 2\left(r_{42}E_x\right)xy - 2\left(r_{42}E_z\right)yz \quad (5.25)$$

5.2 Electro-Optic Measurements

5.2.1 de Sénarmont Compensator

A common measurement technique for assessing the non-linear coefficients of BTO in literature is based on a de Sénarmont compensator. [381, 374, 382, 362, 383, 384, 385] This specific set of components received their name from Henri Hureau de Sénarmont who did extensive work on polarization and isomorphous crystal mixtures. In practice, a de Sénarmont compensator combines a quarter waveplate with a rotatable polarizer, which can be used to totally extinguish the incident beam in case it is polarized. Figure 5.5 shows a schematic of the complete setup.

For a better overview of the setup all optical or all electrical components can be considered. The optical components sequentially consist of a fiber coupled infrared laser (Santec WSL110), a fiber collimator, two alignment mirrors, an iris, a Glan-Taylor prism with extinction ratio 1 : 100000 to ensure the polarization of the input, a half waveplate to arbitrarily rotate the incident polarization, a focusing lens, a optically non-linear sample, a collimating lens, a quarter waveplate, a second Glan-Taylor prism, a focusing lens and a photodetector. The electrical part of the setup can similarly also be split in two by considering the driving and readout electronics separately. The driving electronics mainly consist of a pulser (Agilent 8114A) capable of simultaneously applying AC bias with a large DC offset and two micropositioner probes to connect to the desired electrode pair. To read out the signal, a photodiode (Thorlabs FGA21 InGaAs) is used in photovoltaic mode. This current based signal is fed to a current pre-amplifier (SR570) which outputs a voltage. The voltage is subsequently split in its direct current (DC) and AC components which are respectively read out by a source measure unit (Keithley 2400) and lock-in amplifier (SR 830). Crucially, the reference signal of the lock-in is supplied by the pulser through

transistor-transistor logic.

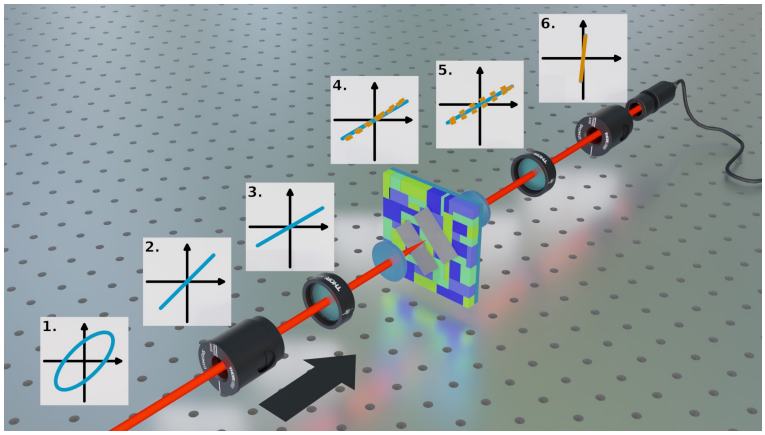

Figure 5.5: 3D render of a de Sénarmont compensator consisting of a prism polarizer, half-waveplate, focusing lens, birefringent sample, collimating lens, quarter-waveplate, second prism polarizer and a photodetector in order from left to right.

This approach leverages the polarization sensitivity of both Glan-Taylor prisms together with the quarter waveplate to create near total extinction of the beam. During measurement, the quarter waveplate and second polarizer are iteratively rotated to minimize the power on the photodiode. This is achieved when the light coming from the quarter waveplate is linearly polarized such that the polarizer can block it nearly completely. At this point, a small applied voltage leads to a change in sample birefringence through the electro-optic effect which is observed as a small increase in transmitted power measured at the photodiode. By applying the small bias using an AC signal and using a lock-in amplifier, a noise free signal can be extracted from the measurement. An additional DC bias, superpositioned on the AC signal, ensures that the domains of *BTO* reside in an aligned orientation. A step by step explanation of the polarization throughout the setup and the effect each component has on it, is given below based on Jones calculus.

Fiber Laser and Glan-Taylor Prism

The employed fiber based IR laser (Santec WSL110) outputs a slightly elliptically polarized beam, an example is shown in Figure 5.6 a). To preserve this present

polarization, a polarization maintaining fiber is used. Once collimated the input light is further polarized by passing it through a Glan-Taylor prism. Its ideal orientation is found by rotating it while constantly monitoring the measured laser power. At the power maximum, the prism has aligned its optical axis with the predominant polarization of the laser as shown in Figure 5.6 b).

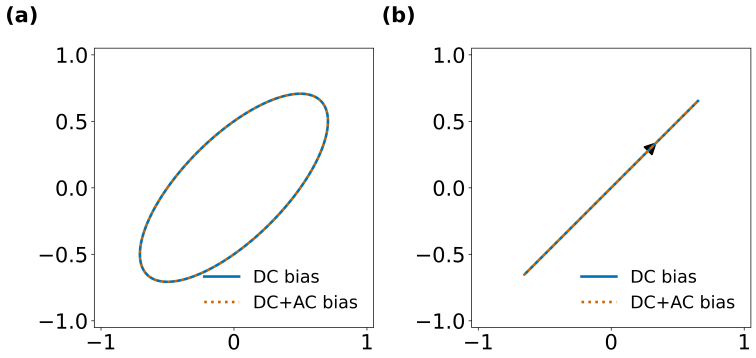

Figure 5.6: a) Simulated example of the elliptically polarized laser output. b) The simulated effect of a polarizer calculated by Jones calculus, oriented to maximize the passing power, on the elliptical polarization from a). The arrow indicates the transmitting axis of the polarizer.

Half-Waveplate

A half-waveplate is employed to arbitrarily rotate the incident polarization as shown in Figure 5.7 a). This waveplate introduces a π phase shift between its fast and slow axis. Therefore, it rotates incident linear polarization having an angle α with the optical axis of the waveplate to $-\alpha$. The half-waveplate is useful due to the elliptically polarized output of the laser, as it allows to maximize the power through the first polarizer and subsequently rotate that polarization to any other angle.

Barium Titanate Birefringence

The laser beam now reaches the BTO sample, which is a birefringent material. It can be interpreted as a general retarder having its optical axis and Δn determined by the present modulation. The linear polarized incident light thus

becomes elliptically polarized as shown in Figure 5.7 b). Application of a small AC bias on patterned electrodes results in a minor change in the birefringence. Consequently, the passing polarization is modulated as well.

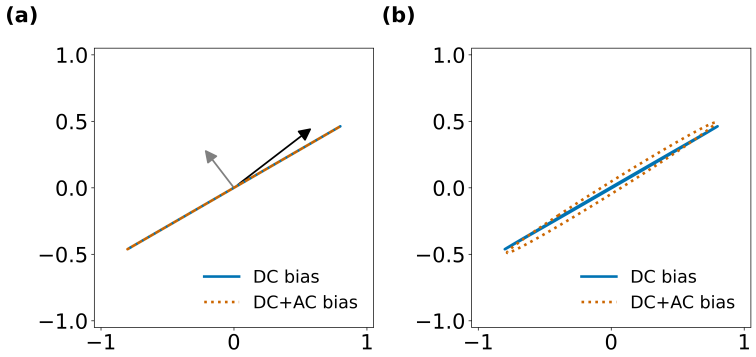

Figure 5.7: a) The simulated effect of a half waveplate on the polarization from Figure 5.6. The black and gray arrow respectively indicate the fast and slow axis of the half waveplate. b) The simulated effect of a $100\mu m$ thick BTO sample on the polarization from a). A much thicker layer was assumed here, compared to the standard $100nm$, to exaggerate the birefringent effect.

Quarter Waveplate

Extraction of the Pockels effect requires totally extinguishing the beam on the photodetector through its polarization, such that small disturbances to the polarization by the electro-optic effect can be easily picked up. To that end, the light should be made linearly polarized again by employing a quarter-waveplate (QWP) such that a subsequent polarizer can block it completely as shown in Figure 5.7. A quarter waveplate introduces a $\pi/2$ phase shift for light propagating along its fast compared to its slow axis, and can be used to create linearly polarized light from arbitrarily elliptically polarized light.

Glan-Taylor Prism (Analyzer)

A second Glan-Taylor prism polarizer is employed to completely extinguish the incoming linearly polarized beam. Unfortunately, the setting of the quarter waveplate and analyzer cannot be analytically calculated, meaning that they

need to be iteratively rotated to find the minimum in transmitted power.

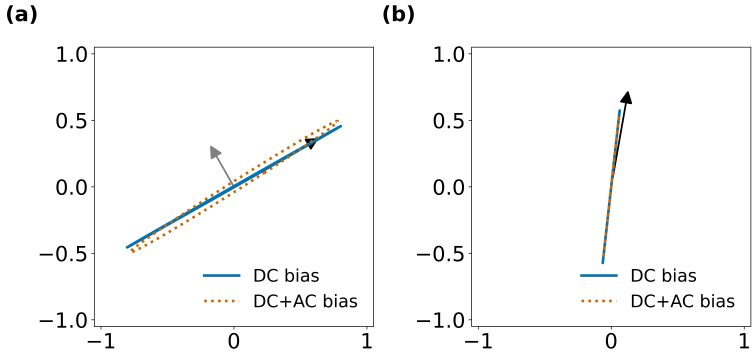

Figure 5.8: a) The effect of a QWP on the polarization from Figure 5.6. The fast and slow axis of the QWP are indicated by a black and gray arrow respectively. b) The effect of a polarizer on the polarized beam from a) which corresponds with the power incident on the photodiode. The black indicates the axis along which the polarized light can pass.

5.2.2 Measurement Operation

During a measurement, the sample is probed with a range of incident polarizations which each require an iterative optimization of the QWP and analyzer to create linear polarization. This optimization is performed while the *BTO* sample is under constant DC bias such that antiparallel domains align and a net optical effect is present. Afterwards, a small AC bias at $17.3kHz$ is applied on top of the present DC bias such that only negligible impact is had on the domain orientation. The analyzer is then stepped over a 180° range and the SMU and lock-in are read out to acquire the DC and AC photodiode power. The AC bias is subsequently shut off, a new incident polarization is set by rotating the half-waveplate (HWP) and the optimization iteration is started again.

Crucially, the *BTO* orientation, measurement geometry and electrode orientation have a significant impact on the signal measured by the photodiode. Due to the patterned electrodes, electric fields can only be applied in the plane of the substrate which corresponds to E_x (along [100]) and E_y (along [010]) in the equations from the previous section which have been adjusted to have the optical fields and electrical fields in the same coordinate system. Consequently,

the polarization vector can only be flipped in a- and b-oriented domains since E_z (along [001]) fields are needed to achieve this in c-oriented BTO. BTO thin films typically have a percentage of both orientations, such that prior screening by x-ray diffraction is employed to reveal the most interesting material for a more elaborate study. Next to that, the electrode pair orientation to the crystal axes determines the fraction of addressed BTO domains as shown in Section 5.2.5. In case of scrambled BTO domains, an electric field along the [100] or [010] direction can only align half of the domains and a lower Pockels signal is consequently measured. Employing electrodes rotated 45° to these axes probes all domains and yields a stronger signal.

5.2.3 Sample Preparation

Metallic electrode pads were patterned onto 2.6cm by 2.6cm dies of BTO thin film by a standard metal lift off in the lab shown in Figure 5.8. This process consists of deposition of both lift-off and patterning resist, UV exposure, development, metal deposition and metal lift-off. First, $LOR1A$ is deposited as lift-off resist on the thin film by spincoating (2000rpm - 30s) after which the sample is baked at 190°C for 5minutes. Immediately afterwards, an $IX845G$ layer is spin coated (4000rpm - 30s) and baked at 120°C for 1 minute.

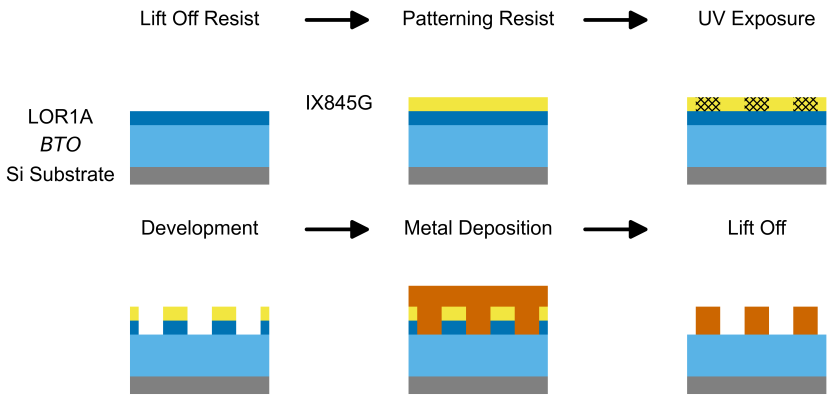

Figure 5.9: Schematic of the metal lift-off procedure employed to pattern metallic electrodes on BTO thin films.

A metal lift-off mask having various electrode sizes and orientations was created and used to expose the resist stack in a Karl Suss MA6 mask aligner at 405nm. Samples were then developed using OPD 5262 for 1 minute under constant agitation, after which they were rinsed in water and dried using an N_2 gun. Aluminium ranging between 100 or 200 nm was deposited on top using physical vapour deposition in a Nimbus 310 from Nexx Sytems. Finally, the lift-off was performed by submerging the samples in Microstrip 2001 heated to $80°C$ for 1 hour. Short exposure to ultrasound near the end was used to speed up the process.

5.2.4 Fitting Procedure

During measurement the analyzer is stepwise rotated while the photodiode signal is read by a source measure unit (SMU) and lock-in amplifier. The behaviour of the signal is largely determined by the employed polarizers and the birefringence of the BTO sample. Therefore, both the power on the SMU (P_{SMU}) and the power perturbation measured by the lock-in ($P_{lock-in}$) follow a squared cosine as found in Figure 5.9. The SMU voltage can thus be fitted by:

$$P_{SMU}(\theta) = A_1 \cos(\theta - \phi)^2 + B_1 \tag{5.26}$$

Here, θ is the rotation angle of the analyzer, A_1 is the amplitude of the signal, ϕ is a phase offset and B_1 is background power. The lock-in signal can be viewed as a disturbance on the SMU voltage readout, as such it can be fit by the difference between two squared cosines of which one is offset by a phaseterm to introduce the Pockels modulation. An equation to fit this can be found from the definition of a derivative applied to eq. 5.26 where δ is linked to an infinitesimal change in orientation of the xy-plane index ellipse influencing the polarization.

$$\frac{dP}{d\theta} = \frac{P(\theta) - P(\theta - \delta)}{\delta} \tag{5.27}$$

Which can be rewritten to give the change in power:

$$\Delta P = P(\theta) - P(\theta - \delta) = \delta \frac{dP}{d\theta} \tag{5.28}$$

The lock-in signal can thus be fitted by:

$$\Delta P = P_{lock-in}(\theta) = A_2(\cos(\theta - \phi - \delta)^2 - \cos(\theta - \phi)^2) + B_2 \tag{5.29}$$

Here, A_2 represents the amplitude of the perturbation and B_2 represents its background. Both signals were used together to fit the strength of the Pockels effect. By dividing eq. 5.29 by eq. 5.26 an equation solely dependant on δ is found. Hence the employed fitting function is:

$$f_{fit}(\theta) = \frac{\Delta P}{P} = \frac{A_1(\cos(\theta - \phi - \delta)2 - \cos(\theta)^2) + B_2}{A_1 \cos(\theta - \phi)^2 + B_1} \tag{5.30}$$

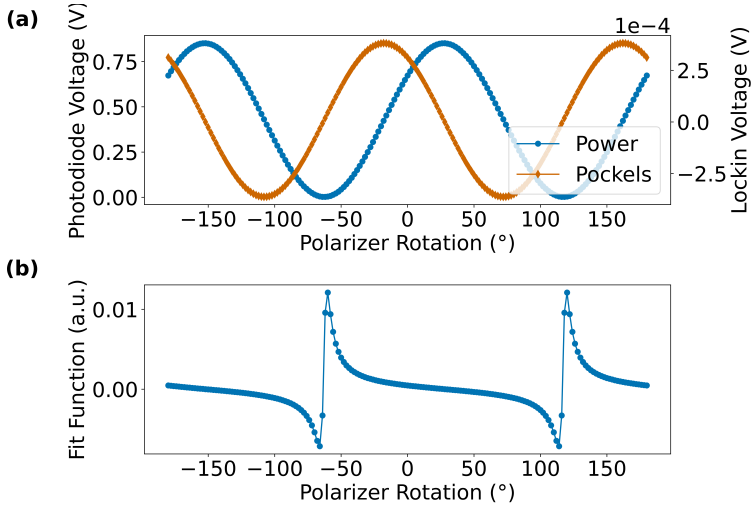

Figure 5.10: a) Simulated SMU and lock-in readout using Jones calculus of a 100nm *BTO* thin film in a de Sénarmont compensator. b) The fitting function used to extract data from a).

Once δ is extracted from measurement data the Pockels coefficient can be found by substituting the refractive index difference due to the Pockels effect into the phase retardation of a birefringent material. For this first equation the eigenvalues of the impermeability tensor need to be found, after which the index modulation for both the x and y component can be treated separately. For a c-oriented *BTO* crystal this would result in:

$$\frac{1}{n_{x,y}^2} = \frac{1}{n_o^2} + r_{13}E_{x,y} \tag{5.31}$$

By extracting $n_{x,y}$ and applying the a Maclaurin expansion, the following is found:

$$\frac{1}{\sqrt{a+x}} = \sqrt{\frac{1}{a}} - \frac{1}{2}(\frac{1}{a})^{3/2}x + \dots \tag{5.32}$$

$$n_{x,y} = n_o - \frac{1}{2}n_o^3 r_{13}E_{x,y} \tag{5.33}$$

The birefringence in the xy plane can thus be written as:

$$\Delta n = -rn_0^3 E_{AC} \tag{5.34}$$

For the retardance of a birefringent crystal is known that:

$$\delta = \frac{2\pi\Delta n d}{\lambda_0} \tag{5.35}$$

Here, Δn is the birefringence, r is the Pockels coefficient, n_0 is the unmodulated refractive index, E_{AC} the applied AC electric field, d is the thickness and λ_0 is the free space wavelength. Combined these yield:

$$r = \frac{2\delta\lambda_0}{\pi d n_0^3 E_{AC} v} \tag{5.36}$$

An additional parameter v is added here to account for the number of BTO domains that align with the electric field which depends on the employed electrode orientation compared to the crystal axes. This value fluctuates between 0.5 and 1 with the extremes corresponding to an electrode pair that enables only half or all domains respectively. Electrode orientations in between similarly lead to intermediate v values. The Pockels coefficients in the extreme cases are typically referred to as r_c when only half the domains contribute and r_{eff} when all domains contribute. These represent the combined effect or contributions by r_{13}, r_{33} and r_{42}. Unfortunately, extracting each separate coefficient requires simulating the crystal modulation and making assumptions about the relation between r_{13} and r_{33} which are addressed by the same electric field component. Finally, it must be noted that the film thickness d is a crucial

parameter in correctly extracting the Pockels coefficients. Looking at eq. 5.36 the Pockels coefficient is inversely related to the layer thickness. In this thesis, both ellipsometry and cross-sectional SEM were used to get accurate values. In doing so, the employed thickness values should only have minimal deviation ($\pm 5\%$) from reality.

5.2.5 Simulations

The framework of Jones calculus employed above to assess the effect of each optical component can similarly be used to simulate various types of *BTO* crystals. Here, the properties of a and c-oriented crystals as well as mixtures of the two under various degree of poling are investigated. First, pure a and c-oriented crystals will be presented. Afterwards, the mixture of both will be addressed. Finally, the fraction of poled domains will be highlighted.

Purely c- and a- oriented BTO

The birefringent effect on the incident polarization is calculated from the perturbation inflicted on the impermeability tensor by applied electric fields through Eq. 5.18. However, this general notation represents c^+-oriented *BTO* and thus requires a tensor rotation to represent any other domain type. In case of a^+ and b^+-oriented domains, a 90° rotation respectively around the y-axis and x-axis is required. A further 180° rotation around the z-axis can be used to find the impermeability tensor for a^- and b^--oriented domains. Moving forward, domains having aligned extraordinary axes will be referred to as parallel whereas their counterparts will be referred to as anti-parallel domains. For each of the six possible domain orientations, a simulation of the Pockels effect is performed with the electric field applied at 45° to the [100] *BTO* crystal axis. The electro-optic coefficients were assumed to be $r_{13} = 19.5pm/V$, $r_{33} = 97pm/V$ and $r_{42} = 1640pm/V$. [380] To better mimic real performance, the E_x and E_y fields for anti-parallel domains were given an opposite sign as these crystals perceive the field from the opposite direction. In each simulation, the xy plane of the index ellipsoid is extract and employed to calculate the thin film optical retardance and its orientation. The created modulation of the incident light was then treated identically as in a measurement and used to extracted the r_{eff} value for all crystals shown in Fig 5.11 a). The expected effective pockels coefficient was calculated using eq. 5.36 with v assumed to be 1 as only a single domain is considered. Next to that, the electrode gap is $10\mu m$, the DC Voltage is $45V$, the AC voltage is $3V_{pp}$, the refractive index is assumed

to be $(n_o, n_e) = (2.268, 2.297)$, the BTO film has a thickness of $100nm$ and the operating wavelength is $1550nm$.

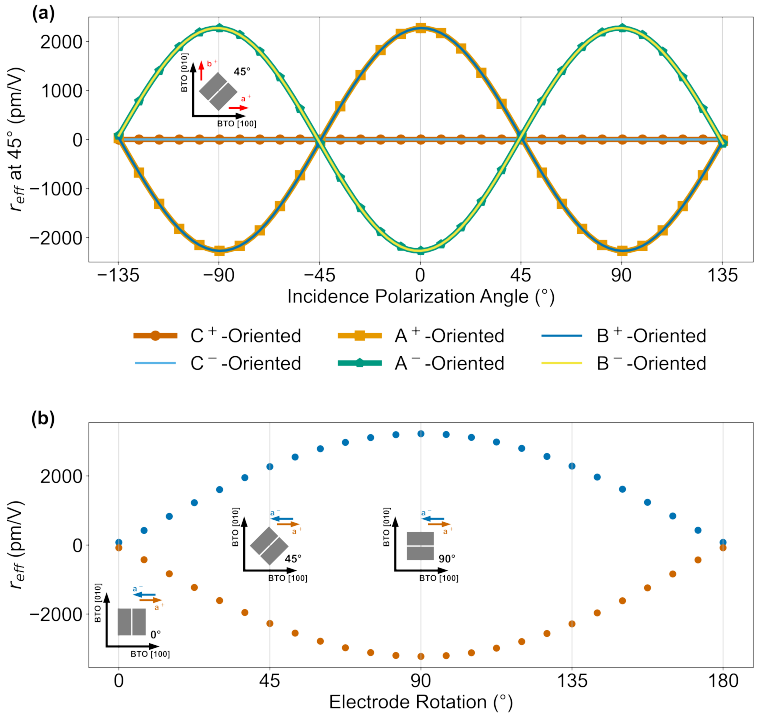

Figure 5.11: a) Electro-optic response for all 6 types of BTO orientation for varying incident polarization. b) The electro-optic response of a^+ and a^- oriented BTO when the electro rotation angle to the BTO [010] axis is varied. The incident polarization is fixed at 0°.

The simulations reveal that c-oriented BTO is not modulated by E_x and E_y fields in the xy plane, as could also be seen from eq. 5.19. As such, it does not affect incident light in a de Sénarmont compensator setup with the sample mounted perpendicularly to the beam. All types of a and b-oriented BTO on the other hand show a strong response. Anti-parallel domains are found to behave oppositely, which should not surprise given that they are addressed by fields with a different sign. Luckily, domains in a real device can be poled in a parallel state through the application of an offset electric field. Afterwards, a similar simulation was performed on two anti-parallel domains (a^+ and a^-) for varying electrode rotation to the BTO [010] crystal axis. The maximal

electro-optic response (δ) occurs at 0° incident polarization and is shown in Fig. 5.11 b). Again, the effective pockels coefficient was calculated using similar values as in Fig. 5.11 a). These simulations indicate that both a-oriented domain types contribute maximally when fields are applied perpendicularly to their polarization vector ($\vec{P}$ along [100]). Here, the field maximally addresses the off-diagonal r_{42} component which causes a significant rotation of the index ellipsoid. Conversely, electric fields aligning with the polarization vector only modulate the refractive index through the much weaker diagonal components of the tensor. Evidently, a comparatively weak but non-zero electro-optic response is encountered here. It should however be noted that *BTO* in reality forms a patchwork of both a and b-oriented ferroelectric domains to relieve stress. As such, the behaviour in Fig. 5.11 b) is unlikely to be encountered in a thin film.

Scrambled BTO

Expanding on the previous section, a more realistic *BTO* thin film was simulated by taking into account both a and b oriented domains. Again, the electrode rotation angle to the *BTO* [010] crystal axis was varied. The concentration of a^+, a^-, b^+, and b^- domains was assumed to be equal. The polarization change caused by each type of domain was calculated separately after which their Jones vectors were averaged. Similar to Fig. 5.11, the power variation due to the pockels effect was divided by the power and fitted with eq. 5.30. The acquired δ was again used to calculate the effective pockels coefficient (r_{eff}). Crucially, the influence of the coercive field was included through a threshold ($E_C = 5 \times 10^5 V/m$) which leads to a further averaging over two antiparallel domain contributions at low DC electric fields. Conversely, the contribution of a single domain is calculated at sufficiently high fields ($E_{dc} > E_C$) as antiparallel domains align themselves here. Figure 5.12 shows the fitted values for several applied DC biases. Here, all values were calculated assuming v in eq. 5.36 is equal to 1 since this shows the effect of the coercive field more clearly. By assuming that all domains contribute, the reported r_{eff} resembles real behaviour better since smaller v values artificially inflate the electro-optic response. A real device would never reach these reported values as the behaviour of the entire film is extrapolated from a fraction. That said, if the actual domain contributions are known, the acquired value can be used to assess the quality of the film and reveal the extent defects and domain misalignment reduce the electro-optic response.

The simulations indicate that unpoled *BTO* films show no net electro-optic response since all domains, if present at identical amounts, cancel out each

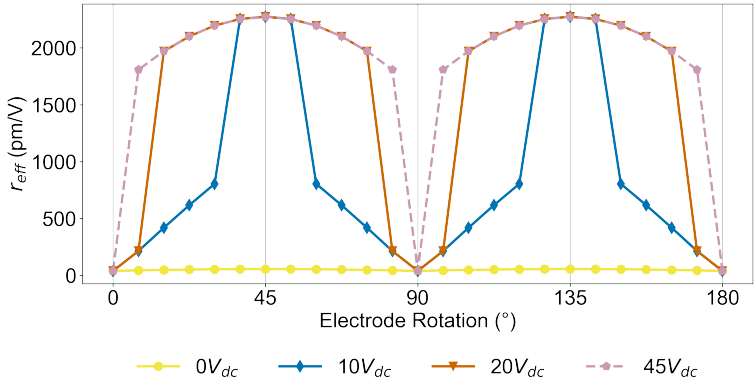

Figure 5.12: The electro-optic response of a *BTO* film containing all types of a and b oriented domains for various applied DC electric fields. The influence of the coercive field shows as a cut-off point after which a significant drop in the effective electro-optic response is encountered.

other. For all other films, a strong electro-optic response corresponding with a net positive contribution from all domains is encountered. This is due to a and b domains aligning since the applied electric field exceeds the coercive field. Evidently, larger applied voltages result in a larger span of electrode rotation angles at which the full film contributes electro-optically. The electro-optic response of a fully poled film only varies slightly with the electrode rotation angle. For example, the film poled at $45V$ at 7.5° shows 79.58% of the effect at 45° . The simulations thus indicate a strong tolerance to misalignment of the electrodes with the *BTO* [010] axis.

Unbalanced A-oriented BTO

A further distinction can now be made investigating the effect of *BTO* films having an unequal fraction of a- and b-oriented domains. Such behaviour might occur when a preferred growth direction was present during fabrication. Similarly, various poling schemes possibly at higher temperature might cause domain migration and/or growth leading to unequal domain fractions. To that end, Fig. 5.13 shows the electro-optic response when varying the amount of b-oriented *BTO* from 10% to 50% with a domains making up the remainder. A DC bias of $20V$ was applied, all other parameters were left identical to earlier simulations.

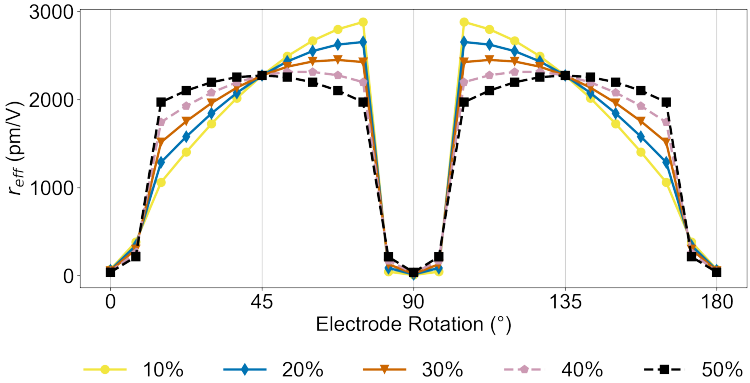

Figure 5.13: The electro-optic response of a *BTO* film containing an unequal fraction of a- and b-oriented *BTO* domains.

The electro-optic response is found to increase when the electric field aligns perpendicularly to the extraordinary axis of the largest fraction. In doing so, the maximal response is no longer encountered at 45° to the *BTO* [001] axis but at larger values. A film containing more b-oriented than a-oriented domains similarly leads to a maximum at lower rotation angles. As such, an unbalanced film has a distinct behaviour with which it can be recognized.

Partially Poled and Mixed BTO

Finally, two additional types of *BTO* films will be considered. First, a partially poled film in which only a subset of domains is poled into a parallel state. The remaining volume of the film stays in its scrambled as-grown state. Next to that, a mixed *BTO* film that contains both a, b and c-oriented domains which can occur during growth when conditions are suboptimal. For both, a portion of the film was considered unpoled or c-oriented and its Jones vector was included in the average of all domain contributions. Again, a DC bias of $20V$ was assumed while the contributing portion of the film was swept.

Both film types result in a nearly identical electro-optic (EO) response in which part of the film is not contributing constructively. Indeed, for partially poled films a fraction of the film remains antiparallel resulting in the opposite optical behaviour. No signal can consequently be measured. A mixed film contains a fraction of c-oriented *BTO* of which the xy plane of the index ellipsoid is

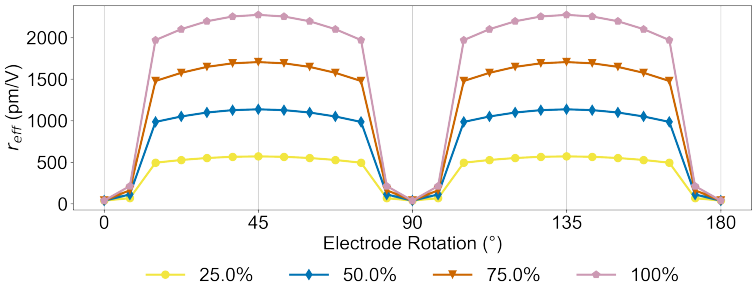

Figure 5.14: The electro-optic response of a partially poled a-oriented or mixed phase *BTO* film.

not modulated by the applied electric fields. Simulating the effective pockels coefficient is thus identical except at electrode rotation angle 0° and 90° where the c-oriented film is not modulated and the partially poled film is weakly modulated. Given that this effect is very minor, Fig. 5.14 only shows a partially poled film.

5.2.6 Results

Electrical Measurements

The presented Pockels measurement probes a complex system in which ferroelectric domains, electric fields, piezoelectric behaviour and current leakage interplay with each other. Unfortunately, the de Sénarmont compensator only assesses one part (the Pockels effect) of a vastly more complex system. To achieve a more complete understanding of all parameters at hand, the current voltage (IV) characteristic before and after prolonged DC bias were measured as this allows for a deeper insight into the ferroelectric domain behaviour. Both the ferroelectric domain size and their orientation are coupled to the current-voltage behaviour since current mainly occurs along domain boundaries. *BTO* layers containing small and scrambled domains typically permit larger currents to pass. Conversely, *BTO* layers with larger well-aligned domains present low leakage currents. The latter is obviously preferred both during a Pockels measurement and in the envisioned holographic display since the present electrons due to a higher leakage have an adverse effect on the desired optical behaviour and would result in inefficient power usage.

Initial IV measurements revealed leakage currents high enough to cause noticeable Joule heating which should be avoided completely. After a high enough temperature increase, the perovskite will undergo a phase change at its Curie temperature ($T_C \approx 120°C$). [386] Here, BTO assumes a cubic crystal lattice instead of the tetragonal one present at room temperature. This is a centrosymmetric lattice, meaning that no non-linear effects are present. MBE grown BTO often has an oxygen deficiency which can increase conductivity through oxygen vacancies. To improve the stoichiometry a post deposition anneal at $800°C$ for 1 hour under a constant O_2 flow was attempted. The IV characteristic of an as-deposited and post-deposition annealed sample is shown in Fig. 5.15 a) and indicates that the anneal drastically reduces the leakage current. The same measurement was performed on a BTO layer transferred on a thick thermal oxide (SiO_2 - $2.5\mu m$) to exclude that oxidation of the carrier wafer dictated the observed effect. The layer transfer was performed with a $200mm$ wafer, through subsequent oxide-oxide bonding, carrier wafer thinning through grinding and a finally a selective etch. Here, an identical behaviour as in Fig. 5.15 a) was found with an even lower current after anneal. Consequently, the observed drop in leakage is attributed to an improvement of the BTO stoichiometry. Interestingly, the IV has different behaviour for the forward and reverse part of the sweep, which seems to coincide with resistive switching linked to oxygen vacancies (V_O) and the ferroelectric polarization that are commonly found in BTO [387, 388, 389, 390]

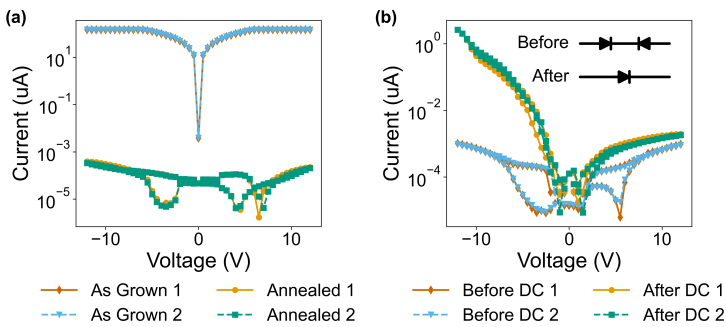

Figure 5.15: a) Current-voltage characteristic comparison between as-deposited and post-annealed BTO samples, the large decrease in leakage is attributed to improved stoichiometry. b) Current-voltage characteristics comparison between a fresh electrode pair and an electrode pair that has been used to perform an electro-optic measurement which stresses the BTO by a prolonged DC bias

Comparing the current-voltage characteristic of *BTO* films before and after a typical Pockels measurement i.e. several hours at high DC bias, shows a large increase in the observed leakage current at negative voltages. Higher leakage might typically be explained through the presence of smaller domains which result in higher conductivity due to more domain boundaries being present. However, a diode like rectifying behaviour with a more than two order of magnitude difference in current is also observed. This can have several origins. Firstly, electrical degradation is known to occur in perovskite titanates due to a variety of reasons including crystal defects (Schottky and point defects), oxygen vacancies, grain size and impurities. [390] The equivalent circuit right after probe landing would be two Schottky barriers (likely at the *BTO*-Si interface due to the mobility of oxygen vacancies) connected back to back resulting in only a small leakage current. After a prolonged exposure to relatively high DC voltages however, a diode like current is observed indicating that the reverse biased Schottky barrier has broken down and became an ohmic contact. The equivalent circuit thus changes to a diode and resistor in series. Oxide perovskites are known for oxygen migration under external bias which can lead to interface modulation. At the anode there would be vacancy depletion at the Ti-*BTO* interface and accumulation at the *BTO*-Si interface. Both of these change the energy levels but do not seem to drastically change the behaviour at each interface. The opposite occurs at the cathode. Here, the depletion at the *BTO*-Si interface can become ohmic given that the modulation of the energy level is large enough.

Alternatively, the observed effect can originate from damage to the layer stack caused by electrical stress or mechanical pressure applied by the probes. It is known that suddenly applying a large electric field to a ferroelectric material can cause it to crack due to ferroelectric domain re-alignment. To test whether this can damage the layer, fresh electrode pairs were contacted and subjected to the typical Pockels measurement bias for 15 minutes. Clear irreversible degradation of the layer stack has taken place as shown in Fig. 5.16 a), although it does not show identical behaviour to samples that were subjected to hours of DC bias. This again hints at effects occurring on a longer time-scale such as oxygen migration. Finally, since the stack only contains thin films, damage due to mishandling of the electrical probes is plausible. This was tested by applying excessive pressure with the probes to a fresh pair of electrodes, after which they were lifted and landed normally. Fig. 5.16 b) shows that mishandling the electrical probes also manages to irreversibly damage the electrical behaviour of the sample. That said, the observed IV behaviour does not show the Schottky behaviour observed after typical measurements.

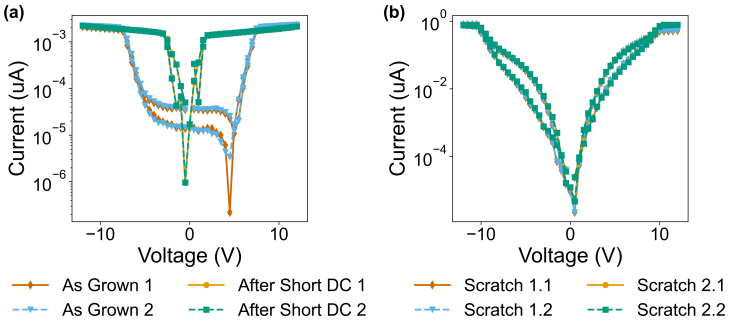

Figure 5.16: a) Current-voltage characteristic comparison between as-grown *BTO* samples exposed to a large but brief electric field. The observed leakage current reaches the same plateau but reaches this sooner indicating electrical degradation of the layer. b) Current-voltage characteristic of two electrode pairs that were first scratched by the electrical probes at a different location. Damage to the thin film is stack is apparent and leads a current increase of several orders of magnitude.

Electro-Optical Measurements

Electro-Optic response at various DC The electrical measurements above show clear degradation of the *BTO* layer after a prolonged exposure to a DC bias which results in larger leakage currents. To gain insight in the degradation threshold a pair of fresh electrodes was connected to and a series of Pockels measurements were performed with increasing DC bias in steps of $6V$. Before and after each measurement, an IV sweep was performed. At low DC bias, the electro-optic response shows poor characteristics likely indicating poor domain alignment. At the same time, the device maintains its back to back diode like leakage current. After high enough sustained DC bias ($12V$) the electro-optic response changes due to ferroelectric domain alignment leading to a stronger net contribution. Similarly, the threshold of $12V_{dc}$ marks a clear change in the IV characteristic, in which the rectifying behaviour of a diode is now observed meaning that one of both Schottky barriers has broken down. This effect appears permanent as measurements days after removing DC exposure still show the rectifying behaviour. During these measurements, an AC bias of 18V was applied.

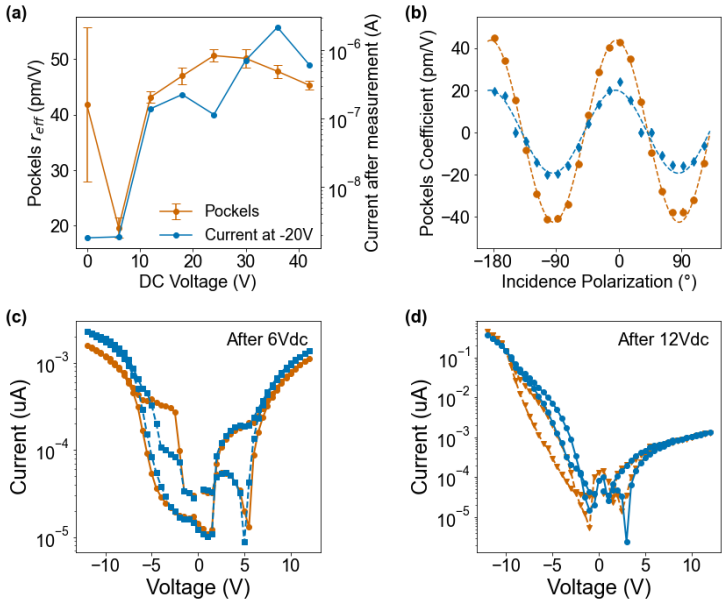

Figure 5.17: a) Measured effective Pockels coefficient at various applied DC bias. b) Measured Pockels coefficient at $6V$ and $12V$. c) IV characteristic of a device before and after a prolonged exposure to $6V$. d) IV characteristic of a device before and after a prolonged exposure to $12V$.

Ferroelectric Domain Poling Sequence Electrical breakdown observed after prolonged DC exposure indicates the *BTO* layer sustains damage. This does not come as surprise as bulk ferroelectric crystals are known to break when exposed to sudden strong electric fields. This can be prevented by applying the electric field in incremental steps which gives the ferroelectric domains time to reorient themselves. As such, various ferroelectric domain poling sequences were attempted prior to the standard electro-optic measurement including gradual DC ramping, intermittent poling and AC poling (bipolar and unipolar). Again, the IV characteristics were recorded before and after each measurement to investigate possible breakdown.

The standard poling approach commonly found in literature applies a strong DC electric field prior to a measurement and possibly lowers it afterwards. To that end, a constant DC field (4×10^6) corresponding to $40V_{dc}$ applied over an electrode gap of $10\mu m$ is assumed as benchmark for various poling

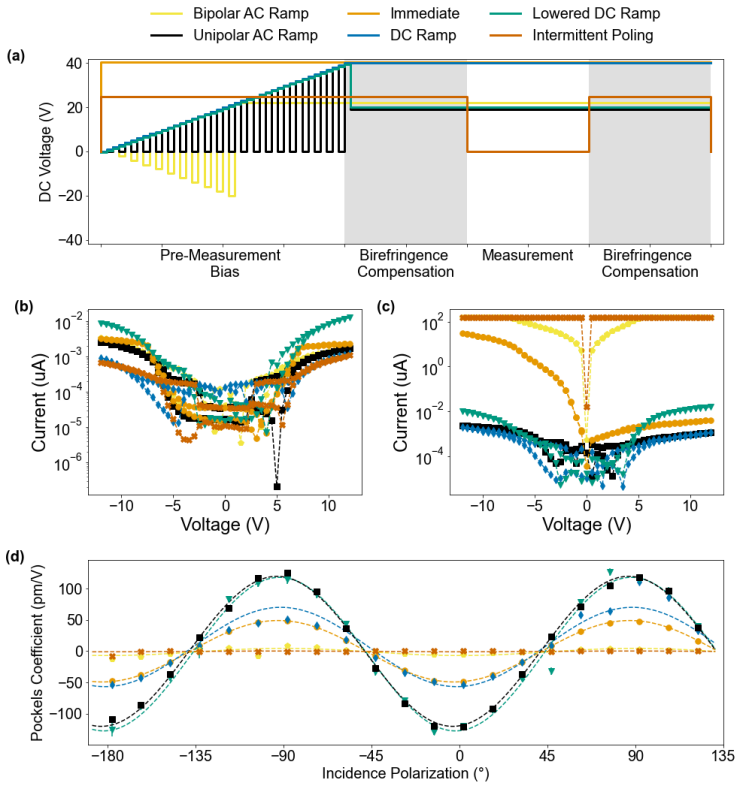

Figure 5.18: a) Schematic of the voltage applied during various ferroelectric poling sequences. b) IV characteristic for the devices shown in d) prior to the Pockels effect measurement. c) IV characteristics of the device in d) after the Pockels effect measurement. d) The electro-optic coefficient reff for various incident polarizations measured after the poling sequences from (a).

sequences applied on a MBE sample. An r_{eff} value of $49.1 \pm 0.3 pm/V$ was found, where the uncertainty is calculated from the covariance of a $sine^2$ fit on the measured Pockels response. IV measurements confirm the sample has degraded electrically, showing the rectifying behaviour at negative voltages discussed prior.

In a first alternative poling attempt, the DC bias was applied intermittently only during the iterative optimization at each incident polarization. The DC bias was set to $25V_{dc}$ as this was found to be the DC voltage showing the strongest electro-optic response with a good fit in Fig. 5.14. However, intermittent

poling does not improve the electro-optic response ($0.6 \pm 1.1pm/V$) nor does it prevent electrical breakdown of the BTO. In fact, the electro-optic response was nearly zero other than at the first data point indicating that the ferroelectric domains completely lost their poled orientation and returned to a scrambled state during each extended period at zero bias. Electrically the BTO appears to have completely degraded, even more than during the standard poling sequence. This is possibly caused by the repeated immediate onset of the DC voltage.

Afterwards, a bipolar AC ramp ($1Hz$) was applied which gradually ramped up to 24V , constantly switching between negative and positive applied fields. Larger voltages were avoided as they led to large leakage currents and accompanying Joule heating. Again, a weak electro-optic response ($r_{eff} = 6 \pm 2pm/V$) was observed. Electrically, the device seems to have completely broken down as it does not show the rectifying behaviour of the benchmark but instead shows a very small resistance. It is likely that the constant switching between negative and positive fields led to more severe degradation than the benchmark measurement in which a large DC field is only applied once. To prevent this behaviour both a unipolar AC ramp and a DC ramp were attempted.

In case of the DC ramp, the voltage was gradually ramped up to $40V_{dc}$ in steps of $1V$ at $0.1Hz$. Afterwards, the voltage was kept at its maximal value for the duration of the measurement. A strong electro-optic response of $63 \pm 9pm/V$ compared to the benchmark was found. Interestingly, this was paired with a large fitting uncertainty as a larger response was observed at positive incident polarizations compared to negative polarizations. The IV characteristic of the device once again indicates a rectifying behaviour at negative voltages. It is plausible that the sustained large electric field further improved the fraction of poled domains contributing. Simultaneously, the device has shown to degrade electrically indicating that the electrical properties can be disconnected from its electro-optic properties. This is plausible as the electrical degradation likely occurs directly below the electrodes whereas the electro-optic response comes from the gap between electrodes.

During the unipolar AC poling sequence the field was ramped similarly to $40V_{dc}$ with a period of $10s$ in which half is biased and the other half grounded. Afterwards, the bias was lowered to 20V. Here, lowering the steady-state voltage was considered in an attempt to further minimize the electrical stress on the device. An remarkable electro-optic response of ($120 \pm 4pm/V$) was found, nearly doubling the electro-optic response attained with the poling sequence from literature.

Finally, a poling sequence based on the DC ramp was applied. Here, instead of keeping the maximal electric field present during the measurement, the field was similarly lowered to half of the maximal value. This poling sequence similarly nearly doubled the electro-optic response ($123 \pm 8pm/V$) of the BTO film. Crucially, the IV characteristic of the device appears nearly identical before and after the measurement.

Further measurements on several dies of the same wafer were performed using the DC ramp poling sequence, which on average showed a response of $111.6pm/V$ shown in Fig. 5.19. The measurements all fall within $96pm/V$ and $132pm/V$. This spread is likely caused by slightly varying crystal properties such as crystal defects and ferroelectric domain fraction influence linked to the device location.

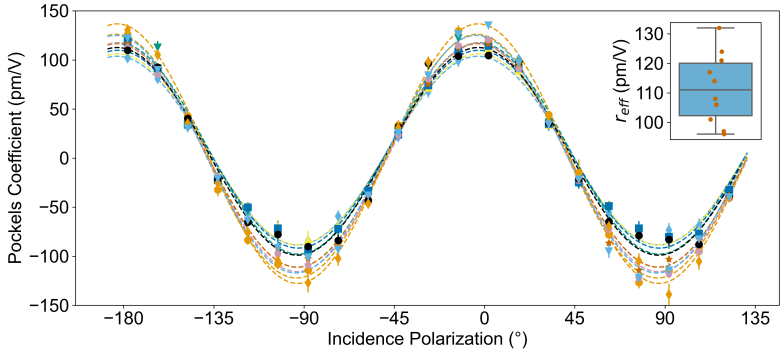

Figure 5.19: Repeated measurement of r_{eff} on the same sample with the optimized domain poling approach.

Orientation Dependence Having established an improved ferroelectric poling approach, the electro-optic response at various electrode orientations to the [100] crystal axis was measured. The designed metal mask contains electrodes at every 7.5° between 0 and 90. Section 5.2.5 details the expectations for such a measurement. For each measurement, the r value was calculated from the fitted δ assuming that the volume fraction of contributing domains is 1, except at electrode oriented at 0° and 90° where the electro-optic coefficient is also referred to as r_c. Consequently, the average r_c value factoring in the data from 0° and 90° is $17.5pm/V$, conversely the coefficient at 45° is $r_{reff} = 119pm/V$.

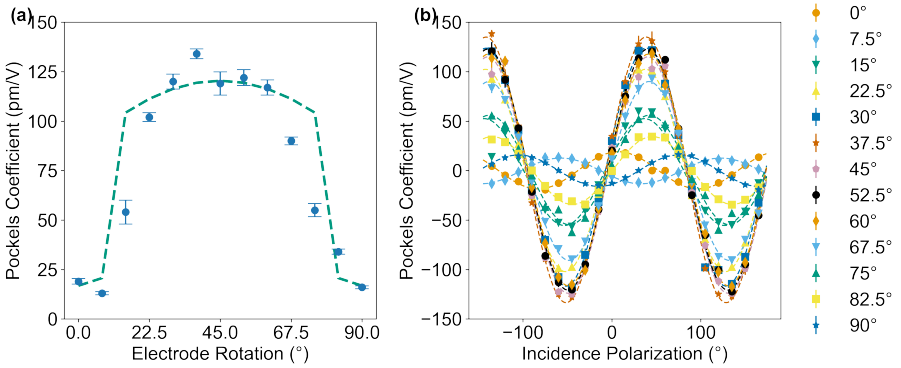

Figure 5.20: a) Extracted electro-optic coefficient at various electrode orientations. Jones calculus was used to simulate the ideal electro-optic response using the disentangled coefficients. b) The electro-optic response for varying incident polarization.

Disentangled Coefficients The electro-optic birefringence modulation in the employed transmission geometry originates from a combination of electro-optic coefficients. The contributing coefficients depend on the electrode rotation to the [100] crystal axis and the crystal orientation. As highlighted before, only a- and b-oriented films can be assessed in the employed de Sénarmont compensator setup. Two cases should be considered. First, for electrodes oriented at 0° and 90° to the [100] crystal axis. Here, the applied electric fields only engages the diagonal tensor elements which contains r_{13} and r_{33}. Secondly, all intermediate electrode angles lead to modulation off the off-diagonal tensor elements meaning that all coefficients contribute namely r_{13}, r_{33} and r_{42}. It is difficult to determine the exact fraction of contributing domains due to uncertainty in the domain structure and coercive field. As such, the volume fraction v is assumed to be 1 for all of these. Extracting the individual components is challenging since they are strongly interlinked due to the fields that enable them.

To best disentangle the coefficients, first r_c is calculated since it only includes the effect of r_{13} and r_{33}. Following a similar approach to Section 5.2.4, applied to an a-oriented BTO crystal the modulation of the refractive index in the xy-plane is given by:

$$n_x = n_e - \frac{1}{2} n_e^3 r_{33} E_x \tag{5.37}$$

$$n_y = n_o - \frac{1}{2} n_o^3 r_{13} E_x \tag{5.38}$$

The birefringence can then be calculated:

$$\Delta n = n_x - n_y = n_e - \frac{1}{2} n_e^3 r_{33} E_x - n_o + \frac{1}{2} n_o^3 r_{13} E_x \tag{5.39}$$

Setting the terms modulated by an electric field equal to $-\frac{1}{2} n_0^3 r_c E$, can be used to extract r_c

$$\frac{1}{2} n_0^3 r_c E = \frac{1}{2} n_e^3 r_{33} E - \frac{1}{2} n_o^3 r_{13} E \tag{5.40}$$

Which means that r_c is equal to:

$$r_c = (\frac{n_e}{n_o})^3 r_{33} - r_{13} \tag{5.41}$$

Finally, r_{13} and r_{33} can be extracted by assuming a relative fraction of 10 between them ($r_{13} \approx 8$ and $r_{33} \approx 80$ at $1550nm$ in bulk crystals). [391] For $r_c = 17.5pm/V$ this results in $r_{13} = 1.9pm/V$ and $r_{33} = 18.6pm/V$. Now, r_{42} can be extracted using the Jones calculus formalism employed above. To that end, the calculated values of r_{13} and r_{33} were employed, while r_{42} was adjusted. The correct $r_{eff} = 119pm/V$ was found for $r_{42} = 88pm/V$. Figure 5.20 shows a simulated result employing the disentangled coefficients and a coercive field of $5 \times 10^5 V/m$. These values differ strongly from the ones presented earlier in equation 5.17 which can have several causes. For example, and x-ray diffraction measurement revealed that this *BTO* film had a c-oriented portion that does not contribute. Secondly, thin film *BTO* commonly does not reach the values of a bulk crystal which is thought to be linked to various crystal defects and present stress and strain influencing the movement of the central Titanium atom.

Various Growth Methods Although *BTO* grown by MBE is known to offer superior crystal characteristics, its growth is slow compared to other common deposition techniques. For this reason, MBE is often considered a limiting step in FAB compatible monolithic integration and other techniques are preferred. On top of that, MBE growth employs barium and titanium from separate solid sources while oxygen gas is pumped into the chamber which tends to react with the sources. This oxidation is a concern as it leads to difficult control of the

evaporation rate and hence off-stoichiometric inclusion of barium and titanium in the thin films which leads to worse electro-optical performance.

That said, various other deposition techniques exist such as pulsed laser deposition (PLD). During PLD growth a laser ablates a pure BTO target and deposits epitaxial BTO. The laser target consists of an a-oriented BTO crystal which is typically made by Czochralski method. Here, three such samples were grown using PLD at various laser pulse power and patterned for electro-optic measurement. The DC ramp poling giving the best results, was applied prior to electro-optic measurement. Again, a strong electro-optic response of $100pm/V$ was encountered. The best PLD sample is benchmarked against the champion MBE sample ($205pm/V$) in Fig. 5.21.

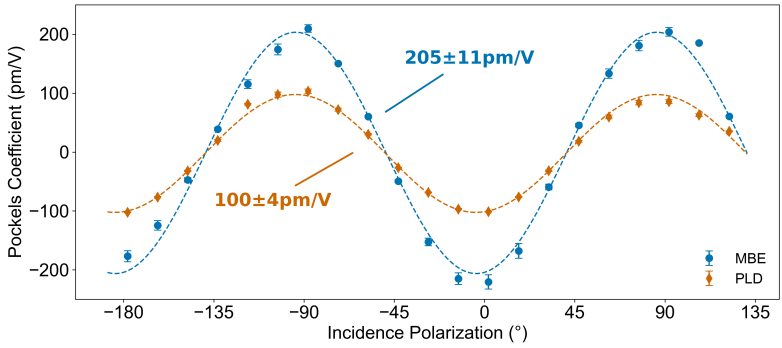

Figure 5.21: Extracted electro-optic coefficient r_{eff} of the best MBE and PLD thin films at various incident polarizations.

5.3 Conclusion

Electro-optic measurements through use of a de Sénarmont compensator transmission geometry have been presented. Simulations using Jones calculus indicate that the pockels effect in c-oriented BTO thin films cannot be observed. On the other hand, a strong electro-optic response is expected from a- and b-oriented thin films. As grown these ab-films form a domain patchwork which tend to align antiparallel to reduce stress, meaning that they require poling to constructively contribute to the birefringence. Simulations indicate that the strongest electro-optical signal from a film having a scrambled domain structure

can be found at 45° to the [100] crystal axis.

Electrically, the MBE material appears very lossy in its as-grown state but an additional high temperature anneal seems to resolve this. After exposure to a strong DC offset the electrical behaviour degrades which might be linked to crystal cracking, probe induced damage and oxygen vacancy migration. Especially, this last effect appears likely since resistive switching, which has previously been shown to be related to oxygen vacancies, has been been observed in IV measurements. The leakage currents fortunately remain small when electric fields are gradually ramped.

Electro-optic measurements reveal that the poling approach when first measuring a device is crucial to its optical response. Gradually increasing the applied electric field (DC) allows domains to align themselves with the applied field. As a consequence, a strongly increased electro-optical response was found when compared to alternative poling strategies and results in literature. The extracted electro-optic coefficients are equal to $r_{eff} = 119 \pm 6pm/V$ and $r_c = 17.5pm/V$. After employing the established Jones formalism the individual coefficients were found to be $r_{13} = 1.9pm/V$, $r_{33} = 18.6pm/V$ and $r_{42} = 88pm/V$. The champion MBE grown wafer showed a strong Pockels effect with r_{eff} equal to $205pm/V$, whereas the best PLD sample resulted in $100pm/V$.

Chapter 6

Wavefront shaping by a waveguide based holographic projector

After presenting both key components of the proposed holographic display this chapter expands its operation. To that end, further considerations for the materials are highlighted, after which simulations of fringing electric fields are used to create any custom refractive index modulation in the waveguide. A driving mechanism based on signal analysis is introduced that allows creation of any desired grating pattern. Finally, optical simulations of focusing gratings, point based holograms and phasemap holograms are performed.

This chapter is partially based on the following published articles, which were reproduced with permission:

Guillaume Croes, Nikolay Smolentsev, Tsang Hsuan Wang, Robert Gehlhaar, and Jan Genoe. Non-linear electro-optic modelling of a Barium Titanate grating coupler. In Mark A. Kahan, editor, *Optical Modeling and Performance Predictions XI*, volume 11484, page 11. SPIE, 8 2020

Guillaume Croes, Robert Gehlhaar, and Jan Genoe. Subwavelength Custom Wavefront Shaping by a Nonlinear Electro-optic Spatial Light Modulator. *ACS Photonics*, 11(2):529–536, 2 2024

6.1 Mode Coupling and Conversion

The envisioned holographic display aims to couple a guided mode to a well controlled radiation mode. This effect can be described by mode coupling theory which accounts for the shape of both modes and the present refractive index modulation. The coupling coefficient between two modes depends on whether transverse or longitudinal electric fields are present. In the case of a TE guided mode only transverse electric fields are present:

$$K^t_{v:q\rho} = \frac{\omega}{4}\int_{-\infty}^{\infty} \Delta\varepsilon_{tq}\overrightarrow{E_{tv}} \cdot \overrightarrow{E_{q\rho}} dz \tag{6.1}$$

Here, K^t is transverse coupling coefficient representing transverse electric fields and ε is the permittivity calculated in the previous chapter. Furthermore, a forward propagating bound mode along the z axis is assumed and denoted with ν. The continuous spectrum of radiation modes is indicated with ρ and q indicates if the modes are symmetric or antisymmetric. In general, this effect is referred to as mode coupling when the diagonal elements of ε aid in coupling, and is called mode conversion when the non-diagonal elements of ε provide coupling. In case of the envisioned BTO holographic display, mode conversion can be achieved by periodic electro-optic modulation the BTO waveguide as strong non diagonal elements are present.

In eq. 5.18 three electro-optic coefficients modulate the impermeability tensor of which r_{13} and r_{33} modulate the tensor diagonal and r_{42} modulates the off-diagonal elements. These coefficients have been reported to be equal to $r_{13} = 19.5pm/V$, $r_{33} = 97pm/V$ and $r_{42} = 1640pm/V$. [380] Ideally, the effect of r_{42} is leveraged, for which the impermeability tensor couples perpendicular electric fields to each other thus leading to the conversion of TE to TM modes and vice versa. We opt to have a TE guided mode that is converted to a TM radiation mode due to the applied grating of which the period determines the out coupling angle. Assuming the mode propagates along x, the TE guided mode only has an E_y component. Net to that, the TMradiation mode has both an E_x and E_z component. Using the wave vector of the employed modes, mode coupling occurs when the following condition applies:

$$\overrightarrow{\beta_r} = \overrightarrow{\beta_0} \pm \frac{2\pi n}{\Lambda} \qquad with\, n = 1, 2, 3, \ldots \tag{6.2}$$

Here, $\overrightarrow{\beta_r}$ is the wave vector of the radiation mode, $\overrightarrow{\beta_0}$ is the wave vector on the guided mode and $\overrightarrow{\Lambda}$ is the grating vector. Figure 6.1 shows a visual

representation of the wavevector space and the influence of an applied grating. In general, a waveguide grating can couple the guided mode to other guided modes, cladding modes and radiation modes. The number of guided and cladding modes is determined by layer thicknesses and their refractive index meaning that only specific $\overrightarrow{k_z} = \overrightarrow{k_0} - \overrightarrow{\beta_r}$ are allowed. Radiation modes on the other hand are unbound such that $\overrightarrow{k_z}$ can take any value. Depending on the chosen crystal orientation only certain elements of the permittivity matrix (i.e. the inverse of eq. 5.18) can couple the desired modal electric fields. In the coordinate system with mode propagation along the x-axis, a TE mode has $(0, E_y, 0)$ as field components while a TM mode has $(E_x, 0, E_z)$ components. Hence for good coupling ε_{yx} and ε_{yz} need to be strongly modulated.

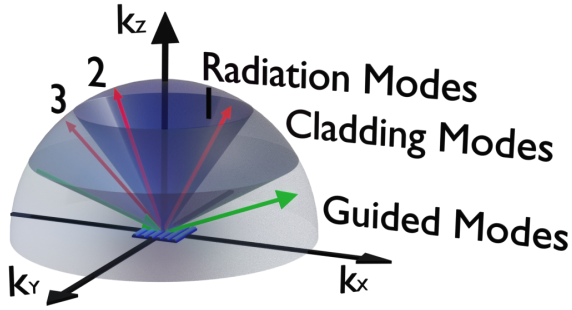

Figure 6.1: Mode coupling dynamics shown in the mode vector space. To illustrate the operation, a guided mode indicated in green is incident on a grating. Three modes are coupled to, which depending on the applied grating period and the waveguide structure can either lead to coupling to other guided modes, cladding or radiation modes. Image reproduced with permission. [342]

6.2 Electric Field Simulations

Finite element FE electric field simulations were performed using COMSOL Multiphysics® to assess all crystal orientations for compatibility with the ε_{yx} and ε_{yz} permittivity elements. [392] A simulation was set up with $500nm$ tall $IGZO$ pillars embedded in an equally tall block of Si_3N_4. Above, sections of $200nm$ and $500nm$ of BTO and air were respectively added. The simulated array size was chosen large enough so that the electric fields from the central pillar nearly vanished (1E6 : 1) within the simulation range such that no edge

effects are present in subsequent superpositions. To accelerate the simulation, two symmetry boundaries were employed along the center x and y axis. The acquired dataset could later be mirrored twice to create the full simulation area. The other boundaries were set as floating potential to prevent artificial clipping in case the simulation was not large enough.

The relative permittivity of c-oriented BTO was assumed to equal $\varepsilon_r = (3600, 3600, 150)$ and was rotated accordingly for the other crystal orientations. [386] The Si_3N_4 and air cladding were respectively given a relative permittivity of $\varepsilon_r = 7$ and $\varepsilon_r = 1$, the $IGZO$ pillars were excluded as they allow no fields inside due to their conductivity. To avoid dielectric breakthrough, the voltage difference between neighbouring pillars was limited to $0.1V$. The influence of both crystal orientations were assessed by simulating a large array of pillars where only the center pillar was biased, leaving the rest grounded.

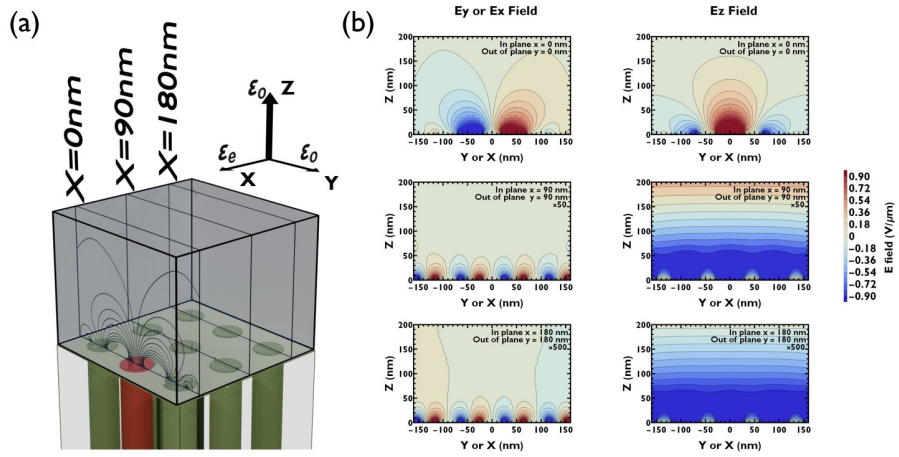

Figure 6.2: a) Schematic showing the pillar array used in the COMSOL FE simulations, red indicates the biased pillar. The planar slices above indicate the plotted area in b). b) Electric field data at the slices shown in a), for which E_y and E_x are shown in the same plot due to symmetry. Image reproduced with permission. [342]

C-oriented BTO

Figure 6.2 a) shows the small section of the performed simulations with the biased pillar indicated in red. The slices indicated in the waveguide above

represent the planes for which the c-oriented electric fields are plotted in Fig. 6.2 b). Both E_x and E_y fields are shown in the same graph since they are equivalent due to the crystal symmetry. Fields further removed from the biased electrode were magnified with values indicated in the plots, to show them on the same scale which illustrates their confined nature. The simulations indicate that c-oriented BTO does not allow electric fields to penetrate significantly, which is expected due to its large in-plane relative permittivity. Consequently, c-oriented BTO only offers modulation of the guided mode near the very bottom of the waveguide. The overlap between the modulation and modal field is thus relatively small making c-oriented BTO not an interesting material for a guided mode SLM.

A and B-oriented BTO

Identical simulations were performed for a- and b-oriented BTO. Here, the crystal orientation was rotated accordingly. A-oriented BTO allows modulation of ε_{yx}, while b-oriented crystals allow modulation of both ε_{yx} and ε_{yz} making them suited for the desired waveguide coupling. This discrepancy in the behaviour or a- and b-oriented films can be explained through equations 5.21 and 5.24. These reveal that the 90° rotation existing between the two domain types creates different impermeability tensors, yielding different contributions. In case both contributions are desired to be identical, the waveguide can be rotated 45° to the principal crystal axes. We find that both types of BTO allow large electric fields to exist deep in the waveguide as is evident from Figure 6.3 b). To our benefit the electric fields remain rather confined above each electrode making electric field superpositions easier since only few neighbouring pillars need to be included before fields decay to negligible values. Again, E_x and E_y fields are plotted in the same graphs, the planes along which fields are identical are indicated in the plots together with their crystal type.

The dashed contour in Figure 6.3 indicates the coercive E_C field of BTO, which represents the domain poling threshold. For proper operation, poled domains are a requirement. The holographic display will thus require repeated poling sequences before and during operation. To that end, applied voltages larger than the ones applied in Figure 6.3, namely 0.1V, will be needed. Fortunately, this voltage can still be increased nearly a tenfold before that the fields induce dielectric breakdown. Every so often, the device will thus have to align domains by applying a larger voltage, ideally through a sweeping motion stretching the entire display. The frequency largely depends on the poling retention, which has shown to exceed many hours. [374] In between those moments, the field

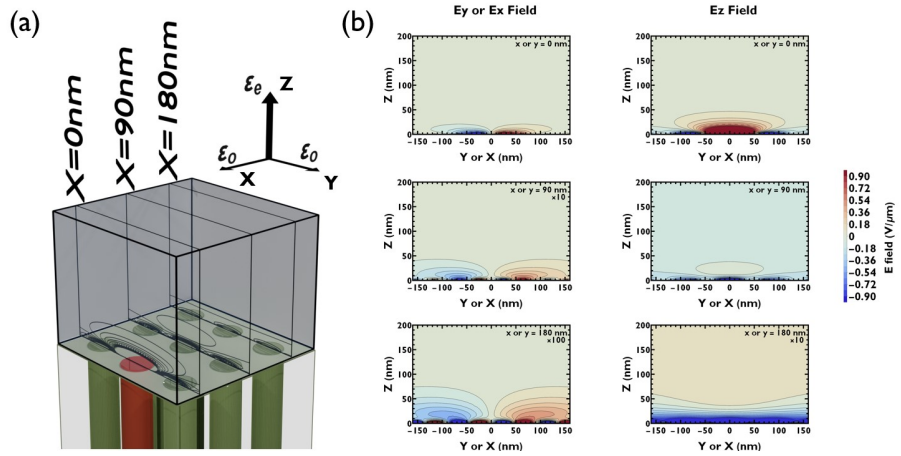

Figure 6.3: a) Schematic showing the pillar array used in the COMSOL FE simulations, red indicates the biased pillar. The planar slices above indicate the plotted area in b). b) Electric field data for both a- and b-oriented BTO, for which E_y and E_x respectively lead to the desired mode conversion. Due to the 90° rotation between them, both orientations result in an identical electric field along 90° rotated axes. Image reproduced with permission. [342]

varies significantly between the lower and top edge of the waveguide. As a consequence, its efficiency similarly varies a lot. The largest index modulation comes from the lower edge of the waveguide due to its stronger electric field. The total effect can be found by integration of the full waveguide.

Keyhole Influence on Field Distribution

Chapter 4 learns us that the constructed metamaterial has a small keyhole at the center of each electrode. This appears since the filling procedure closes of the electrode entrance before the entire pillar is filled. The subsequent planarization step reveals the underlying gaps in the electrodes. Consequently, the real electric fields in the device will not be identical to the ones of the previous sections. To identify the impact of the keyhole, an additional simulation was performed continuing on an a-oriented crystal. To that end, an air gap with a diameter of $10nm$ was added at the center of each electrode, the field extracted from the xz-plane at $x = 0nm$ from this simulation are shown in Fig. 6.4 b) and is compared to the scenario without keyhole.

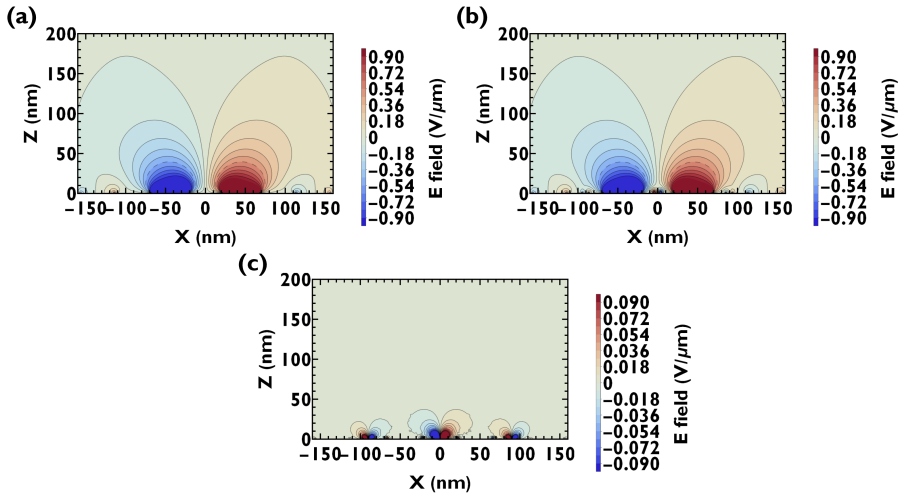

Figure 6.4: a) FE simulated electric field in the xz-plane of an a-oriented BTO slab. Here, the electrode at the center is biased, and all the surrounding ones are grounded. b) FE simulated electric field in the xz-plane of an a-oriented BTO slab. Here, the electrode with keyhole at the center is biased, and all the surrounding ones are grounded. c) The difference in the electric fields of a) and b), which highlights where deviations occur due to the included keyhole.

Figure 6.4 c) shows the difference between the electric field simulated with and without a keyhole. It reveals that only minor deviations to the field immediately adjacent to the pillar electrode occur. The deviation does not significantly permeate into the waveguide slab, meaning that the majority of the present optical power will only see minor deviation from the ideal refractive index modulation.

6.3 Phase grating reconstruction using signal analysis

The sub-wavelength size of the electrodes in the cladding enables the creation of analogue electric field patterns inside the electro-optic waveguide. Here, precise control can be achieved by applying the principles of signal analysis to the sampling and reconstruction of the desired space-varying patterns in waveguides. In doing so, any grating pattern can be created without loss of

information by paying attention to the Nyquist-Shannon sampling theorem. Calculations of complex electrode array patterns can therefore be simplified to the summation of individual electrode contributions. A major difference to the standard procedures used in signal analysis is that this individual contribution is not the Fourier transform of the window function (i.e. a *sinc* function). Instead, the electric field of a single biased pillar surrounded by a grounded array needs to be used. As a consequence, an certain error is expected due to employing a non-optimal reconstruction function.

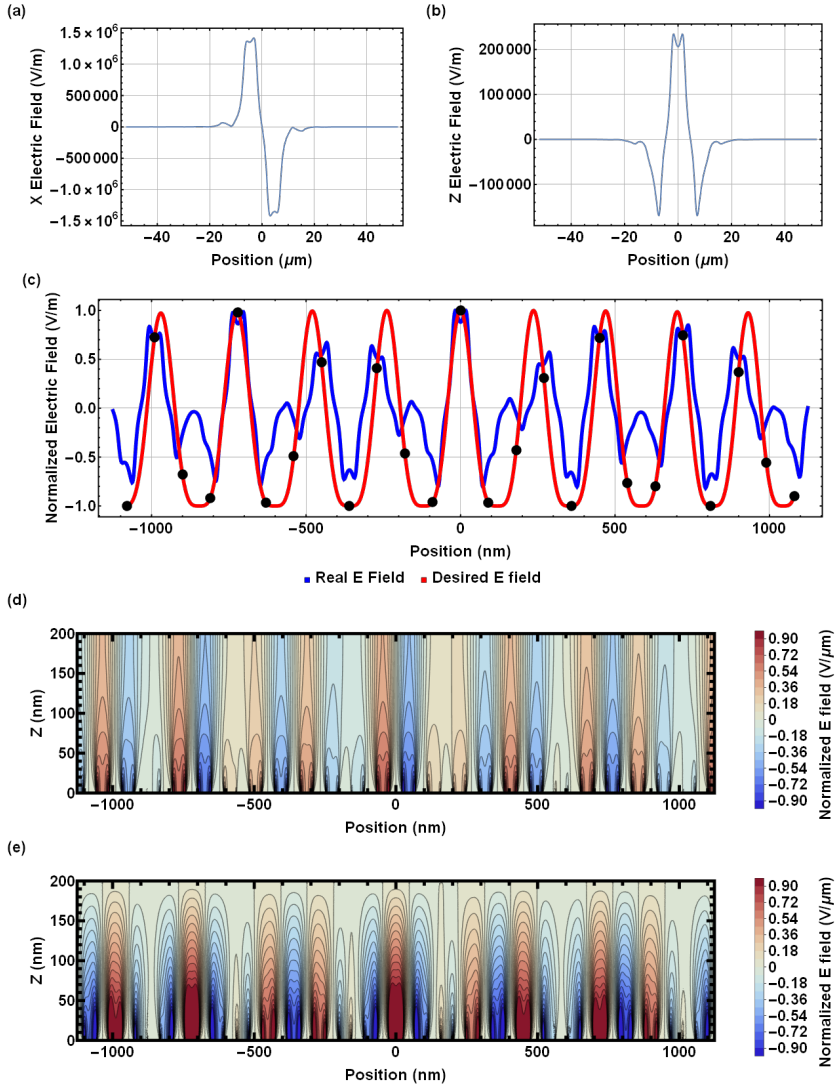

Figure 6.5: a) Electric field E_x along x $50nm$ above the cladding. b) Electric field E_z along x $50nm$ above the cladding. c) Comparison between the desired electric field and the acquired electric field through sampling (black dots) and reconstruction using the fields from a). d) Electric field contours showing the E_x field behaviour throughout the entire waveguide. e) Electric field contours showing the E_z field behaviour throughout the entire waveguide. Image reproduced with permission. [342]

The grating reconstruction based on eq. 6.6 for a focusing grating is highlighted below, its principle can be extended to both point based and phasemap holograms. For each electrode the required voltage can be found in three steps. First, the desired grating needs to be sampled it at the electrode interval. Secondly, the required electric field can be calculated for all sampled data points using the impermeability tensor. Finally, the electric fields can be linked to a voltage be employing the electric field simulations above. Given that all electrodes are identical, their electric fields can be assumed identical as well. The best height to base the reconstruction on is found by calculating the overlap integral of the electrode electric field and mode electric field. In case of a $200nm$ thick a oriented BTO waveguide and a $550nm$ incident wavefront having an effective mode index of 2.317, the highest overlap is found in the bottom half of the waveguide. Therefore, the level $50nm$ above the cladding is used to base further calculations on. Fig. 6.5 a) and b) shows the electric field of a single biased electrode pair $50nm$ above the cladding for both E_x and E_z respectively simulated using COMSOL. The full 2D electric field can be found in data set 1. [393]

To subsequently reconstruct a grating, the intended signal needs to be sampled at the interval of the electrodes. Fig. 6.5 c) shows the desired complex amplitude signal needed to focus light into a single point $10\mu m$ above the waveguide. This pattern corresponds to the square of eq. 6.6 since a square root separates the applied electric field from the acquired index modulation. The grating was sampled with a $90nm$ interval, indicated by the black points. The reconstructed electric field can then be found through super positioning the fields shown in Fig. 6.5 a) with the correct spacing and voltage prefactor at each of the sampled points. It is clear that the reconstructed grating deviates significantly from the desired one due to the use a a non-optimal window function. Nevertheless, Fourier analysis of the acquired grating shows that the pattern mainly includes the desired period. Next to this, smaller periods make up a large portion of the reconstructed grating but these fortunately do not contribute in the coupling dynamics. Looking back to eq. 6.2 helps understand why. Due to the sub-wavelength size of the employed electrodes, the applied gratings can be first order gratings. Since small periods result in a large mode vectors, $\overrightarrow{\beta_r}$ in eq. 6.2 is strongly modulated. Very few of these periods will consequently lead to significant coupling as only narrow regions allow guided, cladding or radiation modes. [348] Fig. 6.5 d) and e) show the complete pattern of the electric field for the section between -1 and $1\mu m$ for both E_x and E_z.

6.4 Gratings for Beam Steering, Beam Focusing and Holography

The envisioned holographic display is a versatile platform that offers possibilities for many applications including beam steering, beam shaping and ultimately also holography. Each of these applications require different modulation of the slab waveguide with various degree of intricacy. Below, all possibilities are expanded on starting from the most simple implementation.

6.4.1 Beam Steering Grating

Coupling from the guided mode to a radiation mode can be achieved through applying a grating with the correct period. As mentioned earlier in eq. 6.2, the waveguide dynamics are best considered from mode vector space. The influence of a grating can thus be assessed by subtracting or adding it from the guided modevector. The out coupling angle of the radiation can be found by considering the free space modevector and the radiation mode vector. [348]

$$\theta_{out} = \sin^{-1}\left(\frac{\overrightarrow{\beta_r}}{\overrightarrow{\beta_{free}}}\right) \tag{6.3}$$

Here, θ_{out} is the out coupling angle of the radiation mode measured from a perpendicular to the waveguide and $\overrightarrow{\beta_{free}}$ is the wavevector of the light in free space.

6.4.2 Focusing Grating

Several approaches can be used to find the equation for a focusing grating i.e. a chirped grating that links the out coupling angle and its accompanying period to the spatial coordinate of the waveguide. In doing so, all out coupled light focuses into a single point. A geometric approach for example requires substituting eq. 6.2 into 6.3 and solving it for Λ. Afterwards, the out coupling angle from each point (x, y, z) along the waveguide needs to be linked to the position. Combining both results yields the instantaneous period at each waveguide position. Implementing this in a sinusoid would require an additional integration to achieve the correct modulation. To avoid this cumbersome step here the focusing grating equation will instead be found from phase matching

each out coupled beam. This approach is beneficial as its results can similarly be used for the holographic projections used in later sections. Figure 6.6 a) shows the pattern of a focusing grating. The resulting grating strongly resembles a Gabor zoneplate. This is no surprise as it fulfils the same purpose with the difference here being that the incoming light is not a collimated beam but a guided mode.

Consider two rays of light being coupled out of the waveguide at different position. Imagine one ray travels purely through free space, for example from the point (x_0, y_0, z_0) on the waveguide to focusing point $P_1 = (x_{P_1}, y_{P_1}, z_{P_1})$. The other ray also originates from (x_0, y_0, z_0) but first travels to (x, y) as guided mode after which it is coupled towards the same focusing point. The phase accumulated for both rays is:

$$\phi_1 = \frac{2\pi}{\lambda}\sqrt{(x_0 - x_{P_1})^2 + (y_0 - y_{P_1})^2 + (-z_{P_1})^2} \tag{6.4}$$

$$\phi_2(x, y) = \frac{2n_{eff}\pi}{\lambda}(x - x_0) + \frac{2\pi}{\lambda}\sqrt{(x - x_{P_2})^2 + (y - P_2)^2 + (-z_{P_2})^2} \tag{6.5}$$

The equation for a focusing grating can now be extracted by setting the argument of a cosine to $\phi_1 - \phi_2$ which makes sure that all rays reach P_1 in phase, enabling constructive interference:

$$\Lambda(x, y) = A(x, y)\cos(\phi_1 - \phi_2(x, y)) \tag{6.6}$$

Here $\Lambda(x, y)$ represents the desired grating profile, $A(x, y)$ is the grating intensity and the cosine is required to yield the correct period from the desired phase differences. Without prefactor eq. 6.6 only leads to phase modulation of the waveguide of which an example is show in Figure 6.5 a) The envisioned holographic display can however use complex amplitude holograms since the amplitude of the grating can be adjusted. To that end, the inverse of a focusing grating can be considered meaning a point source that illuminates the grating plane. The illuminance at every position can be written as:

$$A(x, y) = \frac{I\cos(\theta)}{r^2} = \frac{I\cos\left(\frac{\pi}{2} - \arctan\left(\frac{z_{P_1}}{\sqrt{(x_{P_1} - x)^2 + (y_{P_1} - y)^2}}\right)\right)}{(x_{P_1} - x)^2 + (y_{P_1} - y)^2 + (z_{P_1})^2} \tag{6.7}$$

Here, I is the intensity of the point source, θ is the angle between the illuminated plane and the perpendicular of the light, r is the distance between the point source in point 1 and position (x, y, z) on the surface. The intensity I is set by the desired focusing point, to ease calculations eq. 6.7 can be normalized by setting I equal to the minimum distance between the plane and focusing point i.e. $I = z_{P_2}^2$. An example of both the amplitude factor and the complex amplitude modulation is shown in Figure 6.6 b) and c).

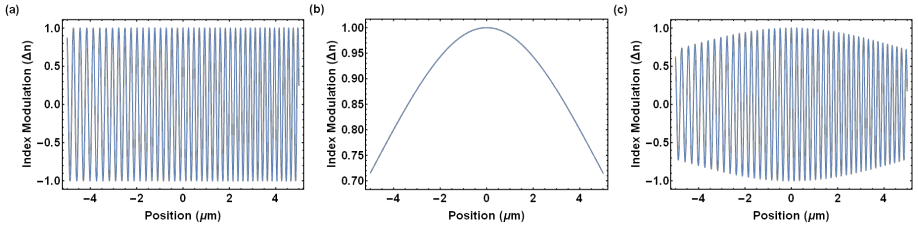

Figure 6.6: a) Chirped phase grating along the x-axis of a waveguide that focuses at $(0, 5)$ μm b) Ideal amplitude of the focusing grating in a). c) Complex amplitude modulation of the waveguide that focuses in a spot 5 μm above the waveguide center. Image reproduced with permission. [342]

Finite difference time domain FDTD simulations in 2D and 3D were performed in Lumerical FDTD. [394] In each, a TE guided mode $(0, E_y, 0)$ was launched into the waveguide and converted to a TM radiation mode $(E_x, 0, E_z)$ due to the non-linear waveguide. The near field was recorded and used for a farfield extrapolation afterwards. 2D simulations were set up to observe the difference between a grating reconstructed by superpositioning electric fields and its idealized counterpart i.e. eq. 6.6. Here, both the phase (grating period) and amplitude modulation (grating strength) combine to yield accurate focusing. Figure 6.7 a) & b) shows an example where the guided mode focuses $10\mu m$ above the slab waveguide surface. In both simulations, the waveguide was $50\mu m$ long and the wavelength was $550nm$. The mean square error (0.000332) between the normalized fields indicates that the electric field based grating matches its idealized counterpart very well. This confirms the idea that reconstructing a signal using a non-optimal window function, namely the electric field of a single biased pillar electrode, provides accurate reconstructions of the desired modulation. Notably, the out coupled intensity in Figure 6.7 b) seems slightly rotated, which we attribute to a higher degree of out coupling and accompanying higher refractive index modulation, likely caused by the sampled points aligning better with the grating maxima. Which is no surprise, since the required grating periods are significantly larger left of the focusing spot. Here, steering only requires slight modulation of the waveguide mode compared to the right side,

where the grating needs to be small enough to steer the mode in an opposite direction. Note that there is no constraint of the focusing distance and as such, near field imaging is possible.

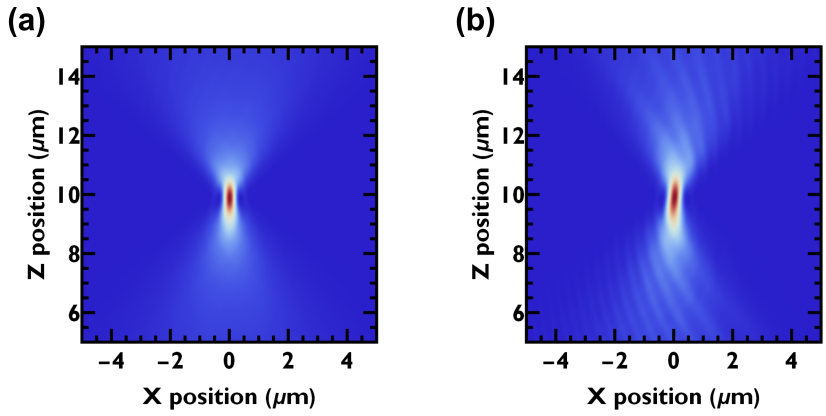

Figure 6.7: a) Outcoupling from an ideal grating (eq. 6.6) focusing 10 μm above the waveguide, extracted from a 2D Lumerical simulation. b) Outcoupling from an approximated grating using electric field and the method described in Section 6.3. In both, the square of the electric field (E_x, E_y, E_z) is shown. Image reproduced with permission. [342]

6.4.3 Holography

Three dimensional holograms can be calculated by various methods including multiplane, polygon and point-based approaches. [191] Unfortunately, reconstruction of a complete 3D scene leads to incredibly large datasets and lengthy (sometimes nearly impossible) calculations with currently available capabilities. To reduce calculation time 2D holograms will be focussed on in this work. In 2D pixel-based images are used to represent the desired amplitude of a scene or projection. Through the years, a wide range of algorithms and techniques have been developed that retrieve the necessary phase in the hologram plane. Below, two such methods are expanded on. One employs point based analogue phase and shares calculations with a focusing grating, the other is based on more commonly used pixelated iterative phase retrieval. Various light propagation methods can be used in these including the Fresnel transform, angular spectrum and triple Fourier transform. More details on these and their

use case is elaborated on in Chapter 7.

Point-based Holography

Holograms can be created from a point map of a desired scene, by calculating the superposition of the 3D focusing grating attached to each point in the scene. To illustrate the approach, the imec logo was downscaled to 100×50 pixels shown in Figure 6.8. For all non white points the previously calculated focusing grating (i.e. eq. 6.6) was superpositioned to create a waveguide hologram with each logo point spaced $610nm$. To increase the point density each nearest neighbour was assumed to have a π phase difference, mimicking interference lithography. This spacing was found by gradually bringing two points closer until both reached a maximal intensity. Depending on the display technology, amplitude information can be included to improve the projection. The envisioned holographic display can modulate both phase (grating period) and amplitude (grating strength).

A Lumerical FDTD simulation was performed in 3D, employing idealized gratings without electric fields to speed up calculations. Compared to the 2D results from above, this simulation better mimics the real device operation as it demands steering from a slab waveguide with the grating vector in the xy-plane. Again, a TE guided mode $(0, E_y, 0)$ was launched into the waveguide and converted to a TM radiation mode $(E_x, 0, E_z)$ due to the non-linear waveguide. The simulation size was 50 by $50\mu m$ with an operating wavelength of $550nm$. The image plane was assumed to be $10\mu m$ above the waveguide surface. No points were placed along the symmetry axis of the slab as steering to these axes requires only one grating component, translating in a stronger coupling coefficient and individual points overshooting the entire superposition. We find that the superpositioned logo in 3D, shown in Figure 6.8 b) matches expectations very well as every single point can be identified. Points further removed from the center on average have a lower intensity which we attribute to limited simulation size. This matches well with Figure 6.6 b) which shows that most optical power comes from directly below every point. Points, for example in the imec dot sit at the edge of the simulation, meaning that a significant portion of their amplitude contribution is cut off.

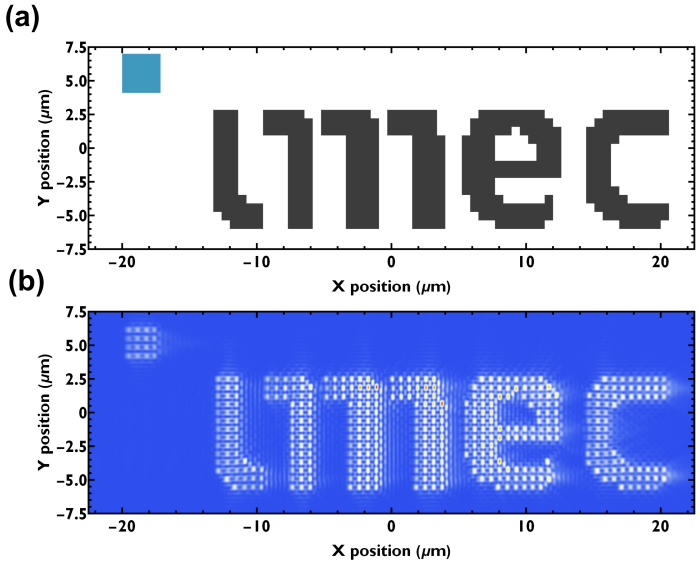

Figure 6.8: a) Pixelated imec logo used as pointmap for 3D simulations. b) A superposition of multiple focusing spots, each representing one pixel out of the pixelated imec logo. Image reproduced with permission. [342]

Phasemap based Holography

More traditional phase holograms based on the GS algorithm were calculated to further demonstrate the capabilities of a waveguide based holographic display. Therefore, an image of a flower was downscaled to 500 by 500 pixels and the standard GS algorithm was employed to extract the desired phasemap for red, green and blue light. [77] We equate red to $640nm$, green to $550nm$ and blue to $465nm$. However, due to the sub-wavelength sized pixels ($90nm$) the most common wavefront propagation methods are not applicable. Instead, a subwavelength corrected farfield calculation based on the Rayleigh-Sommerfeld (RS) diffraction integral was used to negate distortions that otherwise would occur. [395] Chapter 7 will expand on these considerations. A consequence of the employed RS propagation, which also occurs for other single Fourier transform methods, is that the image size is influenced by the employed pixel size through:

$$S_0 = \frac{\lambda D}{d_{pix}} \tag{6.8}$$

Here, S_0 is the projection size, λ the employed wavelength, D the imaging distance and d_{pix} the pixel size. For the blue channel, $180nm$ was chosen as pixel size as it is the size of the smallest attainable grating period since it requires one "ON" electrode and one "OFF" electrode at minimum. Both pixel sizes for green and red were adapted such that an identical image size was attained in the farfield. At a distance of $10cm$, these are $212.9nm$ and $247.7nm$ respectively which leads to an image size of $25.83cm$. Incidentally, the simulation size varied from 90 by $90\mu m$, to 106 by $106\mu m$ and 124 by $124\mu m$ to account for the increasing pixel size. The three calculated holograms were subsequently imported in Lumerical FDTD and used to create the require waveguide grating for the three separate holograms. The same method employed before was used expect the phase that the travelling guided mode accumulates between individual pixels was subtracted from the original hologram. In each simulation, the near field of the TM radiation mode $(E_x, 0, E_z)$ was recorded a few μm above the waveguide, after being launched into the waveguide as TE guided mode $(0, E_y, 0)$. The near field was used for a farfield extrapolation afterwards. The acquired farfield images for each color and the total are shown in Figure 6.9.

The recombined image, shown in Figure 6.9 e), yields an accurate reconstruction of the desired image. A peak signal to noise ratio (PSNR) of 9.262 was attained for the recombined RGB image. We find that the blue channel attains the best PSNR, whereas the red channel the lowest. Some speckle is visible in each image which can be reduced by using more advanced versions of the GS algorithm. Next to that, some degree of vignetting is present. This is rather common in holography and imaging and is typically adjusted for by using the projection of a test image as correction factor on the intended image.

6.5 Conclusion

A brief introduction to mode coupling was presented. Here, both the required mode overlap and the wavevector matching condition were highlighted and applied to the envisioned holographic display. In case of a TE guided mode, coupling is enabled through the modulation of both ε_{yx} and ε_{yz}.

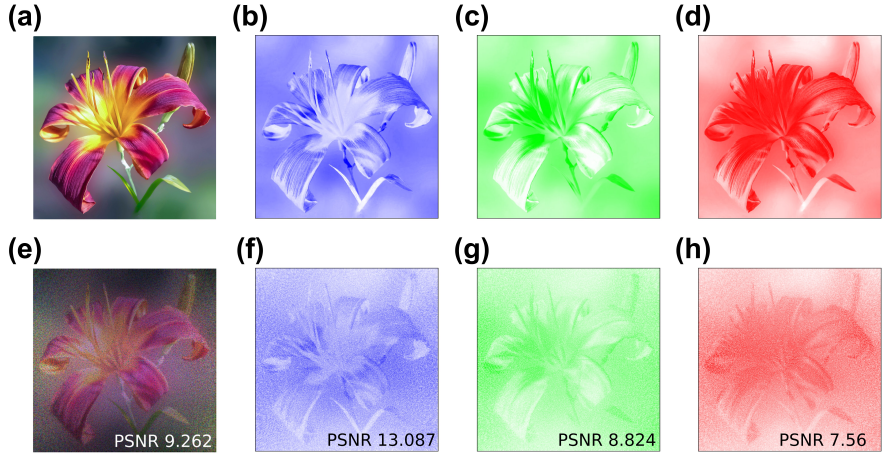

Figure 6.9: a) Flower image used for hologram calculation. b) Blue channel of the flower image. c) Green channel of the flower image. d) Red channel of the flower image. e) Combined farfield projection of the hologram. f) Farfield projection of the blue channel. g) Farfield projection of the green channel. h) Farfield projection of the red channel. Image reproduced with permission. [342]

Finite elements electric field simulations were performed to assess the various types of *BTO* domains. C-oriented *BTO* was found to limit the depth in which the electric field penetrates into the active layer. This is not ideal for mode coupling, as this leads to weak modulation of the permittivity in the center of the waveguide where the largest mode overlap is strongest. Conversely, a- and b-oriented *BTO* allows electric fields to penetrate while keeping the field confined to the region immediately above the electrodes. Furthermore, the required permittivity modulation can be made in both domain types. As such, a- and b-oriented *BTO* are well suited for coupling from waveguide to free space.

A method was introduced, based on signal analysis, that allows suboptimal electric fields to be combined and create any desired electric field pattern. Afterwards, the required grating modulation for various applications including beam steering, beam focusing and holography was presented. In case of holography, two approaches are shown. The first employs a point based algorithm and can be viewed as an extension of a general beam focusing application through superposition. A display segment of 50 by 50μm was simulated and projected the imec logo 10μm above the display. The second method requires a computer generated phase map which is then transformed

into a modulation pattern that supplies each out coupled ray with the correct phase. The desired image can be viewed in the farfield. The phasemap of a flower was calculated through the Gerchberg-Saxton algorithm and employed an approximation of the Rayleigh-Sommerfeld diffraction integral for efficient wavefront propagation. During hologram synthesis and FDTD propagation the RGB colors were treated separately, after which they were combined. The end-result yielded a peak signal to noise ratio of 9.262.

Chapter 7

Computer Generated Holograms for Waveguide based Holographic Displays

As hinted at in the previous Chapter, holograms employing sub-wavelength pixels face some computational challenges. On one hand, holograms can be calculated precisely using computationally intensive techniques. On the other hand, the more commonly used techniques applicable to larger pixel sizes that are less computationally demanding cannot simply be used for smaller pixels without adaptation. Evidently, both options indicate that a new method for sub-wavelength holograms synthesis is needed. This chapter first refreshes the requirements of dynamic wide angle holography and then introduces the widely accepted Gerchberg-Saxton algorithm. This is followed by various propagation methods, the assumptions under which they can be used and their computational load. Afterwards, a solution is proposed to enable high-quality computer generated holograms for displays employing sub-wavelength sized pixels. Finally, various approaches are looked into to prevent loss of information employing the proposed method.

7.1 Requirements for Dynamic Large Angle Holography

Before various hologram synthesis methods are introduced it is beneficial to understand which criterion they should meet. The end goal of dynamic holography would be to supplant the currently existing display technology which is unable to offer authentic 3D images. The requirements to achieve this was previously addressed in Section 2.2. Ideally, the envisioned projection should have (x, y) coordinates in the same order of magnitude as the projection distance z. To achieve such large FOV, a holographic display requires sub-wavelength pixels. Hence, for operation at visible wavelengths (400 nm - 700 nm) pixels below 100 nm are needed when accounting for the refractive index of the waveguide. Due to the technological challenge creating such a structure poses, most efforts have been focused on significantly larger pixel sizes which will be expanded on below.

7.2 Computer Generated Holograms

Computer generated holograms were briefly touched on in Section 2.1.3. Here, the standard version of the Gerchberg-Saxton algorithm was introduced together with Rayleigh-Sommerfeld diffraction which describes scalar wave propagation. Throughout the years, these have cemented themselves as go-to method for finding the phase map of a desired projection. This is first of all due to not requiring physically having to record the hologram, as recording the interference pattern of the object with a reference wave is often cumbersome by requiring a dedicated setup and careful alignment. Computer generated holograms on the other hand can nowadays be calculated rapidly while offering identical reconstructed images. On top of that, CGHs offer the ability to create holograms that cannot be physically recorded. For example, hollow opaque structures cannot be recorded in practice but are of interest to lithography and medicine. Many computer based synthesis approaches exist using an equally wide variety of wavefront propagation methods such as wavelet transform, deep learning and Fourier optics. [396, 397, 398, 399, 400, 401, 402, 403] In this chapter, several wavefront propagation approaches based on Fourier optics are applied to the a generalized version of the Gerchberg-Saxton algorithm, called the error reduction (ER) algorithm. [404] Although Section 2.1.3 already introduced the GS algorithm and RS diffraction, they will be highlighted here again.

7.2.1 The Generalized Gerchberg-Saxton Algorithm (Error Reduction Algorithm)

The Gerchberg-Saxton algorithm is an iterative approach that propagates complex electric fields between the display (nearfield) and the image plane (farfield) of which a schematic is shown in Fig. 7.2. After each propagation (forward and backward) the acquired amplitude and phase profile are split from each other and the phase is multiplied by the desired amplitude to start the next propagation. Typically, the desired image is used in the farfield and a known amplitude distribution is used in the nearfield. In doing so, the algorithm gradually converges while getting constant reinforcement of its target. Interestingly, the GS algorithm does not require a specific type of wave propagation meaning that all the options mentioned above can in theory be used without problem.

The algorithm can be initiated both in the nearfield and farfield. Regardless of where it is started, a known amplitude is multiplied by an input phase of choice at each pixel. The complex amplitude is defined as:

$$E = Ae^{-i\phi} \tag{7.1}$$

Here, E represents the complex amplitude, A represents the amplitude and ϕ represents the phase. Phase profiles mostly fall into four categories namely constant, randomized, quadratic or a combination of these. Fig. 7.1 shows phase profile examples. A constant phase profile simply assumes a fixed value, most likely zero, for the entire hologram. A randomized profile has a randomized value between zero and 2π for each pixel and a quadratic profile has a profile varying with the distance with the center of the hologram, somewhat resembling a Gabor zone plate. The rate at which the phase changes is linked to the propagation distance and hologram size. A common approximation found in literature to the ideal quadratic phase can be written as: [77, 404]

$$\phi = e^{ia(x^2+y^2)} \tag{7.2}$$

Here, ϕ is the phase factor, a is the phase prefactor and x and y are the pixel coordinates. The phase prefactor a is defined as:

$$a = \frac{\pi}{M(1+\frac{S_h}{S_0})} \approx \frac{\pi}{M} \tag{7.3}$$

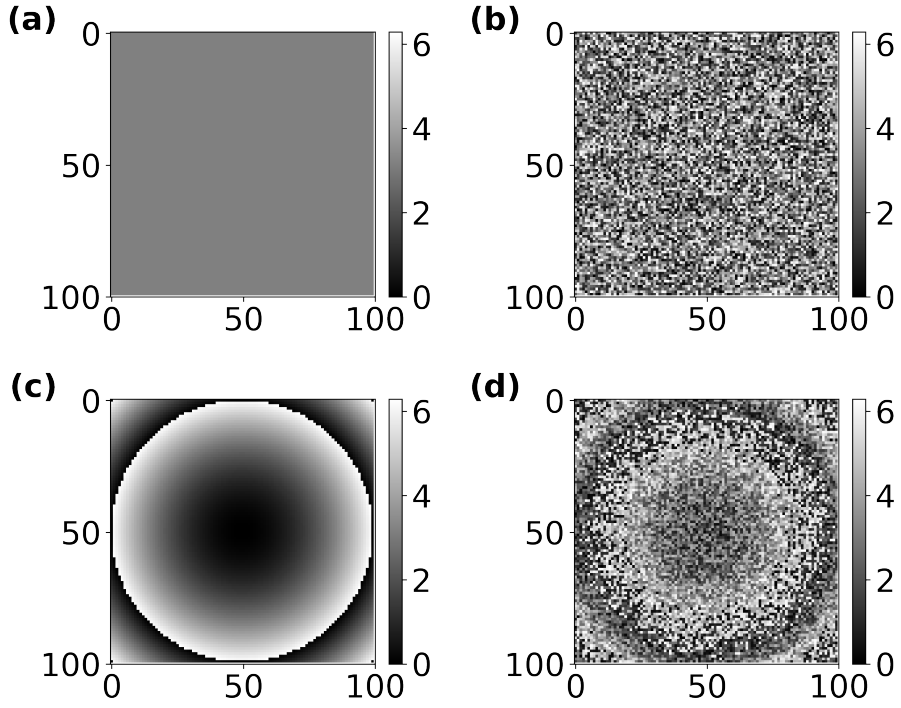

Figure 7.1: a) Constant phase profile b) Random phase profile. c) Quadratic phase profile. d) Combined phase profile.

Here, M is the number of pixels in each row or column, S_h is the size of the hologram in spatial coordinates and S_0 is the size of the projection in spatial coordinates. [405, 406] Finally, combinations of these profiles can be employed to prevent the GS algorithm from getting stuck in local minima.

In contrast to the standard GS algorithm, the ER algorithm adds an object-domain constraint to each iteration. In the farfield, every pixel is evaluated according to eq. 7.4 where ρ represents the domain of positive amplitudes and possibly a well defined support region. A common approach is to exclude all zero padding. The algorithm is known to rapidly decrease the error between desired and acquired farfield amplitude at the initial few loops but has a tendency to plateau in local minima which require a large number of iterations to move past. The ER domain constraint is defined as:

$$G_{k+1}(x,y) = \begin{cases} f(x,y) \text{ with } (x,y) \in \rho \\ 0 \text{ with } (x,y) \notin \rho \end{cases} \tag{7.4}$$

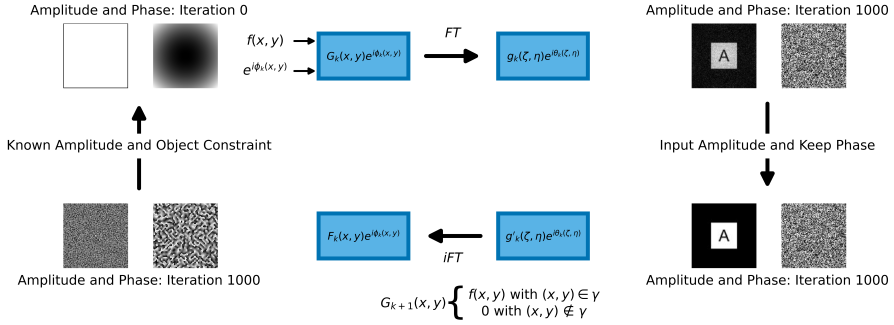

Figure 7.2: A schematic of the error reduction algorithm. The initial amplitude and phase of an example is shown in the top left, the acquired amplitude and phase after 1000 iterations is shown in the other steps.

7.2.2 Rayleigh-Sommerfeld Diffraction

The theory of wavefront propagation was developed over the last several centuries, requiring insights from various physicists to reach the understanding we have today. For example, it was Huygens who realized that each point of a wavefront can be viewed as a secondary spherical source and that constructing their envelope gives the wavefront at a later time. Young introduced the revolutionary concept of interference, after which Fresnel combined both Huygens's and Young's work to create accurate calculations of diffraction patterns. Finally, after Maxwell introduced his theory of electromagnetic waves these earlier ideas were given a solid mathematical footing by Kirchoff. By applying Green's functions to the Helmholtz equation for a propagating wave falling onto a partially obscured plane and assuming a spherical wave spreading from a point source as auxiliary function he was able to create a boundary integral capable of precisely calculating complex diffraction problems. That said, Kirchoff's assumptions on the amplitude and phase $U(x,y,z)$ are not self consistent. The assumptions are (1) that at the aperture the field and its derivative are identical to what they would be without screen ($U(x,y,0) = U_0(x,y,0)$ and ($\frac{\partial U(x,y,z)}{\partial z} = \frac{\partial U_0(x,y,z)}{\partial z}\Big|_{z=0}$) and (2) that in the

shadow of the screen both field and derivative are zero ($U(x, y, 0) = 0$) and ($\frac{\partial U(x,y,z)}{\partial z} = 0$). These unfortunately lead to U having to be zero everywhere. [407]

Not long afterwards, Sommerfeld realized that only one of Kirchoff's assumptions was necessary and proposed a different Green's function to solve the Helmholtz equation leading to the Rayleigh-Sommerfeld diffraction integral. Some assumptions still remain. This approach for example does not include the vectorial nature of electromagnetic waves and assumes they are scalars instead, which holds true when the diffracting aperture is large compared to the wavelength and the fields are not observed too close to the aperture. On top of that, the propagating media are assumed to be homogeneous, isotropic, non-magnetic and non-dispersive in nature. Another major difference between them is the surface they are valid on. The Rayleigh-Sommerfeld diffraction integral can only be used for flat surfaces whereas Kirchoff's diffraction formula can be applied to curved surfaces. Consequently, the employed theory is best matched to the problem at hand. In the case of holography, flat surfaces are common, meaning that the Rayleigh-Sommerfeld diffraction integral will be employed in this work. The Rayleigh-Sommerfeld diffraction integral is written as:

$$U(x, y, z) = \frac{1}{2\pi} \iint U_0(\zeta, \eta, 0) \frac{e^{ikr}}{r^2} (ikr - 1) \cos(\theta) d\zeta d\eta \tag{7.5}$$

with :

$$r = \sqrt{(x - \zeta)^2 + (y - \eta)^2 + z^2} \tag{7.6}$$

Here, $U(x, y, z)$ is the electric field (amplitude and phase) at a position z far removed from the aperture, U_0 is the electric field U at $(\zeta, \eta, 0)$ i.e. the hologram plane and θ represents the diffraction angle the ray makes with the normal on the (x, y) plane. r represents the distance between a point in the aperture and a point in the farfield. The Huygens principle of spherical waves coming from point sources is represented by the factor $\frac{e^{ikr}}{r}$ inside the equation. Most of the time, the equation will be encountered in a simplified form. First, given that $ikr >> 1$, $(1 - ikr)$ can be simplified to ikr. Secondly, the $cos(\theta)$ can be approximated by $\frac{z}{r}$. Applying both would yield:

$$U(x, y, z) = \frac{ik}{2\pi} \iint U_0(\zeta, \eta, 0) \frac{z e^{ikr}}{r^2} d\zeta d\eta \tag{7.7}$$

Accurate wavefront propagation through calculation of eq. 7.5 is crucial in hologram phase retrieval algorithms. The Rayleigh-Sommerfeld equation can be viewed as a convolution between the complex field $U_0(\zeta, \eta, 0)$ and a propagator. In Fourier optics, three common methods exist that enable the calculation of a complex field propagation from the hologram plane to the farfield plane and vice versa. Each of them calculates the Rayleigh-Sommerfeld diffraction integral, but differ in the number of employed Fourier transforms and approximations. Each of these will be expanded on below.

Single Fourier Transform Method

In most cases, an approach applying only a single Fourier transform is used, as it is simply the fastest and most straightforward of the three to solve. To achieve this, the so called Fresnel approximation or sometimes the even more stringent Fraunhofer approximation is often applied to Eq. (7.5). [407] Both approximations are initiated identically by setting $r \approx z$ in the denominator, resulting in:

$$U(x, y, z) \approx \frac{ik}{2\pi z} \iint U_0(\zeta, \eta, 0) e^{ikr} d\zeta d\eta \tag{7.8}$$

This same approximation is not made in the exponential factor, given that ikr is very large meaning that deviations would quickly lead to a large error. Instead, r in the exponential factor can be approximated by a Taylor expansion $\sqrt{x+1} = 1 + \frac{x}{2} - \frac{s^2}{8} + \dots$. This is referred to as the paraxial approximation. By dividing and multiplying by z^2 inside the square root, the Taylor expansion yields:

$$r \approx z + \frac{(x-\zeta)^2 + (y-\eta)^2}{2z} \tag{7.9}$$

Eq. 7.8 can then be rewritten to:

$$U(x, y, z) \approx \frac{ike^{ikz}}{2\pi z} \iint U_0(\zeta, \eta, 0) e^{ik\frac{(x-\zeta)^2+(y-\eta)^2}{2z}} d\zeta d\eta \tag{7.10}$$

After further calculation of the quadratic factors inside the exponent, the equation can be rearranged to the Fourier transform of $U_0(\zeta, \eta, 0)$ multiplied by the Fresnel propagator $e^{\frac{ik(\eta^2+\zeta^2)}{2z}}$. This, so called Fresnel approximation,

can be further simplified by omitting the quadratic terms (η^2 and ζ^2) in the exponent. What remains is the Fourier transform of $U_0(\zeta, \eta, 0)$ multiplied by a prefactor, called the Fraunhofer approximation. The convolution in eq. 7.5 has thus been simplified to an equation that can be solved by the FFT which significantly speeds up calculation time. These are, as a consequence, some of the most employed wavefront propagation methods in the field of holography. It should be noted that the applied approximations are only valid when an image is far removed from the hologram, such that its dimensions are negligible compared to propagation distance. Unfortunately, this forms an issue for video-rate holography, which would like to project lifelike imagery typically having dimensions comparable in magnitude to the imaging distance. Consequently, both common paraxial approximations are not interesting for high-quality holography.

Double Fourier Transform Method - Angular Spectrum

Alternatively, the convolution can be solved by employing two Fourier transforms, which is mostly referred to as the angular spectrum (AS) method. [407] This method propagates the complex field $U_0(\zeta, \eta, 0)$ by first calculating its 2D Fourier transform which decomposes it into its plane wave constituents. Afterwards these are multiplied by an appropriate propagator to bring each to the desired distance, before being inverse Fourier transformed to yield the farfield. To that end, the angular decomposition of the field $U_0(\zeta, \eta, 0)$ can be written as:

$$F(x, y) = \mathcal{F}\{U_0(\zeta, \eta, 0)\} = \iint_{-\infty}^{\infty} U_0(\zeta, \eta, 0) e^{-i(k_\zeta \zeta + k_\eta \eta)} d\zeta d\eta \tag{7.11}$$

Here, k_ζ and k_η are the angular spatial frequencies corresponding to $\frac{2\pi\alpha}{\lambda}$ and $\frac{2\pi\beta}{\lambda}$ respectively. α and β are the direction cosines of the propagating plane wave. The propagation factor can be found from the Helmholtz equation and is known as :

$$U(\zeta, \eta, z) = U_0(\zeta, \eta, 0) e^{ik_z z} \tag{7.12}$$

with:

$$k_z = \sqrt{\left(\frac{2\pi}{\lambda}\right)^2 - k_\zeta^2 - k_\eta^2} \tag{7.13}$$

Equation 7.11 can now be inverted which introduces a $\frac{1}{4\pi^2}$ prefactor. Multiplying with the propagator gives:

$$U(x,y,z) = \frac{1}{4\pi^2}\iint \mathcal{F}\{U_0(\zeta,\eta,0)\}e^{i(k_\zeta\zeta+k_\eta\eta+k_z z)}dk_\zeta dk_\eta \tag{7.14}$$

Similar to the Fresnel transform, the AS approach is a favourite in the field of holography and metasurfaces since it gives very accurate results within acceptable calculation times without having to undertake any approximations. Calculating the angular spectrum assumes that the feature size in both near- and farfield are identical. For wavefront propagation at small FOVs this poses no problem, however large FOVs quickly require computation of very large datasets. Given that the envisioned holographic display aim to employ sub-wavelength sized features, the angular spectrum approach is not ideal.

Triple Fourier Transform Method

The last remaining method employs three Fourier transform. Similar to the angular spectrum approach it does not require any approximations, leading to accurate calculation of the wavefront propagation at the cost of even longer computation time. In the triple Fourier transform (TFT) approach, the convolution from the Rayleigh-Sommerfeld diffraction integral is solved by separately Fourier transforming both the complex field $U_0(\zeta,\eta,0)$ and the propagator which differs for every pixel. [408] Both of these are then multiplied and inverse Fourier transformed to yield the complex field in the farfield. The farfield can thus be found as follows:

$$U(x,y,z) = \mathcal{F}^{-1}\{\mathcal{F}\{U_0(\zeta,\eta,0)\}\cdot\mathcal{F}\{\frac{ikze^{ikr}}{2\pi r^2}\}\} \tag{7.15}$$

Similar to the AS approach, pixels remain identically in size with the TFT approach. As such, this method is also not suited well for hologram calculation when sub-wavelength features are required.

7.2.3 Wavefront Propagation for Sub-Wavelength Features

Evidently, none of the commonly employed methods for wavefront propagation based on Fourier optics can be easily employed to features smaller than the size of a wavelength. The Fresnel transform is not applicable due to its approximations and both the AS and TFT method result in excessively long calculation times. The envisioned waveguide based holographic display thus

needs an alternative wavefront propagator to be used in hologram synthesis. To that end, a single Fourier transform method can be derived from the Rayleigh-Sommerfeld equation by first substituting r for a first order Taylor expansion around $(x, y) = (0, 0)$ and setting $r \approx \sqrt{x^2 + y^2 + z^2}$ which transforms eq. 7.7 to: [395]

$$U(x, y, z) = \frac{-izke^{ikr}}{2\pi r^2} \iint U_0(\zeta, \eta, 0) e^{\frac{-ik(\zeta x + \eta y)}{r}} d\zeta d\eta \tag{7.16}$$

Here, a coordinate transform $(X = \frac{xz}{r}, Y = \frac{yz}{r})$ can be applied in its exponential propagator together with an intensity adjustment $(u(X, Y) = U(x, y)\frac{r^2}{z^2})$ which yields:

$$u(X, Y, z) = \frac{e^{ikr}}{i\lambda z} \iint U_0(\zeta, \eta, 0) e^{\frac{-i2\pi(X\zeta + Y\eta)}{\lambda z}} d\zeta d\eta \tag{7.17}$$

This is equal to the two dimensional Fourier transform of $U_0(\zeta, \eta, 0)$ multiplied by a prefactor.

$$u(X, Y, z) = \frac{e^{ikr}}{i\lambda z} \mathcal{F}\{U_0(\zeta, \eta, 0)\} \tag{7.18}$$

It is thus possible to simplify the convolution from eq. 7.7 significantly and reduce it to a 2D Fourier transform. It must also be noted that this method no longer evaluates the optical fields at the original near- and farfield locations due to the coordinate transform. Instead, this method projects the fields on a spherical surface within the field of view of the original farfield. As a consequence, the effect of the coordinate transform is visible during calculation but not when the projection is evaluated at the original farfield. The coordinate transform however impacts the input image, forming a barrel-like shape from rectangular objects when deviating from the paraxial approximation. As a consequence, the input complex field is compressed more strongly the further it is removed from the axis. It can be thought of as the pixels in question becoming smaller compared to the ones closer to the center. Projecting this data to a rectangular grid thus leads to distant pixels getting merged into the larger pixels of the grid. These subsets of coordinate transformed pixels are averaged which leads to data loss that should be corrected for. Interestingly, single Fourier transform methods scale the pixel size between hologram and image plane. Consequently, the number of pixels between hologram and image is identical in contrast to the AS and TFT method where large differences in the amount of pixels can occur. A more manageable computational load is thus

achieved for methods employing only a single Fourier transform. The stark difference between approaches can be illustrated by considering the image size which is linked to the employed feature size, distance and wavelength according the the following equation.

$$S_0 = \frac{\lambda z}{d} \tag{7.19}$$

Here S_0 is the image size, λ is the wavelength, z is the imaging distance and d is the pixel size. To better frame the issue that arises when employing AS or TFT for large area hologram synthesis, an example calculation of eq. (7.19) for blue light ($465nm$), a $150nm$ feature size and a projection distance of $25cm$ results in an image size of $0.775m$. In case of AS or TFT approach the farfield requires 5.16 by 5.16 million pixels which is simply impossible by current computing standards. On the other hand, the single Fourier transform method evaluates the farfield in spatial frequencies $x = \frac{\zeta}{\lambda z}$ and $y = \frac{\eta}{\lambda z}$. As such, the number of pixels between image and hologram plane remains identical, allowing for very efficient hologram calculation. The number of pixels in the holographic plane can simply be expanded until adequate resolution is attained to deal with the issue of pixels getting smaller further from axis in the image plane. Currently, the single Fourier transform offers a more realistic approach to hologram synthesis. Only when computational capabilities have increased substantially AS and TFT methods can be considered for high-quality video-hologram calculation. [102]

7.3 Data Loss Prevention

Enabling the use of an FFT in sub-wavelength feature size hologram synthesis required a coordinate transform, which leads to image data compression into a smaller area. Several methods for preventing loss of data in the single Fourier transform method were considered. For example, upscaling the image by decreasing the pixel size does not yield major improvement since the compression due to the coordinate transform is worse at smaller pixel sizes leading to a higher degree of data loss. Conversely, by enlarging the image (upscaling where the pixel size remains identical such that several pixels contain the same data) the compression has a increasingly smaller effect. Unfortunately, this means that the resolution in the image plane varies with the perpendicular distance from the propagation axis.

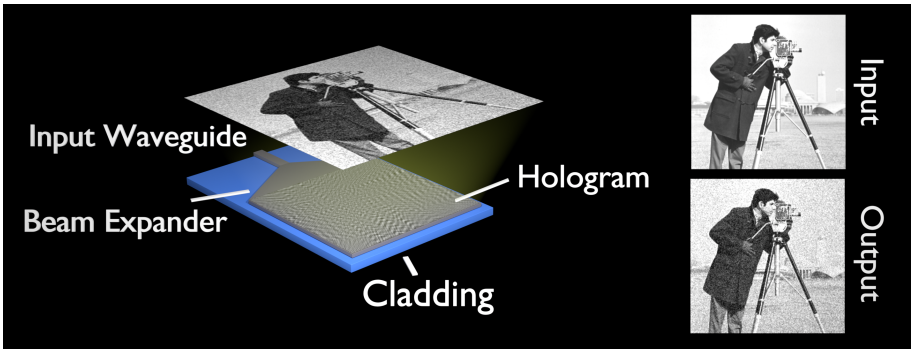

Figure 7.3: A waveguide based holographic projector emits a nearfield wavefront by careful tuning of the applied grating period. The desired image is subsequently created in the farfield. An artists impression of speckle which originates from interference can be found in its output.

7.3.1 Upscale Requirements

The extent of the upscale required to completely preserve the original resolution of the image can be estimated from the coordinate transform. For an object sampled with spacings $\Delta\zeta = \Delta\eta$ such that there are $2N$ by $2N$ samples. The coordinate transformation is most severe where r deviates strongly from z. Hence, it is best evaluated at one of the outermost pixels such as (N, N). The minimum required image upscale factor $(A_{\zeta,N}, A_{\eta,N})$ at (N, N) can be determined from:

$$A_{\zeta,N} = \frac{\zeta_N}{x_N} = \frac{\sqrt{\zeta_N^2 + \eta_N^2 + z^2}}{z} \tag{7.20}$$

$$A_{\eta,N} = \frac{\eta_N}{y_N} = \frac{\sqrt{\zeta_N^2 + \eta_N^2 + z^2}}{z} \tag{7.21}$$

Here (ζ_N, η_N) are the original coordinates of the (N, N) pixel, and (x_N, y_N) of the transformed pixel. For a wavelength of $465nm$, $150nm$ pixel size, imaging distance of $25cm$ and assuming N = 128, $A_\zeta = A_\eta = 2.41$ meaning that pixel $(128, 128)$ gets coordinate transformed to $(53, 53)$. Correcting for this compression thus requires an upscale of $\lceil A_\zeta, A_\eta \rceil$. However, even with an upscale of $\lceil A_\zeta, A_\eta \rceil$, neighbouring pixels can still be coordinate transformed to the same

pixel coordinate due to non-uniform resolution in the image plane. Again, this effect is most prominent for large (ζ, η). The pixel spacing after coordinate transformation can be found by looking at two neighbouring pixels (N, N) and $(N-1, N)$ and employing Eq. (7.20):

$$\Delta_x = \frac{N}{A_{\zeta,N}} - \frac{N-1}{A_{\zeta,N-1}} = \frac{zN}{\sqrt{\zeta_N^2 + \eta_N^2 + z^2}} - \frac{z(N-1)}{\sqrt{\zeta_{N-1}^2 + \eta_N^2 + z^2}} \tag{7.22}$$

Continuing on the previous example, a new relative pixel spacing of 0.244 is found for the example given above. This indicates that an upscale of at least five is needed to ensure no pixel overlaps due to the coordinate transform. Since ζ_N and η_N are coupled to the pixel size, the required upscaling is largely linked to the feature size as well.

7.3.2 Modulation Transfer Function of Upscaled Raster

To qualitatively test the calculated scaling, a grating pattern of 1024×1024 pixels was put through a forward and inverse coordinate transform at various scaling factors and grating pitches to mimic the operation a holographic projection would go through. Again, the parameters from above were assumed namely a wavelength of $465nm$, pixel size of $150nm$ and an image distance of $25cm$. Afterwards, the modulation transfer function (MTF) was calculated to assess the remaining contrast after coordinate transform. For each period, the maximum and minimum value was extracted, its MTF can than be calculated through the contrast:

$$Contrast = \frac{I_{max} - I_{min}}{I_{max} + I_{min}} \tag{7.23}$$

Ideally, a high contrast value is attained throughout the entire inverse coordinate transformed image. This calculation was done in two steps as aliasing is encountered due to the use of two discrete rasters, one after the coordinate transform and one after the inverse coordinate transform. Firstly, the coordinate transform causes multiple pixels to be squeezed into the same point leading to data loss through averaging as shown in Fig. 7.3 a). The subsequent inverse coordinate transform, shown in Fig. 7.4 b), projects the averaged data back to all

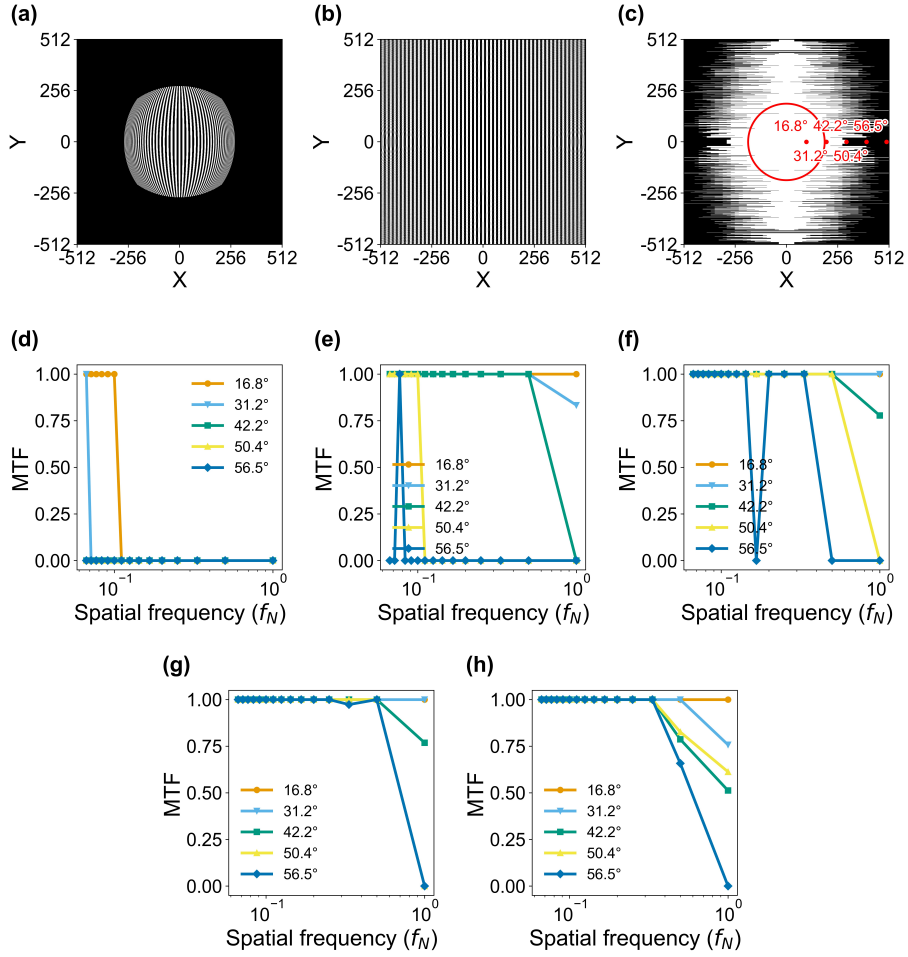

Figure 7.4: Data retention of the coordinate transform at various frequencies and upscale factors. a) Effect of the coordinate transform on a raster grid with 20 pixel period. The employed pixel size is $150nm$, with $25cm$ image distance. No upscale was applied. b) Inverse transformed raster grid which shows artefacts removed from the center. c) Example area (white) in which the raster frequency was conserved through a forward and backward coordinate transform. In the area outside the red circle, enclosing 99 % white points, the MTF is considered zero. Points indicate where the MTF is calculated. d) - h) The MTF after various degrees of upscaling (no to 5×) was applied prior to coordinate transform.

positions initially contributing to the average further exacerbating the data loss. To that end, the largest possible circular range in which no aliasing occurred was first defined by comparing the pitch present in the inverse transformed and initial image. Periods within a 10% margin were considered preserved. Fig. 7.4 c) shows the area in which the periods were conserved in white. Here, the circular range (indicated in red) covers an area that conserves 99% of the enclosed data points. Similar calculations with a different cut off (90% and 99.9%) are shown in Fig. 7.5 and 7.6. Afterwards, the MTF of the coordinate transform was calculated at five points along the x-axis, each separated by 100 pixels starting 100 pixels away from the center which correspond to diffraction angles 16.8°, 31.2°, 42.2°, 50.4° and 56.5°. In case any of these fell outside the earlier defined circular range, the contrast was set to zero as the underlying data had been lost.

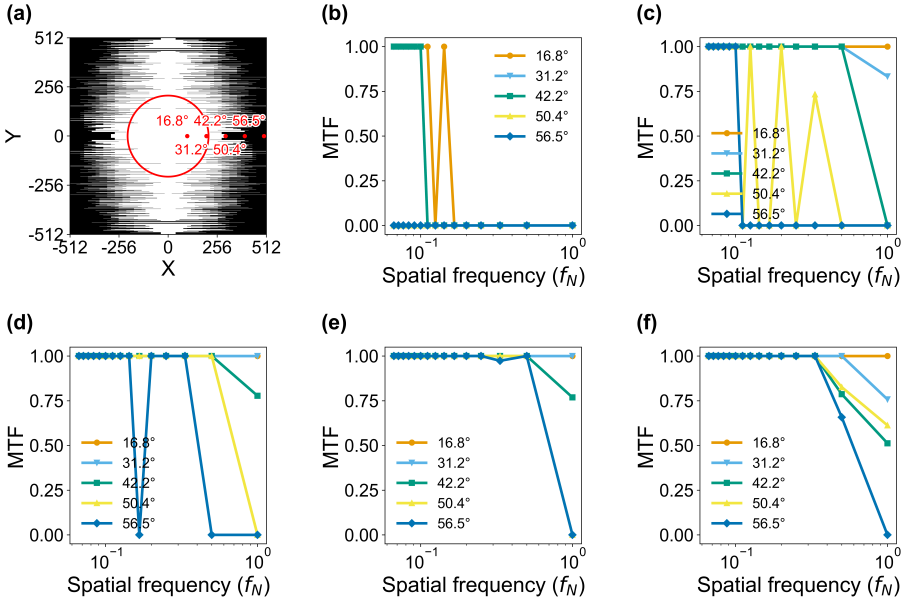

Figure 7.5: Data retention of the coordinate transform at various frequencies and upscale factors. a) Area (white) in which the raster frequency was conserved through a forward and backward coordinate transform with pixel size $150nm$ and $25cm$ image distance. In the area outside the red circle, enclosing 90 % white points, the MTF is considered zero. Points indicate where the MTF is calculated. b) - f) The MTF after various degrees of upscaling (no to 5×) was applied prior to coordinate transform.

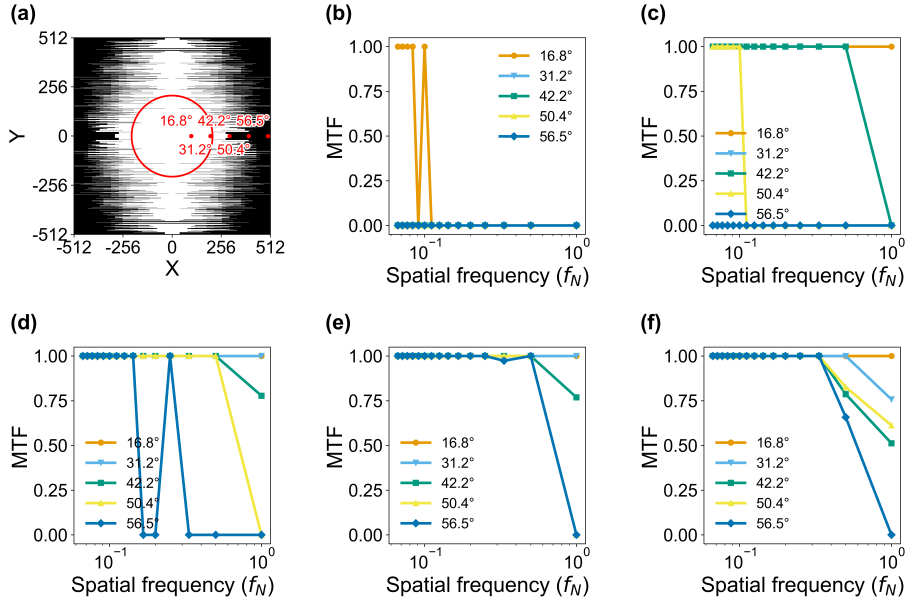

Figure 7.6: Data retention of the coordinate transform at various frequencies and upscale factors. a) Area (white) in which the raster frequency was conserved through a forward and backward coordinate transform with pixel size $150nm$ and $25cm$ image distance. In the area outside the red circle, enclosing 99.9 % white points, the MTF is considered zero. Points indicate where the MTF is calculated. b) - f) The MTF after various degrees of upscaling (no to 5×) was applied prior to coordinate transform.

Fig. 7.4 d)-h) show the MTF after no upscaling or an upscale of three or five was applied. Increasing the scaling factor clearly increases the overall data retention in the image. We find that nearly all frequencies were conserved accurately at an upscale of five except for frequencies nearing the highest spatial frequencies at the outer edge of the image. Further scaling the input could help resolve this better but also would lead to a to drastic reduction in allowable image size or excessively long calculations times. We opt to use the 5× upscale moving forward. In case zero padding is employed to increase the number of spatial frequencies present in the image plane, a lower upscale can be employed tailored to the image area in question.

7.4 Implementations

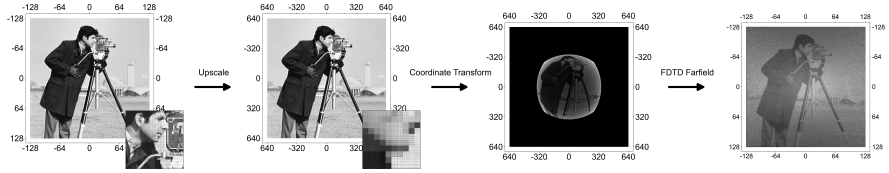

Figure 7.7: Process flow of the proposed method applied to the farfield calculation by finite difference time domain simulation. Here, the upscale ensures data retention, the coordinate transform enables the use of an FFT to speed up phase retrieval and Lumerical FDTD is employed to assess the acquired hologram. The inset in the first two images highlights the effect of the upscaling on the pixels.

The presented approach enabling fast hologram synthesis without data loss is now applied to the envisioned waveguide based holographic display. Chapter 6 has already shown that light can be dynamically coupled out by a periodic modulation scheme that employs local out coupling gratings that provide phase modulation similar to a Lohmann hologram. [73]

The proposed method was applied to the cameraman test image (256 by 256 pixels) of which the process flow is shown in Fig. 7.7. To that end, the image was first upscaled and coordinate transformed before it was used in the standard error reduction GS algorithm (Section 7.2.1) to acquire the desired phase map. Simultaneously, the same procedure was undertaken without upscaling the image for comparison. Afterwards, the acquired phase maps were imported into an FDTD simulation (Lumerical FDTD) [394] in which they were used to set the applied grating modulation of the waveguide based display (Section 6.4.3). This device works as an analogue version of a detour phase (Lohmann) holographic display due to its sub-wavelength pixels. For each row of pixels along the propagation direction, the accumulated propagation phase sampled smaller than the pixel size is subtracted from the calculated CGH out coupling phase. The acquired total phase at all points is then entered into a cosine to yield a grating pattern for each pixel row. The grating is finally imported into the slab waveguide as a weak perturbation of the refractive index. [342] The phase maps can alternatively be applied to any other holographic projectors having sub-wavelength features such as metasurfaces. The extracted farfield projections, shown in Fig. 7.8, accurately reconstruct the desired test image with a normalized standard deviation (NSTD) of 0.365 and 0.330 for the normal

image and enlarged image respectively. To that end, the following formula is known:

$$NSTD = \sqrt{1 - \frac{\left(\sum_{n,m=1}^{N,M} E[n,m]F[n,m]\right)^2}{\left(\sum_{n,m=1}^{N,M} E^2[n,m]\right)^2\left(\sum_{n,m=1}^{N,M} F^2[n,m]\right)^2}} \tag{7.24}$$

Here, M and N are the number of pixels along the x and y dimension, F and E correspond to the intensity of the acquired farfield image and the desired input image. Values closer to zero indicate better image reconstruction. Speckle is found in the both images, which can likely caused by the limited mesh size. A small decrease in the normalized standard deviation (NSTD) is found for the upscaled image. It should be noted that these images are difficult to compare to each other directly as a 25 fold difference in pixels exists between them.

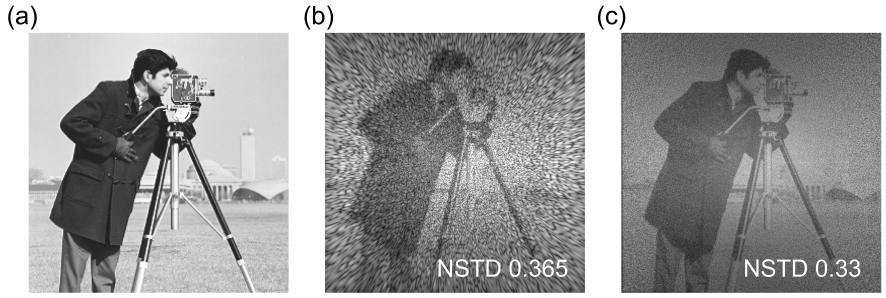

Figure 7.8: a) Desired image b) Non upscaled image projected by the holographic display to the farfield. c) Five times enlarged image projected by the holographic display to the farfield.

7.5 Conclusion

In summary, we have explored the available wavefront propagation techniques based in Fourier optics and applied them to the sub-wavelength features commonly found in metasurfaces. We found that employed farfield propagation methods such as angular spectrum lead to excessively large data sets which inhibit practical implementation. Instead, a method employing a single Fourier transform together with a coordinate transform can be used to achieve

manageable calculation times. During said coordinate transform a significant portion of information is lost due to the limited size of the rasterized grid. To that end, a method was presented that can diminish or even prevent resolution loss by upscaling the input image while keeping the pixel size identical. Consequently, only images several times smaller than the dimensions of the displaying device can be projected without averse effects. This method ensures accurate projection at attainable computational effort. Calculations applied to visible wavelengths for a realistic holographic projector with $150nm$ sized pixels imaging at $25cm$ find an upscale of 5 is required.

Chapter 8

Conclusion and Perspective

At the start of this PhD videoholography was a technology of the future and our goal was to bring it into reality. It is unfortunate but videoholography through a modulated slab waveguide still remains a technology of the future. At the same time, its need has become more apparent than ever. The currently available display technology has reached an innovation plateau. Its achievements are nothing short of a marvel. State of the art display are bright, their colors are vibrant, they attain flicker free refresh rates and have pixels small enough to be undetectable by the naked eye. That said, an identical statement could be made about displays 5 years ago. Objectively speaking, only incremental changes are left for the current widespread type of display revolving around liquid crystals or organic and quantum dot emitters.

Videoholography offers an alternative to this encountered technological stagnation by supplying an information density increased by orders of magnitude. At its core, holography allows the recording and reconstruction of entire wavefronts making it well suited for 3D displays. It sets itself apart from other technologies by employing the phase of incident light leading to the aforementioned information density. As with anything, this comes with its advantages and disadvantages. On one hand, the inclusion of phase information allows the creation of the ultimate display capable projecting a scene undistinguishable from reality. This includes all the required depth cues for 3D vision and thus offers a superior experience without viewer fatigue. On the other hand, such a display poses stringent technological requirements for proper operation. To control the phase of light, sub-wavelength modulation is necessary. These small pixels furthermore need to be switched sufficiently fast

to achieve a flicker free viewing experience.

Several technologies including phase change materials, transparent conductive oxides and MEMS form good candidates to achieve both spatial and temporal holography requirements. That said, these technologies are still at a rather low level of maturity (expect SWAVE) and thus require more time to become a market ready product. On top of that, they have inherent issues that are not necessarily detrimental but might hinder widescale adoption. Phase change materials work therm-optically, consume significant power and need improvement in their material stability. Other approaches, such as conductive oxides only offer a strong optical effect in the skin depth making an active Fabry-Perot cavity like pixel the most straightforward solution. These devices require an intricate design, advanced patterning and precise process control. Currently, their reliability has not yet been given attention. MEMS suffer from relying on physical movement making them prone to damage. Finally, all of these examples have an external light source which can lead to misalignment. The presented approach in this thesis remedies these issues and is in theory capable of providing a robust, fast and large area holographic display. This is a achieved through the use of a slab waveguide serving as active layer modulated by a metamaterial cladding having embedded electrodes. The light source in this device cannot be misaligned as it is integrated onto the chip. Its power consumption is also low as it only requires electrical fields and not currents to achieve the desired effect.

First, this thesis covered the design parameters of the metamaterial cladding after which blanker layers of $IGZO$, SiO_xN_y and Si_3N_4 were deposited. Ellipsometry measurements revealed that $IGZO$ and Si_3N_4 can be matched well in refractive index over the visible range by tuning the Si_3N_4 growth conditions. An etch process was developed to create high aspect ratio holes into a thick Si_3N_4 layer, which could subsequently be filled by an ALD $IGZO$ deposition. CMP was performed to planarize the layer and OCD spectroscopy and Mueller matrix ellipsometry combined with RCWA revealed that accurate modelling required the inclusion of the $IGZO$ electrode for a good fit. Finally, C-AFM measurements revealed that the embedded pillar shows a conductive behaviour although it remains difficult to qualitatively assess conductivity values since a convolution of all resistive contributions was observed.

In the following chapter, the electro-optical behaviour and characterization of BTO is elaborated. First, a general introduction to the first order electro-optic effect was given. The crystal and domain behaviour of BTO were then highlighted. The created electro-optic measurement setup based an a de Sénarmont compensator was presented. Various types of birefringent BTO

devices were then simulated to set expectations for the measurements. *BTO* substrates were patterned using a metal lift-off procedure and subjected to various poling sequences. Gradual poling clearly resulted in well aligned domains and was the preferred method going forward. Champion devices revealed a Pockels effect of $205pm/V$ and $100pm/V$ for MBE and PLD grown material respectively.

The final two chapters cover the theoretical operation of the proposed holographic display, with the first one focusing on creating accurate modulation inside the active layer and the second looking into sub-wavelength pixel hologram synthesis. To that end, the theoretical background for mode conversion was presented, electric field simulations were performed and electric field patterns were created by leveraging signal analysis. Gratings for beam steering, beam focusing and holography were derived. FDTD simulations of both point based holography and phasemap holography were subsequently calculated, a PSNR of 9.262 was attained for the reconstruction of an RGB image with 500 by 500 pixels. Sub-wavelength pixel hologram synthesis was addressed by considering several common wavefront propagation methods found in Fourier optics. These commonly used techniques cannot reconcile fast calculation with sub-wavelength pixels due to either requiring multiple often lengthy Fourier transforms or by specifically requiring pixels larger than the wavelength. Fortunately, this could be circumvented by a coordinate transform which allows using a single Fourier transform but introduced a degree of data loss. A new approach was introduced that upscaled the desired image such that the encountered data loss could be mostly negated. The MTF was calculated for various upscale factors and contrast settings and indicated that a $5\times$ upscale for a holographic projector with 150nm sized pixels imaging at 25cm was best.

As hinted at above, holography is the natural answer for the issues faced by the current display technology. Slowly over the years, the innovations ranging from lasers to lithography needed to create a holographic display have been developed. Videoholography is now closer than ever, perhaps even at our doorstep thanks to SWAVE. That said, other approaches still require significantly more development. To bring the presented slab waveguide based approach towards a mature application more work is still needed. The major and nearest hurdle faced by the videoholography ERC is the bonding between the metamaterial cladding and electro-optically active waveguide. Near the end of my PhD, several oxide-oxide bonding attempts between the metamaterial and *BTO* were made but all came undone during removal of the silicon carrier wafer.

Perhaps, this is a good moment to reflect on that chosen path. Clearly, the

bonding between the metamaterial and BTO cannot withstand the conditions bonding requires. That is to say, a sequential polishing to thin the carrier wafer and a final selective wet etch to expose BTO. Future work could thus revolve around this, and look towards a thin bonding oxide on both wafers to improve adhesion. Unfortunately, this introduces another challenge as even the thinnest of bonding oxides layers range around 10nm. These would thus introduce a $20nm$ gap between the waveguide and electrodes, which adversely effect the electric field distribution since the permittivity contrast between BTO and common oxides is too high. As a result, a large amount of the electric field will no longer penetrate the waveguide, which is crucial to create adequate refractive index modulation. In hindsight, it is thus uncertain if oxide-oxide bonding is the best method to create the holographic display. An alternative would be to start the device stack from the as-grown BTO layer, and deposit the metamaterial on top of it. This way, bonding to a new carrier wafer can be moved to a different and more compatible layer, for example the metal backplane which is embedded into SiO_2. The most crucial step here will be the pillar electrode etching into the thick SiN. The utmost care needs be taken such that the BTO layer underneath is not damaged while still completely removing the SiN. In hindsight, even the Si_3N_4 layer can be put into question. Optical measurements on the completed metamaterial show that it behaves optically isotropic over the entire visible range. With this in mind, SiO_2 might have been better suited as cladding material, as it would have resulted in better mode confinement by lowering the effective index of the metamaterial.

Another aspect deserving future attention is the electrical driving enabling each of the electrodes which needs to be designed and its operation programmed. Both these aspects can be tackled simultaneously, but would require a few years to address properly. Next to the display, the major issue remaining for videoholography is tied to the required large data quantity and accompanying bandwidth. Current data processing and network capabilities cannot meet the demands for high quality holography in a practical implementation. Enabling efficient and versatile hologram synthesis and driving will require multiple years of advancement in computational power and data processing. Videoholography will thus likely not reach its full potential in the foreseeable future. Instead, it will exist in a limited capacity with either a constrained FOV such that larger pixel sizes can be used or with a reduced number of focal planes such that the information quantity is kept attainable.

At the same time, other applications can leverage techniques stemming from holography. Beam steering, 3D printing and LiDAR already use spatial light modulators or optical phased arrays to encode phase information into their

reflected or emitted light. The presented metamaterial should also not be underestimated as it enabled electrical driving without incurring optical losses, which is useful to a broad range of optical applications. One such applications is a gain tunable laser which currently is a novel research topic considered at imec. A high-quality holographic display seems to be inevitable, but the technology requires more time to reach the needed maturity. The future is bright, let's see what it brings.

Appendix A

Ellipsometry Fitting Models

A.1 Indium Gallium Zinc Oxide

Table A.1: Ellipsometry fitting parameters of the IGZO model.

	Tauc-Lorentz				Drude	
	Amp (eV)	Eo (eV)	Br (eV)	Eg (eV)	ρ (Ωcm)	S. Time (fs)
Amorph.	101.53	4.50	5.60	3.12	0.0036	2.23

A.2 Silicon Oxynitride

Table A.2: Ellipsometry fitting parameters of the $SiON$ model. The employed numbering is identical to Figure 4.3.

	TL Parameter				
	Amp (eV)	Eo (eV)	Br (eV)	Eg (eV)	MSE
1	28.97	7.58	1.43	3.25	19.74
2	26.64	7.55	0.53	3.80	18.40
3	25.86	7.79	0.38	3.87	15.83
4	28.56	8.29	0.32	4.14	12.84
5	42.34	9.29	0.75	5.03	10.91
6	16.36	10.72	0.09	3.08	11.46

A.3 Silicon Nitride

Table A.3: Ellipsometry fitting parameters of the Si_3N_4 model. The employed numbering is identical to Figure 4.5.

	TL Parameter				
	Amp (eV)	Eo (eV)	Br (eV)	Eg (eV)	MSE
1	110.62	8.31	4.37	4.76	27.14
2	50.99	8.12	3.71	2.98	15.57
3	53.08	7.86	4.81	2.75	17.39
4	57.56	7.42	5.95	2.65	20.02
5	50.26	6.73	5.21	2.48	17.22
6	61.95	6.68	6.45	2.45	18.59
7	64.51	6.34	6.42	2.39	14.93
8	65.54	5.97	6.13	2.34	15.90

Bibliography

[1] Martin J. Tovée. *An Introduction to the Visual System*. Cambridge University Press, 7 2008.

[2] T. Shibata, J. Kim, D. M. Hoffman, and M. S. Banks. The zone of comfort: Predicting visual discomfort with stereo displays. *Journal of Vision*, 11(8):11–11, 7 2011.

[3] David M. Hoffman, Ahna R. Girshick, Kurt Akeley, and Martin S. Banks. Vergence–accommodation conflicts hinder visual performance and cause visual fatigue. *Journal of Vision*, 8(3):33, 3 2008.

[4] Helmut Gernsheim. *A concise history of photography*. Dover Publications, 1986.

[5] Robert Hirsch. *Seizing the light : a history of photography*. McGraw-Hill, 2000.

[6] Niépce J. Window at Le Gras, 1827. `https://www.hrc.utexas.edu/niepce-heliograph/` [Accessed: 05-10-2024].

[7] L. Daguerre. Boulevard du Temple, 1997.

[8] Science Museum Collection Group. William Henry Fox Talbot Collection.

[9] Jack H. Coote. *The Illustrated History of Photography*. Fountain Press, 1993.

[10] James Clerk Maxwell and W. D. (William Davidson) Niven. *The scientific papers of James Clerk Maxwell*. Dover Publications, 2003.

[11] Brian Coe. *The birth of photography : the story of the formative years, 1800-1900*. Ash & Grant, 1976.

[12] History of the autochrome | National Science and Media Museum blog. https://blog.scienceandmediamuseum.org.uk/autochromes-the-dawn-of-colour-photography/ [Accessed: 05-10-2024].

[13] Brian Coe. *Colour photography : the first hundred years, 1840-1940*. Ash & Grant, 1978.

[14] Muybridge E. The Horse in Motion, 6 1878. https://www.loc.gov/pictures/item/97502309 [Accessed: 05-10-2024].

[15] Tissandier G. Le Kinétoscope d'Edison: Revue des sciences et de leurs applications aux arts et à l'industrie. *La Nature*, pages 325–326, 1894.

[16] George Elwood Smith and Murray Hill. Three dimensional charge coupled devices, 12 1970.

[17] Willard Sterling Boyle, Magnolia Pl, and George Elwood Smith. Buried channel charge coupled devices, 4 1973.

[18] J.B. Williams. *The Electronics Revolution*. Springer International Publishing, Cham, 2017.

[19] Fujifilm. Introducing FUJIFILM GFX100 II, 2023. https://fujifilm-x.com/global/news/introducing-fujifilm-gfx100-ii/ [Accessed: 05-10-2024].

[20] Kirsch R. Walden Kirsch, 1957. https://www.nist.gov/mathematics-statistics/first-digital-image [Accessed: 05-10-2024].

[21] Ang O. Kombinierter Fernseh- und Rundfunkempfänger, 1933.

[22] Gregory Kramida. Resolving the Vergence-Accommodation Conflict in Head-Mounted Displays. *IEEE Transactions on Visualization and Computer Graphics*, 22(7):1912–1931, 7 2016.

[23] Hong Hua. Advances in Head-Mounted Light-Field Displays for Virtual and Augmented Reality. *Information Display*, 32(4):14–21, 7 2016.

[24] Yao Zhou, Jufan Zhang, and Fengzhou Fang. Vergence-accommodation conflict in optical see-through display: review and prospect. *Results in Optics*, 5:100160, 12 2021.

[25] Meta. Meta Quest 3 Reveal, 2023.

[26] Apple. Worldwide Developers Conference (WWDC), 2023.

[27] David Dunn, Cary Tippets, Kent Torell, Petr Kellnhofer, Kaan Aksit, Piotr Didyk, Karol Myszkowski, David Luebke, and Henry Fuchs. Wide Field Of View Varifocal Near-Eye Display Using See-Through Deformable Membrane Mirrors. *IEEE Transactions on Visualization and Computer Graphics*, 23(4):1322–1331, 4 2017.

[28] David Dunn, Qian Dong, Henry Fuchs, and Praneeth Chakravarthula. Mitigating vergence-accommodation conflict for near-eye displays via deformable beamsplitters. In Wolfgang Osten, Hagen Stolle, and Bernard C. Kress, editors, *Digital Optics for Immersive Displays*, page 104. SPIE, 5 2018.

[29] Sheng Liu, Dewen Cheng, and Hong Hua. An optical see-through head mounted display with addressable focal planes. In *2008 7th IEEE/ACM International Symposium on Mixed and Augmented Reality*, pages 33–42. IEEE, 9 2008.

[30] Kurt Akeley, Simon J. Watt, Ahna Reza Girshick, and Martin S. Banks. A stereo display prototype with multiple focal distances. *ACM Transactions on Graphics*, 23(3):804–813, 8 2004.

[31] Scott C Cahall. Separated pupil optical systems for virtual and augmented reality and methods for displaying images using same. 5 2016.

[32] Brian T. Schowengerdt, Mrinal Murari, and Eric J. Seibel. Volumetric Display using Scanned Fiber Array. *SID Symposium Digest of Technical Papers*, 41(1):653, 2010.

[33] Jannick P. Rolland, Myron W. Krueger, and Alexei Goon. Multifocal planes head-mounted displays. *Applied Optics*, 39(19):3209, 7 2000.

[34] Douglas Lanman and David Luebke. Near-eye light field displays. *ACM Transactions on Graphics*, 32(6):1–10, 11 2013.

[35] Hong Hua and Bahram Javidi. A 3D integral imaging optical see-through head-mounted display. *Optics Express*, 22(11):13484, 6 2014.

[36] Edward H Adelson and James R Bergen. The Plenoptic Function and the Elements of Early Vision. In *Computational Models of Visual Processing*, pages 3–20. MIT Press, 1991.

[37] Marc Levoy and Pat Hanrahan. Light field rendering. In *Proceedings of the 23rd annual conference on Computer graphics and interactive techniques*, pages 31–42, New York, NY, USA, 8 1996. ACM.

[38] Nikhil Balram and Ivana Tošić. Light-Field Imaging and Display Systems. *Information Display*, 32(4):6–13, 7 2016.

[39] Yasuhiro Takaki, Kosuke Tanaka, and Junya Nakamura. Super multi-view display with a lower resolution flat-panel display. *Optics Express*, 19(5):4129, 2 2011.

[40] Gewei Yan, Jiayi Li, Chenxi Zhao, Zengxiang Lu, and Zhaojun Liu. Investigation of Volumetric Three-Dimensional Display Technologies. *SID Symposium Digest of Technical Papers*, 51(S1):136–139, 7 2020.

[41] Barry Blundell and Adam J. Schwarz. *Volumetric three-dimensional display systems*. Wiley, 2000.

[42] Gregg E. Favalora, Joshua Napoli, Deirdre M. Hall, Rick K. Dorval, Michael Giovinco, Michael J. Richmond, and Won S. Chun. 100-million-voxel volumetric display. In Darrel G. Hopper, editor, *Cockpit Displays IX: Displays for Defense Applications*, volume 4712, pages 300–312. SPIE, 8 2002.

[43] Xinzhu Sang, Frank C. Fan, C. C. Jiang, Sam Choi, Wenhua Dou, Chongxiu Yu, and Daxiong Xu. Demonstration of a large-size real-time full-color three-dimensional display. *Optics Letters*, 34(24):3803, 12 2009.

[44] H. Maeda, K. Hirose, J. Yamashita, K. Hirota, and M. Hirose. All-around display for video avatar in real world. In *The Second IEEE and ACM International Symposium on Mixed and Augmented Reality, 2003. Proceedings.*, pages 288–289. IEEE Comput. Soc, 2003.

[45] Elizabeth Downing, Lambertus Hesselink, John Ralston, and Roger Macfarlane. A Three-Color, Solid-State, Three-Dimensional Display. *Science*, 273(5279):1185–1189, 8 1996.

[46] Shiro Suyama, Sakuichi Ohtsuka, Hideaki Takada, Kazutake Uehira, and Sigenobu Sakai. Apparent 3-D image perceived from luminance-modulated two 2-D images displayed at different depths. *Vision Research*, 44(8):785–793, 4 2004.

[47] Ivan T. Lima and Val R. Marinov. Volumetric Display Based on Two-Photon Absorption in Quantum Dot Dispersions. *Journal of Display Technology*, 6(6):221–228, 6 2010.

[48] Voxon Photonics. Voxon VX1, 2017. `https://voxon.co/voxon-vx1-available-for-purchase/` [Accessed: 05-10-2024].

[49] D. E. Smalley, E. Nygaard, K. Squire, J. Van Wagoner, J. Rasmussen, S. Gneiting, K. Qaderi, J. Goodsell, W. Rogers, M. Lindsey, K. Costner, A. Monk, M. Pearson, B. Haymore, and J. Peatross. A photophoretic-Trap volumetric display. *Nature*, 553(7689):486–490, 2018.

[50] Shree K. Nayar and Vijay N. Anand. 3D volumetric display using passive optical scatterers. In *ACM SIGGRAPH 2006 Sketches on - SIGGRAPH '06*, page 106, New York, New York, USA, 2006. ACM Press.

[51] Kota Kumagai, Satoshi Hasegawa, and Yoshio Hayasaki. Volumetric bubble display. *Optica*, 4(3):298, 3 2017.

[52] Ryuji Hirayama, Diego Martinez Plasencia, Nobuyuki Masuda, and Sriram Subramanian. A volumetric display for visual, tactile and audio presentation using acoustic trapping. *Nature*, 575(7782):320–323, 11 2019.

[53] Smalley Daniel. Volumetric Displays: Turning 3-D Inside-Out. *Optics & Photonics News*, 2018.

[54] Barry G. Blundell. On the Uncertain Future of the Volumetric 3D Display Paradigm. *3D Research*, 8(2):11, 6 2017.

[55] SWAVE Photonics. Swave Photonics Developing World's First True Holographic Display Technology To Power Reality-First Spatial Computing, 2024. `https://swave.io/swave-photonics-developing-worlds-first-true-holographic-display-technology-to-power-reality-first-spatial-computing/` [Accessed: 05-10-2024].

[56] D. Gabor. A New Microscopic Principle. *Nature*, 161(4098):777–778, 5 1948.

[57] Dennis Gabor. Holography, 1948-1971. *Science*, 177(4046):299–313, 7 1972.

[58] Gabor D. Microscopy by reconstructed wave-fronts. *Proceedings of the Royal Society of London. Series A. Mathematical and Physical Sciences*, 197(1051):454–487, 7 1949.

[59] G. L. Rogers. Gabor Diffraction Microscopy: the Hologram as a Generalized Zone-Plate. *Nature*, 166(4214):237–237, 8 1950.

[60] T. H. Maiman. Optical and Microwave-Optical Experiments in Ruby. *Physical Review Letters*, 4(11):564–566, 6 1960.

[61] T. H. Maiman. Stimulated Optical Radiation in Ruby. *Nature*, 187(4736):493–494, 8 1960.

[62] A. L. Schawlow and C. H. Townes. Infrared and Optical Masers. *Physical Review*, 112(6):1940–1949, 12 1958.

[63] Emmett N. Leith and Juris Upatnieks. Reconstructed Wavefronts and Communication Theory. *Journal of the Optical Society of America*, 52(10):1123, 10 1962.

[64] Emmett N. Leith and Juris Upatnieks. Wavefront Reconstruction with Continuous-Tone Objects*. *Journal of the Optical Society of America*, 53(12):1377, 12 1963.

[65] Emmett N. Leith and Juris Upatnieks. Wavefront Reconstruction with Diffused Illumination and Three-Dimensional Objects*. *Journal of the Optical Society of America*, 54(11):1295, 11 1964.

[66] Denisyuk Y. N. Photographic Reconstruction of the Optical Properties of an Object in Its Own Scattered Radiation Field. *Soviet Physics Doklady*, 7:543, 1962.

[67] G. Lippmann. Sur la théorie de la photographie des couleurs simples et composées par la méthode interférentielle. *Journal de Physique Théorique et Appliquée*, 3(1):97–107, 1894.

[68] K. S. Pennington and L. H. Lin. Multicolor Wavefront Reconstruction. *Applied Physics Letters*, 7(3):56–57, 8 1965.

[69] A. A. Friesem and R. J. Fedorowicz. Recent Advances in Multicolor Wavefront Reconstruction. *Applied Optics*, 5(6):1085, 6 1966.

[70] Emanuel Marom. Color Imagery by Wavefront Reconstruction. *JOSA, Vol. 57, Issue 1, pp. 101-102*, 57(1):101–102, 1 1967.

[71] P. J. van Heerden. A New Optical Method of Storing and Retrieving Information. *Applied Optics*, 2(4):387, 4 1963.

[72] L. K Anderson. Holographic Optical Memory for Bulk Data Storage. *Bell Lab Report*, 46:318, 1968.

[73] B. R. Brown and A. W. Lohmann. Complex Spatial Filtering with Binary Masks. *Applied Optics*, 5(6):967, 6 1966.

[74] A. W. Lohmann and D. P. Paris. Binary Fraunhofer Holograms, Generated by Computer. *Applied Optics, Vol. 6, Issue 10, pp. 1739-1748*, 6(10):1739–1748, 10 1967.

[75] James P. Waters. Holographic Image Synthesis Utilizing Theoretical Methods. *Applied Physics Letters*, 9(11):405–407, 12 1966.

[76] A. Chutjian and R. J. Collier. Recording and Reconstructing Three-Dimensional Images of Computer-Generated Subjects by Lippmann Integral Photography. *Applied Optics*, 7(1):99, 1 1968.

[77] R W Gerchberg and W O Saxton. A Practical Algorithm for the Determination of Phase from Image and Diffraction Plane Pictures. *Optik*, (35):227–246, 1972.

[78] Lord Rayleigh. On the passage of waves through apertures in Plane screens, and allied problems. *The London, Edinburgh, and Dublin Philosophical Magazine and Journal of Science*, 43(263):259–272, 4 1897.

[79] Michał Makowski. Iterative design of multiplane holograms: experiments and applications. *Optical Engineering*, 46(4):045802, 4 2007.

[80] Michal Makowski, Maciej Sypek, and Andrzej Kolodziejczyk. Colorful reconstructions from a thin multi-plane phase hologram. *Optics Express*, 16(15):11618, 7 2008.

[81] Alejandro Velez-Zea. Iterative multiplane hologram generation with mixed constraint. *Applied Optics*, 60(2):224, 1 2021.

[82] Alejandro Velez-Zea, John Fredy Barrera-Ramirez, and Roberto Torroba. Alternative constraints for improved multiplane hologram generation. *Applied Optics*, 61(5):B8, 2 2022.

[83] Hao Zhang, Liangcai Cao, and Guofan Jin. Computer-generated hologram with occlusion effect using layer-based processing. *Applied Optics*, 56(13):F138, 5 2017.

[84] Jung-Ping Liu and Heng-Kuang Liao. Fast occlusion processing for a polygon-based computer-generated hologram using the slice-by-slice silhouette method. *Applied Optics*, 57(1):A215, 1 2018.

[85] Shuangting Liu, Hui Wei, Ni Li, Zihan Liu, and Jiaqi Zhang. Occlusion calculation algorithm for computer generated hologram based on ray tracing. *Optics Communications*, 443:76–85, 7 2019.

[86] Erdem Sahin, Elena Stoykova, Jani Mäkinen, and Atanas Gotchev. Computer-Generated Holograms for 3D Imaging. *ACM Computing Surveys*, 53(2):1–35, 3 2021.

[87] Xu Zhang, Guoqiang Lv, Zi Wang, Ziang Hu, Shanshan Ding, and Qibin Feng. Resolution-enhanced holographic stereogram based on integral imaging using an intermediate-view synthesis technique. *Optics Communications*, 457:124656, 2 2020.

[88] Pierre St. Hilaire. Modulation transfer function and optimum sampling of holographic stereograms. *Applied Optics*, 33(5):768–774, 2 1994.

[89] Michael W. Halle, Stephen A. Benton, Michael A. Klug, and John S. Underkoffler. Ultragram: a generalized holographic stereogram. In Stephen A. Benton, editor, *https://doi.org/10.1117/12.44722*, volume 1461, pages 142–155. SPIE, 7 1991.

[90] Natan T. Shaked, Barak Katz, and Joseph Rosen. Review of three-dimensional holographic imaging by multiple-viewpoint-projection based methods. *Applied Optics*, 48(34):H120, 12 2009.

[91] David Abookasis and Joseph Rosen. Three types of computer-generated hologram synthesized from multiple angular viewpoints of a three-dimensional scene. *Applied Optics*, 45(25):6533, 9 2006.

[92] Yusuke Sando, Masahide Itoh, and Toyohiko Yatagai. Color computer-generated holograms from projection images. *Optics Express*, 12(11):2487, 5 2004.

[93] Yanfeng Su, Zhijian Cai, Kai Wu, Lingyan Shi, Feng Zhou, Haidong Chen, and Jianhong Wu. Projection-Type Multiview Holographic Three-Dimensional Display Using a Single Spatial Light Modulator and a Directional Diffractive Device. *IEEE Photonics Journal*, 10(5):1–12, 10 2018.

[94] Mark E. Lucente. Interactive computation of holograms using a look-up table. *Journal of Electronic Imaging*, 2(1):28, 1 1993.

[95] Liang Shi, Beichen Li, Changil Kim, Petr Kellnhofer, and Wojciech Matusik. Towards real-time photorealistic 3D holography with deep neural networks. *Nature*, 591(7849):234–239, 3 2021.

[96] Liang Shi, Beichen Li, and Wojciech Matusik. End-to-end learning of 3D phase-only holograms for holographic display. *Light: Science & Applications*, 11(1):247, 8 2022.

[97] Kyoji Matsushima and Tomoyoshi Shimobaba. Band-limited angular spectrum method for numerical simulation of free-space propagation in far and near fields. *Optics Express*, 17(22):19662, 10 2009.

[98] Wooyoung Lee, Dajeong Im, Jeongyeup Paek, Joonku Hahn, Hwi Kim, Y J Hong, H.-J Kim, J Choi, J.-H Hahn, H Park, S.-W Kim, N Min, and B Chen. Semi-analytic texturing algorithm for polygon computer-generated holograms References and links. 2014.

[99] Seymour Trester. Computer-simulated Fresnel holography. *European Journal of Physics*, 21(4):317–331, 7 2000.

[100] Muharrem Bayraktar and Meriç Özcan. Method to calculate the far field of three-dimensional objects for computer-generated holography. *Applied Optics*, 49(24):4647, 8 2010.

[101] Yan Zhao, Liangcai Cao, Hao Zhang, Dezhao Kong, and Guofan Jin. Accurate calculation of computer-generated holograms using angular-spectrum layer-oriented method. *Optics Express*, 23(20):25440, 10 2015.

[102] Pierre-Alexandre Blanche. Holography, and the future of 3D display. *Light: Advanced Manufacturing*, 2(4):1, 12 2021.

[103] Hou-Tong Chen, Antoinette J Taylor, and Nanfang Yu. A review of metasurfaces: physics and applications. *Reports on Progress in Physics*, 79(7):076401, 7 2016.

[104] Hui-Hsin Hsiao, Cheng Hung Chu, and Din Ping Tsai. Fundamentals and Applications of Metasurfaces. *Small Methods*, 1(4):1600064, 4 2017.

[105] Jie Hu, Sankhyabrata Bandyopadhyay, Yu-hui Liu, and Li-yang Shao. A Review on Metasurface: From Principle to Smart Metadevices. *Frontiers in Physics*, 8:502, 1 2021.

[106] S. Pancharatnam. Generalized theory of interference and its applications. *Proceedings of the Indian Academy of Sciences - Section A*, 44(6):398–417, 12 1956.

[107] M V Berry. Quantal phase factors accompanying adiabatic changes. *Proceedings of the Royal Society of London. A. Mathematical and Physical Sciences*, 392(1802):45–57, 3 1984.

[108] Yinghui Guo, Mingbo Pu, Fei Zhang, Mingfeng Xu, Xiong Li, Xiaoliang Ma, and Xiangang Luo. Classical and generalized geometric phase in electromagnetic metasurfaces. *Photonics Insights*, 1(1):R03, 8 2022.

[109] Chandroth Pannian Jisha, Stefan Nolte, and Alessandro Alberucci. Geometric Phase in Optics: From Wavefront Manipulation to Waveguiding. *Laser & Photonics Reviews*, 15(10):2100003, 10 2021.

[110] Eliahu Cohen, Hugo Larocque, Frédéric Bouchard, Farshad Nejadsattari, Yuval Gefen, and Ebrahim Karimi. Geometric phase from Aharonov–Bohm to Pancharatnam–Berry and beyond. *Nature Reviews Physics*, 1(7):437–449, 6 2019.

[111] Julio C. Gutiérrez-Vega. Pancharatnam–Berry phase of optical systems. *Optics Letters*, 36(7):1143, 4 2011.

[112] Jeeva Anandan. The geometric phase. Technical report, 1992.

[113] Lei Zhang, Shuo Liu, Lianlin Li, and Tie Jun Cui. Spin-Controlled Multiple Pencil Beams and Vortex Beams with Different Polarizations Generated by Pancharatnam-Berry Coding Metasurfaces. *ACS Applied Materials & Interfaces*, 9(41):36447–36455, 10 2017.

[114] Robert C. Devlin, Mohammadreza Khorasaninejad, Wei Ting Chen, Jaewon Oh, and Federico Capasso. Broadband high-efficiency dielectric metasurfaces for the visible spectrum. *Proceedings of the National Academy of Sciences*, 113(38):10473–10478, 9 2016.

[115] Zhixiong Shen, Shenghang Zhou, Xinan Li, Shijun Ge, Peng Chen, Wei Hu, and Yanqing Lu. Liquid crystal integrated metalens with tunable chromatic aberration. *Advanced Photonics*, 2(03):1, 5 2020.

[116] Weijie Luo, Shulin Sun, He-Xiu Xu, Qiong He, and Lei Zhou. Transmissive Ultrathin Pancharatnam-Berry Metasurfaces with nearly 100% Efficiency. *Physical Review Applied*, 7(4):044033, 4 2017.

[117] Guoxing Zheng, Holger Mühlenbernd, Mitchell Kenney, Guixin Li, Thomas Zentgraf, and Shuang Zhang. Metasurface holograms reaching 80% efficiency. *Nature Nanotechnology*, 10(4):308–312, 4 2015.

[118] Ke Li, Yinghui Guo, Mingbo Pu, Xiong Li, Xiaoliang Ma, Zeyu Zhao, and Xiangang Luo. Dispersion controlling meta-lens at visible frequency. *Optics Express*, 25(18):21419, 9 2017.

[119] Lingling Huang, Holger Mühlenbernd, Xiaowei Li, Xu Song, Benfeng Bai, Yongtian Wang, and Thomas Zentgraf. Broadband Hybrid Holographic Multiplexing with Geometric Metasurfaces. *Advanced Materials*, 27(41):6444–6449, 11 2015.

[120] Elhanan Maguid, Igor Yulevich, Michael Yannai, Vladimir Kleiner, Mark L Brongersma, and Erez Hasman. Multifunctional interleaved geometric-phase dielectric metasurfaces. *Light: Science & Applications*, 6(8):e17027–e17027, 2 2017.

[121] Dandan Wen, Fuyong Yue, Guixin Li, Guoxing Zheng, Kinlong Chan, Shumei Chen, Ming Chen, King Fai Li, Polis Wing Han Wong, Kok Wai Cheah, Edwin Yue Bun Pun, Shuang Zhang, and Xianzhong Chen. Helicity multiplexed broadband metasurface holograms. *Nature Communications*, 6(1):8241, 9 2015.

[122] Peng Chen, Bing-Yan Wei, Wei Hu, and Yan-Qing Lu. Liquid-Crystal-Mediated Geometric Phase: From Transmissive to Broadband Reflective Planar Optics. *Advanced Materials*, 32(27):1903665, 9 2019.

[123] René Geromel, Roman Rennerich, Thomas Zentgraf, and Heinz Kitzerow. Geometric-phase metalens to be used for tunable optical tweezers in microfluidics. *Liquid Crystals*, pages 1–11, 1 2023.

[124] Hang Wang, Fang Ling, and Bin Zhang. Tunable metasurfaces for independent control of linearly and circularly polarized terahertz waves. *Optics Express*, 28(24):36316, 11 2020.

[125] Yujie Dong, Xiyu Sun, Yan Li, and Yi Liu. Full-space terahertz metasurface based on thermally tunable InSb. *Journal of Physics D: Applied Physics*, 55(45):455105, 11 2022.

[126] Peng Zhang, Bo Fang, Tianqi Zhao, Chenxia Li, Changyu Shen, Zhi Hong, and Xufeng Jing. Terahertz wave tunable metalens based on Phase change material coded metasurface. *Journal of Lightwave Technology*, 2023.

[127] Michael Chen, Minseok Kim, Alex M.H. Wong, and George V. Eleftheriades. Huygens' metasurfaces from microwaves to optics: a review. *Nanophotonics*, 7(6):1207–1231, 6 2018.

[128] S. A. Schelkunoff. Some Equivalence Theorems of Electromagnetics and Their Application to Radiation Problems. *Bell System Technical Journal*, 15(1):92–112, 1 1936.

[129] C. L. Holloway, E. F. Kuester, J. A. Gordon, J. O'Hara, J. Booth, and D. R. Smith. An Overview of the Theory and Applications of Metasurfaces: The Two-Dimensional Equivalents of Metamaterials. *IEEE Antennas and Propagation Magazine*, 54(2):10–35, 4 2012.

[130] Karim Achouri, Mohamed A. Salem, and Christophe Caloz. General Metasurface Synthesis Based on Susceptibility Tensors. *IEEE Transactions on Antennas and Propagation*, 63(7):2977–2991, 7 2015.

[131] M. Albooyeh, Sergei Tretyakov, and Constantin Simovski. Electromagnetic characterization of bianisotropic metasurfaces on refractive substrates: General theoretical framework. *Annalen der Physik*, 528(9-10):721–737, 10 2016.

[132] E.F. Kuester, M.A. Mohamed, M. Piket-May, and C.L. Holloway. Averaged transition conditions for electromagnetic fields at a metafilm. *IEEE Transactions on Antennas and Propagation*, 51(10):2641–2651, 10 2003.

[133] C.L. Holloway, M.A. Mohamed, E.F. Kuester, and A. Dienstfrey. Reflection and Transmission Properties of a Metafilm: With an Application to a Controllable Surface Composed of Resonant Particles. *IEEE Transactions on Electromagnetic Compatibility*, 47(4):853–865, 11 2005.

[134] Teemu Niemi, Antti O. Karilainen, and Sergei A. Tretyakov. Synthesis of Polarization Transformers. *IEEE Transactions on Antennas and Propagation*, 61(6):3102–3111, 6 2013.

[135] Carl Pfeiffer and Anthony Grbic. Metamaterial Huygens' Surfaces: Tailoring Wave Fronts with Reflectionless Sheets. *Physical Review Letters*, 110(19):197401, 5 2013.

[136] Michael Selvanayagam and George V. Eleftheriades. Discontinuous electromagnetic fields using orthogonal electric and magnetic currents for wavefront manipulation. *Optics Express*, 21(12):14409, 6 2013.

[137] Manuel Decker, Isabelle Staude, Matthias Falkner, Jason Dominguez, Dragomir N. Neshev, Igal Brener, Thomas Pertsch, and Yuri S. Kivshar. High-Efficiency Dielectric Huygens' Surfaces. *Advanced Optical Materials*, 3(6):813–820, 6 2015.

[138] Weitao Song, Xinan Liang, Shiqiang Li, Dongdong Li, Ramón Paniagua-Domínguez, Keng Heng Lai, Qunying Lin, Yuanjin Zheng, and Arseniy I. Kuznetsov. Large-Scale Huygens' Metasurfaces for Holographic 3D Near-Eye Displays. *Laser & Photonics Reviews*, 15(9):2000538, 9 2021.

[139] Yao-Wei Huang, Ho Wai Howard Lee, Ruzan Sokhoyan, Ragip A. Pala, Krishnan Thyagarajan, Seunghoon Han, Din Ping Tsai, and Harry A. Atwater. Gate-Tunable Conducting Oxide Metasurfaces. *Nano Letters*, 16(9):5319–5325, 9 2016.

[140] Francesco Monticone, Nasim Mohammadi Estakhri, and Andrea Alù. Full Control of Nanoscale Optical Transmission with a Composite Metascreen. *Physical Review Letters*, 110(20):203903, 5 2013.

[141] Jierong Cheng, Davood Ansari-Oghol-Beig, and Hossein Mosallaei. Wave manipulation with designer dielectric metasurfaces. *Optics Letters*, 39(21):6285, 11 2014.

[142] Michael Selvanayagam and George V. Eleftheriades. Polarization Control Using Tensor Huygens Surfaces. *IEEE Transactions on Antennas and Propagation*, 62(12):6155–6168, 12 2014.

[143] Carl Pfeiffer, Cheng Zhang, Vishva Ray, L. Jay Guo, and Anthony Grbic. Polarization rotation with ultra-thin bianisotropic metasurfaces. *Optica*, 3(4):427, 4 2016.

[144] Carl Pfeiffer, Naresh K. Emani, Amr M. Shaltout, Alexandra Boltasseva, Vladimir M. Shalaev, and Anthony Grbic. Efficient Light Bending with Isotropic Metamaterial Huygens' Surfaces. *Nano Letters*, 14(5):2491–2497, 5 2014.

[145] Wenyu Zhao, Huan Jiang, Bingyi Liu, Jie Song, Yongyuan Jiang, Chengchun Tang, and Junjie Li. Dielectric Huygens' Metasurface for

High-Efficiency Hologram Operating in Transmission Mode. *Scientific Reports*, 6(1):30613, 7 2016.

[146] Katie E. Chong, Lei Wang, Isabelle Staude, Anthony R. James, Jason Dominguez, Sheng Liu, Ganapathi S. Subramania, Manuel Decker, Dragomir N. Neshev, Igal Brener, and Yuri S. Kivshar. Efficient Polarization-Insensitive Complex Wavefront Control Using Huygens' Metasurfaces Based on Dielectric Resonant Meta-atoms. *ACS Photonics*, 3(4):514–519, 4 2016.

[147] Zhuochao Wang, Xumin Ding, Kuang Zhang, Badreddine Ratni, Nawaz Burokur, Xuemai Gu, Qun Wu, Z Wang, X Ding, K Zhang, X Gu, Q Wu, B Ratni, and S N Burokur. Huygens Metasurface Holograms with the Modulation of Focal Energy Distribution. *Advanced Optical Materials*, 6(12):1800121, 6 2018.

[148] Zhuochao Wang, Xumin Ding, Shengying Liu, Kuang Zhang, and Qun Wu. Polarization-multiplexed Huygens metasurface holography. *Optics Letters*, 45(19):5488, 10 2020.

[149] Weitao Song, Xinan Liang, Shiqiang Li, Parikshit Moitra, Xuewu Xu, Emmanuel Lassalle, Yuanjin Zheng, Yongtian Wang, Ramón Paniagua-Domínguez, Arseniy I Kuznetsov, W Song, Y Wang, X Liang, S Li, P Moitra, X Xu, E Lassalle, R Paniagua-Domínguez, A I Kuznetsov, and Y Zheng. Retinal Projection Near-Eye Displays with Huygens' Metasurfaces. *Advanced Optical Materials*, 11(5):2202348, 3 2023.

[150] Filippo Costa, Agostino Monorchio, and Giuliano Manara. An Overview of Equivalent Circuit Modeling Techniques of Frequency Selective Surfaces and Metasurfaces. *The Applied Computational Electromagnetics Society Journal (ACES)*, 29(12):960–976, 8 2021.

[151] Shulin Sun, Qiong He, Shiyi Xiao, Qin Xu, Xin Li, and Lei Zhou. Gradient-index meta-surfaces as a bridge linking propagating waves and surface waves. *Nature Materials*, 11(5):426–431, 5 2012.

[152] Mingbo Pu, Po Chen, Changtao Wang, Yanqin Wang, Zeyu Zhao, Chenggang Hu, Cheng Huang, and Xiangang Luo. Broadband anomalous reflection based on gradient low-Q meta-surface. *AIP Advances*, 3(5), 5 2013.

[153] Yuval Yifat, Michal Eitan, Zeev Iluz, Yael Hanein, Amir Boag, and Jacob Scheuer. Highly Efficient and Broadband Wide-Angle Holography Using Patch-Dipole Nanoantenna Reflectarrays. *Nano Letters*, 14(5):2485–2490, 5 2014.

[154] Ke Chen, Yijun Feng, Francesco Monticone, Junming Zhao, Bo Zhu, Tian Jiang, Lei Zhang, Yongjune Kim, Xumin Ding, Shuang Zhang, Andrea Alù, and Cheng-Wei Qiu. A Reconfigurable Active Huygens' Metalens. *Advanced Materials*, 29(17):1606422, 5 2017.

[155] Bo O. Zhu, Junming Zhao, and Yijun Feng. Active impedance metasurface with full 360° reflection phase tuning. *Scientific Reports*, 3(1):3059, 10 2013.

[156] Minyeong Yoo and Sungjoon Lim. Active metasurface for controlling reflection and absorption properties. *Applied Physics Express*, 7(11):112204, 11 2014.

[157] Quan Li, Zhen Tian, Xueqian Zhang, Ningning Xu, Ranjan Singh, Jianqiang Gu, Peng Lv, Lin-Bao Luo, Shuang Zhang, Jiaguang Han, and Weili Zhang. Dual control of active graphene–silicon hybrid metamaterial devices. *Carbon*, 90:146–153, 8 2015.

[158] O. V. Polischuk, V. S. Melnikova, and V. V. Popov. Giant cross-polarization conversion of terahertz radiation by plasmons in an active graphene metasurface. *Applied Physics Letters*, 109(13), 9 2016.

[159] Jürgen Sautter, Isabelle Staude, Manuel Decker, Evgenia Rusak, Dragomir N. Neshev, Igal Brener, and Yuri S. Kivshar. Active tuning of all-dielectric metasurfaces. *ACS Nano*, 9(4):4308–4315, 4 2015.

[160] Minseok Kim, Junho Jeong, Joyce K. S. Poon, and George V. Eleftheriades. Vanadium-dioxide-assisted digital optical metasurfaces for dynamic wavefront engineering. *Journal of the Optical Society of America B*, 33(5):980, 5 2016.

[161] Prasad P Iyer, Mihir Pendharkar, Jon A Schuller, P P Iyer, M Pendharkar, and J A Schuller. Electrically Reconfigurable Metasurfaces Using Heterojunction Resonators. *Advanced Optical Materials*, 4(10):1582–1588, 10 2016.

[162] Cheng Hung Chu, Ming Lun Tseng, Jie Chen, Pin Chieh Wu, Yi Hao Chen, Hsiang Chu Wang, Ting Yu Chen, Wen Ting Hsieh, Hui Jun Wu, Greg Sun, and Din Ping Tsai. Active dielectric metasurface based on phase-change medium. *Laser & Photonics Reviews*, 10(6):986–994, 11 2016.

[163] Tianyou Li, Lingling Huang, Juan Liu, Yongtian Wang, and Thomas Zentgraf. Tunable wave plate based on active plasmonic metasurfaces. *Optics Express*, 25(4):4216, 2 2017.

[164] Ehsan Arbabi, Amir Arbabi, Seyedeh Mahsa Kamali, Yu Horie, Mohammad Sadegh Faraji-Dana, and Andrei Faraon. MEMS-tunable dielectric metasurface lens. *Nature Communications 2018 9:1*, 9(1):1–9, 2 2018.

[165] Rashid Zia, Jon A. Schuller, Anu Chandran, and Mark L. Brongersma. Plasmonics: the next chip-scale technology. *Materials Today*, 9(7-8):20–27, 7 2006.

[166] Mark L. Brongersma and Vladimir M. Shalaev. The Case for Plasmonics. *Science*, 328(5977):440–441, 4 2010.

[167] Ekmel Ozbay. Plasmonics: Merging Photonics and Electronics at Nanoscale Dimensions. *Science*, 311(5758):189–193, 1 2006.

[168] Fei Ding, Yuanqing Yang, Rucha A. Deshpande, and Sergey I. Bozhevolnyi. A review of gap-surface plasmon metasurfaces: Fundamentals and applications. *Nanophotonics*, 7(6):1129–1156, 6 2018.

[169] Nanfang Yu, Patrice Genevet, Francesco Aieta, Mikhail A. Kats, Romain Blanchard, Guillaume Aoust, Jean Philippe Tetienne, Zeno Gaburro, and Federico Capasso. Flat optics: Controlling wavefronts with optical antenna metasurfaces. *IEEE Journal on Selected Topics in Quantum Electronics*, 19(3), 2013.

[170] Xingjie Ni, Alexander V. Kildishev, and Vladimir M. Shalaev. Metasurface holograms for visible light. *Nature Communications*, 4(1):2807, 12 2013.

[171] Nanfang Yu, Patrice Genevet, Mikhail A. Kats, Francesco Aieta, Jean-Philippe Tetienne, Federico Capasso, and Zeno Gaburro. Light Propagation with Phase Discontinuities: Generalized Laws of Reflection and Refraction. *Science*, 334(6054):333–337, 10 2011.

[172] Xingjie Ni, Naresh K. Emani, Alexander V. Kildishev, Alexandra Boltasseva, and Vladimir M. Shalaev. Broadband Light Bending with Plasmonic Nanoantennas. *Science*, 335(6067):427–427, 1 2012.

[173] Anders Pors, Michael G. Nielsen, René Lynge Eriksen, and Sergey I. Bozhevolnyi. Broadband focusing flat mirrors based on plasmonic gradient metasurfaces. *Nano Letters*, 13(2):829–834, 2 2013.

[174] Nanfang Yu, Francesco Aieta, Patrice Genevet, Mikhail A Kats, Zeno Gaburro, and Federico Capasso. A Broadband, Background-Free Quarter-Wave Plate Based on Plasmonic Metasurfaces. *Nano Lett*, 12:11, 2012.

[175] Nina Meinzer, William L. Barnes, and Ian R. Hooper. Plasmonic meta-atoms and metasurfaces. *Nature Photonics*, 8(12):889–898, 12 2014.

[176] Jeffrey N. Anker, W. Paige Hall, Olga Lyandres, Nilam C. Shah, Jing Zhao, and Richard P. Van Duyne. Biosensing with plasmonic nanosensors. *Nature Materials*, 7(6):442–453, 6 2008.

[177] Patrice Genevet and Federico Capasso. Holographic optical metasurfaces: a review of current progress. *Reports on Progress in Physics*, 78(2):024401, 2 2015.

[178] William L. Barnes, Alain Dereux, and Thomas W. Ebbesen. Surface plasmon subwavelength optics. *Nature*, 424(6950):824–830, 8 2003.

[179] Shulin Sun, Kuang-Yu Yang, Chih-Ming Wang, Ta-Ko Juan, Wei Ting Chen, Chun Yen Liao, Qiong He, Shiyi Xiao, Wen-Ting Kung, Guang-Yu Guo, Lei Zhou, and Din Ping Tsai. High-Efficiency Broadband Anomalous Reflection by Gradient Meta-Surfaces. *Nano Letters*, 12(12):6223–6229, 12 2012.

[180] Bo Wang, Baogang Quan, Jingwen He, Zhenwei Xie, Xinke Wang, Junjie Li, Qiang Kan, and Yan Zhang. Wavelength de-multiplexing metasurface hologram. *Scientific Reports*, 6(1):35657, 10 2016.

[181] P.R. West, S. Ishii, G.V. Naik, N.K. Emani, V.M. Shalaev, and A. Boltasseva. Searching for better plasmonic materials. *Laser & Photonics Reviews*, 4(6):795–808, 11 2010.

[182] Alexandra Boltasseva and Harry A. Atwater. Low-Loss Plasmonic Metamaterials. *Science*, 331(6015):290–291, 1 2011.

[183] Jacob B. Khurgin and Alexandra Boltasseva. Reflecting upon the losses in plasmonics and metamaterials. *MRS Bulletin*, 37(8):768–779, 8 2012.

[184] Alexandra Boltasseva. Empowering plasmonics and metamaterials technology with new material platforms. *MRS Bulletin*, 39(5):461–468, 5 2014.

[185] Gururaj V. Naik, Vladimir M. Shalaev, and Alexandra Boltasseva. Alternative Plasmonic Materials: Beyond Gold and Silver. *Advanced Materials*, 25(24):3264–3294, 6 2013.

[186] Fei Zhou, Ye Liu, Weiping Cai, W L Barnes, A Dereux, T W Ebbesen, H J Lezec, A Degiron, E Devaux, R A Linke, L Martin-Moreno, and F J Garcia-Vidal. Plasmonic holographic imaging with V-shaped nanoantenna array. *Optics Express, Vol. 21, Issue 4, pp. 4348-4354*, 21(4):4348–4354, 2 2013.

[187] Wei Ting Chen, Kuang Yu Yang, Chih Ming Wang, Yao Wei Huang, Greg Sun, I. Da Chiang, Chun Yen Liao, Wei Lun Hsu, Hao Tsun Lin, Shulin Sun, Lei Zhou, Ai Qun Liu, and Din Ping Tsai. High-efficiency broadband meta-hologram with polarization-controlled dual images. *Nano Letters*, 14(1):225–230, 1 2014.

[188] Paloma A. Huidobro, Matthias Kraft, Stefan A. Maier, and John B. Pendry. Graphene as a Tunable Anisotropic or Isotropic Plasmonic Metasurface. *ACS Nano*, 10(5):5499–5506, 5 2016.

[189] Antonino Cala Lesina, Dominic Goodwill, Eric Bernier, Lora Ramunno, and Pierre Berini. Tunable Plasmonic Metasurfaces for Optical Phased Arrays. *IEEE Journal of Selected Topics in Quantum Electronics*, 27(1), 1 2021.

[190] Zi-Lan Deng and Guixin Li. Metasurface optical holography. *Materials Today Physics*, 3:16–32, 12 2017.

[191] Qiang Jiang, Guofan Jin, and Liangcai Cao. When metasurface meets hologram: principle and advances. *Advances in Optics and Photonics*, 11(3):518, 2019.

[192] Amir Arbabi, Ehsan Arbabi, Yu Horie, Seyedeh Mahsa Kamali, and Andrei Faraon. Planar metasurface retroreflector. *Nature Photonics*, 11(7):415–420, 7 2017.

[193] M. Khorasaninejad, A. Y. Zhu, C. Roques-Carmes, W. T. Chen, J. Oh, I. Mishra, R. C. Devlin, and F. Capasso. Polarization-Insensitive Metalenses at Visible Wavelengths. *Nano Letters*, 16(11):7229–7234, 11 2016.

[194] Amir Arbabi, Yu Horie, Mahmood Bagheri, and Andrei Faraon. Dielectric metasurfaces for complete control of phase and polarization with subwavelength spatial resolution and high transmission. *Nature Nanotechnology*, 10(11):937–943, 2015.

[195] Seyedeh Mahsa Kamali, Ehsan Arbabi, Amir Arbabi, Yu Horie, and Andrei Faraon. Highly tunable elastic dielectric metasurface lenses. *Laser & Photonics Reviews*, 10(6):1002–1008, 11 2016.

[196] Sonny Vo, David Fattal, Wayne V. Sorin, Zhen Peng, Tho Tran, Marco Fiorentino, and Raymond G. Beausoleil. Sub-Wavelength Grating Lenses With a Twist. *IEEE Photonics Technology Letters*, 26(13):1375–1378, 7 2014.

[197] Amir Arbabi, Yu Horie, Alexander J. Ball, Mahmood Bagheri, and Andrei Faraon. Subwavelength-thick lenses with high numerical apertures and large efficiency based on high-contrast transmitarrays. *Nature Communications*, 6(1):7069, 5 2015.

[198] Yaoyao Liang, Hongzhan Liu, Faqiang Wang, Hongyun Meng, Jianping Guo, Jinfeng Li, and Zhongchao Wei. High-Efficiency, Near-Diffraction Limited, Dielectric Metasurface Lenses Based on Crystalline Titanium Dioxide at Visible Wavelengths. *Nanomaterials*, 8(5):288, 4 2018.

[199] Ehsan Arbabi, Amir Arbabi, Seyedeh Mahsa Kamali, Yu Horie, and Andrei Faraon. Multiwavelength polarization-insensitive lenses based on dielectric metasurfaces with meta-molecules. *Optica*, 3(6):628, 6 2016.

[200] Philippe Lalanne, Simion Astilean, Pierre Chavel, Edmond Cambril, and Huguette Launois. Design and fabrication of blazed binary diffractive elements with sampling periods smaller than the structural cutoff. *Journal of the Optical Society of America A*, 16(5):1143, 5 1999.

[201] Mikael P. Backlund, Amir Arbabi, Petar N. Petrov, Ehsan Arbabi, Saumya Saurabh, Andrei Faraon, and W. E. Moerner. Removing orientation-induced localization biases in single-molecule microscopy using a broadband metasurface mask. *Nature Photonics*, 10(7):459–462, 7 2016.

[202] Ehsan Arbabi, Amir Arbabi, Seyedeh Mahsa Kamali, Yu Horie, and Andrei Faraon. Multiwavelength metasurfaces through spatial multiplexing. *Scientific Reports*, 6(1):32803, 9 2016.

[203] J.P. Balthasar Mueller. Metasurface Polarization Optics: Independent Phase Control of Arbitrary Orthogonal States of Polarization. *Physical Review Letters*, 118(11):113901, 3 2017.

[204] Guixin Li, Shuang Zhang, and Thomas Zentgraf. Nonlinear photonic metasurfaces. *Nature Reviews Materials*, 2, 2017.

[205] Alexander Krasnok, Mykhailo Tymchenko, and Andrea Alù. Nonlinear metasurfaces: a paradigm shift in nonlinear optics. *Materials Today*, 21(1):8–21, 1 2018.

[206] Shay Keren-Zur, Lior Michaeli, Haim Suchowski, and Tal Ellenbogen. Shaping light with nonlinear metasurfaces. *Advances in Optics and Photonics*, 10(1):309, 3 2018.

[207] Euclides Almeida, Ora Bitton, and Yehiam Prior. Nonlinear metamaterials for holography. *Nature Communications*, 7(1):12533, 8 2016.

[208] Weimin Ye, Franziska Zeuner, Xin Li, Bernhard Reineke, Shan He, Cheng-Wei Qiu, Juan Liu, Yongtian Wang, Shuang Zhang, and Thomas Zentgraf. Spin and wavelength multiplexed nonlinear metasurface holography. *Nature Communications*, 7(1):11930, 6 2016.

[209] V. Berger. Nonlinear Photonic Crystals. *Physical Review Letters*, 81(19):4136–4139, 11 1998.

[210] Noa Voloch Bloch, Keren Shemer, Asia Shapira, Roy Shiloh, Irit Juwiler, and Ady Arie. Twisting Light by Nonlinear Photonic Crystals. *Physical Review Letters*, 108(23):233902, 6 2012.

[211] Asia Shapira, Irit Juwiler, and Ady Arie. Nonlinear computer-generated holograms. *Optics Letters*, 36(15):3015, 8 2011.

[212] Shay Keren-Zur, Ori Avayu, Lior Michaeli, and Tal Ellenbogen. Nonlinear Beam Shaping with Plasmonic Metasurfaces. *ACS Photonics*, 3(1):117–123, 1 2016.

[213] Lei Wang, Sergey Kruk, Kirill Koshelev, Ivan Kravchenko, Barry Luther-Davies, and Yuri Kivshar. Nonlinear Wavefront Control with All-Dielectric Metasurfaces. *Nano Letters*, 18(6):3978–3984, 6 2018.

[214] Omri Wolf, Salvatore Campione, Alexander Benz, Arvind P. Ravikumar, Sheng Liu, Ting S. Luk, Emil A. Kadlec, Eric A. Shaner, John F. Klem, Michael B. Sinclair, and Igal Brener. Phased-array sources based on nonlinear metamaterial nanocavities. *Nature Communications*, 6(1):7667, 7 2015.

[215] Mykhailo Tymchenko, J. Sebastian Gomez-Diaz, Jongwon Lee, Nishant Nookala, Mikhail A. Belkin, and Andrea Alù. Gradient Nonlinear Pancharatnam-Berry Metasurfaces. *Physical Review Letters*, 115(20):207403, 11 2015.

[216] Nadav Segal, Shay Keren-Zur, Netta Hendler, and Tal Ellenbogen. Controlling light with metamaterial-based nonlinear photonic crystals. *Nature Photonics*, 9(3):180–184, 3 2015.

[217] Nishant Nookala, Jongwon Lee, Mykhailo Tymchenko, J. Sebastian Gomez-Diaz, Frederic Demmerle, Gerhard Boehm, Kueifu Lai, Gennady Shvets, Markus-Christian Amann, Andrea Alu, and Mikhail Belkin. Ultrathin gradient nonlinear metasurface with a giant nonlinear response. *Optica*, 3(3):283, 3 2016.

[218] Euclides Almeida, Guy Shalem, and Yehiam Prior. Subwavelength nonlinear phase control and anomalous phase matching in plasmonic metasurfaces. *Nature Communications*, 7(1):10367, 1 2016.

[219] Jaeyeon Yu, Seongjin Park, Inyong Hwang, Daeik Kim, Frederic Demmerle, Gerhard Boehm, Markus-Christian Amann, Mikhail A. Belkin, and Jongwon Lee. Electrically tunable nonlinear polaritonic metasurface. *Nature Photonics*, 16(1):72–78, 1 2022.

[220] Davide Rocco, Marco Gandolfi, Andrea Tognazzi, Olesiya Pashina, George Zograf, Kristina Frizyuk, Carlo Gigli, Giuseppe Leo, Sergey Makarov, Mihail Petrov, and Costantino De Angelis. Opto-thermally controlled beam steering in nonlinear all-dielectric metastructures. *Optics Express*, 29(23):37128, 11 2021.

[221] Sebastian Busschaert, Nikolaus Flöry, Sotirios Papadopoulos, Markus Parzefall, Sebastian Heeg, and Lukas Novotny. Beam Steering with a Nonlinear Optical Phased Array Antenna. *Nano Letters*, 19(9):6097–6103, 9 2019.

[222] Zhenwei Xie, Ting Lei, Guangyuan Si, Xianyou Wang, Jiao Lin, Changjun Min, and Xiaocong Yuan. Meta-Holograms with Full Parameter Control of Wavefront over a 1000 nm Bandwidth. *ACS Photonics*, 4(9):2158–2164, 9 2017.

[223] Jiao Lin, Patrice Genevet, Mikhail A. Kats, Nicholas Antoniou, and Federico Capasso. Nanostructured holograms for broadband manipulation of vector beams. *Nano Letters*, 13(9):4269–4274, 9 2013.

[224] Changjun Min, Jinpeng Liu, Ting Lei, Guangyuan Si, Zhenwei Xie, Jiao Lin, Luping Du, and Xiaocong Yuan. Plasmonic nano-slits assisted polarization selective detour phase meta-hologram. *Laser and Photonics Reviews*, 10(6):978–985, 11 2016.

[225] Mohammadreza Khorasaninejad, Antonio Ambrosio, Pritpal Kanhaiya, and Federico Capasso. Broadband and chiral binary dielectric meta-holograms. *Science Advances*, 2(5), 5 2016.

[226] F. S. Chen. Optically Induced Change of Refractive Indices in LiNbO3 and LiTaO3. *Journal of Applied Physics*, 40(8):3389–3396, 7 1969.

[227] A. Ashkin, G. D. Boyd, J. M. Dziedzic, R. G. Smith, A. A. Ballman, J. J. Levinstein, and K. Nassau. Optically-induced refractive index inhomogeneities in LiNbO3 and LiTaO3. *Applied Physics Letters*, 9(1):72–74, 1966.

[228] F. S. Chen, J. T. LaMacchia, and D. B. Fraser. Holographic storage in Lithium Niobate. *Applied Physics Letters*, 13(7):223–225, 10 1968.

[229] Deanna McMillen, Tracy Hudson, Julie Wagner, and Jere Singleton. Holographic recording in specially doped lithium niobate crystals. *Optics Express*, 2(12):491, 6 1998.

[230] K. Buse, A. Adibi, and D. Psaltis. Non-volatile holographic storage in doubly doped lithium niobate crystals. *Nature*, 393(6686):665–668, 6 1998.

[231] Fai H. Mok. Angle-multiplexed storage of 5000 holograms in lithium niobate. *Optics Letters*, 18(11):915, 6 1993.

[232] M.N. Ernstoff, A.M. Leupp, M.J. Little, and H.T. Peterson. Liquid crystal pictorial display. In *1973 International Electron Devices Meeting*, pages 548–551. IRE, 1973.

[233] N. Collings, W. A. Crossland, P. J. Ayliffe, D. G. Vass, and I. Underwood. Evolutionary development of advanced liquid crystal spatial light modulators. *Applied Optics*, 28(22):4740, 11 1989.

[234] Kristina M. Johnson, Douglas J. McKnight, and Ian Underwood. Smart Spatial Light Modulators Using Liquid Crystals on Silicon. *IEEE Journal of Quantum Electronics*, 29(2):699–714, 1993.

[235] D. P. Resler, D. S. Hobbs, R. C. Sharp, L. J. Friedman, and T. A. Dorschner. High-efficiency liquid-crystal optical phased-array beam steering. *Optics Letters*, 21(9):689, 5 1996.

[236] Stephan Reichelt, Ralf Häussler, Gerald Fütterer, Norbert Leister, Hiromi Kato, Naru Usukura, and Yuuichi Kanbayashi. Full-range, complex spatial light modulator for real-time holography. *Optics Letters*, 37(11):1955, 6 2012.

[237] David Vettese. Liquid crystal on silicon. *Nature Photonics 2010 4:11*, 4(11):752–754, 2010.

[238] Zichen Zhang, Zheng You, and Daping Chu. Fundamentals of phase-only liquid crystal on silicon (LCOS) devices. *Light: Science & Applications 2014 3:10*, 3(10):e213–e213, 10 2014.

[239] Hamamatsu Photonics. Wide wavelength band type, 2024. `https://www.hamamatsu.com/eu/en/product/optical-components/lcos-slm/wide_wavelength_bandwidth_type.html` [Accessed: 05-10-2024].

[240] HOLOEYE Photonics AG. GAEA-2.1 Phase Only LCOS-SLM, 2024. `https://holoeye.com/products/spatial-light-modulators/gaea-2-phase-only/` [Accessed: 05-10-2024].

[241] Santec Holdings Corporation. SLM-210, 2024. https://www.santec.com/en/products/components/slm/slm-210/ [Accessed: 05-10-2024].

[242] Thorlabs. EXULUS-4K1/M Spatial Light Modulator, 2024. https://www.thorlabs.com/thorproduct.cfm?partnumber=EXULUS-4K1/M [Accessed: 05-10-2024].

[243] Meadowlark Optics. Spatial Light Modulators, 2024. https://www.meadowlark.com/product-category/slms/ [Accessed: 05-10-2024].

[244] Mukesh Sharma, Netta Hendler, and Tal Ellenbogen. Electrically Switchable Color Tags Based on Active Liquid-Crystal Plasmonic Metasurface Platform. *Advanced Optical Materials*, 8(7):1901182, 4 2020.

[245] Maxim V. Gorkunov, Alena V. Mamonova, Irina V. Kasyanova, Alexander A. Ezhov, Vladimir V. Artemov, Ivan V. Simdyankin, and Artur R. Geivandov. Double-sided liquid crystal metasurfaces for electrically and mechanically controlled broadband visible anomalous refraction. *Nanophotonics*, 11(17):3901–3912, 9 2022.

[246] J. B. Pendry. Negative Refraction Makes a Perfect Lens. *Physical Review Letters*, 85(18):3966–3969, 10 2000.

[247] R. A. Shelby, D. R. Smith, and S. Schultz. Experimental Verification of a Negative Index of Refraction. *Science*, 292(5514):77–79, 4 2001.

[248] N. I. Landy, S. Sajuyigbe, J. J. Mock, D. R. Smith, and W. J. Padilla. A Perfect Metamaterial Absorber. *Physical Review Letters*, 100(20):207402, 3 2008.

[249] Zhenhe Ma, Xianghe Meng, Xiaodi Liu, Guangyuan Si, and Yan Jun Liu. Liquid Crystal Enabled Dynamic Nanodevices. *Nanomaterials 2018, Vol. 8, Page 871*, 8(11):871, 10 2018.

[250] Arash Nemati, Qian Wang, Minghui Hong, and Jinghua Teng. Tunable and reconfigurable metasurfaces and metadevices. *Opto-Electronic Advances*, 1(5):18000901–18000925, 2018.

[251] Tong Cui, Benfeng Bai, and Hong Bo Sun. Tunable Metasurfaces Based on Active Materials. *Advanced Functional Materials*, 29(10), 3 2019.

[252] Amr M. Shaltout, Vladimir M. Shalaev, and Mark L. Brongersma. Spatiotemporal light control with active metasurfaces. *Science*, 364(6442), 2019.

[253] Chang Won Lee, Hee Jin Choi, and Heejeong Jeong. Tunable metasurfaces for visible and SWIR applications. *Nano Convergence*, 7(1):1–11, 12 2020.

[254] Ruizhe Zhao, Lingling Huang, and Yongtian Wang. Recent advances in multi-dimensional metasurfaces holographic technologies. *PhotoniX*, 1(1), 12 2020.

[255] Xiaoguang Zhao, Zhenci Sun, Lingyun Zhang, Zilun Wang, Rongbo Xie, Jiahao Zhao, Rui You, and Zheng You. Review on Metasurfaces: An Alternative Approach to Advanced Devices and Instruments. *Advanced Devices & Instrumentation*, 2022:1–19, 9 2022.

[256] I. C. Khoo, D. H. Werner, X. Liang, A. Diaz, and B. Weiner. Nanosphere dispersed liquid crystals for tunable negative-zero-positive index of refraction in the optical and terahertz regimes. *Optics Letters*, 31(17):2592, 9 2006.

[257] Qian Zhao, Lei Kang, Bo Du, Bo Li, Ji Zhou, Hong Tang, Xiao Liang, and Baizhe Zhang. Electrically tunable negative permeability metamaterials based on nematic liquid crystals. *Applied Physics Letters*, 90(1):11112, 1 2007.

[258] Manuel Decker, Christian Kremers, Alexander Minovich, Isabelle Staude, Andrey E. Miroshnichenko, Dmitry Chigrin, Dragomir N. Neshev, Chennupati Jagadish, and Yuri S. Kivshar. Electro-optical switching by liquid-crystal controlled metasurfaces. *Optics Express*, 21(7):8879, 4 2013.

[259] Bernhard Atorf, Holger Mühlenbernd, Mulda Muldarisnur, Thomas Zentgraf, and Heinz Kitzerow. Electro-optic tuning of split ring resonators embedded in a liquid crystal. *Optics Letters*, 39(5):1129, 3 2014.

[260] Bernhard Atorf, Holger Mühlenbernd, Thomas Zentgraf, and Heinz Kitzerow. All-optical switching of a dye-doped liquid crystal plasmonic metasurface. *Optics Express*, 28(6):8898, 3 2020.

[261] James A. Dolan, Haogang Cai, Lily Delalande, Xiao Li, Alex B. F. Martinson, Juan J. de Pablo, Daniel López, and Paul F. Nealey. Broadband Liquid Crystal Tunable Metasurfaces in the Visible: Liquid Crystal Inhomogeneities Across the Metasurface Parameter Space. *ACS Photonics*, 8(2):567–575, 2 2021.

[262] Alexander Minovich, Dragomir N. Neshev, David A. Powell, Ilya V. Shadrivov, and Yuri S. Kivshar. Tunable fishnet metamaterials infiltrated by liquid crystals. *Applied Physics Letters*, 96(19), 4 2010.

[263] Yibo Ni, Chen Chen, Shun Wen, Xinyuan Xue, Liqun Sun, and Yuanmu Yang. Computational spectropolarimetry with a tunable liquid crystal metasurface. *eLight*, 2(1):1–10, 12 2022.

[264] Seung-Yeol Lee, Yong-Hae Kim, Seong-M. Cho, Gi Heon Kim, Tae-Youb Kim, Hojun Ryu, Han Na Kim, Han Byeol Kang, Chi-Young Hwang, and Chi-Sun Hwang. Holographic image generation with a thin-film resonance caused by chalcogenide phase-change material. *Scientific Reports*, 7(1):41152, 1 2017.

[265] Jianxiong Li, Simon Kamin, Guoxing Zheng, Frank Neubrech, Shuang Zhang, and Na Liu. Addressable metasurfaces for dynamic holography and optical information encryption. *Science Advances*, 4(6), 6 2018.

[266] Qian Wang, Edward T. F. Rogers, Behrad Gholipour, Chih-Ming Wang, Guanghui Yuan, Jinghua Teng, and Nikolay I. Zheludev. Optically reconfigurable metasurfaces and photonic devices based on phase change materials. *Nature Photonics*, 10(1):60–65, 1 2016.

[267] Jing Zhao, Chunmei Ouyang, Xieyu Chen, Yanfeng Li, Caihong Zhang, Longcheng Feng, Biaobing Jin, Jiajun Ma, Yi Liu, Shoujun Zhang, Quan Xu, Jiaguang Han, and Weili Zhang. Temperature-controlled terahertz polarization conversion bandwidth. *Optics Express*, 29(14):21738, 7 2021.

[268] Ling Wang, Weijun Hong, Li Deng, Shufang Li, Chen Zhang, Jianfeng Zhu, and Hongjun Wang. Reconfigurable Multifunctional Metasurface Hybridized with Vanadium Dioxide at Terahertz Frequencies. *Materials*, 11(10):2040, 10 2018.

[269] Alexej V. Pogrebnyakov, Jeremy A. Bossard, Jeremiah P. Turpin, J. David Musgraves, Hee Jung Shin, Clara Rivero-Baleine, Nikolas Podraza, Kathleen A. Richardson, Douglas H. Werner, and Theresa S. Mayer. Reconfigurable near-IR metasurface based on Ge_2 Sb_2 Te_5 phase-change material. *Optical Materials Express*, 8(8):2264, 8 2018.

[270] Jiajia Chen, Xieyu Chen, Kuan Liu, Shoujun Zhang, Tun Cao, and Zhen Tian. A Thermally Switchable Bifunctional Metasurface for Broadband Polarization Conversion and Absorption Based on Phase-Change Material. *Advanced Photonics Research*, page 2100369, 4 2022.

[271] Ann-Katrin U. Michel, Dmitry N. Chigrin, Tobias W. W. Maß, Kathrin Schönauer, Martin Salinga, Matthias Wuttig, and Thomas Taubner. Using Low-Loss Phase-Change Materials for Mid-Infrared Antenna Resonance Tuning. *Nano Letters*, 13(8):3470–3475, 8 2013.

[272] Yiguo Chen, Xiong Li, Yannick Sonnefraud, Antonio I. Fernández-Domínguez, Xiangang Luo, Minghui Hong, and Stefan A. Maier. Engineering the Phase Front of Light with Phase-Change Material Based Planar lenses. *Scientific Reports*, 5(1):8660, 3 2015.

[273] Sajjad Abdollahramezani, Omid Hemmatyar, Mohammad Taghinejad, Hossein Taghinejad, Alex Krasnok, Ali A. Eftekhar, Christian Teichrib, Sanchit Deshmukh, Mostafa A. El-Sayed, Eric Pop, Matthias Wuttig, Andrea Alù, Wenshan Cai, and Ali Adibi. Electrically driven reprogrammable phase-change metasurface reaching 80% efficiency. *Nature Communications*, 13(1):1696, 3 2022.

[274] M. Tayyab Nouman, Jihyun Hwang, Mohd. Faiyaz, Gyejung Lee, Do-Young Noh, and Jae-Hyung Jang. Dynamic-Metasurface-Based Cavity Structures for Enhanced Absorption and Phase Modulation. *ACS Photonics*, 6(2):374–381, 2 2019.

[275] Chenglong Zheng, Jie Li, Zhen Yue, Jitao Li, Jingyu Liu, Guocui Wang, Silei Wang, Yating Zhang, Yan Zhang, and Jianquan Yao. All-Dielectric Trifunctional Metasurface Capable of Independent Amplitude and Phase Modulation. *Laser & Photonics Reviews*, 16(7):2200051, 7 2022.

[276] Ming Zhang, Mingbo Pu, Fei Zhang, Yinghui Guo, Qiong He, Xiaoliang Ma, Yijia Huang, Xiong Li, Honglin Yu, and Xiangang Luo. Plasmonic Metasurfaces for Switchable Photonic Spin-Orbit Interactions Based on Phase Change Materials. *Advanced Science*, 5(10):1800835, 10 2018.

[277] Chi-Young Hwang, Gi Heon Kim, Jong-Heon Yang, Chi-Sun Hwang, Seong M. Cho, Won-Jae Lee, Jae-Eun Pi, Ji Hun Choi, Kyunghee Choi, Hee-Ok Kim, Seung-Yeol Lee, and Yong-Hae Kim. Rewritable full-color computer-generated holograms based on color-selective diffractive optical components including phase-change materials. *Nanoscale*, 10(46):21648–21655, 2018.

[278] Kaichen Dong, Sukjoon Hong, Yang Deng, He Ma, Jiachen Li, Xi Wang, Junyeob Yeo, Letian Wang, Shuai Lou, Kyle B. Tom, Kai Liu, Zheng You, Yang Wei, Costas P. Grigoropoulos, Jie Yao, and Junqiao Wu. A Lithography-Free and Field-Programmable Photonic Metacanvas. *Advanced Materials*, 30(5), 2 2018.

[279] Xingbo Liu, Qiu Wang, Xueqian Zhang, Hua Li, Quan Xu, Yuehong Xu, Xieyu Chen, Shaoxian Li, Meng Liu, Zhen Tian, Caihong Zhang, Chongwen Zou, Jiaguang Han, and Weili Zhang. Thermally Dependent Dynamic Meta-Holography Using a Vanadium Dioxide Integrated Metasurface. *Advanced Optical Materials*, 7(12):1900175, 6 2019.

[280] Jason Midkiff, Kyoung Min Yoo, Jong-Dug Shin, Hamed Dalir, Mohammad Teimourpour, and Ray T. Chen. Optical phased array beam steering in the mid-infrared on an InP-based platform. *Optica*, 7(11):1544, 11 2020.

[281] Jie Sun, Erman Timurdogan, Ami Yaacobi, Ehsan Shah Hosseini, and Michael R. Watts. Large-scale nanophotonic phased array. *Nature*, 493(7431):195–199, 1 2013.

[282] Hiroyuki Ito, Yuma Kusunoki, Jun Maeda, Daichi Akiyama, Naoya Kodama, Hiroshi Abe, Ryo Tetsuya, and Toshihiko Baba. Wide beam steering by slow-light waveguide gratings and a prism lens. *Optica*, 7(1):47, 1 2020.

[283] Thermo-Optic Coefficients. In *Handbook of Optical Constants of Solids*, pages 115–261. Elsevier, 1 1997.

[284] Ami Yaacobi, Jie Sun, Michele Moresco, Gerald Leake, Douglas Coolbaugh, and Michael R. Watts. Integrated phased array for wide-angle beam steering. *Optics Letters*, 39(15):4575, 8 2014.

[285] Daisuke Inoue, Tadashi Ichikawa, Akari Kawasaki, and Tatsuya Yamashita. Demonstration of a new optical scanner using silicon photonics integrated circuit. *Optics Express*, 27(3):2499, 2 2019.

[286] Karel Van Acoleyen, Hendrik Rogier, and Roel Baets. Two-dimensional optical phased array antenna on silicon-on-Insulator. *Optics Express*, 18(13):13655, 6 2010.

[287] William S. Rabinovich, Peter G. Goetz, Marcel W. Pruessner, Rita Mahon, Mike S. Ferraro, Doe Park, Erin Fleet, and Michael J. DePrenger. Two-dimensional beam steering using a thermo-optic silicon photonic optical phased array. *Optical Engineering*, 55(11):111603, 8 2016.

[288] Seong-Hwan Kim, Jong-Bum You, Yun-Gi Ha, Geumbong Kang, Dae-Seong Lee, Hyeonho Yoon, Dong-Eun Yoo, Dong-Wook Lee, Kyoungsik Yu, Chan-Hyun Youn, and Hyo-Hoon Park. Thermo-optic control of the longitudinal radiation angle in a silicon-based optical phased array. *Optics Letters*, 44(2):411, 1 2019.

[289] Chao Li, Xianyi Cao, Kan Wu, Xinwan Li, and Jianping Chen. Lens-based integrated 2D beam-steering device with defocusing approach and broadband pulse operation for Lidar application. *Optics Express*, 27(23):32970, 2019.

[290] Xianyi Cao, Gaofeng Qiu, Kan Wu, Chao Li, and Jianping Chen. Lidar system based on lens assisted integrated beam steering. *Optics Letters*, 45(20):5816, 10 2020.

[291] Dorian Treptow, Raúl Bola, Estela Martín-Badosa, and Mario Montes-Usategui. Artifact-free holographic light shaping through moving acousto-optic holograms. *Scientific Reports*, 11(1):21261, 10 2021.

[292] D. E. Smalley, Q. Y.J. Smithwick, V. M. Bove, J. Barabas, and S. Jolly. Anisotropic leaky-mode modulator for holographic video displays. *Nature*, 498(7454):313–317, 2013.

[293] Valery V. Proklov and E. M. Korablev. Guided-wave multichannel acousto-optic devices based on collinear wave propagation. In Antoni Sliwinski, Piotr Kwiek, B. Linde, and A. Markiewicz, editors, *Acousto-Optics and Applications*, volume 1844, pages 112–125. SPIE, 11 1992.

[294] U. Rust and E. Strake. Acoustooptical Coupling of Guided to Substrate Modes in Planar Proton-Exchanged LiNbO3-Waveguides. In *Integrated Photonics Research*, page ME4, Washington, D.C., 4 1992. OSA.

[295] Kenchi Ito and Kazumi Kawamoto. An optical deflector using collinear acoustooptic coupling fabricated on proton-exchanged LiNbO3. *Japanese Journal of Applied Physics, Part 1: Regular Papers and Short Notes and Review Papers*, 37(9 A):4858–4865, 9 1998.

[296] C. S. Tsai, Q. Li, and C. L. Chang. Guided-wave two-dimensional acousto-optic scanner using proton-exchanged lithium niobate waveguide. *Fiber and Integrated Optics*, 17(3):157–166, 1998.

[297] Daniel E. Smalley, Sundeep Jolly, Gregg E. Favalora, and Michael G. Moebius. Status of Leaky Mode Holography. *Photonics 2021, Vol. 8, Page 292*, 8(8):292, 7 2021.

[298] Bingzhao Li, Qixuan Lin, and Mo Li. Frequency–angular resolving LiDAR using chip-scale acousto-optic beam steering. *Nature*, 620(7973):316–322, 8 2023.

[299] Kamran Qaderi and Daniel E. Smalley. Leaky-mode waveguide modulators with high deflection angle for use in holographic video displays. *Optics Express*, 24(18):20831, 9 2016.

[300] David S. Ginley and Clark Bright. Transparent Conducting Oxides. *MRS Bulletin*, 25(8):15–18, 8 2000.

[301] Elvira Fortunato, David Ginley, Hideo Hosono, and David C. Paine. Transparent Conducting Oxides for Photovoltaics. *MRS Bulletin*, 32(3):242–247, 3 2007.

[302] Andreas Stadler. Transparent Conducting Oxides—An Up-To-Date Overview. *Materials*, 5(12):661–683, 4 2012.

[303] Albert de Jamblinne de Meux, Ajay Bhoolokam, Geoffrey Pourtois, Jan Genoe, and Paul Heremans. Oxygen vacancies effects in a-IGZO:

Formation mechanisms, hysteresis, and negative bias stress effects. *physica status solidi (a)*, 214(6):1600889, 6 2017.

[304] Lishu Liu, Zengxia Mei, Aihua Tang, Alexander Azarov, Andrej Kuznetsov, Qi-Kun Xue, and Xiaolong Du. Oxygen vacancies: The origin of n -type conductivity in ZnO. *Physical Review B*, 93(23):235305, 6 2016.

[305] Gururaj V. Naik, Jongbum Kim, and Alexandra Boltasseva. Oxides and nitrides as alternative plasmonic materials in the optical range. *Optical Materials Express*, 1(6):1090, 10 2011.

[306] Yu Wang, Antonio Capretti, and Luca Dal Negro. Wide tuning of the optical and structural properties of alternative plasmonic materials. *Optical Materials Express*, 5(11):2415, 11 2015.

[307] H. Kim, M. Osofsky, S. M. Prokes, O. J. Glembocki, and A. Piqué. Optimization of Al-doped ZnO films for low loss plasmonic materials at telecommunication wavelengths. *Applied Physics Letters*, 102(17):171103, 4 2013.

[308] Viktoriia E. Babicheva, Alexandra Boltasseva, and Andrei V. Lavrinenko. Transparent conducting oxides for electro-optical plasmonic modulators. *Nanophotonics*, 4(1):165–185, 6 2015.

[309] Wallace Jaffray, Soham Saha, Vladimir M. Shalaev, Alexandra Boltasseva, and Marcello Ferrera. Transparent conducting oxides: from all-dielectric plasmonics to a new paradigm in integrated photonics. *Advances in Optics and Photonics*, 14(2):148, 6 2022.

[310] Eyal Feigenbaum, Kenneth Diest, and Harry A. Atwater. Unity-Order Index Change in Transparent Conducting Oxides at Visible Frequencies. *Nano Letters*, 10(6):2111–2116, 6 2010.

[311] Soo Jin Kim and Mark L. Brongersma. Active flat optics using a guided mode resonance. *Optics Letters*, 42(1):5, 1 2017.

[312] Junghyun Park, Byung Gil Jeong, Sun Il Kim, Duhyun Lee, Jungwoo Kim, Changgyun Shin, Chang Bum Lee, Tatsuhiro Otsuka, Jisoo Kyoung, Sangwook Kim, Ki-Yeon Yang, Yong-Young Park, Jisan Lee, Inoh Hwang, Jaeduck Jang, Seok Ho Song, Mark L. Brongersma, Kyoungho Ha, Sung-Woo Hwang, Hyuck Choo, and Byoung Lyong Choi. All-solid-state spatial light modulator with independent phase and amplitude control for three-dimensional LiDAR applications. *Nature Nanotechnology*, 16(1):69–76, 1 2021.

[313] Zhaolin Lu, Wangshi Zhao, and Kaifeng Shi. Ultracompact electroabsorption modulators based on tunable epsilon-near-zero-slot waveguides. *IEEE Photonics Journal*, 4(3):735–740, 2012.

[314] Junghyun Park, Ju-Hyung Kang, Xiaoge Liu, and Mark L. Brongersma. Electrically Tunable Epsilon-Near-Zero (ENZ) Metafilm Absorbers. *Scientific Reports*, 5(1):15754, 11 2015.

[315] A. V. Krasavin and A. V. Zayats. Photonic Signal Processing on Electronic Scales: Electro-Optical Field-Effect Nanoplasmonic Modulator. *Physical Review Letters*, 109(5):053901, 7 2012.

[316] Viktoriia E. Babicheva and Andrei V. Lavrinenko. Plasmonic modulator optimized by patterning of active layer and tuning permittivity. *Optics Communications*, 285(24):5500–5507, 11 2012.

[317] Alok P. Vasudev, Ju-Hyung Kang, Junghyun Park, Xiaoge Liu, and Mark L. Brongersma. Electro-optical modulation of a silicon waveguide with an "epsilon-near-zero" material. *Optics Express*, 21(22):26387, 11 2013.

[318] Ho W. Lee, Georgia Papadakis, Stanley P. Burgos, Krishnan Chander, Arian Kriesch, Ragip Pala, Ulf Peschel, and Harry A. Atwater. Nanoscale conducting oxide PlasMOStor. *Nano Letters*, 14(11):6463–6468, 11 2014.

[319] Jinqiannan Zhang, Jingyi Yang, Michael Schell, Aleksei Anopchenko, Long Tao, Zhongyuan Yu, and Ho Wai Howard Lee. Gate-tunable optical filter based on conducting oxide metasurface heterostructure. *Optics Letters*, 44(15):3653, 8 2019.

[320] Hongwei Zhao, Ran Zhang, Hamid T. Chorsi, Wesley A. Britton, Yuyao Chen, Prasad P. Iyer, Jon A. Schuller, Luca Dal Negro, and Jonathan Klamkin. Gate-tunable metafilm absorber based on indium silicon oxide. *Nanophotonics*, 8(10):1803–1810, 9 2019.

[321] Junghyun Park, Ju-Hyung Kang, Soo Jin Kim, Xiaoge Liu, and Mark L. Brongersma. Dynamic Reflection Phase and Polarization Control in Metasurfaces. *Nano Letters*, 17(1):407–413, 1 2017.

[322] Ghazaleh Kafaie Shirmanesh, Ruzan Sokhoyan, Ragip A. Pala, and Harry A. Atwater. Dual-Gated Active Metasurface at 1550 nm with Wide (300°) Phase Tunability. *Nano Letters*, 18(5):2957–2963, 5 2018.

[323] Sun Il Kim, Junghyun Park, Byung Gil Jeong, Duhyun Lee, Ki Yeon Yang, Yong Young Park, Kyoungho Ha, and Hyuck Choo. Two-dimensional beam steering with tunable metasurface in infrared regime. *Nanophotonics*, 11(11):2719–2726, 6 2022.

[324] Ghazaleh Kafaie Shirmanesh, Ruzan Sokhoyan, Pin Chieh Wu, and Harry A. Atwater. Electro-optically Tunable Multifunctional Metasurfaces. *ACS Nano*, 14(6):6912–6920, 6 2020.

[325] Carlos Errando-Herranz, Nicolas Le Thomas, and Kristinn B Gylfason. Low-power optical beam steering by microelectromechanical waveguide gratings. *Optica*, 2019.

[326] Yuhua Chang, Jingxuan Wei, and Chengkuo Lee. Metamaterials – from fundamentals and MEMS tuning mechanisms to applications. *Nanophotonics*, 9(10):3049–3070, 8 2020.

[327] Zang Guanxing, Ziji Liu, Wenjun Deng, and Weiming Zhu. Reconfigurable metasurfaces with mechanical actuations: towards flexible and tunable photonic devices. *Journal of Optics*, 23(1):013001, 1 2021.

[328] Prakash Pitchappa, Manukumara Manjappa, Chong Pei Ho, Ranjan Singh, Navab Singh, and Chengkuo Lee. Active Control of Electromagnetically Induced Transparency Analog in Terahertz MEMS Metamaterial. *Advanced Optical Materials*, 4(4):541–547, 4 2016.

[329] Youmin Wang, Guangya Zhou, Xiaosheng Zhang, Kyungmok Kwon, Pierre-A. Blanche, Nicholas Triesault, Kyoung-sik Yu, and Ming C. Wu. 2D broadband beamsteering with large-scale MEMS optical phased array. *Optica*, 6(5):557, 5 2019.

[330] Shaowei He, Huimin Yang, Yunhui Jiang, Wenjun Deng, and Weiming Zhu. Recent Advances in MEMS Metasurfaces and Their Applications on Tunable Lens. *Micromachines*, 10(8):505, 7 2019.

[331] Tapashree Roy, Shuyan Zhang, Il Woong Jung, Mariano Troccoli, Federico Capasso, and Daniel Lopez. Dynamic metasurface lens based on MEMS technology. *APL Photonics*, 3(2):21302, 2 2018.

[332] Christopher A. Dirdal, Paul C. V. Thrane, Firehun T. Dullo, Jo Gjessing, Anand Summanwar, and Jon Tschudi. MEMS-tunable dielectric metasurface lens using thin-film PZT for large displacements at low voltages. *Optics Letters*, 47(5):1049, 3 2022.

[333] Aaron L. Holsteen, Ahmet Fatih Cihan, and Mark L. Brongersma. Temporal color mixing and dynamic beam shaping with silicon metasurfaces. *Science*, 365(6450):257–260, 7 2019.

[334] Prakash Pitchappa, Chong Pei Ho, You Qian, Lokesh Dhakar, Navab Singh, and Chengkuo Lee. Microelectromechanically tunable multiband metamaterial with preserved isotropy. *Scientific Reports*, 5(1):11678, 12 2015.

[335] Byung-Wook Yoo, Mischa Megens, Tianbo Sun, Weijian Yang, Connie J. Chang-Hasnain, David A. Horsley, and Ming C. Wu. A 32 × 32 optical phased array using polysilicon sub-wavelength high-contrast-grating mirrors. *Optics Express*, 22(16):19029, 8 2014.

[336] Longqing Cong, Prakash Pitchappa, Chengkuo Lee, and Ranjan Singh. Active Phase Transition via Loss Engineering in a Terahertz MEMS Metamaterial. *Advanced Materials*, 29(26), 7 2017.

[337] Longqing Cong, Prakash Pitchappa, Yang Wu, Lin Ke, Chengkuo Lee, Navab Singh, Hyunsoo Yang, and Ranjan Singh. Active Multifunctional Microelectromechanical System Metadevices: Applications in Polarization Control, Wavefront Deflection, and Holograms. *Advanced Optical Materials*, 5(2):1600716, 1 2017.

[338] Texas Instruments. DLPLCR67EVM Evaluation board, 2024. `https://www.ti.com/tool/DLPLCR67EVM` [Accessed: 05-10-2024].

[339] Omer Tzang, Eyal Niv, Sakshi Singh, Simon Labouesse, Greg Myatt, and Rafael Piestun. Wavefront shaping in complex media with a 350 kHz modulator via a 1D-to-2D transform. *Nature Photonics*, 13(11):788–793, 11 2019.

[340] Silicon Light Machines. Grating Light Valve G8192, 2024. `https://www.siliconlight.com/en/products/module.html` [Accessed: 05-10-2024].

[341] H. G. Craighead. Nanoelectromechanical systems. *Science*, 290(5496):1532–1535, 11 2000.

[342] Guillaume Croes, Robert Gehlhaar, and Jan Genoe. Subwavelength Custom Wavefront Shaping by a Nonlinear Electro-optic Spatial Light Modulator. *ACS Photonics*, 11(2):529–536, 2 2024.

[343] Jeungmo Kang, Yoonhee Cho, and Woojin Jang. Long-Term Reliability Characteristics of OLED Panel and Luminaires for General Lighting Applications. *Applied Sciences*, 11(1):74, 12 2020.

[344] Asim Kumar Roy Choudhury. Characteristics of light sources. In *Principles of Colour and Appearance Measurement*, pages 1–52. Elsevier, 2014.

[345] Mateus Corato-Zanarella, Andres Gil-Molina, Xingchen Ji, Min Chul Shin, Aseema Mohanty, and Michal Lipson. Widely tunable and narrow-linewidth chip-scale lasers from near-ultraviolet to near-infrared wavelengths. *Nature Photonics*, 17(2):157–164, 2 2023.

[346] Hiroshi Hashiguchi, Toshihiko Baba, and Hiroyuki Arai. Optical Beam Expander with Parabolic Photonic Bandgap Reflector for Efficient Excitation of Optical Leaky Wave Antenna. *Journal of Lightwave Technology*, 37(9):2094–2099, 5 2019.

[347] H. Kogelnik. Theory of Dielectric Waveguides. In *Integrated Optics*, pages 13–81. Springer, Berlin, Heidelberg, 1975.

[348] Guillaume Croes, Nikolay Smolentsev, Tsang Hsuan Wang, Robert Gehlhaar, and Jan Genoe. Non-linear electro-optic modelling of a Barium Titanate grating coupler. In Mark A. Kahan, editor, *Optical Modeling and Performance Predictions XI*, volume 11484, page 11. SPIE, 8 2020.

[349] Ginés Lifante. *Integrated Photonics: Fundamentals*. Wiley, 1 2003.

[350] G. E. Jellison and F. A. Modine. Parameterization of the optical functions of amorphous materials in the interband region. *Applied Physics Letters*, 1996.

[351] R. W. Collins, Ilsin An, H. Fujiwara, Joungchel Lee, Yiwei Lu, Joohyun Koh, and P. I. Rovira. Advances in multichannel spectroscopic ellipsometry. *Thin Solid Films*, 313-314:18–32, 2 1998.

[352] Hiroyuki Fujiwara. Spectroscopic Ellipsometry: Principles and Applications. *Spectroscopic Ellipsometry: Principles and Applications*, pages 1–369, 10 2007.

[353] John Freudenthal. Intuitive interpretation of Mueller matrices of transmission, 2018.

[354] Oriol Arteaga. Useful Mueller matrix symmetries for ellipsometry. *Thin Solid Films*, 571:584–588, 11 2014.

[355] Guillaume Croes, Renaud Puybaret, Janusz Bogdanowicz, Umberto Celano, Robert Gehlhaar, and Jan Genoe. Photonic metamaterial with a subwavelength electrode pattern. *Applied Optics*, 62(17):F14, 6 2023.

[356] S Subhechha, N Rassoul, A Belmonte, R Delhougne, K Banerjee, G L Donadio, H Dekkers, M J Van Setten, H Puliyalil, M Mao, S Kundu, M Pak, L Teugels, D Tsvetanova, N Bazzazian, L Klijs, H Hody, A Chasin, J Heijlen, L Goux, and G S Kar. First demonstration of sub-12 nm Lg gate last IGZO-TFTs with oxygen tunnel architecture for front gate devices. 1:978–982, 2021.

[357] S. Subhechha, N. Rassoul, A. Belmonte, H. Hody, H. Dekkers, M. J. van Setten, A. Chasin, S.H. Sharifi, S. Sutar, L. Magnarin, U. Celano,

H. Puliyalil, S. Kundu, M. Pak, L. Teugels, D. Tsvetanova, N. Bazzazian, K. Vandersmissen, C. Biasotto, D. Batuk, J. Geypen, J. Heijlen, R. Delhougne, and G. S. Kar. Ultra-low Leakage IGZO-TFTs with Raised Source/Drain for $V_t > 0$ V and $I_{on} > 30$ μA/μm. In *2022 IEEE Symposium on VLSI Technology and Circuits (VLSI Technology and Circuits)*, volume 2022-June, pages 292–293. IEEE, 6 2022.

[358] Hendrik F. W. Dekkers, Michiel J. van Setten, Attilio Belmonte, Adrian V. Chasin, Subhali Subhechha, Nouredine Rassoul, Anastasia V. Glushkova, Romain Delhougne, and Gouri Sankar Kar. Deposition, Characterization, and Performance of Spinel $InGaZnO_4$. *ACS Applied Electronic Materials*, 4(3):1238–1249, 3 2022.

[359] Tsang-Hsuan Wang, Po-Chun (Brent) Hsu, Maxim Korytov, Jan Genoe, and Clement Merckling. Polarization control of epitaxial barium titanate (BaTiO3) grown by pulsed-laser deposition on a MBE-SrTiO3/Si(001) pseudo-substrate. *Journal of Applied Physics*, 128(10):104104, 9 2020.

[360] Tsang-Hsuan Wang, Robert Gehlhaar, Thierry Conard, Paola Favia, Jan Genoe, and Clement Merckling. Interfacial control of SrTiO3/Si(0 0 1) epitaxy and its effect on physical and optical properties. *Journal of Crystal Growth*, 582:126524, 3 2022.

[361] Tsang-Hsuan Wang, Jan Genoe, and Clement Merckling. *Study of Barium Titanate Epitaxy on Silicon toward Its Application in Video Holography*. PhD thesis, 2023.

[362] Kristy J Kormondy, Youri Popoff, Marilyne Sousa, Felix Eltes, Daniele Caimi, Marta D Rossell, Manfred Fiebig, Patrik Hoffmann, Chiara Marchiori, Michael Reinke, Morgan Trassin, Alexander A Demkov, Jean Fompeyrine, and Stefan Abel. Microstructure and ferroelectricity of BaTiO3 thin films on Si for integrated photonics. *Nanotechnology*, 28(7):075706, 2 2017.

[363] W. P. Mason and B. T. Matthias. Theoretical Model for Explaining the Ferroelectric Effect in Barium Titanate. *Physical Review*, 74(11):1622–1636, 12 1948.

[364] A. von Hippel. Ferroelectricity, Domain Structure, and Phase Transitions of Barium Titanate. *Reviews of Modern Physics*, 22(3):221–237, 7 1950.

[365] Frederick Seitz and David Turnbull. *Solid State Physics*. 1957.

[366] Helen Megaw. Temperature changes in the crystal structure of barium titanium oxide. *Proceedings of the Royal Society of London. Series A. Mathematical and Physical Sciences*, 189(1017):261–283, 4 1947.

[367] C.J. Xiao, C.Q. Jin, and X.H. Wang. Crystal structure of dense nanocrystalline batio3 ceramics. *Materials Chemistry and Physics*, 111(2):209–212, 2008.

[368] Satoshi Wada, Koichi Yako, Hirofumi Kakemoto, Takaaki Tsurumi, and Takanori Kiguchi. Enhanced piezoelectric properties of barium titanate single crystals with different engineered-domain sizes. *Journal of Applied Physics*, 98(1):14109, 7 2005.

[369] Abhijit Pramanick, Anderson D. Prewitt, Jennifer S. Forrester, and Jacob L. Jones. Domains, domain walls and defects in perovskite ferroelectric oxides: A review of present understanding and recent contributions. *Critical Reviews in Solid State and Materials Sciences*, 37(4):243–275, 1 2012.

[370] Sangwook Kim, Gopal Prasad KHANAL, Hyunwook Nam, Ichiro Fujii, Shintaro Ueno, and Satoshi Wada. Effects of AC-and DC-bias field poling on piezoelectric properties of Bi-based ceramics. *Journal of the Ceramic Society of Japan*, 127(6):353–356, 2019.

[371] Vignesh Kannan, Morgan Trassin, and Dennis M. Kochmann. Kinetics of ferroelectric switching in poled barium titanate ceramics: Effects of electrical cycling rate. *Materialia*, 25:101553, 9 2022.

[372] Toshio Ogawa. Poling Field Dependence of Ferroelectric Properties in Barium Titanate Ceramics. *Japanese Journal of Applied Physics*, 40(9S):5630, 9 2001.

[373] John E. Daniels, Clayton Cozzan, Supphatuch Ukritnukun, Goknur Tutuncu, Jerome Andrieux, Julia Glaum, Chris Dosch, Wook Jo, and Jacob L. Jones. Two-step polarization reversal in biased ferroelectrics. *Journal of Applied Physics*, 115(22):224104, 6 2014.

[374] Stefan Abel, Thilo Stöferle, Chiara Marchiori, Christophe Rossel, Marta D. Rossell, Rolf Erni, Daniele Caimi, Marilyne Sousa, Alexei Chelnokov, Bert J. Offrein, and Jean Fompeyrine. A strong electro-optically active lead-free ferroelectric integrated on silicon. *Nature Communications*, 4(1):1671, 6 2013.

[375] Bing Jiang, Yang Bai, Wuyang Chu, Yanjing Su, and Lijie Qiao. Direct observation of two 90° steps of 180° domain switching in BaTiO3 single crystal under an antiparallel electric field. *Applied Physics Letters*, 93(15):152905, 10 2008.

[376] Z. H. Zhang, X. Y. Qi, and X. F. Duan. Direct determination of the polarization direction of domains in BaTiO 3 single crystal. *Applied Physics Letters*, 89(24):242905, 12 2006.

[377] Z.H. Zhang, X.Y. Qi, and X.F. Duan. Two-step evolution mechanism of multi-domains in BaTiO3 single crystal investigated by in situ transmission electron microscopy. *Scripta Materialia*, 58(6):441–444, 3 2008.

[378] Naoya Shibata, Scott D. Findlay, Yuji Kohno, Hidetaka Sawada, Yukihito Kondo, and Yuichi Ikuhara. Differential phase-contrast microscopy at atomic resolution. *Nature Physics*, 8(8):611–615, 8 2012.

[379] Takao Matsumoto, Masanari Koguchi, Keigo Suzuki, Hitoshi Nishimura, Yasuhiro Motoyoshi, and Nobuyuki Wada. Ferroelectric 90° domain structure in a thin film of BaTi O3 fine ceramics observed by 300 kV electron holography. *Applied Physics Letters*, 92(7):72902, 2 2008.

[380] Robert W. Boyd. The Electrooptic and Photorefractive Effects. In *Nonlinear Optics*, pages 485–513. 2003.

[381] S. Abel, D. Caimi, M. Sousa, T. Stöferle, C. Rossel, C. Marchiori, A. Chelnokov, and J. Fompeyrine. Electro-optical properties of barium titanate films epitaxially grown on silicon. page 82630Y, 2 2012.

[382] Kristy J. Kormondy, Stefan Abel, Florian Fallegger, Youri Popoff, Patrick Ponath, Agham B. Posadas, Marilyne Sousa, Daniele Caimi, Heinz Siegwart, Emanuele Uccelli, Lukas Czornomaz, Chiara Marchiori, Jean Fompeyrine, and Alexander A. Demkov. Analysis of the Pockels effect in ferroelectric barium titanate thin films on Si(0 0 1). *Microelectronic Engineering*, 147:215–218, 11 2015.

[383] Marc Reynaud, Pei-Yu Chen, Wente Li, Therese Paoletta, Sunah Kwon, Dae Hun Lee, Ilya Beskin, Agham B. Posadas, Moon J. Kim, Chad M. Landis, Keji Lai, John G. Ekerdt, and Alexander A. Demkov. Electro-optic response in epitaxially stabilized orthorhombic 2mm BaTiO3. *Physical Review Materials*, 5(3):035201, 3 2021.

[384] Marc Reynaud, Zuoming Dong, Hyoju Park, Wente Li, Agham B. Posadas, Jamie H. Warner, Daniel Wasserman, and Alexander A. Demkov. Microstructural analysis and electro-optic properties of thick epitaxial 3 films integrated on silicon (001). *Physical Review Materials*, 6(9):095201, 9 2022.

[385] Yiyang Wen, Yilin Cao, Haisheng Chen, Xiaona Du, Jiaxing Guo, Jiaying Shen, Fan Zhang, Taiyu Bian, Yu An, Hongda Ren, Zhenping Wu, Weiwei Liu, and Yang Zhang. Enhanced Electro-Optic Coefficients in Single-Crystalline $BaTiO_3$ Thin Films Enabled by Domain Alignment. *Advanced Optical Materials*, page 2303058, 4 2024.

[386] Walter J. Merz. The Electric and Optical Behavior of BaTiO3 Single-Domain Crystals. *Physical Review*, 76(8):1221, 10 1949.

[387] M. Grossmann, S. Hoffmann, S. Gusowski, R. Waser, S. K. Streiffer, C. Basceri, C. B. Parker, S. E. Lash, and A. I. Kingon. Resistance degradation behavior of Ba0.7Sr0.3TiO3 thin films compared to mechanisms found in titanate ceramics and single crystals. *Integrated Ferroelectrics*, 22(1-4):83–94, 1998.

[388] Ming Li, Jian Zhou, Xiaosai Jing, Min Zeng, Sujuan Wu, Jinwei Gao, Zhang Zhang, Xingsen Gao, Xubing Lu, J.-M. Liu, and Marin Alexe. Controlling Resistance Switching Polarities of Epitaxial $BaTiO_3$ Films by Mediation of Ferroelectricity and Oxygen Vacancies. *Advanced Electronic Materials*, 1(6):1500069, 6 2015.

[389] Marina Tyunina. Oxygen Vacancies in Perovskite Oxide Piezoelectrics. *Materials*, 13(24):5596, 12 2020.

[390] Pedram Yousefian, Betul Akkopru-Akgun, Clive A. Randall, and Susan Trolier-McKinstry. Electrical Degradation in Dielectric and Piezoelectric Oxides: Review of Defect Chemistry and Associated Characterization Techniques. 3 2024.

[391] Pietro Bernasconi, Marko Zgonik, and Peter Günter. Temperature dependence and dispersion of electro-optic and elasto-optic effect in perovskite crystals. *Journal of Applied Physics*, 78(4):2651–2658, 8 1995.

[392] COMSOL Multiphysics® v. 6.1. `www.comsol.com` [Accessed: 05-10-2024].

[393] Guillaume Croes, Robert Gehlhaar, and Jan Genoe. COMSOL Fringing Electric Fields in Barium Titanate, 1 2024. `https://figshare.com/articles/dataset/COMSOL_Fringing_Electric_Fields_in_Barium_Titanate/24943233` [Accessed: 05-10-2024].

[394] Lumerical Inc. `www.lumerical.com/` [Accessed: 05-10-2024].

[395] Hui Pang, Shaoyun Yin, Qiling Deng, Qi Qiu, and Chunlei Du. A novel method for the design of diffractive optical elements based on the Rayleigh–Sommerfeld integral. *Optics and Lasers in Engineering*, 70:38–44, 7 2015.

[396] Denis Lebrun, Samir Belaïd, and Cafer Özkul. Hologram reconstruction by use of optical wavelet transform. *Applied Optics*, 38(17):3730, 6 1999.

[397] Cristina Buraga-Lefebvre, Sébastien Coëtmellec, Denis Lebrun, and Cafer Özkul. Application of wavelet transform to hologram analysis: three-dimensional location of particles. *Optics and Lasers in Engineering*, 33(6):409–421, 6 2000.

[398] M. Liebling, T. Blu, and M. Unser. Fresnelets: new multiresolution wavelet bases for digital holography. *IEEE Transactions on Image Processing*, 12(1):29–43, 1 2003.

[399] Yair Rivenson, Yibo Zhang, Harun Günaydın, Da Teng, and Aydogan Ozcan. Phase recovery and holographic image reconstruction using deep learning in neural networks. *Light: Science & Applications*, 7(2):17141–17141, 10 2017.

[400] Hao Wang, Meng Lyu, and Guohai Situ. eHoloNet: a learning-based end-to-end approach for in-line digital holographic reconstruction. *Optics Express*, 26(18):22603, 9 2018.

[401] Zhenbo Ren, Zhimin Xu, and Edmund Y. Lam. End-to-end deep learning framework for digital holographic reconstruction. *Advanced Photonics*, 1(01):1, 1 2019.

[402] Tomoyoshi Shimobaba, Takayuki Takahashi, Yota Yamamoto, Yutaka Endo, Atsushi Shiraki, Takashi Nishitsuji, Naoto Hoshikawa, Takashi Kakue, and Tomoyosh Ito. Digital holographic particle volume reconstruction using a deep neural network. *Applied Optics*, 58(8):1900, 3 2019.

[403] Kaiqiang Wang, Jiazhen Dou, Qian Kemao, Jianglei Di, and Jianlin Zhao. Y-Net: a one-to-two deep learning framework for digital holographic reconstruction. *Optics Letters*, 44(19):4765, 10 2019.

[404] J.R. Fienup. Phase retrieval algorithms a comparison. *Applied Optics*, 21(15):2758, 8 1982.

[405] David Fischer and Stefan Sinzinger. Evaluation of quadratic phase hologram calculation algorithms in the Fourier regime. *Applied Optics*, 59(6):1501, 2 2020.

[406] Chuan Shen, Yifei Qi, Jiali Sun, Shiqi Lv, and Sui Wei. Optimized iterative method for generating phase-only Fourier hologram based on quadratic phase. *Optics Communications*, 500:127313, 2021.

[407] Joseph W. Goodman. *Introduction to Fourier optics*. Roberts and Company Publishers, 2005.

[408] Jianqing Huang, Weiwei Cai, Yingchun Wu, and Xuecheng Wu. Recent advances and applications of digital holography in multiphase reactive/nonreactive flows: a review. *Measurement Science and Technology*, 33(2):022001, 2 2022.

Statement on the use of Generative AI

I did use the generative AI assistance tools namely, MS Copilot and ChatGPT for language assistance and spell checking. Next to that, ChatGPT was used for optimizing priorly written programming code for efficiency.

The text, code, and images in this thesis are my own (unless otherwise specified). Generative AI has only been used in accordance with the KU Leuven guidelines and appropriate references have been added. I have reviewed and edited the content as needed and I take full responsibility for the content of the thesis.

Curriculum Vitae

Guillaume Croes was born in Hasselt, Belgium, on June 27th 1995. He earned his Bachelor's degree in Experimental Physics from UHasselt in 2016. He then pursued a Master's degree in Applied Physics (Bio-Nano track) at the University of Technology Eindhoven in the Netherlands. During his studies, he joined Solliance Thin Film Solar Research for an internship titled "$CuGaO_2$ High Hole Mobility TCO for Si-Perovskite Tandem Solar Cells." For his master's thesis, supervised by Prof. R. Coehoorn, he joined imec as an intern, working on "Light Emission from Quasi 2D Layered Perovskites".

In January 2019, he continued at imec as a PhD researcher within the VIDEO HOLOGRAPHY ERC project led by Prof. Jan Genoe, which aimed to develop a video-rate holographic display. About a year later, he was awarded a Strategic Basic Research Fellowship from FWO ($1S91520N$) funding 4 years of research spanning from November 2020 to October 2023. At the end of 2023, he started a full-time position at imec, focusing on FMCW LiDAR.

List of Publications

First Author Contributions

Peer Reviewed Articles

1. **Croes, Guillaume**, Puybaret, R., Bogdanowicz, J., Celano, U., Gehlhaar, R. & Genoe, J. Photonic metamaterial with a subwavelength electrode pattern. *Applied Optics* **62,** F14 (2023).
2. **Croes, Guillaume**, Gehlhaar, R. & Genoe, J. Subwavelength Custom Wavefront Shaping by a Nonlinear Electro-optic Spatial Light Modulator. *ACS Photonics* **11,** 529–536 (2024).

Conference Presentations and Proceedings

1. **Croes, Guillaume**, Smolentsev, N., Wang, T. H., Gehlhaar, R. & Genoe, J. *Non-linear electro-optic modelling of a Barium Titanate grating coupler* in *Optical Modeling and Performance Predictions XI* (ed Kahan, M. A.) **11484** (SPIE, 2020), 11.
2. **Croes, Guillaume**, Gehlhaar, R. & Genoe, J. *Sub-wavelength custom reprogrammable active photonic platform for high-resolution beam shaping and holography* in *Active Photonic Platforms (APP) 2022* (eds Subramania, G. S. & Foteinopoulou, S.) **PC12196** (SPIE, 2022), 84.
3. **Croes, Guillaume**, Gehlhaar, R. & Genoe, J. *Hologram wavefront shaping by a nonlinear electro-optic spatial light modulator* in *Holography: Advances and Modern Trends VIII* (eds Fimia, A. & Hrabovský, M.) **12574** (SPIE, 2023), 8.

Other Contributions

Peer Reviewed Articles

1. Yan, J., **Croes, Guillaume**, Fakharuddin, A., Song, W., Heremans, P., Chen, H. & Qiu, W. Exploiting Two-Step Processed Mixed 2D/3D Perovskites for Bright Green Light Emitting Diodes. *Advanced Optical Materials* **7** (2019).
2. Fakharuddin, A., Qiu, W., **Croes, Guillaume**, Devižis, A., Gegevičius, R., Vakhnin, A., Rolin, C., Genoe, J., Gehlhaar, R., Kadashchuk, A., Gulbinas, V. & Heremans, P. Reduced Efficiency Roll-Off and Improved Stability of Mixed 2D/3D Perovskite Light Emitting Diodes by Balancing Charge Injection. *Advanced Functional Materials* **29** (2019).
3. Pintor Monroy, M. I., Goldberg, I., Elkhouly, K., Georgitzikis, E., Clinckemalie, L., **Croes, Guillaume**, Annavarapu, N., Qiu, W., Debroye, E., Kuang, Y., Roeffaers, M. B. J., Hofkens, J., Gehlhaar, R. & Genoe, J. All-Evaporated, All-Inorganic CsPbI3 Perovskite-Based Devices for Broad-Band Photodetector and Solar Cell Applications. *ACS Applied Electronic Materials* **3,** 3023–3033 (2021).
4. Elkhouly, K., Goldberg, I., Zhang, X., Annavarapu, N., Hamdad, S., **Croes, Guillaume**, Rolin, C., Genoe, J., Qiu, W., Gehlhaar, R. & Heremans, P. Electrically assisted amplified spontaneous emission in perovskite light-emitting diodes. *Nature Photonics* **18,** 132–138 (2024).

Patents

1. Gehlhaar, R., **Croes, Guillaume**, Elkhouly, K. & Genoe, J. *electro-optical element for spatial optical feedback modulation* 2023.

FACULTY OF ENGINEERING TECHNOLOGY
DEPARTMENT OF ELECTRICAL ENGINEERING
Kapeldreef 75
B-3001 Leuven
Guillaume.Croes@imec.be